UNIVERSIDAD DE CHILE
FACULTAD DE CIENCIAS FÍSICAS Y MATEMÁTICAS
DEPARTAMENTO DE ASTRONOMÍA

A 3-D PERSPECTIVE TO THE INTERNAL PROPERTIES OF LOW AND HIGH-REDSHIFT GALAXIES

TESIS PARA OPTAR AL GRADO DE
DOCTOR EN CIENCIAS, MENCIÓN ASTRONOMÍA

JUAN ANDRÉS MOLINA TOBAR

PROFESOR GUÍA:
ANDRÉS ESCALA ASTORQUIZA

MIEMBROS DE LA COMISIÓN:
EDUARDO IBAR PLASSER
MARK SWINBANK
GUILLERMO BLANC MENDIBERRI
PAULINA LIRA TEILLERY

Este trabajo ha sido parcialmente financiado por CATA, CONICYT y DAS

SANTIAGO DE CHILE
2019

RESUMEN DE LA MEMORIA PARA OPTAR
AL TÍTULO DE DOCTOR EN CIENCIAS, MENCIÓN ASTRONOMÍA
POR: JUAN ANDRÉS MOLINA TOBAR
FECHA: 2019
PROF. GUÍA: ANDRÉS ESCALA ASTORQUIZA

UNA PERSPECTIVA TRIDIMENSIONAL A LAS PROPIEDADES INTERNAS DE GALAXIAS A BAJO Y ALTO CORRIMIENTO AL ROJO

En el presente trabajo estudio la morfología y cinemática de dos muestras de galaxias a bajo y alto corrimiento al rojo (redshift). Analizo la cinemática interna de estas galaxias con objetivo de encontrar posibles correlaciones entre el estado cinemático del medio interestelar (ISM en inglés) y sus propiedades físicas, incluyendo el estudio de la actividad de formación estelar y posibles tendencias evolutivas con respecto al tiempo cósmico. Utilizando observaciones de espectroscopía de campo integrado ('IFS' en inglés) y observaciones inteferométricas tomadas por el gran conjunto milimétrico/submilimétrico de Atacama ('ALMA' en inglés), caracterizo las propiedades del gas ionizado y molecular en galaxias a distintos redshifts.

La dinámica de galaxias es caracterizada por medio del modelaje de los mapa morfo-cinemáticos bidimensionales. Estos son derivados por medio del ajuste de las lineas de emission observadas en cada pixel en los diferentes cubos de datos. Modelos fotométricos realizados a las imágenes en banda ancha de las galaxias son implementados para asistir el modelaje cinemático y sobrellevar la degeneración de parámetros.

A un redshift de $z = 0.8 - 2.2$, presento observaciones espacialmente resueltas de once galaxias detectando la linea de emisión H-alpha (Hα). Combinando estas observaciones con datos de una campaña previa, construyo una muestra total de veinte galaxias. Encuentro que la interacción entre galaxias podría ser el mecanismo que controla la actividad de formación estelar a $z \approx 2.2$, siendo gradualmente menos importante ya a $z \approx 0.8$.

Para dos galaxias seleccionadas desde la muestra anterior, se observa la linea de emisión CO($J = 2-1$), resuelta a escalas de un kilopársec, usando ALMA. La emisión proveniente de sólo una galaxia es detectada a estas escalas. Para este sistema se observa una concordancia entre la morfo-cinemática detectada por el gas ionizado y el gas molecular. Para esta galaxia, derivo una fracción de materia oscura ($f_{\rm DM} \equiv M_{\rm DM}/M_{\rm dyn}$) de 0.6 ± 0.1, consistente con el valor promedio de $f_{\rm DM}$ obtenido desde el análisis de sobreposición y promedio de curvas de rotación de galaxias en un rango de redshift similar.

Por otro lado, a bajo redshift, también ocupo observaciones espacialmente resueltas del contenido de gas molecular, hechas por ALMA, en galaxias hasta $z \approx 0.35$. Encuentro una correlación entre la cinemática galáctica y la razón de luminosidad entre la linea de emisión del Carbono ionizado y el infrarojo ([CII]/IR), sugiriendo que el llamado 'déficit del [CII]' está relacionado con el estado dinámico de las galaxias.

De mis resultados, concluyo que el estado morfo-cinemático de las galaxias está íntimamente relacionado a las propiedades físicas del ISM. Esto implica que la dinámica galáctica no puede ser pasada por alto para obtener una completa caracterización de la evolución de galaxias a través del tiempo cósmico.

Abstract

A 3-D PERSPECTIVE TO THE INTERNAL PROPERTIES OF LOW AND HIGH-REDSHIFT GALAXIES

In the present work, I study the morpho-kinematics of two moderate galaxy samples at low- and high-redshift. I analyse the internal kinematics of these galaxies aiming to find possible correlations between the kinematic state of the interstellar medium (ISM) and its physical properties, including the study of the star formation activity and possible evolutionary trends with cosmic time. Through the use of Integral Field Unit (IFU) and Atacama Large Millimeter/submillimeter Array (ALMA) observations, I characterize the ionized and molecular ISM gaseous phases on galaxies at different redshifts.

The galaxy dynamics are characterized through the modelling of the two-dimensional morpho-kinematic maps. These are derived by fitting the observed emission lines in each pixel of the datacubes. Photometric models from broad-band galaxy images are implemented to aid the kinematic modelling and overcome parameter degeneracy.

At redshift $z = 0.8 - 2.2$, I present spatially-resolved observations of eleven galaxies detected in the H-alpha emission line (Hα). Combining these observations with data from a previous campaign, I construct a total sample of twenty galaxies. I find that galaxy interactions might be the dominant mechanism controlling the star-formation activity at $z \approx 2.2$ but they become gradually less important down to $z \approx 0.8$.

For two galaxies taken from the above sample, I observe the CO($J = 2 - 1$) emission line, resolved at ∼kpc-scales, using ALMA. I just detect the emission coming from one galaxy at these scales. For this system, I observe that the morpho-kinematics traced by the ionized and molecular gas agree. For this galaxy, I derive a dark matter fraction ($f_{\rm DM} \equiv M_{\rm DM}/M_{\rm dyn}$) of 0.6 ± 0.1, in agreement with the average $f_{\rm DM}$ value derived from stacked rotation curve analysis of galaxies at similar redshift range.

On the other hand, at low-redshift, I use ALMA spatially-resolved observations of molecular gas on galaxies up to $z \approx 0.35$. I find a correlation between the galactic kinematics and the ionized Carbon to Infra-red luminosity ratio ([CII]/IR), suggesting that the so-called '[CII] deficit' is related to the dynamical state of the galaxies.

I conclude that the morpho-kinematic state of galaxies is intimately related to the ISM physical properties. This implies that the galaxy dynamics can not be overlooked to obtain a complete characterisation of the evolution of galaxies across cosmic time.

Agradecimientos

Agradezco a mi profesor guía, Andrés Escala, quien me dio la oportunidad de trabajar junto a él y hacer posible esta tesis. Junto con el profesor Eduardo Ibar, les agradesco especialmente de proveerme las herramientas necesarias para hacer investigación, por introducirme en sus redes de colaboración, por apoyarme en la participación en importantes conferencias, por todas sus contribuciones durante mi trabajo, por las buenas experiencias compartidas y, por sobre todo, haberme brindado la confianza y libertad necesaria que me ha permitido elaborar y desarrollar mis propios proyectos científicos.

Agradezco el apoyo de todas las personas con quienes he compartido en Calán durante estos años. Todas las experiencias vividas serán gratamente recordadas. Una mención especial a los castores/marmotas cascarrabias y los autodenominados 'weonos' del tercer piso con quienes siempre ha sido un placer compartir. Particularmente agradesco a Grecco Oyarzun por aportar cordura en nuestros tiempos de ocio, a Matias Díaz por no haberme formateado el pc, a Jorge Martínez por haber estado siempre presente en Calán, a Juan Pablo Cordero por siempre poner la gota de seriedad e incentivo a trabajar, a Sebastián Marchi por siempre brindar tranquilidad y serenidad en la oficina y a José Peña por guiarnos en el camino de la sabiduría gurística. Agradezco también a Wamba quien, a pesar de haber llegado recién este año, se ha integrado muy bien a nuestra oficina.

También agradesco a la Comisión Nacional de Investigación en Científica y Tecnológica (CONICYT) a través de sus becas de Doctorado Nacional (CONICYT-PCHA/Doctorado-Nacional/2014-21140483), al Departamento de Astronomía de la Universidad de Chile, a la Sociedad Chilena de Astronomía (SOCHIAS) a través de la beca Adelina Gutiérrez y al Centro de Astrofísica y Tecnologías Afines (CATA) por su apoyo y financiación.

Esta tesis usa estos datos obtenidos por ALMA: ADS/JAO.ALMA#2017.1.01674.S, ADS/JAO.ALMA#2015.1.00862.S, ADS/JAO.ALMA#2015.1.01012.S, ADS/JAO.ALMA#2012.1.00402.S, ADS/JAO.ALMA#2013.1.00530.S, ADS/JAO.ALMA#2012.1.01080.S. ALMA es una colaboración de ESO (representado sus miembros estados), NSF (USA) and NINS (Japón), junto con NRC (Canada), NSC y ASIAA (Taiwan), y KASI (República de Corea), en cooperación con la República de Chile. El Joint ALMA Observatory es operado por ESO, AUI/NRAO y NAOJ. Este trabajo también está basado en observaciones recolectadas por la Organización Europea para Investigación Astronómica en el Hemisferio Sur bajo el programa ESO con ID: 092.A-0090(A).

Finalmente, agradesco a los árbitros anónimos por su gran dedicación en la leectura, comentarios y sugerencias a cada una de las publicaciones que conforman esta tesis.

Contents

List of Tables

List of Figures

Chapter 1

Introduction

Large scale surveys suggest that the properties of the Universe are the same for all observers when a large volume is considered. The Universe is said to be homogeneous and isotropic, i.e., there is no preferred direction and the distribution of matter is the same wherever an observer looks. This implies that the Universe can be treated as one entity and its dynamics are described by the general relativity theory. However, on small scales, the Universe is neither isotropic nor homogeneous. The 'building blocks' of the Universe are called galaxies, which often congregate in groups and clusters connected to each other through long filaments. These cosmic connections form the cosmic web, the structure which seems to repeat itself when viewed in hundred of Mega-Parsecs (Mpc), suggesting the isotropy and homogeneity of the Universe.

The lambda cold dark matter (ΛCDM) paradigm is successful to explain the large-scale structure of the Universe in great detail (e.g. Spergel et al. 2007; Vogelsberger et al. 2014; Schaye et al. 2015). In this scenario, dark matter (DM) is the most abundant matter in the universe and it is distributed in haloes, leading the structure formation through the gravitational collapse (e.g. Springel et al. 2005). In a ΛCDM cosmological model, structure forms hierarchically with objects growing through a series of halo mergers and the feeding of gas from the intergalactic medium (IGM, Kereš et al. 2005). The baryonic matter concentrates in the centres of the DM haloes, forming galaxies and stars.

Understanding how galaxies form and evolve over cosmic time is a major goal in modern extragalactic astrophysics. It requires the characterization of the stellar mass build-up within the DM haloes across cosmic time, a problem which is usually addressed by studying the cosmic star formation rate density (SFRD, e.g. Madau et al. 1996), i.e, the study of the star formation activity, normalized by volume and across cosmic time. The SFRD has important implications for the reionization of the Universe, the cosmic chemical evolution, the transformation of gas into stars and the build-up of stellar mass. It can be characterized by three main phases: (1) an steady rise at early cosmic times ($z \sim 10 - 6$, Bouwens et al. 2011), corresponding to the epoch when first luminous objects reionized the neutral IGM (e.g. Finkelstein et al. 2012); (2) the peak epoch at $z \sim 1 - 3$, during about half of the actual stars where formed (e.g. Reddy et al. 2008; Shapley 2011); and (3) the subsequent one order of magnitude decline to the present value (e.g. Madau et al. 1996; Madau & Dickinson 2014)

The overall decline of the SFRD since $z \sim 2$ (e.g. Madau et al. 1996; Sobral et al. 2013a; Khostovan et al. 2015) coincides with the decrease of the average fraction of molecular gas mass in galaxies (e.g. Tacconi et al. 2010; Geach et al. 2012; Carilli & Walter 2013). This behaviour is thought to match the cosmic evolution of the mass in stars, and the molecular gas content ($M_{\rm H_2}$) of the Universe, hence it provides a logical interpretation for the interplay between, perhaps, the main actors controlling the growth of galaxies (e.g. Madau & Dickinson 2014). One possible scenario is that the high levels of star formation at those redshifts may be promoted and maintained by the continuously fed gas from the intergalactic medium and therefore, the star-formation activity may be driven by internal dynamical processes within the interstellar medium (ISM; Kereš et al. 2005; Bournaud et al. 2007; Dekel et al. 2009b). In this case, secular processes drive the galaxy evolution and spatially-resolved observations of the morpho-kinematics of galaxies are critical to measure their internal dynamical properties.

Large observational programs surveying hundreds of galaxies in the local Universe (e.g. MANGA & SAMI; Allen et al. 2015; Bundy et al. 2015), but also at high-redshift ($z \sim 1$; e.g. Stott et al. 2016), have started to study the cosmic evolution of the global ISM properties (e.g. Wisnioski et al. 2015). These data have lead to a sequence of discoveries with profound implications on, for example, how stars are born within the galactic disk (e.g. Förster Schreiber et al. 2009) and the relative amount of dark matter content to the total mass in galaxies at early times (e.g. Genzel et al. 2017; Lang et al. 2017; Tiley et al. 2019). Two topics that the astronomy community has been intensely debating in the last years (e.g. Whitaker et al. 2014; Wisnioski et al. 2015; Stott et al. 2016; Burkert et al. 2016; Simons et al. 2017; Turner et al. 2017; Drew et al. 2018; Förster Schreiber et al. 2018; Girard et al. 2018; Guo et al. 2018; Lovell et al. 2018; Patrício et al. 2018; Tacconi et al. 2018; Teklu et al. 2018; Übler et al. 2018; Xue et al. 2018; Price et al. 2019). However, most of this research has been based on near Infrared (IR) observations of emission lines that trace the ionized gas ISM phase, i.e, the un-obscured gaseous phase of galaxies.

Observations of the molecular gas distribution in galaxies are critical. Local Universe studies have characterized the molecular gas morphology (e.g. Helfer et al. 2003), and the rate at which the molecular gas is converted into stars (e.g. Leroy et al. 2008, 2013). However, the molecular gas kinematics have been just recently measured the in a significant number of galaxies ($\gtrsim$ 100, e.g. Bolatto et al. 2017). Beyond the local Universe, molecular gas observations mostly correspond to point-like observations (e.g. Tacconi et al. 2010, 2013) and spatially-resolved observations of the most bright, massive or highly magnified galaxies (e.g. Swinbank et al. 2015). The evolution of the molecular gas dynamical and morphological properties across cosmic times remains a major gap in our knowledge (Carilli & Walter, 2013). These observations may be also essential to understand the star formation activity and the formation of galaxies (Genzel et al., 2008; Obreschkow et al., 2009).

Great efforts are being made to study the molecular gas properties in galaxies at earlier epochs. With the Atacama Large Millimeter/submillimeter Array (ALMA) is now possible to obtain spatially-resolved observations of the molecular gas content beyond the local Universe (e.g. Saintonge et al. 2013). Furthermore, with this interferometer, galaxies can be observed at spatial scales comparable to those reached from the ionized gas based observations. However, it must be considered that observing the spatial distribution of the molecular gas content in star-forming galaxies is still, relatively to ionized gas tracers, highly

time consuming. This is true even for the present times of ALMA and the NOrthem Extended Millimetre Array (NOEMA). Therefore, studying the molecular gas distribution and dynamics in moderate galaxy samples in the early Universe is still a great challenge, however is key to understand the ISM properties and galactic evolution across cosmic time.

This thesis is carried out in the era of large telescopes and interferometric radio-telescopes, such as the Very-Large Telescope (VLT) and ALMA, where sub arc-second observations make possible to resolve the spatial distribution of the interstellar medium (ISM) in large samples of galaxies across different cosmic epochs. The possibility to take observations which deliver data-cubes (i.e. a spectrum per pixel) allow to study the internal motion of the gas using different absorption/emission line ISM tracers, i.e., the observation of the gas *kinematics* and posterior characterization of the state of the galaxies via their galactic dynamics.

Further improvements to the observational angular resolution below the decimals of arc-seconds are not currently possible at near-IR wavelengths. By using adaptive-optics (AO) techniques, the large telescopes that detect light at the optical (3800Å–7400Å) and near-Infrared (8000Å–30000Å) wavelengths are already obtaining diffraction-limited observations, i.e., at the physical limit of their optical system. On the other hand, ALMA was designed to deliver millimetre/submillimetre observations at comparable angular resolution, and beyond, using its longest baselines. During the next decade higher angular resolution observations will become possible to be performed with the next generation of space and ground based telescopes, such as the James Webb Space Telescope (JWST), the Thirty Meter Telescope (TMT), the Giant Magellan Telescope (GMT) and the Extremely-Large Telescope (ELT).

In the next sections of this chapter, I will introduce the astronomical context of this work, highlighting the spatially-resolved study of low- and high-redshift galaxy samples. I will overview the kinematic studies of star-forming galaxies from the literature, highlighting the main ionized gas galaxy surveys that are related to my thesis project. I will comment on the state-of-the-art molecular gas spatially-resolved observations of galaxies across different cosmic times, and I will also briefly review the current knowledge about the star-formation activity on galaxies at kilo-parsec (kpc) scales. Finally, I will summarize the main objectives of this thesis work and give a brief outline of its structure.

1.1 Historical Perspective

More than 100 years have passed since the first measurement of the kinematic on galaxies. Vesto M. Slipher discovered the rotation of galaxies by detecting the tilt of an absorption spectral line while observing M105 (Slipher, 1914). He recognized this spectral line behaviour as 'a similar phenomenon when observing planets'. Regardless of the observational limitations, during this epoch, the rotation of several spirals were measured (e.g. Pease 1916). Most of the early work on galactic dynamics was focused in the study of rotation from observations targeting the ionized hydrogen (HII) regions (e.g. Babcock 1941; Mayall & Aller 1942) and later using the neutral hydrogen (HI) 21-cm line (van de Hulst et al. 1957; Argyle 1965). This early rotation-based work culminated with two main discoveries; (1) the correlation between the luminosities and rotational velocities and; (2) the flatness of the rotation curves at larger

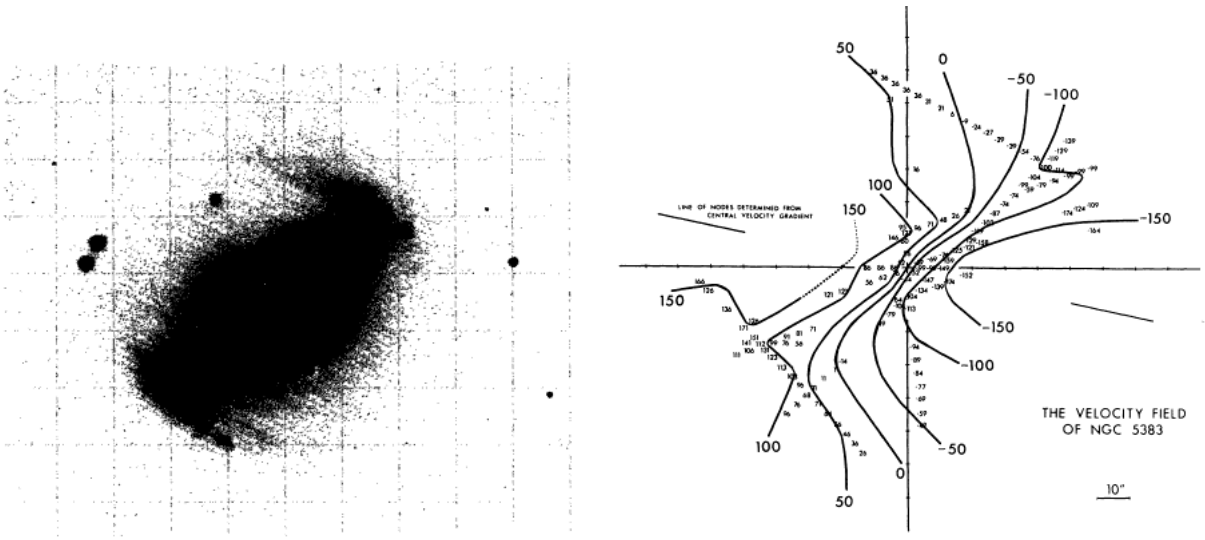

Figure 1.1: The kinematics of bars illustrated for the NGC5383 case. *Left*: Optical picture of the galaxy. *Right*: Velocity field derived from the emission lines observed on the optical slit spectra. Both images are taken from (Peterson et al., 1978).

radii in local galaxies. The well-known Tully-Fisher Relationship (TFR; Tully & Fisher 1977) and the basic evidence of dark matter haloes (Rubin & Ford, 1970; Roberts & Rots, 1973; Rubin et al., 1978), respectively.

During this epoch, the galaxy structure and kinematics were also analysed (e.g. Lindblad 1959). The surface photometry studies revealed the exponential nature of the surface brightness light distribution of disc galaxies (de Vaucouleurs, 1958, 1959; Freeman, 1970). With the advent of improved angular resolution HI observations and the ability to overcome the spiral arm confusion (Allen, 1975), the density-wave theory (Lin & Shu, 1964, 1966) proved to be successful to explain the spiral pattern in nearby galactic discs (e.g Rots 1975). On the optical side, long-slit optical observations were mostly focused on the study of the non-circular motions presented in the nuclear part of galaxies, such as bars and/or oval distortions (Fig. 1.1; e.g. van der Kruit & Allen 1978). This proved the importance of the internal secular evolution in the evolution of disc galaxies (Kormendy & Kennicutt, 2004).

On the other hand, millimetre and sub-millimetre radio telescopes started their development in the early sixties. By using the '5-foot' ($\approx$1.52 m) telescope, the earlier observations were focused to understand the properties of the Sun, Venus and Jupiter atmospheres. Given the success of such observations, the '36-foot' ($\approx$ 11 m) radio-telescope was build by the end of the decade and immediately started to revolutionize the astronomic knowledge at this wavelength range.

One of the first ISM molecules observed at millimetre wavelengths was the Carbon Monoxide molecule ($^{12}C^{16}O$, hereafter CO). Its emission was discovered by Wilson et al. (1970) in the Orion nebula using the 36-foot telescope. During the seventies, many other molecules were also detected (e.g. silicon monoxide, ethyl alcohol). During this decade, surveys of molecular clouds in the Galaxy allowed to determine the molecular gas spatial distribution in the inner part of the Milky Way (e.g. Solomon et al. 1972; Scoville & Solomon 1975), the

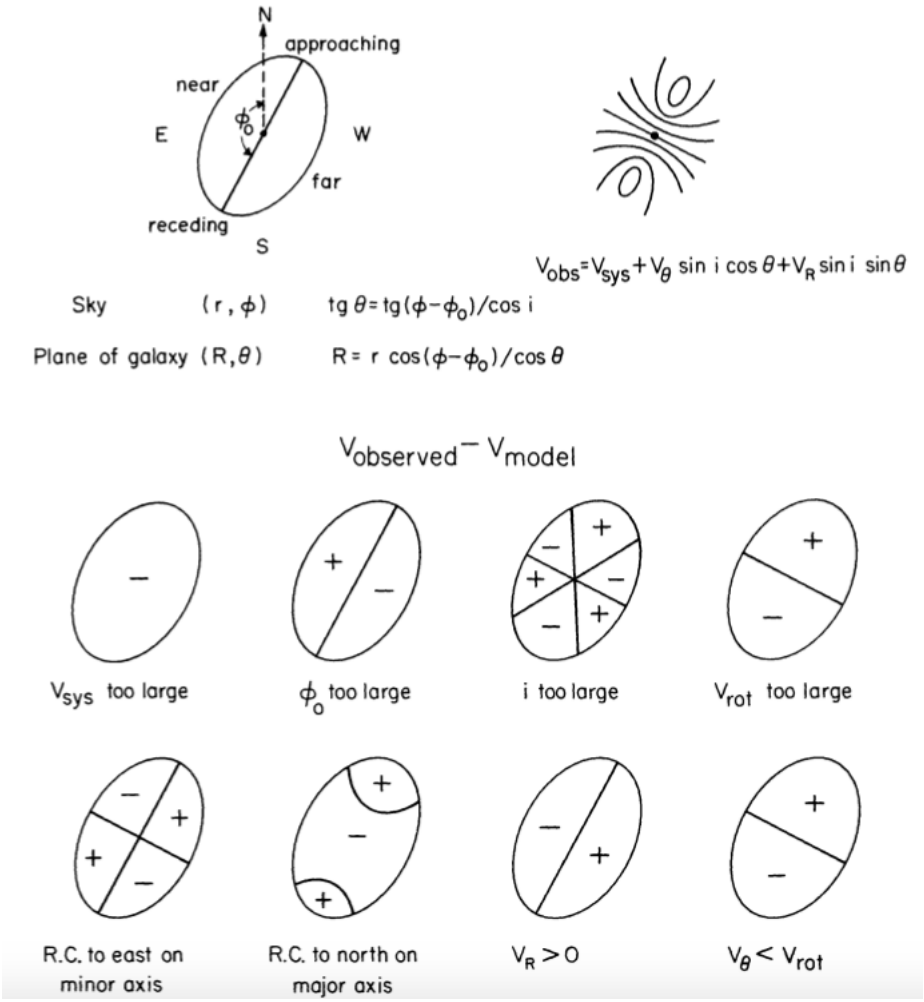

Figure 1.2: Representation of the galactic disc rotation and the determination of disc parameters. The galaxy with the motion described in *top-left* shows a rotation pattern represented in *top-right* where lines represent iso-velocity contours. The closed iso-velocity contours encircle the region where the maximum velocity is observed. In this picture, $V_{\rm sys}$ is the systemic velocity, V_θ and $V_{\rm R}$ are the tangential and radial velocities. 'i' is the inclination angle of the normal to the galaxy plane to the line-of-sight (LOS). ϕ_0 is the position angle (PA) of the major kinematic axis and R.C. detones 'rotation centre'. The residual maps scketches the case where all but one of the kinematic parameters are chosen correctly. The patterns in the residual maps are different, indicating that all of them can be determined independently from the velocity field. The last two residual map examples show the effect of non-circular motions in the radial and tangential direction. This representation is taken from Warner et al. (1973).

dominant gaseous phase in terms of mass (Stecker et al., 1975). In parallel, the first extra-galactic CO emission was also detected by these early Galactic surveys (e.g. Rickard et al. 1975). In the next decades, several of hundred galaxies were also observed in CO emission (Young & Scoville, 1991). The first detections at a significant redshifts ($z \gtrsim 1$) corresponded to Ultra Luminous Infrared Galaxies (ULIRGs), revealing very large molecular gas reservoirs (e.g. Brown & Vanden Bout 1991). However, those observations were limited by telescope sensitivity, impeding the rapid grow of CO observations at early cosmic epochs (Solomon & Vanden Bout, 2005).

Early kinematic modelling was mainly used to describe the galactic rotation pattern observed from the HI and HII data. Rotation velocities ($V_{\rm rot}$) were derived from the velocity field by assuming that the measurements refer to positions on a single inclined plane. The other important assumption was that the ordered rotation was dominant compared to the non-circular motions, i.e., non-circular motions are not producing the observed large-scale pattern from the data (van der Kruit & Allen, 1978). Chi-square (χ^2) numerical recipes were usually implemented to derive the kinematic parameters in the line-of-sight velocity field (Fig. 1.2; e.g. Warner et al. 1973).

Signal-to-noise (S/N) is one of the main problems that limit the study of kinematics in high-redshift galaxies ($z \sim 1$; e.g. Lilly et al. 1995). Based on multi-slit spectrograph observations, early work was focussed to determine the integrated velocity dispersion values (e.g. Koo et al. 1995). These measurements were principally used to test the possible evolution of the TFR across cosmic times (Fisher et al., 1996). The first resolved long-slit work at significant redshift, i.e. constructing true rotation curves, was done by Vogt et al. (1996) using the Keck telescope. Although limited by spatial resolution ($0\farcs8 - 0\farcs95$ seeing), this work found that high-redshift galaxies present similar rotation curves to low-redshift counterparts and that 'some massive discs were in place by $z \sim 1$' (Vogt et al., 1996). The spatial resolution is a key limitation, a problem that even modern spatially resolved kinematic studies have to deal with. In the favoured cosmological model (ΛCDM), one arcsecond corresponds to $\sim 1.8 - 8.6$ kpc for $0.1 < z < 2$. This scale is comparable to the local spiral galaxies size which have exponential scale length of few kpcs (typically $\sim 1 - 5$ kpc; Freeman 1970), meaning that galaxies at high-redshift are just marginally spatially-resolved in observations carried under natural seeing conditions ($\sim 0\farcs5 - 1''$). Kinematic models including the convolution with the observational Point Spread Function (PSF) were developed to overcome this spatial resolution limitation (Vogt et al., 1996; Simard & Pritchet, 1998), a procedure that is in the core of modern kinematic fitting algorithms.

1.1.1 The structure of local galaxies

Within the ΛCDM cosmology, galaxies lie within dark matter haloes in which the non-baryonic component dominates the galactic dynamics and stablish the large scale structure for galaxy formation (e.g. Blumenthal et al. 1985). Galaxies in the local Universe can be categorized in two groups, depending on colour, commonly referred as the 'red sequence' and the 'blue cloud' (Strateva et al., 2001; Baldry et al., 2004). Most of the galaxies lie in one of these two groups, while the rest are located between them in the so-called 'green valley'. The red sequence and blue cloud colour classes also separate the galaxies by morphology.

The majority of the red sequence galaxies are early-type (or elliptical) massive galaxies with negligible gas, star-formation activity and kinematics dominated by velocity dispersion (σ_v, de Zeeuw & Franx 1991), while mostly of the blue cloud systems are rotating star-forming disc galaxies presenting an exponential radial density profile (Blanton & Moustakas, 2009; van der Kruit & Freeman, 2011). The latter systems also present a tight correlation ($\lesssim 0.3$ dex) between the star formation rate (SFR) and stellar mass ($M_\star$) of the galaxies, defining the so-called 'main-sequence' of star-forming galaxies (e.g. Brinchmann et al. 2004; Noeske et al. 2007; Whitaker et al. 2012).

When the rotational motions of disc galaxies are studied, 'flat' rotation curves arise from the observational data (Rubin & Ford, 1970; Rubin et al., 1978). This occurs in the regime where the luminous matter surface brightness exponentially decreases, but the rotation velocity ($V_{\rm rot}$), e.g. traced by HI, remains flat or increasing. The typical values of rotational velocity at the outskirts of local galaxies are in the range $150-300\,{\rm km\,s^{-1}}$ (Glazebrook, 2013). The baryonic TFR relates the rotational velocity determined by the dark matter content and the baryonic matter traced by luminosity or stellar mass in galaxies (e.g. Verheijen 2001). This relationship suggests that galaxies present a roughly constant ratio of dark matter to stellar mass, in clear contradiction to the spatial distribution of baryonic matter within galaxies. This 'fine-tuning' of the ΛCDM model have motivated the develop of alternative theories of gravity, such as the 'MOdified Newtonian Dynamics' (MOND) framework in which the dark matter content is not longer needed (e.g. McGaugh & de Blok 1998; McGaugh 2012).

The vertical structure of local disc galaxies has been also studied. It can be separated in the 'thin' and 'thick' discs components (see Fig. 1.3). The thick disc component contain old, red and low metallicity stellar populations (Yoachim & Dalcanton, 2008). It has low surface brightness, with scale height in the order of $\sim 1400\,{\rm pc}$ and vertical velocity dispersion ($\sigma_{v,z}$) of $\sim 40\,{\rm km\,s^{-1}}$ (Pasetto et al., 2012). On the contrary, the thin disk is the most visible component of disc galaxies, where young stellar populations with typical ages up to $\sim$10 Gyr are located. The stellar thin disc is typically found to have a $200-300\,{\rm pc}$ scale height with vertical velocity dispersions values in the order of $\sim 20\,{\rm km\,s^{-1}}$ (van der Kruit & Freeman, 2011).

The gaseous phase of the ISM is located in even a thinner layer within the thin disc. In this region, giant molecular clouds (GMCs), dust, HII regions and blue massive young stars are located. This thinner layer has scale height of only $\sim$50 pc with velocity dispersion values of only $\sim 5-10\,{\rm km\,s^{-1}}$ in the Milky Way. In this region is where today the star-formation activity takes place with the youngest stars sharing the kinematics of the gas where they form (Glazebrook, 2013). As the stellar age increases, stars start to scatter off, rising the velocity dispersion values. This kinematic evolutionary trend explains why the thin stellar disc has larger characteristic velocity dispersion value than the thinner layer. The lag of the stellar disc rotation behind the gas disc, a phenomenon known as 'asymmetric drift', can also be explained by the different $\sigma_{v,z}$ values measured from both components (Binney & Tremaine, 2008). The higher stellar velocity dispersion values provide an additional dynamical support against the galaxy self-gravity. Hence, the gravitational stability of the stellar component is not longer provided just by rotation.

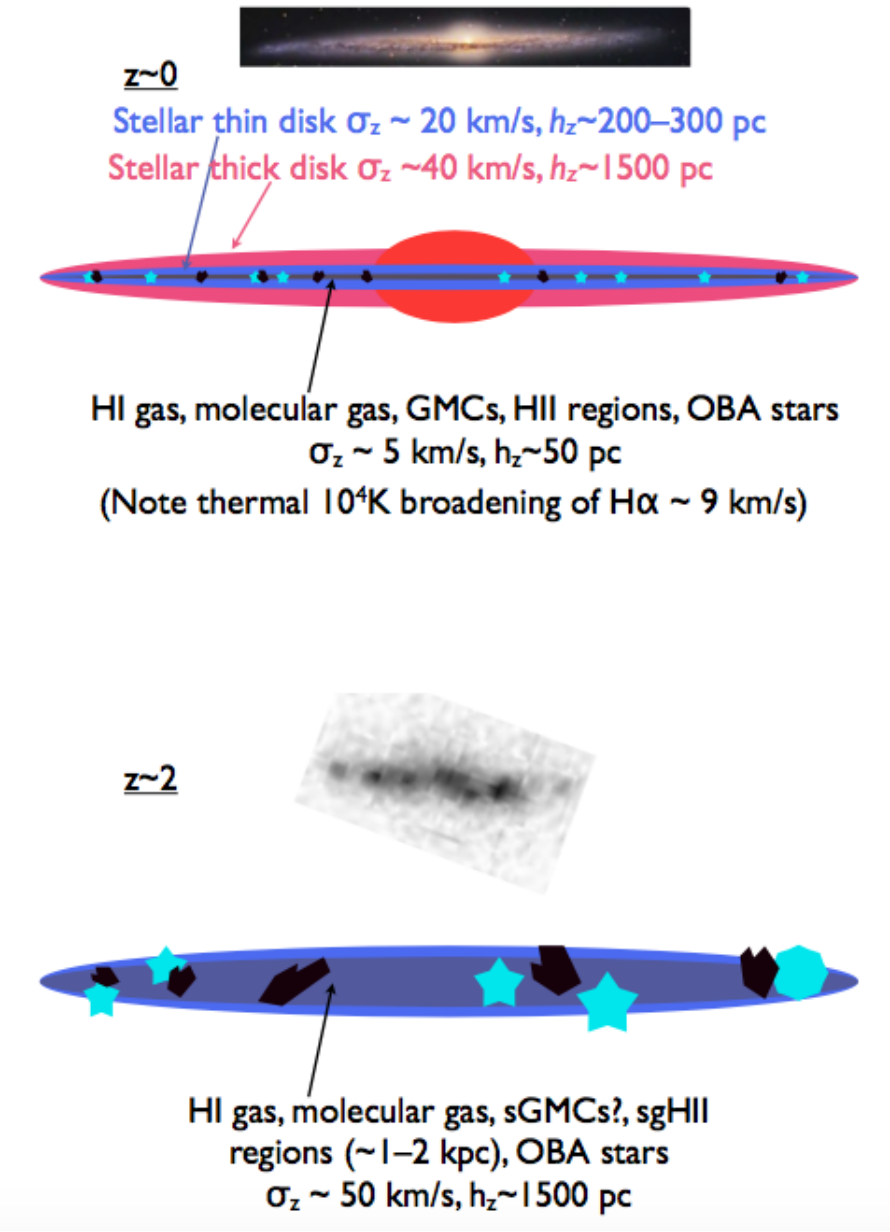

Figure 1.3: Illustration showing the edge-on vertical structure of local disc galaxies and, in comparison, a $z \sim 1$ high-redshift galaxy. *Top:* thin and thick stellar disc components of the local spirals (including the Milky Way) and the thinner gas layer in the centre where the GMCs, HII regions, the diffuse gas phase and young stars are located. *Bottom:* a highly turbulent clumpy high-redshift thick ($\sim$ 1 kpc) disc containing massive HII regions and possible super-Giant Molecular Clouds. This image is adapted from Glazebrook (2013).

The kinematics of the thinner layer can be measured by observing the ionized gas emission, which is usually measured by observing the H$\alpha\lambda$6562.8 emission line. In star-forming disc galaxies, this emission line mainly comes from HII regions, being originated by the recombination of the hydrogen atoms previously ionized by the ultraviolet flux coming from the blue massive young stars. Given the low velocity dispersion of the HII regions in the thinner galactic layout, the Hα line width is mainly dominated by the thermal broadening due to the HII ionized gas characteristic temperature ($\approx 10^4\,\mathrm{K} \sim 9\,\mathrm{km\,s^{-1}}$) and the turbulent broadening due to HII internal motions ($\sim 20\,\mathrm{km\,s^{-1}}$; Shields 1990). This raises the typical dispersion velocity values to the $\sim 20 - 25\,\mathrm{km\,s^{-1}}$ values typically found by observations (Andersen et al., 2006; Epinat et al., 2010).

Is worth to mention that higher Hα velocity dispersion values are also seen in galaxies. Those values are usually interpreted as indicators of outflowing gas from the disc plane (e.g Westmoquette et al. 2008; Arribas et al. 2014). These gaseous outflows could be produced by different feedback processes such as supernovae explosions, stellar winds or active galactic nuclei (AGN; e.g. Harrison et al. 2014; Förster Schreiber et al. 2018; Rodríguez del Pino et al. 2019). In the latter case, non-obscured AGN-driven outflows are easily recognized from the broad emission line widths as these can reach from the few hundreds (∼300) to the thousands of $\mathrm{km\,s^{-1}}$ (e.g. Genzel et al. 2011; Wisnioski et al. 2012).

1.2 Integral Field Unit observations

In the last two-decades, the development of astronomical instrumentation, such as Integral Field Spectroscopy (IFS), has played a key role in spatially-resolved studies in a diverse class of sources. With this technique, it is possible to collect a spectrum of every point in the 2-D image of an object (Allington-Smith, 2006), which is contrasted with the classical technique of long-slit spectroscopy where spectra are collected along a 1-D slice (whose direction must be chosen in advance; e.g. Fig. 1.1). Moreover, by using AO technology, Integral Field Unit (IFU) observations with angular diffraction limited resolution – typically $\approx 0\farcs15$ arcsec on 8-m telescopes– have been achieved. This is important as one arcsecond corresponds to $\sim 8\,\mathrm{kpc}$ at $1 < z < 3$ in the ΛCDM cosmology, i.e. a spatial scale comparable to the sizes of disc galaxies at high-redshifts.

This thesis uses observations taken with the Spectrograph for INtegral Field Observations in the Near Infrared (SINFONI; Eisenhauer et al. 2003) instrument, which is a flexible IFS on the 8-m VLT capable of both natural seeing and AO modes of operation. With SINFONI the dynamics of galaxies are measured by observing emission lines within the field-of-view (FoV). This is done by means of the measurement of the emission line shift produced by the rotational motions and the emission line width broadening usually assumed to be produced by unresolved motions within the PSF of the observation. Specifically, I measure the ionized gas kinematics of galaxies traced by the Hα hydrogen recombination emission line. For that reason I review the main ionized gas galaxy surveys at low- and high-redshift that are related to this work.

1.2.1 Low-redshift galaxy IFU surveys

At low redshift, IFU surveys have measured the morpho-kinematics of large galaxy samples in great detail. Surveys have covered both red-sequence early types galaxies (e.g. Cappellari et al. 2007) and blue cloud star-forming disc galaxies (e.g. Sánchez et al. 2012), principally aiming to study evolutionary trend fingerprints on large galaxy samples. Local galaxy major mergers are also studied in detail (e.g. Colina et al. 2005; Piqueras López et al. 2012), although they comprise up to the $\sim 1-2\%$ of the total local galaxy population (Xu et al., 2012). These studies, however, are not representative of the bulk of the merger galaxy population. The analysis of their merging structure is usually addressed individually and based on prominent morphology properties (e.g. double nuclei, tidal tails). Nevertheless, on-going major mergers usually display complex ionized gas kinematics maps, and non-parametric kinematic techniques, such as *kinemetry* (Krajnović et al., 2006) may be helpful to analyse such kind of systems. In this section, I review some of the most influential IFU-based local galaxy surveys for this thesis, mentioning in particular their main results.

The CALIFA survey

The CALIFA ('Calar Alto Legacy Integral Field Area') survey is a legacy IFU survey sampling ∼600 galaxies in the local Universe ($0.005 < z < 0.03$). The survey is designed to address fundamental issues in galaxy evolution by mapping entire galaxies in their emission and absorption properties. The galaxies were selected from the Sloan Digital Sky Survey (SDSS) Data-Release 7 (Abazajian et al., 2009) by imposing an isophotal diameter size (D_{25}) in the range of $45'' < D_{25} < 80''$ and a declination value DEC $> 7^{\circ}$ due to telescope location and visibility constrains. The stellar mass range covered is $9.75 < M_{\star} < 11.44$ (Walcher et al., 2014). The CALIFA survey principally aims to derive the stellar population content in age and metallicity, the distribution of the ionized gas, and its chemical abundance (Sánchez et al., 2012).

This survey shows that local galaxies without clear evidence of interaction present negative metallicity gradient within two disc half-light radii ($r_{1/2,\mathrm{g}}$; Sánchez et al. 2014). Beyond that radius, there is a flattening in the metallicity which is probably related to the secular evolution of galaxies. The galaxy metal content is found to be correlated with stellar mass density and stellar mass. This suggests that galaxy discs grow inside-out, with metal enrichment driven by the local star formation history (SFH) with probably small galaxy-by-galaxy variation (Sánchez et al., 2014).

The inside-out growth of galaxies scenario is also supported by stellar structure analysis done for CALIFA galaxies (Pérez et al., 2013). Negative stellar population age radial gradients are present in most of the galaxies, with larger gradients observed in the most massive ($\sim 10^{11}\,M_{\odot}$) disc galaxies. By performing SFH analysis using stellar population spectral synthesis fossil record techniques, massive galaxies in CALIFA show evidence of faster inner and outer regions growth compared to systems with lower mass, i.e. a signal of spatially preserved downsizing (González Delgado et al., 2015).

The SAMI survey

The SAMI ('Sydney-AAO Multi-object Integral field spectrograph') survey is one of the largest IFU surveys observing galaxies in the local Universe (Bryant et al., 2015). The SAMI survey targets 3400 galaxies drawn from the Galaxy And Mass Assembly survey (GAMA survey; Liske et al. 2015). The galaxy sample is restricted to $0.004 < z < 0.113$ and stellar mass range of $7.5 < \log(M_\star/M_\odot) < 11.6$, with low-$M_\star$ galaxies preferentially observed at lower redshifts (Bryant et al., 2015) . The three main scientific drivers of this survey are[1]: (1) how does the galaxy's environment influence its evolution?; (2) how does gas get into and out of galaxies?; and (3) how is mass and angular momentum built up in galaxies?.

The second main scientific driver is addressed by the analysis of skewed emission line profiles which reflect different kinematic components overlapping on the line-of-sight (e.g. Ho et al. 2014, 2016; Tescari et al. 2018). Skewed emission line profiles can be produced, for example, by a narrow kinematic component consistent with HII emission combined with a broad kinematic component induced by shock excitation (e.g. Ho et al. 2014). In the particular case of the SAMI data, Ho et al. (2016) concluded that the shock excitation is consistent with being produced by intermittent starburst episodes as the analysed systems do not show evidence of AGN activity.

On the other hand, trough the analysis of angular momentum in galactic disks, Cortese et al. (2016) show that the angular momentum increases monotonically with $M_\star$, and that the scatter in this relation strongly correlates with optical morphology and/or Sérsic index. They also find that, in terms of kinematic properties, late-type galaxies (spirals) and early-type (ellipticals) fast rotators form a continuous class of objects.

The MANGA survey

The MANGA ('Mapping Nearby Galaxies at Apache Point Observatory') survey is one of three core programs in the fourth-generation SDSS that aims to observe a sample of 10000 nearby galaxies (Bundy et al., 2015). This IFU survey covers the 3600-10300 Å wavelength range allowing the characterization of multiples spectral features in the galaxy spectral energy distribution (SED). The survey redshift coverage is $0.01 - 0.15$, targeting galaxies with $M_\star > 10^9 M_\odot$. From this large galaxy sample, MANGA aims to address the following key science questions: (1) how are galaxy discs growing at the present day, and what is the source of the gas supplying this growth?; (2) What are the relative roles of stellar accretion, major mergers, and secular evolution processes in contributing to the present mass assembly in galactic bulges and ellipticals?; (3) How is the shut-down of the star formation activity regulated by internal processes within galaxies?; (4) How is the angular momentum distributed among different galactic components, and how have their assembly affected the components through time? (Bundy et al., 2015).

To the date, one of the major results from this survey is the characterization of the spatially-resolved excitation properties of star-forming galaxies (Belfiore et al., 2016). By

[1] https://sami-survey.org/science-overview

using the Baldwin, Phillips & Telervich (BPT) diagram (Baldwin et al., 1981), Belfiore et al. (2016) show that extra-planar and inter-arm low ionisation emission line regions (LIER) can be identified as diffuse ionised gas. Zhang et al. (2017) suggest that a possible ionisation source could be the escaping hardened radiation from star-forming regions and ionising photons from old stellar populations.

By using spectral fitting techniques (e.g. Wilkinson et al. 2015) to the pixel-by-pixel spectra, the MANGA survey large wavelength coverage allows to derive spatially-resolved star population parameters such as age, metallicity and star-formation histories (e.g. Goddard et al. 2017). Within the MANGA galaxy sample, early-type galaxies tend to present positive age gradients, suggesting an 'outside-in' growth scenario, while late-type (star-forming) galaxies have negative age gradients, pointing to 'inside-out' formation of discs (Goddard et al., 2017).

The DYNAMO survey

The DYnamics of Newly Assembled Massive Objects (DYNAMO) survey is an Hα spatially resolved sample of sixty-seven local ($z \sim 0.1$) 'typical' and starburst galaxies designed to study galaxy evolution through comparison with high-redshift galaxy samples (Green et al., 2014). The stellar mass range covered in this survey is $10^{9-11}\,M_{\odot}$.

The kinematic analyses performed in DYNAMO galaxies have showed that this survey has a mean ionized gas velocity dispersion of $\approx$50 km s^{-1}, with rotational velocity to dispersion velocity ratios ($V_{\mathrm{rot,H}\alpha}/\sigma_{v,\mathrm{H}\alpha}$) in the range of $2-10$. Two third of the DYNAMO galaxies are consistent with being rotation dominated turbulent galactic discs with large gas content, presenting similar properties to the measured in high-redshift galaxies (Fisher et al., 2014). Further $\sim$100 pc resolution Hubble Space Telescope (*HST*) follow-up observations have showed that DYNAMO galaxies also host large ($\sim$ 300 pc) and massive ($\sim 10^{9}\,M_{\odot}$) clumps. These clumps have SFR surface densities (Σ_{SFR}) $\sim$ 100 times higher than the estimated in nearby HII regions (Fisher et al., 2017). By degrading the spatial resolution of the DYNAMO images to create mock high-redshift galaxy observations, Fisher et al. (2017) also show that the clustering of clumps systematically increases the apparent size of the clumps seen in $\sim$kpc-scale resolution maps, strongly affecting their measured properties.

1.2.2 High-redshift galaxy IFU surveys

Although at high-redshift the recovered spatial resolution is modest compared with the local IFU surveys, it is enough to test the competing models for galaxy growth (Glazebrook, 2013). Taking advantage of IFU observations, significant effort has been invested to measure the morpho-kinematics of the gas within star-forming galaxies at $z \sim 1-3$ (e.g. Fig. 1.3). At these redshifts, IFU-based observations use tracers of the ionized gas content to observe galaxy samples in seeing limited conditions ($0\farcs6$ in $K-$band, e.g. Wisnioski et al. 2015; Stott et al. 2016; Turner et al. 2017), with further improvements in spatial resolution being possible by the use of AO-aided observations. These have delivered $0\farcs15$ ($\sim$kpc-scale) spatial resolution

data on smaller galaxy samples mainly sampling the 'main-sequence' of star-forming galaxies (e.g. Förster Schreiber et al. 2009; Swinbank et al. 2012b; Förster Schreiber et al. 2018), i.e. those galaxies that shows a tight (< 0.3 dex) dependence of SFR on stellar mass (e.g. Noeske et al. 2007; Whitaker et al. 2012). In this section, I review the major and most influential IFU-based high-redshift surveys for this thesis, mentioning in particular their specific kinematic results.

The SINS survey

The SINS ('Spectroscopic Imaging survey in the Near-infrared with SINFONI') survey is one of the earliest large IFU surveys observing main-sequence galaxies at $z \sim 2$ (Förster Schreiber et al., 2009). This survey has given an insightful view of the galaxy properties at the peak epoch of the cosmic star formation rate density. The observations were carried out from 2003 to 2008 and sixty-two galaxies were reported with Hα emission line kinematics. Twelve galaxies were observed with AO (Förster Schreiber et al., 2009). The stellar mass range of the full sample of galaxies is $2 - 300 \times 10^9\,M_\odot$.

One of the principal results from this survey is that around one third of the observed galaxies were consistent with being rotating star-forming turbulent discs, with large ionized gas velocity dispersions and $V_{\mathrm{rot,H}\alpha}/\sigma_{v,\mathrm{H}\alpha}$ values in the range of 2–4 (Förster Schreiber et al., 2006). Another one third were consistent with systems with no dominant rotation velocity but high velocity dispersion values ($\sigma_v \sim 50 - 100\,\mathrm{km\,s^{-1}}$), these systems were called 'dispersion dominated' galaxies (Law et al., 2007). The high $\sigma_{v,\mathrm{H}\alpha}$ values were also associated as evidence of turbulence (or random) motions across the galaxy with a possible origin being a recent accretion of gas from the cosmic web (Genzel et al., 2008). The remaining third did not present clear disc-like pattern, being finally associated as 'merger-like' systems. However, it should be noted that the fraction of galaxies classified as 'dispersion dominated' systems drops with spatial resolution (Newman et al., 2013).

Another major result is that galaxies at high-redshift looks clumpy, with ∼kpc-sized massive ($\sim 10^{8-9}\,M_\odot$) giant clumps. These clumps are part of the galactic disc and not minor merging galaxies as the observed smooth velocity fields suggest. These clumps may originate in regions where the gas is prone to collapse due to self-gravity (Genzel et al., 2011), in consistency with the gravitational instability linear theory (e.g. Toomre 1964). This theory also dictates that the maximum mass that these clumps can reach is dictated by the gas surface density and the rotation velocity amplitude of the galactic disc (e.g. Escala & Larson 2008).

The MASSIV survey

The Mass Assembly Survey with SINFONI in VVDS (MASSIV, Epinat et al. 2009) is an IFU survey targeting 84 galaxies at $0.9 < z < 1.8$ taken from the VIMOS-VLT Deep Survey Database (VVDS). From these, eleven galaxies are observed with AO (Contini et al., 2012). The survey samples the main-sequence of star-forming galaxies in the stellar mass range between $4 - 200 \times 10^9\,M_\odot$, with a possibly bias towards dusty star-forming systems with lack of UV emission (Contini et al., 2012).

As a difference from the SINS survey, MASSIV, considers multiple classification parameters, setting two principal criteria. The first criterion classifies galaxies as 'rotators' and 'non-rotators'. The second criterion accounts between isolated and merging/interacting galaxies, being possible some overlap with the first criterion (e.g. some rotators are interacting, Epinat et al. 2012). This morpho-kinematic approach includes the kinematic information in the galaxy maps, and the galaxy morphology or the galaxy-to-galaxy spatial separation seen in the IFU data. From this survey, Epinat et al. (2012)) found that the non-rotators systems (50%) tend to be classified as mergers/interacting as well, while few rotators (20%) were classified as interacting. The typical disc average $\sigma_{v,\mathrm{H}\alpha}$ value is found to be $\sim$60 km s^{-1}, in concordance with the SINS survey (Förster Schreiber et al., 2006).

Vergani et al. (2012) found that MASSIV galaxies classified as regular rotators show small scatter in the baryonic TFR, whist non rotators depart significantly from this relation. They suggest that the baryonic TFR zero-point does not appear to be evolved since $z = 0$. By studying the metallicity of the galaxies through the [NII]/Hα emission line ratio (Pettini & Pagel, 2004), they also suggest that metallicity gradients are more frequently negative in metal-rich galaxies and more frequently positive in low-metallicity galaxies (Queyrel et al., 2012).

The SHiZELS survey

Based on VLT-SINFONI $H\alpha$ observations of main-sequence galaxies taken from the HiZELS survey (Sobral et al., 2012, 2013b, 2015)), the SINFONI-HiZELS survey (SHiZELS; Swinbank et al. 2012b) is an AO-aided IFU survey which started by targeting nine galaxies at three precise redshift slices, 0.84, 1.47 and 2.23. This survey sampled star-forming galaxies in the $1 - 10 \times 10^9\,M_\odot$ stellar mass range.

Detailed two-dimensional kinematic modelling was performed to analyse this galaxy sample. From the nine galaxies observed in the SINFONI AO-aided mode, a total of six were classified as disc-like systems. By measuring the rotational velocity at 2.2 disc scale lengths ($V_{2.2}$), Swinbank et al. (2012b) studied the cosmic evolution of the rest-frame $B-$band and baryonic TFRs. They found that the rest-frame $B-$band TFR showed a strong evolution with redshift, however the baryonic TFR showed a much more modest evolution in the same redshift range. The different evolutionary trends between both relationships can be understood by considering the evolution of the $B-$band mass-to-light ratio (M/L_B) on galaxies across cosmic time. Galaxies at high-redshift have higher SFRs at fixed $M_\star$ content, thus, presenting a younger stellar population and lower the M/L_B ratio when compared to local galaxies with similar $M_\star$ value.

By analysing the internal clumpy structure observed in these systems, Swinbank et al. (2012a) found that these massive clumps are with consistent being created in situ in the galactic disc, in consistency with the findings reported for the SINS survey (Genzel et al., 2011). They also showed that these clumps follow the same scaling relations than local GMCs (Larson, 1981), but in a denser ISM environment. This also suggests that the star formation activity traced by the Hα emission line in high-redshift discs is similar to the observed in local spiral galaxies, but occurring in systems with a gas-rich and turbulent ISM.

The KMOS^{3D} survey

The KMOS^{3D} survey (Wisnioski et al., 2015) uses the $K-$band Multi-Object Spectrograph (KMOS; Sharples et al. 2004, 2013) on the VLT to observe $\sim$740 galaxies in the near-IR at seeing-limited conditions. The KMOS^{3D} survey is drawn from the 3D-*HST* survey to trace the evolution of spatially-resolved kinematics and star formation activity from 5 Gyr of cosmic history. The Hα emission is traced for main-sequence galaxies in the stellar mass range of $\sim 10^{9-11}\,M_{\odot}$ at $z = 0.7 - 1.1$ and $z = 1.9 - 2.7$.

From two-dimensional kinematic analysis, Wisnioski et al. (2015) found that 93% of galaxies at $z \sim 1$ and 74% at $z \sim 2$ are consistent with being rotationally supported systems, i.e, they show a smooth velocity gradient and $V_{\rm rot,H\alpha}/\sigma_{v,\rm H\alpha} > 1$. However, the high-redshift discs differ significantly from nearby spiral galaxies, the measured velocity dispersion values from the Hα emission ($\sigma_{v,\rm H\alpha} \gtrsim 25\,{\rm km\,s^{-1}}$) reveal turbulent ionized gas discs, in consistency with previous galaxy surveys observing remarkably smaller galaxy samples.

Wisnioski et al. (2015) also suggest that the evolution of the observed turbulent motions in galaxies across cosmic time is consistent with expectations from the gravitational instability theory. Nevertheless, this suggestion is based on the assumption that the majority of the galaxies are consistent with being marginally stable discs systems (Toomre, 1964). The KMOS^{3D} data also has been useful to study diverse key questions such as, for example, the evolution of the metallicity content and metallicity gradients over cosmic time (Wuyts et al., 2016), the angular momentum distribution of star-forming galaxies (Burkert et al., 2016), and the average dark matter fraction on galaxies from stacked rotation curve analysis (Lang et al., 2017).

The KROSS survey

The KMOS Redshift One Spectroscopic Survey (KROSS; Stott et al. 2016) is a $z = 0.8 - 1.0$ near-IR survey of 795 main-sequence star-forming galaxies drawn from the HiZELS survey. The galaxies are observed in Hα emission with the KMOS instrument on the VLT at seeing-limited conditions. The survey covers a galaxy stellar mass range of $\sim 10^{9-11}\,M_{\odot}$.

By performing a kinematic analysis to the KROSS sample, Stott et al. (2016) measured that 83 ± 5 percent of the galaxies are consistent with being dynamically dominated by rotation motions ($V_{\rm rot,H\alpha}/\sigma_{v,\rm H\alpha} > 1$). Galaxies tend to show turbulent discs with high gas to baryonic mass fractions, and most of them are consistent with being prone to gravitational instabilities in their galactic disc. Those conclusions are in agreement with the KMOS^{3D} survey findings (Wisnioski et al., 2015).

Particularly, Stott et al. (2016) found that the averaged velocity dispersion values and total SFR are not correlated, suggesting that the stellar feedback from star formation may not be the origin of the disc turbulence. By calculating the molecular gas mass from the Kennicutt-Schimidt star formation law (Kennicutt, 1998a) and comparing with the dynamical and stellar masses, they infer an average dark matter to total mass fraction of $\sim 65 \pm 12$ percent within 2.2 galactocentric scale length radius ($r_{\rm d}$). The KROSS data is still under analysis, although

those data have been already used to study properties of the star-forming galaxies such as the origin of disc turbulence in star-forming galaxies (Johnson et al., 2017), the evolution of the TFR across cosmic time (Tiley et al., 2016b) and the average outer rotation curve shape of galaxies by using stacking analyses (Tiley et al., 2019).

1.3 Sub-mm/mm molecular gas observations

Spatially resolved sub-mm observations of the CO light distributions are reported in the literature since at least three decades (e.g. Young & Scoville 1991). For galaxies at a distance $\lesssim$20 Mpc, those observations usually employed an angular resolution, given by the synthesized beam size, in the order of $45-60$ arc-seconds ($\sim 1-4$ kpc). They were focused to the study of the molecular gas radial distribution and its comparison to the HI distribution in the context of the evolution of galaxies (Rengarajan & Verma, 1986). The dynamics of galaxies were also measured (Downes & Solomon, 1998). Once the CO emission line is detected, the rotational and random motions can be identified by the emission line shift and line width broadening in an analogous manner than the ionized gas emission lines.

ALMA is revolutionizing the astronomical knowledge at mm/sub-mm wavelengths. With its 12-m antennas, the interferometer is able to reach up to a $\sim$ 16 km array configuration baseline which also allows to perform sub arc-second angular resolution measurements, i.e., delivering the same spatial resolution than the AO-aided 8-m optical/near-IR telescope observations in moderate time-scales[2]. This means that ALMA is able to observe the kpc-scale structure of the ISM in galaxies at high-redshift, but without the diffraction-limit restrictions that IFU AO-aided observations suffer. In this work, I specifically measure the galactic molecular gas kinematics traced by the rotational low-J transitions of the CO molecule using ALMA observations.

1.3.1 CO molecule as gas tracer

The absence of an electric dipole moment in the hydrogen molecule (H_2) implies that direct detections of cold H_2 gas are difficult to be obtained (e.g. Papadopoulos & Seaquist 1999; Bothwell et al. 2013) and tracers of the molecular gas are needed. One of the methods –and perhaps the most common one– to estimate the molecular gas content is through the CO line luminosity (e.g. Solomon et al. 1987; Downes & Solomon 1998; Solomon & Vanden Bout 2005; Bolatto et al. 2013) of rotational low-J transitions (e.g. $J = 1 - 0$ or $J = 2 - 1$). Because the CO emission line is generally optically thick ($\tau_{\rm CO} \approx 1$) within GMCs, its brightness temperature ($T_{\rm b}$) is related to the temperature of the optically thick gas sheet, and not to the temperature distribution across GMC. The mass of the self gravitating entity, such as a molecular cloud, is related to the emission linewidth, which reflects the velocity dispersion of the gas (Bolatto et al., 2013). Therefore, the molecular gas to CO luminosity relation for one GMC can be expressed as $M_{\rm H_2,GMC} = \alpha_{\rm CO,GMC} L'_{\rm CO,GMC}$, where $M_{\rm H_2,GMC}$ is defined to include the helium mass, so that $M_{\rm H_2,GMC} = M_{\rm gas,GMC}$, the whole gas mass (hence, the

[2]https://almascience.nrao.edu/about-alma/alma-basics

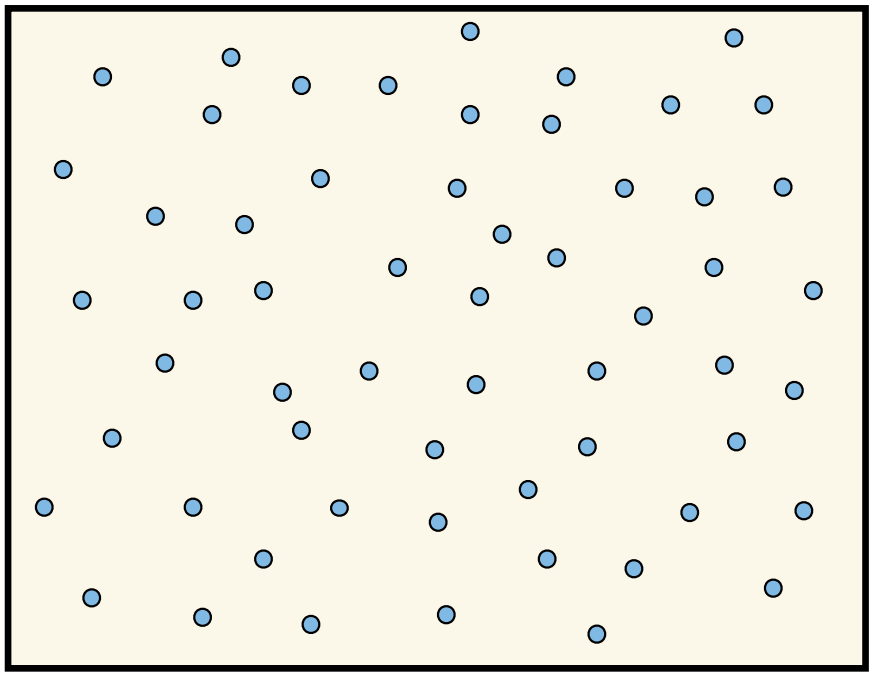

Figure 1.4: Cartoon illustrating the 'mist' model (Dickman et al., 1986). The blue circles represent the optically thick GMCs ('tiny water droplets') embedded in the optically thin ISM ('air').

virial mass) for the giant molecular cloud (Solomon & Vanden Bout, 2005) and $\alpha_{\rm CO,GMC}$ is the CO-to-H_2 conversion factor for that cloud. Within the Milky Way, the observed relation between virial mass and CO line luminosity for Galactic GMCs (Solomon et al., 1987) yields $\alpha_{\rm CO} \approx 4.6\,M_\odot\,({\rm K\,km\,s^{-1}\,pc^2})^{-1}$.

To extrapolate from one GMC to a galaxy, one needs to assume that the CO luminosity of an entire galaxy ($L'_{\rm CO}$; e.g. as defined by Solomon & Vanden Bout 2005) comes from an ensemble of non-overlapping virialized emitting clouds. Then if; (1) the intrinsic brightness temperature of those clouds is mostly independent of the cloud size; (2) these clouds follow the size-line width relationship (Larson, 1981; Heyer et al., 2009); and (3) the clouds have a similar surface density, then the molecular gas to CO luminosity relation can be expressed as $M_{\rm H_2} = \alpha_{\rm CO} L'_{\rm CO}$, where $M_{\rm H_2}$ is the molecular gas mass of the host galaxy (including the helium mass, Solomon & Vanden Bout 2005) and $\alpha_{\rm CO}$ is the galactic CO-to-H_2 conversion factor. This is the so-called 'mist' model (e.g. Fig. 1.4, Dickman et al. 1986). This model seems to be a good approximation for nearby galaxies, where virial mass and CO luminosity measurements on extragalactic GMCs exhibit a good correlation in a roughly a dozen systems suggesting an $\alpha_{\rm CO}$ value comparable to the derived in the Galaxy (Bolatto et al., 2008).

Although the mist model estimates the molecular gas content successfully in the Milky Way and nearby galaxies (e.g. Bolatto et al. 2008), it overestimates the molecular gas mass in more dynamically disrupted systems, such as ULIRGs (Downes & Solomon, 1998). Unlike Galactic clouds or molecular gas distributed in the disc of nearby galaxies, CO emission maps from ULIRGs show that the molecular gas is contained in dense rotating discs or rings. The CO emission may not come from individual virialized clouds, but from a filled inter-cloud

medium, so the line-width is determined by the total dynamical mass ($M_{\rm dyn}$) in the region (i.e., including gas and stars). The optically thick CO line emission may trace a medium bound by the gravitational potential around the galactic centre (Downes et al., 1993; Solomon et al., 1997). In order to estimate the $M_{\rm H_2}$ content from $L'_{\rm CO}$ in those systems a different approach is required. Downes & Solomon (1998) used kinematic and radiative transfer models to derive $M_{\rm H_2}/L'_{\rm CO}$ ratios in ULIRGs, where most of the CO flux is assumed to come from a warm inter-cloud medium. The models yielded $\alpha_{\rm CO} \approx 0.8\,M_{\odot}\,({\rm K\,km\,s^{-1}\,pc^2})^{-1}$, a ratio which is roughly six times lower than the standard $\alpha_{\rm CO}$ value for the Milky Way. It should be noted that this $\alpha_{\rm CO}$ value is usually adopted to estimate the molecular gas content in other non-virialized environments such as galaxy mergers (Solomon & Vanden Bout, 2005).

The mist model also does not consider the effect of the ISM metallicity on the CO emission. Systems with metallicity below $12 + \log{\rm O/H} \approx 8.0$ have almost no CO emission, suggesting that CO is faint in absolute luminosity terms (Elmegreen et al., 1980). These systems also show lower CO-to-FIR luminosity ratios compared to spiral galaxies (Tacconi & Young, 1987). The low metal abundance imply that the ISM has low carbon (C), oxygen (O) and dust abundances (e.g. Draine et al. 2007). The latter provides much of the far-ultraviolet (far-UV) shielding needed for non-strongly self-shielding molecules, such as CO, to prevent its photo-dissociation (Bolatto et al., 2013). The relative CO to H_2 content, is thus, sensitive to the metallicity of the environment.

The CO-to-H_2 conversion factor has been also studied in numerical simulations. Hydrodynamical models are used to calculate the CO emission, the linewidth, and density, but due to computational limitations, the simulations are limited in spatial resolution, approximate chemistry and assumed thermal balance in the implemented sub-grid models (Bolatto et al., 2013). Even though different simulations agree that $\alpha_{\rm CO}$ depends on the gas temperature, the most important factor is the velocity amplitude of the gas turbulence traced by the observed velocity dispersion (i.e. the emission linewidth; Shetty et al. 2011; Narayanan et al. 2012). A result that is also found observationally by studying LIRGs galaxies (Papadopoulos et al., 2012). As turbulence increases, the self-absorption of the CO line emission decreases and then more CO-emitted photons escape from the gas cloud. Nevertheless, from galaxy hydrodynamical simulations, Narayanan et al. (2012) also found that galaxies that have similar physical conditions have similar CO-to-H_2 conversion factors. They found that it seems to be independent of galaxy morphology or evolutionary state. Thus, rather than bimodal $\alpha_{\rm CO}$ values for disc- and ULIRG-like galaxies, they suggest that there is a continuum of conversion values that vary with galactic environment.

1.3.2 Local galaxy CO surveys

Local galaxy surveys have been designed to characterise the molecular gas content of galaxies using the low-J rotational CO emission (e.g. Leroy et al. 2008). Spatially-resolved studies have been successful in characterising the morphology of the molecular gas distribution in nearby disc galaxies (e.g. Helfer et al. 2003). The rate at which the molecular gas is converted into stars has also been extensively studied (e.g. Bigiel et al. 2008; Leroy et al. 2013). However, the kinematics of the molecular gas content have been just recently measured in significant number of galaxies ($\gtrsim 100$, e.g. Bolatto et al. 2017). Morpho-kinematic studies

are, in particular, critical for understanding how gas moves across the galaxy. The gas transportation through the galactic disc and how it leads to star formation is also an open and active field of research. In this section I present a brief review to the most influential CO-based local galaxy surveys, focusing in particular on their main results.

BIMA-SONG survey

The Berkeley-Illinois-Maryland Association Survey of Nearby Galaxies (BIMA-SONG) is a CO(1-0) emission imaging single-dish survey targeting 44 nearby spiral galaxies (Regan et al., 2001). The sources were selected by Hubble type Sa through Sd galaxies at a distance lower than $d \lesssim 27$ Mpc and avoiding highly inclined systems ($i \leq 70°$; Helfer et al. 2003). It used the 10-element Berkeley-Illinois-Maryland Association (BIMA) millimetre interferometer (Welch et al., 1996) to study the spatial distribution and kinematics of the molecular gas at spatial resolution of 6 arc-seconds, i.e. a few hundred parsecs at ~ 12 Mpc, the average survey galaxy distance (Helfer et al., 2003).

At sub-kpc spatial resolution, the BIMA-SONG survey showed that the CO emission does not usually peak in the nuclear regions of nearby galaxies (Regan et al., 2001), in contradiction with the conventional view at that epoch from low resolution observations (Young et al., 1995). The spatial distribution of the CO light can not only be described by a single-component exponential disc-like profile, specially in the central part of galaxies where strong deviations are observed (Helfer et al., 2003). In galaxies, the CO radial profiles are found to follow a bulge-disk two component distribution, similarly to that seen in stellar light profiles (Regan et al., 2001).

The evolution of galaxies was also studied in the context of the molecular gas distribution in barred and unbarred spirals. Sheth et al. (2005) found that BIMA-SONG barred spirals have higher molecular gas concentrations in the central kpc region. They concluded that the relatively high central gas concentrations are produced by radial inflows driven by the galactic bar, indicating that secular evolutionary processes are undoubtedly present (see also Sakamoto et al. 1997). The estimated inflow rates may be insufficient to explain a possible late-type to early-type galaxy evolutionary path, but they might be enough to produce a pseudobulge structure (Kormendy & Kennicutt, 2004; Sheth et al., 2005).

HERACLES survey

The HERACLES (HEterodyne Receiver Array CO Line Extragalactic Survey; Leroy et al. 2009) survey is one of the most detailed CO(2-1) surveys of nearby galaxies to date. A total of 18 local galaxies were observed during this observational campaign using the IRAM 30-m telescope. The HERACLES survey was observed at $\approx 13''$ angular resolution, delivering $\sim$500 pc spatial resolution for the galaxies. These galaxies are also part of The HI Nearby Galaxy Survey (THINGS; Walter et al. 2007) and the Spitzer Infrared Nearby Galaxies Survey (SINGS; Kennicutt et al. 2003), allowing a detailed multi-wavelength study of the ISM phases, along with the embedded star formation activity and both young and old stellar components (Bigiel et al., 2008; Leroy et al., 2008, 2013).

Together with earlier CO(1-0) observations, the HERACLES survey also characterised the CO(2-1)/CO(1-0) emission line intensity ratio (Leroy et al., 2009). The mean value is found to be ~ 0.8, with most of the measurements lying in the $0.6 - 1.0$ range. The average ratio is comparable with that found in our Galaxy, suggesting that the CO emission is optically thick with an excitation temperature of $\sim 10\,\mathrm{K}$ when local thermodynamic equilibrium is assumed. By analysing the radial HI and H_2 gas profiles, Leroy et al. (2008) also found that the HI-to-H_2 gas transitions occur at HI surface densities of $\sim 10\,M_\odot\,\mathrm{pc}^{-2}$. Above this threshold, most of the gas is found to be molecular.

The HERACLES data was also used to study the CO-to-H_2 conversion factor in nearby galaxies (Sandstrom et al., 2013). Aided by the far-IR data taken from the 'Key Insights into Nearby Galaxies: A Far-Infrared Survey with Herschel' (KINGFISH; Kennicutt et al. 2011) and the THINGS HI data, spatially resolved α_{CO} values and dust-to-gas ratios (DGRs) were derived jointly. From this analysis, Sandstrom et al. (2013) observed generally flat radial α_{CO} profiles within their galaxy sample. However, lower CO-to-H_2 conversion factors were observed in the central kpc region of galaxies. Interestingly, Sandstrom et al. (2013) found that α_{CO} values seems to be strongly correlated with stellar surface density ($\Sigma_\star$), but just weakly correlated with gas metallicity; as expected from the small metallicity range covered by the observations. The mean CO-to-H_2 conversion factor for this galaxy sample was $\sim 3.1\,M_\odot\,\mathrm{pc}^{-2}\,(\mathrm{K\,km\,s^{-1}})^{-1}$, a value slightly lower than the α_{CO} value found for the Milky Way galaxy ($\approx 4.6\,M_\odot\,(\mathrm{K\,km\,s^{-1}\,pc^2})^{-1}$; Solomon et al. 1987).

EDGE-CALIFA survey

From the Extragalactic Database Galaxy Evolution (EDGE) survey, the EDGE-CALIFA survey uses the Combined Array for Millimeter-wave Astronomy (CARMA) interferometer to observe the spatially-resolved CO emission in more than one hundred of nearby galaxies ($z < 0.03$) with already IFU mapping from the CALIFA survey (Bolatto et al., 2017).The angular resolution is in the 4–5 arcsecond range, allowing spatial resolutions between 400 pc to 3 kpc with a median value of ~ 1.4 kpc for the survey. This survey samples a bluer local galaxy population than the previous BIMA-SONG and HERACLES spatially-resolved CO surveys.

Bolatto et al. (2017) found, in the EDGE-CALIFA galaxies, that the molecular gas tends to present similar spatial extension than the ionized gas and stellar content. By performing kinematic analysis for the EDGE-CALIFA and CALIFA surveys data, Levy et al. (2018) and Leung et al. (2018) compared the molecular gas kinematics with the ionized gas and stellar kinematics, respectively. Levy et al. (2018) find that CO-based rotation velocities tend to be higher than the rotational velocities derived from the Hα data. They suggest that an extra-planar diffuse ionized gas component (eDIG) along with the decrease of the rotational motions with galactic scale height may cause such discrepancies. On the other hand Leung et al. (2018) show that the underlying mass distribution (traced by CO kinematics) can be recovered from the stellar kinematics once the radial and vertical stellar velocity dispersions are carefully considered/modelled.

1.3.3 High-redshift galaxy CO observations

High-redshift star-forming galaxies are rich in molecular gas and dust (Carilli & Walter, 2013), with molecular gas fractions ($f_{\rm H_2} \equiv \frac{M_{\rm H_2}}{M_{\rm H_2}+M_\star}$) which could reach up to ~ 0.8. This value is almost an order of magnitude higher compared to the seen in local galaxies ($f_{\rm H_2} \sim 0.1$; Leroy et al. 2009; Geach et al. 2011; Carilli & Walter 2013). However, most of the kinematic information of galaxies at high-redshift comes from optical and Hα emission line observations (Glazebrook, 2013). Beyond the local Universe, molecular gas kinematic observations have remained a challenge. Most of the radio interferometers suffer from instrumental limitations to deliver sensitive sub-arcsecond angular resolution observations in feasible time scales. Therefore, most of the resolved CO detections have been limited to the most massive/luminous yet rare galaxies or highly magnified gravitationally lensed sources (e.g. Saintonge et al. 2013; Chen et al. 2017; Calistro Rivera et al. 2018).

Detailed CO observations towards gravitationally lensed galaxies at high-redshift have revealed molecular gas dynamics consistent with the expected from rotating turbulent clumpy disks (e.g. Motta et al. 2018). The measured dynamics are also consistent with the picture inferred from ionized gas IFU observations to $z \sim 1-3$ galaxies. Sub-kpc observations of the ISM morphology in these systems suggest the presence of massive GMCs, with masses of the order of $\sim 10^{8-9}\,M_\odot$ (Swinbank et al., 2015). However, inaccuracies in the gravitational lensing model may lead distorted galaxy disc and internal ISM morphologies (e.g. Swinbank et al. 2011), potentially introducing systematic uncertainties in the derived physical properties. Is worth to mention that Hodge et al. (2012) analysed the dynamics of a single $z = 4.05$ very bright Sub-Millimetre galaxy (SMG). The CO(2-1) emission line was observed by the Very Large Array (VLA) using a total of 120 hours of integration time. The $0\farcs2$ (≈ 1.4 kpc) map resolution showed a clear disc-like morpho-kinematics with velocity dispersion value of $\sim$100 km s^{-1} and massive clumpy ($\sim 10^9\,M_\odot$) molecular gas structure.

The CO emission coming from main-sequence star-forming galaxies has also been measured (e.g. Tacconi et al. 2010) at an angular resolution of $\sim 0\farcs5 - 1''$. The global kinematics of the larger star-forming galaxies were measured (Tacconi et al., 2013). They found that in $z \sim 1.2-2.2$ main-sequence galaxies, the CO emission linewidth agree with the Hα emission linewidths. This suggests that the CO velocity dispersions are high and comparable to the Hα-based values (Tacconi et al., 2013).

Detailed spatial comparisons between CO and Hα observations are scarce. Genzel et al. (2013) presented a comprehensive study of the CO(3-2) and seeing-limited Hα dynamics for a PHIBSS massive galaxy ($M_\star \approx 10^{11}\,M_\odot$), finding that the CO and the Hα emission trace the same rotation curve. By using near-IR *HST* $V-$, $I-$, $J-$ and $H-$band images, Genzel et al. (2013) also present evidence for variable dust extinction across the galactic disc, a major caveat to be considered when interpreting optical light. Übler et al. (2018) performed a similar kinematic analysis in another massive star-forming galaxy. They also found an agreement between the Hα and CO data. The data also suggest that star-forming galaxies at high-redshift seems to have higher baryonic matter content within one half-light radius when compared to local galaxies, in concordance with previous studies (e.g. Wuyts et al. 2016; Genzel et al. 2017; Lang et al. 2017).

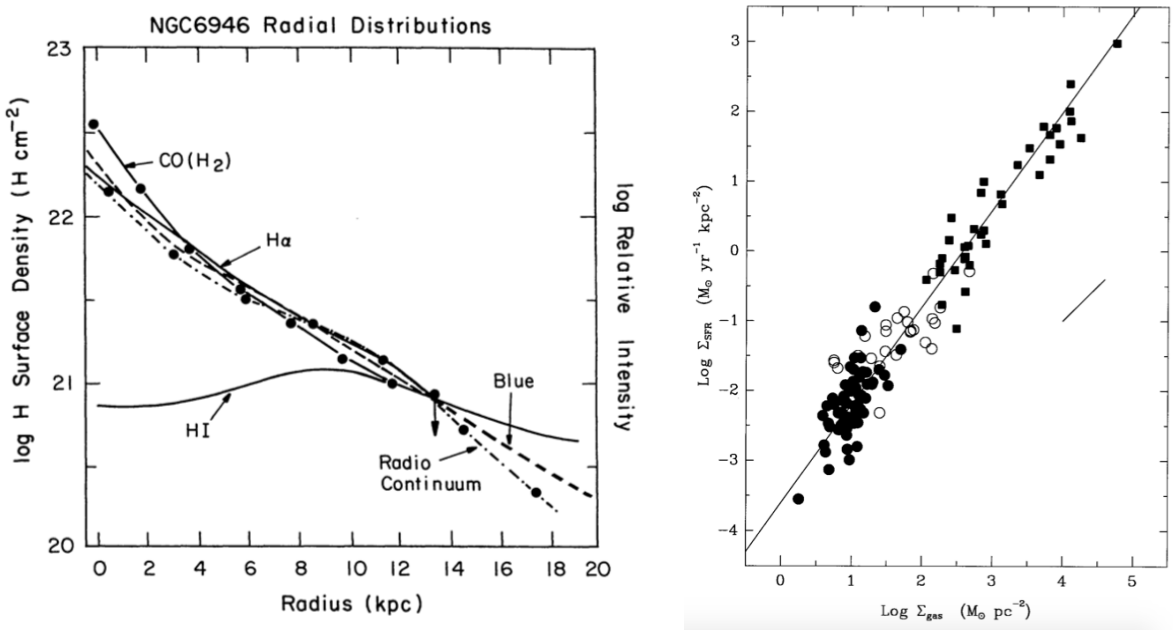

Figure 1.5: *Left*: Radial distributions of the CO (H_2), HI, Hα, blue and radio continuum in the NGC6946 galaxy. This image is taken from Young & Scoville (1991). *Right*: The star formation law for the normal spirals (filled circles) and starburst (squares) local galaxy samples. Open circles show the values corresponding to the centres of the normal disc galaxies. The solid line show the power law relation with an index $N = 1.40$. This figure is taken from (Kennicutt, 1998a).

1.4 The star formation activity

The mechanisms controlling the star formation activity in galaxies is an active research area in modern astrophysics. In a nutshell, this research area tries to understand and describe how efficiently galaxies turn their gas into stars. Early observational work mainly focused on the study of the star formation and molecular gas tracers in spatially resolved disc-like galaxies (Fig. 1.5; Young & Scoville 1991), however the theoretical framework was developed decades earlier. Schmidt (1959) was the first to propose a power-law relationship between the star formation activity of galaxies and their gas content. This relationship was confirmed later by Kennicutt (1998a,b), who revealed a clear relationship between the disc-averaged total galaxy gas (atomic plus molecular) surface density ($\Sigma_{\rm gas}$) and the rate of star formation per surface area ($\Sigma_{\rm SFR}$), the Kennicutt-Schmidt relationship (hereafter, 'KS law'; Fig. 1.5). This relationship has been used to constrain theoretical models and has become a critical input to numerical simulations for galaxy evolution models (e.g Springel & Hernquist 2003; Krumholz & McKee 2005; Vogelsberger et al. 2014; Schaye et al. 2015). Using this relationship the characteristic time that a given galaxy would convert its gas mass content, $M_{\rm gas}$, can be computed if it maintains its present star formation rate (SFR). This time scale is called the depletion time, $t_{\rm dep}$.

Since Kennicutt (1998a,b)'s work, the KS law has been tested in numerous spatially-resolved surveys on local galaxies (e.g. Wong & Blitz 2002; Kennicutt et al. 2007; Bigiel et al. 2008; Villanueva et al. 2017). These surveys have allowed to trace the $\Sigma_{\rm SFR}$, atomic gas

surface density ($\Sigma_{\rm HI}$), molecular gas surface density ($\Sigma_{\rm H_2}$) and study how these quantities relate to each other (e.g. Leroy et al. 2008, 2013). One of the first conclusions extracted from these observations was that star formation in galaxies is more strongly correlated with $\Sigma_{\rm H_2}$ than $\Sigma_{\rm HI}$ (especially at $\Sigma_{\rm gas} > 10\,M_{\odot}\,{\rm pc}^{-2}$), with an observed average molecular gas depletion time of $t_{\rm dep} \approx 2.2 \pm 0.3\,{\rm Gyr}$ (Leroy et al., 2013). The $\Sigma_{\rm SFR} - \Sigma_{\rm H_2}$ relationship has a slope $N = 1 \pm 0.15$, i.e. it is consistent with being linear at first order. However outliers are also detected (e.g. Saintonge et al. 2012; Utreras et al. 2016), suggesting possible variations of the star formation efficiency (SFE$\equiv \Sigma_{\rm SFR}/\Sigma_{\rm H_2} = t_{\rm dep}^{-1}$), which are in general related to the presence of a nuclear starburst activity (e.g. Leroy et al. 2013).

When additional data from high-redshift star-forming galaxies are included, the KS law seems to show an apparent bimodal behaviour where 'disc-like' and 'starburst' galaxies appear to fill the $\Sigma_{\rm H_2} - \Sigma_{\rm SFR}$ plane in different loci (Daddi et al., 2010). Starburst galaxies are consistent with experiencing an enhanced star formation efficiency. Nevertheless, by comparing $\Sigma_{\rm SFR}$ with $\Sigma_{\rm H_2}$ per galaxy free-fall time ($t_{\rm ff}$; Krumholz et al. 2012) and/or orbital time ($t_{\rm orb}$; Daddi et al. 2010), a single power-law relationship can be recovered. The $\Sigma_{\rm SFR} - \Sigma_{\rm H_2}/t_{\rm ff}$ relation can be interpreted as a dependence of the star formation law on the local volume density of the gas, whilst the $\Sigma_{\rm SFR} - \Sigma_{\rm H_2}/t_{\rm orb}$ relation suggests that the star formation law is affected by the global rotation of the galaxy. Thus, the relevant timescale gives critical information about the physical processes that may control the star formation activity.

I highlight, however, that considering the local or global dynamics in the star formation law is not the unique way to reconcile the observed bi-modality into a single power-law relationship. Since the KS law relates the SFRs with the available molecular gas content (in surface density variables), uncertainties behind the estimation of the latter quantity may also induce the observed bi-modality (e.g. Narayanan et al. 2012). Indeed, when just the CO luminosities are compared to the SFRs, a smooth transition between the 'disc' and 'starburst' bimodal sequences seems plausible (e.g. Cheng et al. 2018). A detailed characterization of the galactic dynamics may help to constrain the $\alpha_{\rm CO}$ values (e.g. Solomon & Vanden Bout 2005; Tacconi et al. 2008), and hence, to determine the shape of star formation Kennicutt-Schimidt law.

1.5 This Thesis

This manuscript corresponds to my thesis project and it presents the compendium of the work done during my Ph.D. studies at the Departamento de Astronomía of the Universidad de Chile. The main focus of my thesis work is the extraction and characterization of the morpho-kinematics properties of galaxies at low- and high-redshift through the use of sophisticated computational algorithms. Specifically, this thesis focuses on the kinematic modelling and analysis of galaxy samples at $z < 0.35$ and $0.8 < z < 2.2$. By performing IFU observations, I characterize the ionized gas dynamics in galaxies through the observations of the Hα emission line, but I also use the molecular gas galactic dynamics traced by the CO($J = 1-0$) or CO($J = 2-1$) emission lines using ALMA and the Atacama Pathfinder EXperiment (APEX). Taking advantage of the synergy between the VLT-SINFONI instrument and ALMA, I compare the morpho-kinematic properties of both phases of the ISM in order

to characterise galaxies at low- and high-redshift. The data used in this work come from two observational campaigns observed by the VLT-SINFONI instrument and three campaigns observed by ALMA between 2013 to 2017.

This work will serve as an starting point to be expanded in future ALMA-based moderate and large galaxy surveys planned to characterize the molecular gas dynamics and its comparison with the ionized gas spatially-resolved observations.

1.5.1 Main Scientific Goals

The summarized goals of this thesis are:

- To characterize the ionized and molecular gas ISM phase kinematics and dynamics in galaxy samples at low- and high-redshift.
- To study the luminosity-based global galactic properties such as SFR, $M_\star$, $M_{\rm H_2}$, $f_{\rm gas}$, etc., and their dependence as a function of parameters extracted from the galaxy morpho-kinematic analysis.
- Analyse the correlation between the ionized and molecular gas morphology and dynamics in main-sequence star-forming galaxies at $z \sim 1.5$.
- To study the star-formation activity on ∼kpc scales at $z \sim 1.5$.

1.5.2 Outline

In chapter 2 of this thesis, I describe the different numerical techniques performed to model and analyse the galactic dynamics of the previously mentioned observations. In chapter 3, I present a detailed kinematic analysis of the ionized gas ISM phase for a sub-sample of galaxies taken from the HiZELS survey at $z \sim 0.8 - 2.2$ (Molina et al., 2017). In chapter 4, I present ALMA follow-up observations of the molecular gas content in two galaxies previously observed in Hα at $\sim 0\farcs15$ angular resolution taken from HiZELS (Molina et al., 2019b). I compare the kinematic and morphology of both ISM phases and I study the total baryonic mass content and star-formation activity in these sources. In chapter 5, I present the molecular gas dynamics of a sub-sample of galaxies taken from the Valparaíso-ALMA/APEX Emission Line Survey (VALES) at $z \sim 0.1 - 0.3$ (Molina et al., 2019a). In this chapter, I also present the analysis of the correlations between the molecular gas dynamics with different spatially-integrated galaxy properties. Finally, I summarize the main discussions and conclusion of the thesis and their implications, along with ideas for future work.

Chapter 2

Methods

In this Chapter, I describe the procedures implemented to analyse the ALMA and SINFONI datacubes that allowed me to develop my thesis project. Most of the analyses are based on computational scripts which are classified in three main sections. In section 2.1, I explain the procedure used to extract the kinematic information from the observed emission lines. In section 2.2, I describe the methods used to model the kinematics of the galaxies from the two-dimensional velocity fields. Finally, in section 2.3, I describe the procedures used to extract the global kinematic and morphological quantities for each galaxy. The procedures implemented to perform the data reduction processes are not explained here but presented in each particular chapter.

Throughout this thesis, I adopt a ΛCDM cosmology with Ω_Λ=0.73, Ω_m=0.27, and H_0=70 $\mathrm{km\,s^{-1}\,Mpc^{-1}}$, implying that a spatial resolution of $1\farcs0$ corresponds to a physical scale of $\approx 8.16\,\mathrm{kpc}$ at $z = 1$. I also assume a Chabrier (2003) initial mass function (IMF) and a solar oxygen abundance of 8.69±0.05 in the $12+\log_{10}(\mathrm{O/H})$ metallicity scale (Asplund et al., 2009).

2.1 Emission Line Fitting

Spectral lines are powerful diagnostics that help to constrain the physical conditions in astronomical objects. Doppler shifts of absorption/emission lines in the frequency/wavelength domain allow to measure projected velocities. These velocities yield, for example, the redshifts of extragalactic sources and the rotation curves for spatially-resolved galaxies. On the other hand, turbulent and thermal random motions contribute to line broadening that can be used to measure the mass content for Galactic giant molecular clouds. The physical conditions, chemistry and dynamics of the ISM can be constrained by single or multiple spectral-line observations.

In order to construct the two-dimensional moment maps to characterize the dynamical properties of galaxies, I mainly follow the approach presented in Swinbank et al. (2012b) to extract the emission line information. To do these analyses, I start by spatially binning the

datacubes up to the scale given by the angular resolution of the observations. This boosts the signal-to-noise in individual pixels. Then, I estimate the noise per spectral channel from an area that does not contain any source emission. In this step, I implement a 3-sigma clipping procedure aiming to avoid any possible sky-line features that may arise in the data and artificially increase the noise level.

With the spectra in hand, I perform an emission line fitting approach by using a χ^2 minimization procedure using the MPFIT function (Markwardt, 2009) implemented in the Interactive Data Language (IDL) programming language. In this procedure, a Gaussian profile is fitted to the emission line to estimate the intensity, line-of-sight velocity and velocity dispersion values from the Gaussian area, centroid and width, respectively. I note that, in the case of the SINFONI observations, I mask the channels where OH sky-line features are detected before fitting the emission line.

I calculate the signal-to-noise of the best-fitted Gaussian function ('singlet') by comparing the χ^2 value respect to that obtained by fitting a straight line to the spectrum. In this way, I define the S/N of the line as: $\mathrm{S/N} = \sqrt{\chi^2_{\mathrm{Straight-line}} - \chi^2_{\mathrm{singlet}}}$. I impose a threshold of $\mathrm{S/N} > 5$ to detect the emission line. If this criterion is not achieved, then I increase the binning by considering the next neighbouring pixels and I repeat the Gaussian fit to the emission line. This iteration is allowed to be repeated up to two times. If in the final iteration the fit still fails to achieve the required S/N, then I skip to the next pixel (e.g. Fig. 2.1).

Depending if I am analysing ALMA or SINFONI observations, I need to subtract the instrumental broadening (σ_{inst}) to the emission linewidths. For the ALMA observations there is no instrumental broadening effect ('line spread function') that needs to be considered, thus I do not apply any correction to the observed linewidths. On the other hand, for the Hα SINFONI observations which will be presented later in the text, the instrumental broadening effect needs to be considered. This correction is performed within the MPFIT fitting routine. In this case, I consider an extra σ_{inst} term in the Gaussian profile by adding it in quadrature to the Gaussian width ($\sigma^2_{\mathrm{fit}} = \sigma^2_{\mathrm{inst}} + \sigma^2_{\mathrm{obs}}$). The instrumental broadening is measured from the intrinsic width of the OH lines (seen in the sky spectrum) by fitting a single Gaussian profile.

In the case of the high-redshift ($z \sim 0.8-2.2$) SINFONI observations, the targeted emission corresponds to the Hα recombination emission line. For these observations, Hα is not the unique emission line that can be observed within the SINFONI's $J-$, $H-$ or $K-$band. This emission line is surrounded by the ionized Nitrogen doublet ([NII]$\lambda\lambda 6548, 6583$), the next two brighter emission lines in the SINFONI's wavelength range. The detection of the [NII] emission lines, helps for example to, study of the metallicity of the ISM by the use of the Hα/[N II] emission line ratio estimate (e.g. Pettini & Pagel 2004). Thus, in this case, I consider two additional steps in the emission line fitting procedure.

When the Hα single emission line best-fit ('singlet') signal-to-noise threshold ($\mathrm{S/N} > 5$) is achieved, then I fit simultaneously the Hα and [NII]λ6583 emission lines allowing the centroid, intensity and width of the Gaussian profiles to vary, but coupling the FWHM of both emission lines. If the H$\alpha-$[NII] double Gaussian best-fit ('doublet') has a $\mathrm{S/N} > 3$ (calculated as: $\sqrt{\chi^2_{\mathrm{singlet}} - \chi^2_{\mathrm{doublet}}}$), then the [NII]$\lambda$6583 emission line is detected. In this case, I proceed to

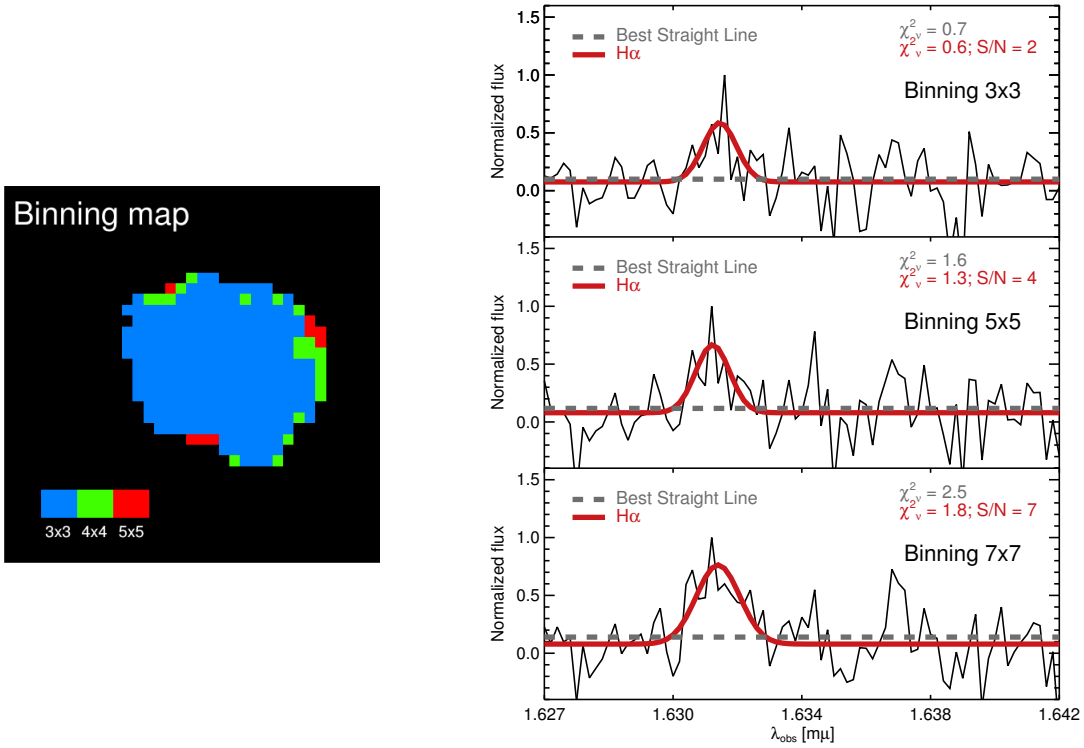

Figure 2.1: Example of the binning procedure illustrated for the Hα observation for a particular galaxy (named 'SHiZELS-19'). *Left*: Two-dimensional map showing the binning step applied for each pixel in the datacube as indicated by the colour-bar. The pixel width is 0.″5 and the PSF FWHM is contained within $\approx$ 0.″15 which is equivalent to three pixels width. Thus, in the first binning step, the spectrum is averaged over a $3 \times 3\,\mathrm{pix}^2$ squared area. For this galaxy, in the final binning step, I average the spectrum over a $5 \times 5\,\mathrm{pix}^2$ squared area. *Right*: Average spectrum obtained from the three binning steps (from top to bottom). In each step the spectrum is fitted by the straight line and a Gaussian profile. The S/N of the Gaussian best-fit is calculated as the root of the subtraction between both χ^2 values. The binning step procedure allows to recover fainter emission lines towards the galaxy outskirts.

fit the Hα and [NII]$\lambda\lambda$6548, 6583 emission lines ('triplet') simultaneously. Again, I allow the centroid, intensity and width of the Gaussian profiles to vary, but I couple the FWHM of the Hα and [NII]$\lambda\lambda$6548, 6583 emission lines. If the N[II]$-$H$\alpha-$[NII] triple Gaussian best-fit has a S/N > 3 (calculated as: $\sqrt{\chi^2_{\mathrm{doublet}} - \chi^2_{\mathrm{triplet}}}$) then the [NII]$\lambda$6548 emission line is also detected (e.g. Fig 2.2). In the last two steps, if the S/N criterion is not achieved, then I skip to the next pixel.

Finally, the intensity, velocity and velocity dispersion two-dimensional maps are constructed by collecting the intensity, velocity and velocity dispersion values from the detected emission lines in the datacube. The intensity map corresponds to the spatial distribution of the emission line velocity-integrated flux density projected on the sky, the velocity map corresponds to the projected component of the galactic rotation velocity across the line-of-sight traced by the emission line centroid Doppler shift, and the velocity dispersion map corresponds to the unresolved motions traced by the linewidth within the resolution element area.

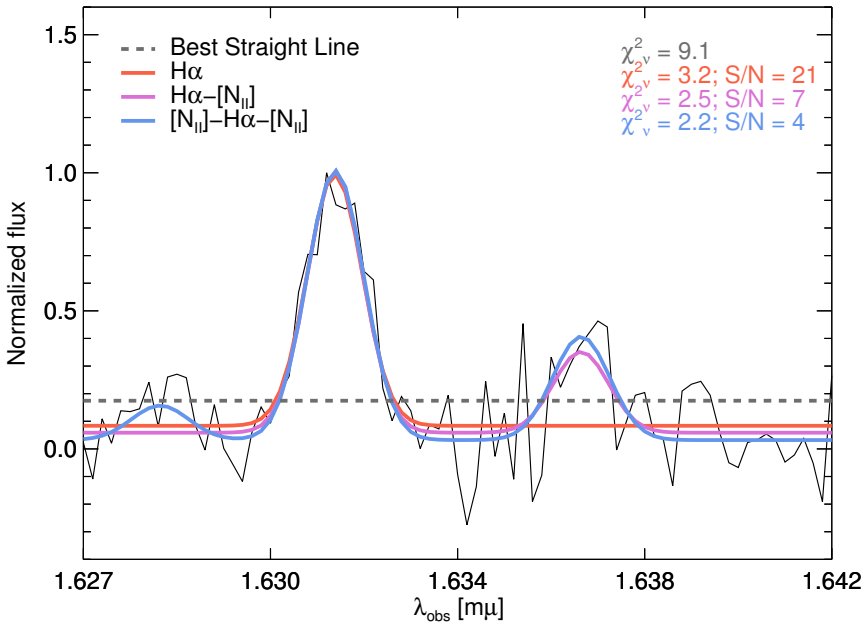

Figure 2.2: Example of the additional emission line fitting steps used to detect the [NII]$\lambda\lambda$6548, 6583 doublet emission lines for the SHiZELS-19 galaxy. The best-fitted straight line (dashed line) tend to be offset to higher values compared to the background level due to the presence of the three emission lines, evidencing that this fit is not a good representation of the data. In this case, I am able to detect up to the [NII]λ6548 emission line as the imposed S/N threshold is achieved.

2.2 Kinematic Model

The kinematic model approach used in this work adopt a standard procedure that is usually implemented to model the two-dimensional projected rotation velocities of high-redshift galaxies (e.g. Glazebrook 2013). From a schematic point of view, it can be resumed as:

(1) adopt a 'rotating disc model' with a given velocity profile,

(2) constraint the model by using photometric parameters derived from broad-band image,

(3) convolve the kinematic model with the spatial resolution,

(4) minimise with respect to the data using some fitting procedure, and

(5) derive the dynamical parameters using the kinematic modelling.

This approach allows to maintain the simplicity of the kinematic model trying overcome two major issues, the low S/N data that impede the use sophisticated models with multiple parameters to be fitted, and the coarse spatial resolution that traduces to severe beam-smeared data. However, it should be noted that this idealized kinematic model entails an strong assumption: the analysed galaxies must present a disc-like dynamics. In the following sub-sections, I present in detail the computational routines used to develop this work.

[3]http://www.gama-survey.org/

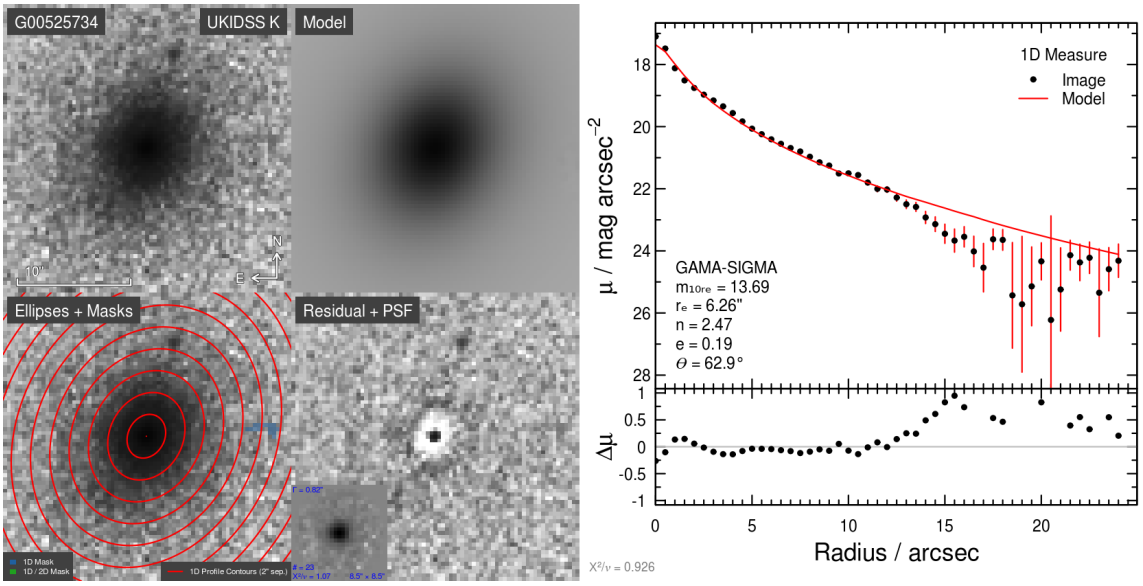

Figure 2.3: The best-fitted two-dimensional K-band Sérsic model to the HATLAS083745 galaxy published by the GAMA team[3]. *Left*: Two dimensional maps of the data, best-fit model, data with overplotted best-fit one-dimensional tilted rings (red) and residuals, including the PSF in the bottom-left corner of this pannel. *Right*: One-dimensional surface brightness (μ) profile and residuals ($\Delta\mu$). The best-fitted parameters are written in the pannel. θ is the photometric position angle, 'e' is the ellipticity, 'n' is the Sérsic index, r_e is the effective (half-light) radius and m_{10r_e} is the magnitude value inside ten times the r_e value.

2.2.1 Morphological models

With the advent of the multiple IFS surveys at high-redshift (e.g. Förster Schreiber et al. 2009; Wisnioski et al. 2015; Stott et al. 2016), kinematic models have experienced a rapid development (with the corresponding increase in complexity) by taking into account multiple galaxy components and adding multiple degrees of freedom (e.g. Swinbank et al. 2017). The latter increases the parameter degeneracy, especially regarding inclination angle when low spatially-resolved observations are analysed. Thus, additional information must be considered in order to derive robust kinematic parameters from the observed velocity fields.

With the aim to minimise parameter degeneracy, I support the kinematic analysis by taking into account previous Sérsic broad-band photometry models (e.g. Fig 2.3; Sérsic 1963). I use the broad-band image models to characterise stellar component of each galaxy through the half-light radius ($r_{1/2,\mathrm{phot}}$), the orientation of major axis indicated by the position angle ($\mathrm{PA_{phot}}$), and the inclination angle derived from the observed minor-to-major axis ratio (b/a). I use this inclination value to constraint the galactic inclination of the ionized and/or molecular gas content in the kinematic modelling. I note, however, that the error estimates produced by the Sérsic broad-band models are determined from the covariance matrix used in the fitting procedure. As a result, the uncertainty of the inclination value tend to be underestimated (Häussler et al., 2007; Bruce et al., 2012). Therefore, I adopt more reasonable error estimate to the galactic inclination and discuss its choice in the following subsection.

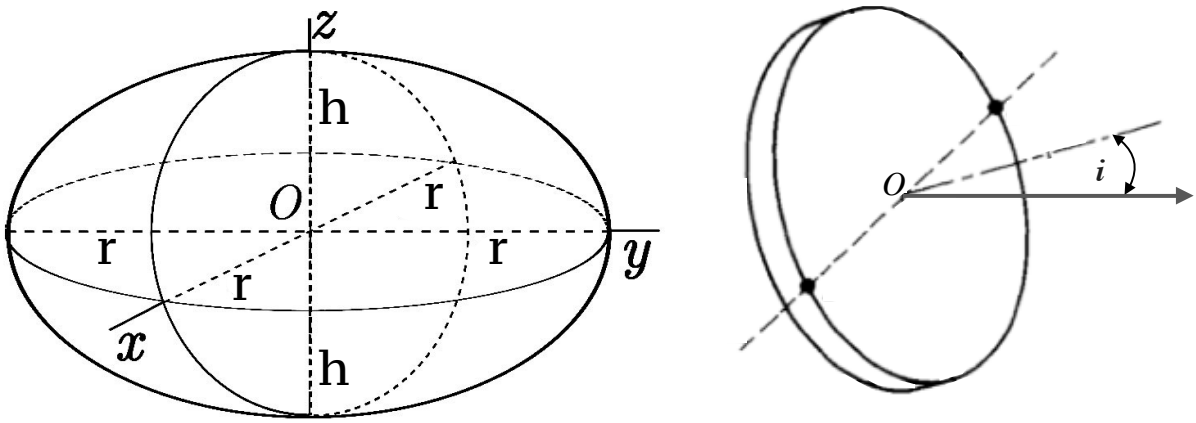

Figure 2.4: Illustration of the galaxy morphological and projection models used in this work. *Left*: Oblate spheroidal geometry. The minor axis is aligned in the z direction. In this case, the middle and major axis have the same length '$2r$'. *Right*: Projection geometry showed for a thin disc to improve visualization. The arrow represents the line-of-sight direction. I note that for a face-on galaxy, the inclination angle 'i' is equal to zero.

2.2.2 Inclination angles

A correct estimate of inclination angle is a critical issue for kinematic analyses. This parameter is used to correct the observed velocity field, which is the projected component of the intrinsic velocity field of the galaxy across the line-of-sight. To take into account the galactic 'disc thickness', I model the galaxies as oblate spheroid systems (e.g. Fig. 2.4). By using the observed minor-to-major axis ratio, the inclination angle can be expressed as:

$$\cos^2(\mathrm{i}) = \frac{(b/a)^2 - \mathrm{q}_0^2}{1 - \mathrm{q}_0^2}, \tag{2.1}$$

where 'i' is the galaxy inclination angle and q_0 is the intrinsic minor-to-major axis ratio of the galaxy. For edge-on systems ($\mathrm{i} = 90\,\mathrm{deg}$) is straightforward to see that $\mathrm{q}_0 = b/a$ (Holmberg, 1958). On the other hand, in the thin-disc approximation (i.e. $\mathrm{q}_0 = 0$), the Equation 2.1 is reduced to the simplistic approximation $(b/a) = \cos(\mathrm{i})$ (e.g. Fig. 2.4).

Although, a priori, I have no information about the 'disc thickness' for the galaxies studied in this thesis, I adopt $\mathrm{q}_0 = 0.14$ and 0.2 values for the low- and high-redshift galaxy samples, respectively. The former value is the mean q_0 value found in edge-on disc galaxies at low-redshift ($z < 0.05$; Mosenkov et al. 2015), while the latter is a q_0 value that seems appropriate for the high-redshift galaxy population (Law et al., 2012).

The error estimates for the inclination angle are calculated by following the results of the Monte Carlo methodology used by Epinat et al. (2012). An 1-σ inclination angle relative uncertainty equal to 10% is assumed. Then, I adopt the inclination angle derived from the broad-band morphological analysis (using GALFIT's b/a estimations) as initial guess for the kinematic modelling and I search for the best-fit value within a 3-σ range.

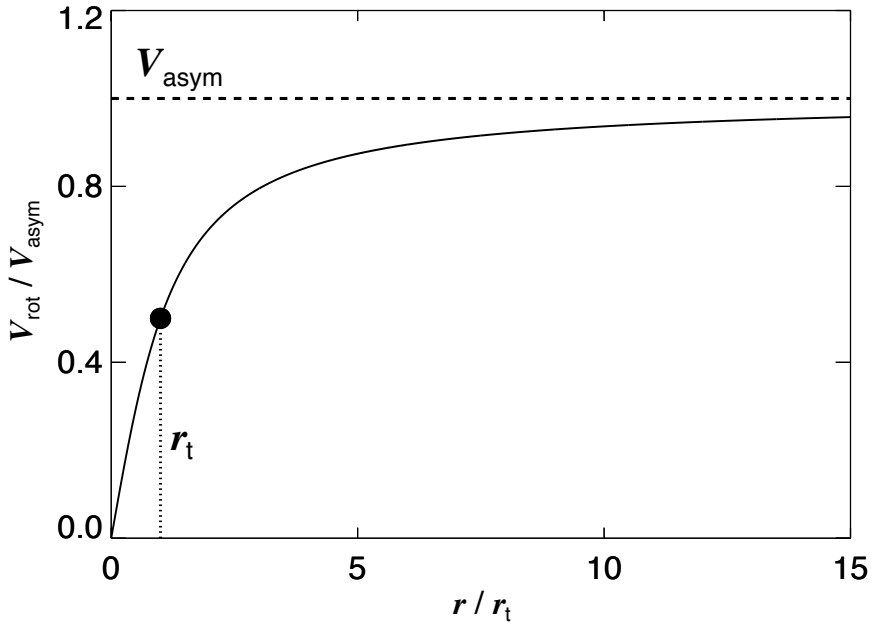

Figure 2.5: The the arctan velocity profile. Both axis are normalized with respect to the main parameters, the asymtotic velocity $V_{\rm asym}$ and the turn over radius $r_{\rm t}$.

For the galaxies without broad-band image or reliable GALFIT fitting, I do not constrain the inclination angle in the kinematic modelling procedure. In this case, the inclination angle value is assumed to vary between 0 to 90 deg (i.e. from a face-on to an edge-on galaxy), with an initial guess of i $\sim 55°$. This value corresponds to $(b/a) \sim 0.7$, the mean axis ratio derived by Law et al. (2012) for a randomly oriented spheroidal galaxy population.

2.2.3 Single-map kinematic modelling

I attempt to model a single two-dimensional velocity field by first identifying the dynamical centre. I follow Swinbank et al. (2012b) to construct two-dimensional velocity map models with an input rotation curve following an arctan function:

$$V(r) = \frac{2}{\pi} V_{\rm asym} \arctan(r/r_{\rm t}), \tag{2.2}$$

where $V_{\rm asym}$ is the asymptotic rotational velocity and $r_{\rm t}$ is the effective radius at which the rotation curve turns over (Courteau, 1997). This velocity profile handle smooth velocity transitions and changing rotation curve slopes with just few free parameters (Fig. 2.5; Courteau 1997), giving a reasonable good fit to the beam-smeared rotation curves measured in galaxies at high-redshift (e.g. Fig. 2.6; Swinbank et al. 2012b). It should be noted that this profile emerges naturally from the standard parametrization of dark halo density profiles (Gilmore et al., 1990).

The two-dimensional kinematic model has six free parameters ($V_{\rm asym}$, $r_{\rm t}$, $[x/y]$ centre, position angle and disc inclination) and it is convolved by the PSF or synthesized beam with the aim to recover unbiased kinematic parameters. A genetic algorithm (Charbonneau, 1995) is used to find the best-fit model (Swinbank et al., 2012b) and the parameter uncertainties are calculated by considering a confidence limit of $\Delta\chi^2_\nu = 1$.

2.2.4 Double-map kinematic modelling

For some galaxies, I have molecular gas ALMA and ionized gas Hα SINFONI observations from which I could estimate kinematic information by attempting to model the two-dimensional velocity fields jointly. For each map, I assume an input rotation curve following the arctan function (Eq. 2.2). Then, I model both maps by coupling the inclination angle parameter, i.e. assuming that both ISM gaseous phases are co-planar. I do not attempt to lock the dynamical centres through RA−DEC coordinates as the SINFONI astrometry is not accurate enough to allow it. I also allow the possibility that their rotational motions can be out of phase, i.e. both ISM phases could have different kinematic position angles.

Therefore, in these cases, the modelling has eleven free parameters ($V_{\rm asym,CO}$, $r_{\rm t,CO}$, PA$_{\rm CO}$, $[x/y]_{\rm CO}$, $V_{\rm asym,H\alpha}$, $r_{\rm t,H\alpha}$, PA$_{\rm H\alpha}$, $[x/y]_{\rm H\alpha}$, and inclination angle) and, in agreement with the single map modelling case, the CO and Hα model maps are convolved by the synthesized beam or PSF, respectively (Fig. 2.6). Then a genetic algorithm (Charbonneau, 1995) is used to find the best-fit model and the parameter uncertainties are calculated by considering the confidence limit of $\Delta\chi^2_\nu = 1$ (e.g. Swinbank et al. 2012b). The total χ^2 of the model is calculated as the sum of the χ^2 obtained from each two-dimensional modelled map.

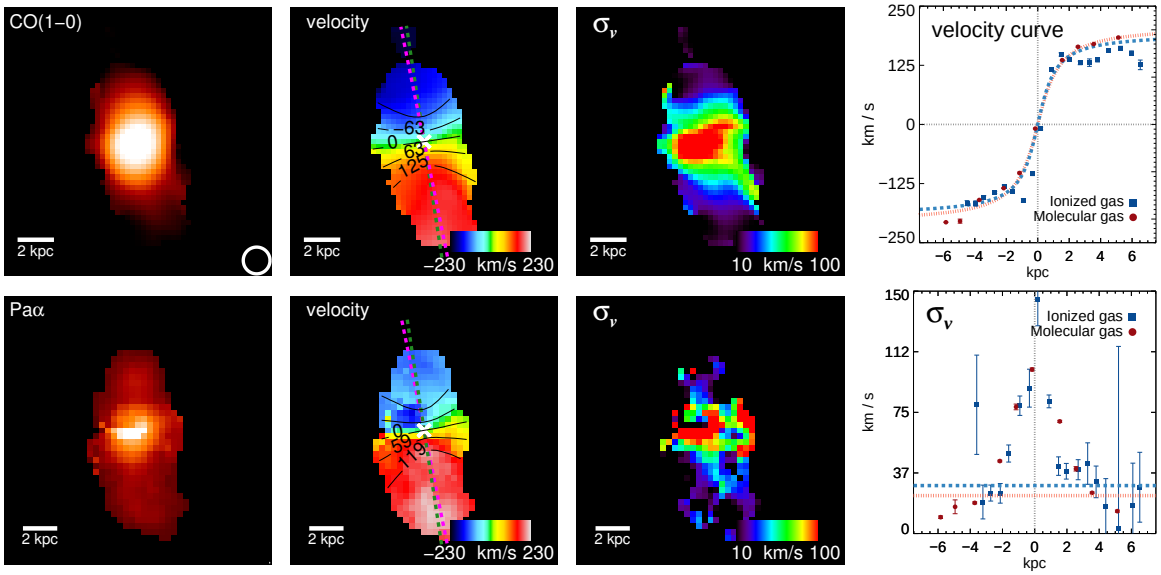

Figure 2.6: Example of the intensity, velocity, and velocity dispersion maps (1st to 3th columns) for HATLAS114625 obtained from CO(1-0) (*top*) and Paschen-α (Paα, *bottom*) emission lines. In the 4th column, I show the one-dimensional rotational velocity (top) and velocity dispersion (bottom) profiles across each major kinematic axis for both observations. The spatial scale for each observation is showed in each moment map. The CO(1-0) intensity map also shows the synthesized beam size at its bottom-right corner. The velocity maps have over-plotted the kinematic centre and the velocity contours from their best-fit disc model. The green- and pink-dashed lines represent the molecular and ionized gas major kinematic axes, respectively. The one-dimensional profiles are constructed by using the best-fit kinematic parameters and a slit width equal to half of the synthesized beam/PSF FWHM. In each one-dimensional profile, the error bars show the 1-σ uncertainty and the vertical dashed grey line represents the best-fit dynamical centre. In the velocity profile panel, the red- and blue-dashed curves show the velocity curve extracted from the beam-smeared CO and Paα two-dimensional best-fit models, respectively. In the σ_v profile panel, the red- and blue-dashed lines show the average galactic value for the CO and Paα observations, respectively.

2.2.5 Kinematic asymmetries

In order to obtain a detailed characterization of the ionized and molecular gas kinematics, I quantify the kinematic deviations from the ideal rotating disc by performing a '*kinemetry*' analysis (Krajnović et al., 2006). This technique has been well calibrated and tested at low-redshift (e.g. Krajnović et al. 2006), whilst at high-redshift it has been used to determine the strength of deviations of the observed velocity and dispersion maps from an ideal rotating disc (e.g. Alaghband-Zadeh et al. 2012; Shapiro et al. 2008; Swinbank et al. 2012b).

Briefly, *kinemetry* proceeds to analyse the two-dimensional kinematic maps using azimuthal profiles in an outward series of best fitting tilted rings (see Fig. 2.7). The kinematic profile as a function of azimuthal angle is then expanded harmonically, which is equivalent to a Fourier transformation with coefficients $k_{n,v}$ and $k_{n,\sigma}$ at each tilted ring for the velocity and velocity dispersion maps, respectively. In the velocity map, the first order decomposition '$k_{1,v}$' is equivalent to the rotational velocity value, and therefore, the ideal rotating disc case is simply described by the cosine law along the tilted rings [$V(\theta) = k_{1,v}\cos(\theta)$]. The high-order terms describe the kinematic anomalies with respect to the ideal rotating disc case. I note that *kinemetry* stops the radial fitting when there are less than 75% of the pixels sampled along the best-fit tilted ring (see Krajnović et al. 2006 for more details).

In the literature, the kinematic deviations from the ideal disc case have been characterized by computing three different estimators: (1) the $k_{5,v}/k_{1,v}$ ratio (Krajnović et al., 2006); (2) the $K_{\rm V} = (k_{2,v} + k_{3,v} + k_{4,v} + k_{5,v})/4k_{1,v}$ and $K_\sigma = (k_{1,\sigma} + k_{2,\sigma} + k_{3,\sigma} + k_{4,\sigma} + k_{5,\sigma})/5k_1, v$ quantities (Shapiro et al., 2008); and (3) the $(k_{3,v}+k_{5,v})/2k_{1,v}$ and $(k_{2,\sigma}+k_{4,\sigma})/2k_{1,v}$ fractions (Bloom et al., 2018).

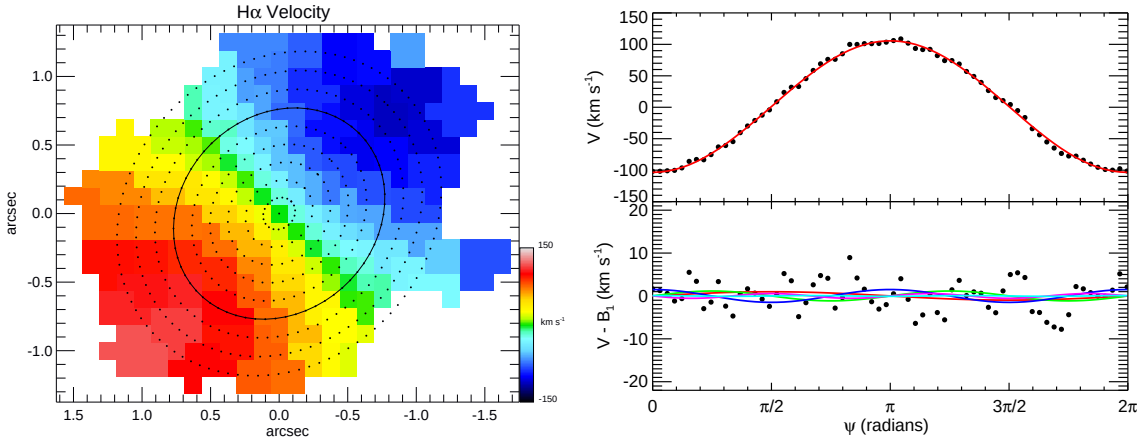

Figure 2.7: *Left:* Idealized velocity field of a disc galaxy. The tilted rings overlaid correspond to the best-fit *kinemetry* solution at each radius. The solid line emphasizes one tilted ring, while the rest of the tilted rings are represented with the black dots. *Right:* Harmonic expansion as a function of azimuthal angle along the solid tilted ring. The top panel shows the measured velocities and the rotation velocity coefficient (red line); the bottom panel shows the residuals from this fit and the higher order coefficients measured as a function of the azimuthal angle. Both images are taken from Shapiro et al. (2008).

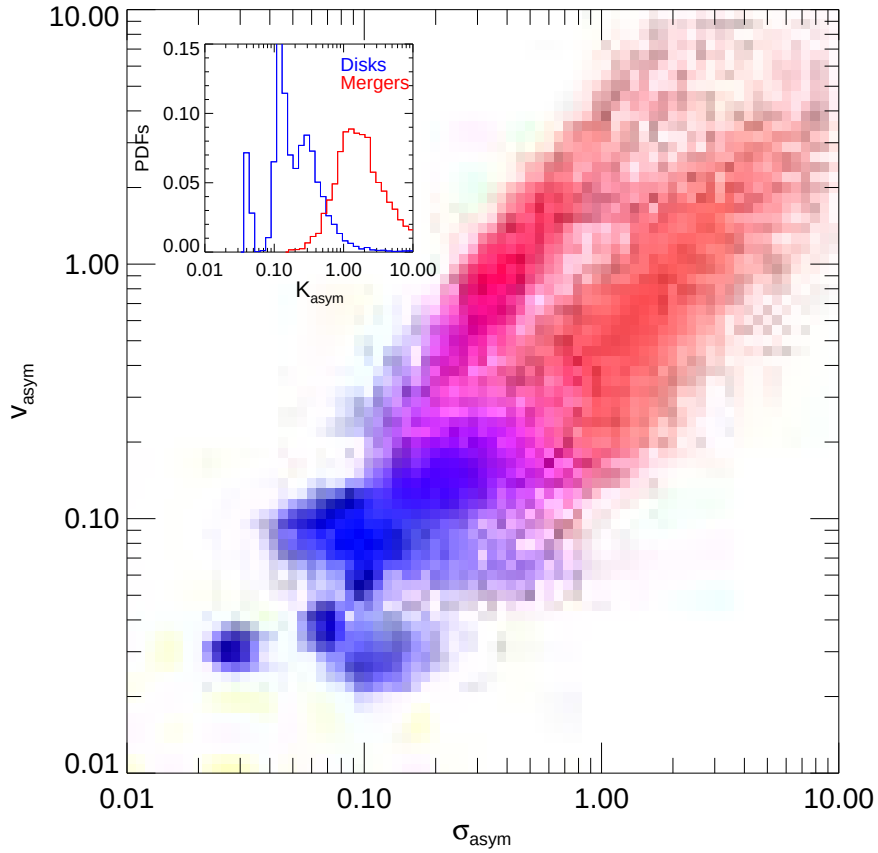

Figure 2.8: $K_{\rm V}$ and K_σ asymmetry measures (in this case labelled as $\rm V_{asym}$ and $\sigma_{\rm asym}$) for a template of galaxies presented in Shapiro et al. (2008). Template discs and merger systems are represented in blue and red, respectively. In the top-left corner is shown the one-dimensional probability distribution function (PDF) of the $K_{\rm Tot}$ parameter (labelled as $\rm K_{asym}$). The $K_{\rm Tot} < 0.5$ threshold is used to separate the two classes. This image is taken from Shapiro et al. (2008)

The first case is the traditional dimensionless ratio that describes the kinematic asymmetries just in the velocity map. It does not consider the low-order coefficients as these are used by *kinemetry* to find the best-fitted tilted rings at a given radius (Krajnović et al., 2006). The second case was used to classify high-redshift galaxy mergers which tend to present extremely disturbed kinematic fields (e.g. Fig. 2.8; Shapiro et al. 2008). In this case, the strong deviations from the idealised case produces large $K_{\rm V}$ and K_σ values. The total asymmetry is defined as $K^2_{\rm Tot} = K^2_{\rm V} + K^2_\sigma$ and a threshold of $K_{\rm Tot} < 0.5$ is used to differentiate discs from mergers (Shapiro et al., 2008). The third case consists on a slight modification to the second case as it takes into account that, in moderately disturbed systems, the even/odd moments contribution measured from the rotation velocity/velocity dispersion maps are negligible (Bloom et al., 2018).

When I use *kinemetry*, I restrict the inclination and position angles within the 1-σ error range given by the best-fit two-dimensional model. The $k_{n,v}$ and $k_{n,\sigma}$ errors are derived by bootstrapping via Monte-Carlo simulations the errors in measured velocities, velocity dispersions, and estimated dynamical parameters.

2.3 Global Morpho-Kinematic Properties

Once the best-fit kinematic model for a galaxy is determined, I use it to characterize the basic galaxy morphology and global kinematics. I develop computational routines that use the spatially-resolved information in the datacubes and two-dimensional maps to estimate de-projected the galaxy size and the amplitude of the ordered and random/turbulent motions. I use these basic parameters to characterize the global morpho-kinematic properties in each galaxy and to further characterize the galaxy samples as a whole. More sophisticated procedures implemented to characterize the galaxy morpho-kinematics that the ones described here, are presented in each particular chapter where they are used.

2.3.1 Spatial extent

In the analyses presented in this work, I measure the spatial extent of galaxies by using the half-light radii ($r_{1/2}$). These radii are derived from the collapsed continuum subtracted datacubes, where the encircled emission line flux decays to half its total integrated value. The total integrated value is defined as the total intensity within a Petrosian radius ($\mathrm{R_P}$). I adopt the SDSS survey Petrosian radius definition with $R_{\mathrm{P,lim}} = 0.2$ (e.g. Conselice et al. 2002). Briefly, the Petrosian radius is the radius at which en encircled average surface brightness is $R_{\mathrm{P,lim}}$ times the surface brightness at that radius. I account for the ellipticity and position angle of the galaxy obtained from the best-fit disc model. The half-light radius 1-σ uncertainties are derived by bootstrapping via Monte-Carlo simulations the errors in measured emission line intensity and estimated dynamical parameters of each galaxy. The half-light radii are obtained after the measured values are corrected for beam-smearing effects by subtracting the spatial resolution element (synthesized beam or PSF width) in quadrature.

2.3.2 Rotational Velocity and velocity dispersion

In this work, I use the dynamical centre and position angle derived from the best-fit dynamical model to extract the one-dimensional rotation curve across the major kinematic axis of each velocity map in each galaxy. I define the rotational velocity for the CO and/or Hα velocity maps ($V_{\mathrm{rot,CO}}$ and $V_{\mathrm{rot,H}\alpha}$, respectively) as the velocity observed at two half-light radii in the rotation curve and corrected for inclination (e.g. Fig. 2.6).

As a consequence of the usually modest spatial resolution of the observations (specially those at high-redshift) compared to the angular extension of the sources, there is a contribution to the derived linewidths from the beam-smeared large-scale velocity motions across the galaxy which must be corrected for (Davies et al., 2011). This correction can be done for each pixel in different manners (e.g. Glazebrook 2013). One possibility is to subtract the local velocity gradient ($\Delta V/\Delta R$) in quadrature (e.g. Swinbank et al. 2012b):

$$\sigma^2_{\mathrm{rec}} = \sigma^2_{\mathrm{obs}} - (\Delta V/\Delta R)^2, \tag{2.3}$$

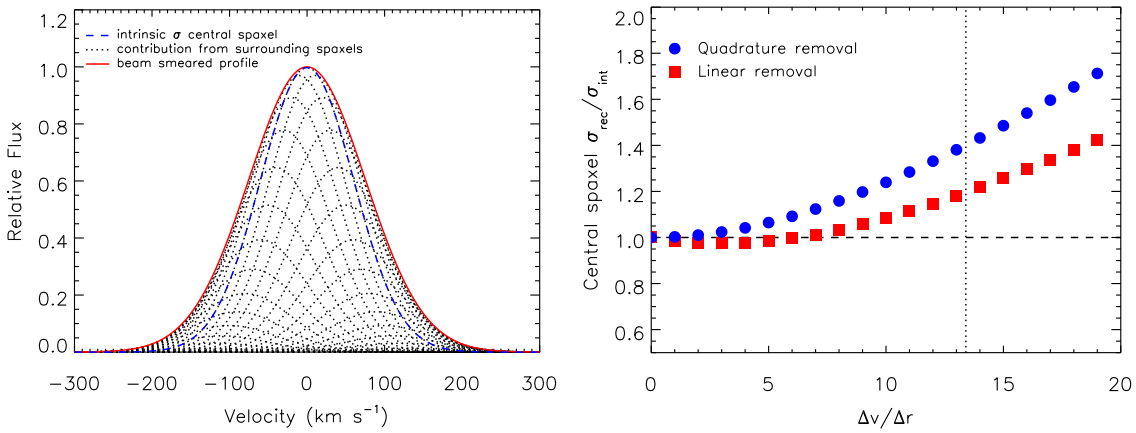

Figure 2.9: *Left:* One-dimensional representation of the contributions to the emission line width of the central pixel from from neighbour pixels due to beam smearing effects. *Right:* The ratio of the recovered line width to the intrinsic value in terms of velocity dispersion ($\sigma_{\rm rec}/\sigma_{\rm int}$) when the beam smearing correction procedure proposed by Stott et al. (2016) is used. The corrected line widths obtained by using the linear and quadrature removal of the local velocity gradient are compared. The vertical dotted line shows the median velocity gradient ($\Delta V/\Delta R = 13.4\,{\rm km\,s^{-1}\,pixel^{-1}}$) obtained for the KROSS survey. At this $\Delta V/\Delta R$ values 20 percent residual is obtained from the linear removal compared to the 40 percent excess obtain when $\Delta V/\Delta R$ is removed in quadrature. In general, the linear removal procedure is able to deliver better results than the quadrature technique. Both images are taken from Stott et al. (2016).

where $\sigma_{\rm obs}$ is the observed velocity dispersion value associated to an emission line, $\sigma_{\rm rec}$ is the 'recovered' velocity dispersion value which aims to be equal to the intrinsic value $\sigma_{\rm int}$ and $\Delta V/\Delta R$ is calculated across the resolution element area of the observations. I remind that, for the observations used in this work, the resolution element corresponds to the synthesized beam and PSF binned area in the ALMA and SINFONI data, respectively. Similarly, a second procedure is to, simply, subtract the local velocity gradient linearly (Eq. A1 from Stott et al. 2016):

$$\sigma_{\rm rec} = \sigma_{\rm obs} - (\Delta V/\Delta R). \tag{2.4}$$

From these two possibilities, I use the linear subtraction as this procedure seems to perform better the removal of the local velocity gradient than the quadrature technique (Fig. 2.9; Stott et al. 2016). However, by using the linear subtraction procedure, $\sim 20\%$ residuals in the velocity dispersion fields are expected to remain, especially on the centres of each galaxy map where large velocity gradients are expected to be present (Fig. 2.9; Stott et al. 2016). Thus, to minimize such effects, I define the global velocity dispersion for the CO and/or Hα emissions ($\sigma_{v,{\rm CO}}$ and $\sigma_{v,{\rm H}\alpha}$, respectively) as the median value taken from the pixels beyond the central galactic zone, i.e., at the outskirts of the galaxy. The zone size is defined as three times the size of the angular resolution (depending on the case) and this zone is centred at the projected dynamical centre in the velocity dispersion map (e.g. Fig. 2.6).

In the case of CO ALMA observations, I note that the CO emission linewidth has been traditionally used as a measure of the dynamical mass within a GMC. However, this assumption needs that the GMC size is virialized and resolved in the observations (e.g. Solomon et al. 1987). The spatially-resolved CO observations that are analysed in this thesis present smooth CO intensity maps without any evidence of clumpiness at usually $\gtrsim$kpc scales. Thus, throughout this work, I interpret the CO emission linewidth as a tracer of the molecular gas random motions seen over the angular resolution of the observations. This is the key property as I can study the dynamics of the molecular gas directly. This opens a window of dynamical analyses which is not necessary the same as those performed in IFS galaxy surveys which use (mainly) the ionized gas to characterise the dynamical state of galaxies.

Chapter 3

The dynamics, merger rates & metallicity gradients of 'typical' star-forming galaxies at $z = 0.8 - 2.2$

In this Chapter[4], I present AO-aided SINFONI-IFU spectroscopy of eleven Hα emitting galaxies selected from the HiZELS survey in three redshift slices, z =0.8, 1.47 and 2.23. I obtain spatially-resolved ($\sim 0\farcs15$ resolution, $\sim$kpc scales) dynamics of star-forming galaxies ($M_\star = 10^{9.5-10.5}\,M_\odot$ and SFR = 2–30 $M_\odot\,\mathrm{yr}^{-1}$) near the peak of the cosmic star-formation rate history. Combining these observations with a previous SINFONI-HiZELS campaign, I construct a sample of twenty homogeneously selected galaxies and detected in Hα emission with IFU AO-aided observations – the 'SHiZELS' survey, with roughly equal number of galaxies per redshift slice, at z = 0.8, 1.47, and 2.23. By modelling the galactic dynamics, I explore the stellar mass Tully-Fisher relationship, I classify galaxies between disc-like and merger systems, I study the metallicity gradients derived from the [N II]/Hα emission line and finally I study the evolution of the metallicity gradients across cosmic time. Throughout the chapter, the assumed ΛCDM cosmology implies that at redshift 0.8, 1.47 and 2.23, a spatial resolution of $0\farcs1$ corresponds to a physical scale of 0.74, 0.84 and 0.82 kpc, respectively.

[4]These results were published in Molina, et al. 2017, MNRAS, 466, 892

3.1 Introduction

Determining the physical processes that control star-formation and mass assembly at high-redshift is an area of intense debate. At $z = 1 - 2$, galaxies were actively forming stars and rapidly growing their stellar mass content (e.g. Madau et al., 1996; Sobral et al., 2009). However, studies also found a strong decline in SFR from that epoch to the present day: the cosmic star-formation rate density of the Universe has dropped by more than an order of magnitude (e.g. Karim et al., 2011; Gilbank et al., 2011; Rodighiero et al., 2011; Sobral et al., 2013a). The primary causes of the subsequent decline of the star-formation rate activity since $z = 1 - 2$ is still under debate.

Two main explanations have emerged to explain how galaxies maintained such high levels of star formation at those redshifts: (1) the rate of mergers and tidal interactions may have been higher at that epoch, driving quiescent discs into bursts of star-formation (e.g. Bridge et al., 2007; Conselice et al., 2009); and (2) galaxies were continuously fed gas from the intergalactic medium, promoting and maintaining star-formation activity driven by internal dynamical processes within the interstellar medium (e.g Kereš et al. 2005; Bournaud et al. 2009; Dekel et al. 2009b).

To test the predictions from these galaxy evolution models, a method for distinguishing between mergers and galaxy discs needs to be implemented. Three main methods of estimating the merger fraction are: counting close pairs of galaxies, assuming that they will subsequently merge (e.g. Lin et al., 2008; Bluck et al., 2009); using a method of identifying galaxies with merging morphology (e.g. Conselice et al., 2003, 2008, 2009; Lotz et al., 2008; Stott et al., 2013b); and employing detailed IFS observations to look for dynamical merger signatures (e.g. Shapiro et al., 2008; Förster Schreiber et al., 2009; Bellocchi et al., 2012; Contini et al., 2012; Swinbank et al., 2012b).

If secular processes drive the galaxy discs evolution, the internal dynamical properties of galaxies at the peak epoch of the volume-averaged SFR are needed to be measured in order to constrain how the structural properties of galaxy discs have varied over cosmic time and test if the prescriptions developed to understand the star-formation processes at $z = 0$ are still valid in the ISM of galaxies at high-redshift.

For example, if the structural properties of galaxy discs have varied over cosmic time, evidence in kinematic scaling relations would be expected to be seen. Within this scenario, one potential evidence would be an evolution of the Tully-Fisher relationship (Tully & Fisher, 1977), which describes the interdependence of baryonic and dark matter in galaxies by studying the evolution of the stellar mass versus circular velocity. It traces a simple means of the build-up of galaxy discs at different epochs. In particular, hydrodynamic models suggest that the zero-point of the stellar mass Tully-Fisher relationship should evolve by ~ -1.1 dex at fixed circular velocity between $z = 0 - 2$ (McCarthy et al., 2012). At a given rotational velocity, the stellar mass in a high-redshift disc galaxy should be smaller than a low-redshift counterpart as star-formation builds it up.

A second potential observational tool to constrain galaxy evolution models is the measure of the chemical abundance within galaxies using a simple disc model. If the gas accretion

in high-redshift galaxies is via accretion of pristine gas from the IGM along filaments onto the galaxy disc at 10–20 kpc from the galaxy centre, then the inner disks of galaxies should be enriched by star-formation and supernovae whilst the outer-disc is continually diluted by pristine material, leaving strong negative abundance gradients (Dekel et al., 2009b,a). This gradient would flatten if the IGM gas is redistributed, e.g. via merger interactions.

To chart the evolution of star-forming galaxies with cosmic time, I exploit the panoramic (degree-scale) HiZELS. This survey targets Hα emitting galaxies in four precise ($\delta z = 0.03$) redshift slices: $z = 0.4$, 0.8, 1.47 and 2.23 (Geach et al., 2008; Sobral et al., 2009, 2010, 2011, 2012, 2013b). This survey provides a large luminosity-limited sample of homogeneously selected Hα emitters at the cosmic star-formation density peak epoch, and provides a powerful resource for studying the properties of starburst galaxies and the star-forming galaxies that shows a tight dependence of SFR on stellar mass, the so-called 'main-sequence' of star-forming galaxies (Noeske et al., 2007; Pannella et al., 2009; Elbaz et al., 2011). Most of the HiZELS galaxies will likely evolve into $\sim L^*$ galaxies by $z = 0$ (Sobral et al., 2011), but are seen at a time when they are assembling most of their stellar mass, and thus are seen at a critical stage in their evolutionary history.

3.2 Sample selection, Observations & Data Reduction

3.2.1 HiZELS

To select the targets for IFU observations, I exploited the large sample of sources from the HiZELS imaging of the COSMOS, SA22 and UDS fields (Best et al., 2013; Sobral et al., 2013b, 2015, 2016) to select Hα emitters sampling the so-called 'main-sequence' of star-forming galaxies at $z = 0.8 - 2.23$ (Fig. 3.1). The HiZELS survey is based on observations obtained using the Wide Field Camera (WFCAM) on the 3.8-m United Kingdom Infrared Telescope (UKIRT; Geach et al. 2008; Sobral et al. 2009). Taking the advantage of the large sample I could select galaxies which lie close ($< 30''$) to bright ($R < 15.0$) stars, such that natural guide star adaptive optics correction (NGS correction) could be applied to achieve high spatial resolution.

For this programme, eighteen galaxies were selected with stellar mass between $M_\star = 10^{9.5-10.5}\,M_\odot$ and Hα fluxes greater than $f_{H\alpha} \geq 0.7 \times 10^{-16}$erg s^{-1} cm^{-2} to ensure that their star-formation properties and dynamics could be mapped in a few hours. Out of the eighteen galaxies observed with SINFONI, I detect eleven of them with high enough signal-to-noise. Given the significant sky-noise in near-IR spectra, source detection was optimally performed by detailed visual inspection of dynamical and linewidth features within the data-cubes (using IDL and QFitsView).

Although the rate of detection of bright Hα emitters derived from the sample may seem modest ($\sim$60%), the detection rate for this particular campaign is comparable to the detection rate derived from the previous SINFONI campaign ($\sim$65%; Swinbank et al. 2012b). I note that both samples were drawn from the same HiZELS survey. However, the detection rate

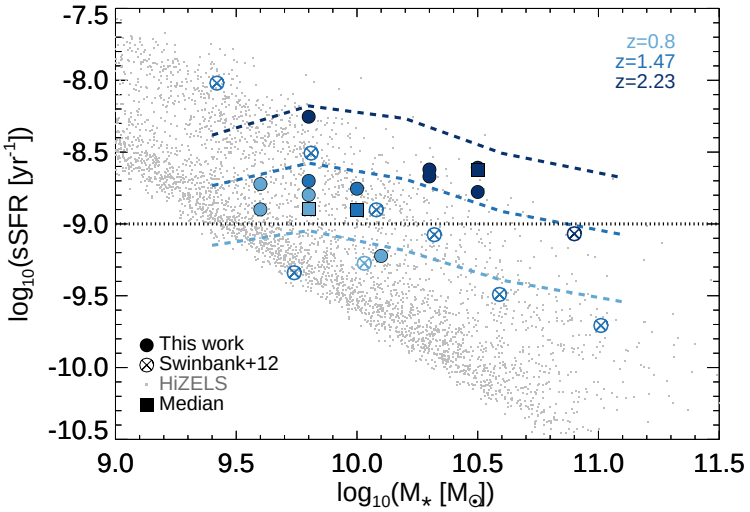

Figure 3.1: The relation between specific star formation rate (sSFR) and stellar mass for the HiZELS survey (grey dots; Sobral et al. 2013b, 2014), Swinbank et al. (2012b)'s sample (circles with X) and this galaxy sample (filled circles). I colour-coded this sample and the Swinbank et al. (2012b) sample by redshift. The sky blue, blue and dark blue colours represent the sources at $z = 0.8$, 1.47, 2.23 respectively. The filled squares represent the median values per redshift. The black dotted line shows the sSFR$= 10^{-9}\,\mathrm{yr}^{-1}$ value. The colour-coded dashed lines represent the location of the main sequence of star-forming galaxies at each redshift slice from Karim et al. (2011), demonstrating that this sample and Swinbank et al. (2012b)'s sample are 'typical' for each epoch.

derived from the non-AO KROSS survey (using KMOS; Stott et al. 2016) −which was also drawn from the HiZELS survey at $z \sim 0.8$− is nearly ∼92%. The non-detected sources tend to be typically fainter in Hα flux and have lower stellar mass values compared to the detected galaxies. This suggests that the modest rate of detection derived from the sample and the previous SINFONI campaign may be inherent to the AO-observations low sensitivity.

3.2.2 SINFONI Observations

To measure the dynamics of the sample from the nebular Hα emission line, I used the SINFONI IFU (Eisenhauer et al., 2003) on the European Southern Observatory (ESO) VLT (Project 092.A-0090(A); P.I. E.Ibar). I use the $3'' \times 3''$ field of view at spatial resolution of $0\farcs1\,\mathrm{pixel}^{-1}$. At $z = 0.8$, 1.47 and 2.23 the Hα emission line is redshifted to ∼1.18, 1.61 and 2.12 μm and into the J, H and K-bands, respectively. The spectral resolution in each band is $\lambda/\Delta\lambda \sim 3700$, and OH sky-lines are considerably narrower (~ 4 Å full width half maximum – FWHM) compared to the galaxy linewidths. A NGS correction is applied since each target is close to a bright guide star.

The observational setups for these targets were done in the same manner as in Swinbank et al. (2012b)[5]. To observe the targets, an ABBA chop sequences are used (OBs with individual exposures of 600 seconds), nodding $1\farcs6$ across the IFU. In order to achieve higher

[5]Designed by E. Ibar

signal-to-noise ratios on sources at higher redshifts, there are used 2, 3 and 4 OB's for the $z = 0.8$, 1.47 and 2.23 galaxies, implying a total observing time of 4.8, 7.2 and 9.6 ks respectively. The observations were carried between 2013 October 27 and 2014 September 3 in $\sim 0\farcs8$ seeing and photometric conditions. The median Strehl achieved for the observations is 33% (Table 3.1).

Individual exposures were reduced by using the SINFONI `ESOREX` data reduction pipeline which extracts flat-fields, wavelength calibrates and produces the datacubes for each exposure[6]. The final datacube for each galaxy was generated by aligning manually the individual OBs on average (shifting them by $\lesssim 0\farcs2 \sim 2$ pix) and then combining these by using a sigma-clipping average at each pixel and wavelength. This procedure minimised the effect of the OH emission/absorption features seen in the final datacube.

3.2.3 Stellar Masses

Stellar masses are computed by fitting SEDs to the rest-frame UV, optical and near-infrared data available ($FUV, NUV, U, B, g, V, R,$ i$, I, z, Y, J, H, K, 3.6, 4.5, 5.8$ and 8.0 μm collated in Sobral et al. 2014, and references therein), following Sobral et al. (2011). The SED templates were generated with the Bruzual & Charlot (2003) package using Bruzual (2007) models, a Chabrier (2003) IMF and an exponentially declining star formation history with the form $e^{-t/\tau}$, with τ in the range 0.1–10 Gyr. The SEDs were generated for a logarithmic grid of 200 ages (from 0.1 Myr to the maximum age at each redshift being studied). Dust extinction was applied to the templates using Calzetti et al. (2000) extinction law with $E(B-V)$ in the range 0 to 0.5 (in steps of 0.05) roughly corresponding to a Hα extinction $A_{\rm H\alpha}$ ∼0–2 mag. The models are generated with different metallicities, including solar (Sobral et al., 2011)[7]. For each source, the stellar mass and the dust extinction are computed as the median values of the 1-σ best fits over the range of parameters (see Table 3.1).

3.2.4 Star-Formation Rates

The star-formation rates of the sample are measured from the Hα emission line flux calculated from the HiZELS survey. Adopting the Kennicutt (1998b) calibration and assuming a Chabrier IMF, the SFRs are derived from the observed Hα luminosity ($L^{\rm obs}_{\rm H\alpha}$) and given by $\mathrm{SFR}^{\rm obs}_{\rm H\alpha}(M_\odot\,\mathrm{yr}^{-1}) = 4.6\times10^{-42}\,L^{\rm obs}_{\rm H\alpha}(\mathrm{erg\,s}^{-1})$. At the three redshift ranges of the sample, the average Hα fluxes of the galaxies correspond to SFRs (uncorrected for extinction) of $\mathrm{SFR}^{\rm obs}_{\rm H\alpha}(M_\odot\,\mathrm{yr}^{-1}) \approx 3$, 6 and 21 $M_\odot\,\mathrm{yr}^{-1}$ at $z = 0.8$, 1.47 and 2.23 respectively. The median $E(B-V)$ for the sample is $E(B-V) = 0.2 \pm 0.1$ (see Table 3.1), which correspond to an Hα extinction $A_{\rm H\alpha} = 0.79 \pm 0.16$ ($A_{\rm V} = 0.96 \pm 0.20$). This suggests reddening corrected star-formation rates of $\mathrm{SFR}^{\rm corr}_{\rm H\alpha}(M_\odot\,\mathrm{yr}^{-1}) \approx 6$, 13 and 43 $M_\odot\,\mathrm{yr}^{-1}$ at $z = 0.8$, 1.47 and 2.23 respectively. Hereafter, I use an extinction value of $A_{\rm H\alpha} = 1.0$ mag as used in previous works based on the HiZELS survey (e.g. Sobral et al. 2012; Stott et al. 2013a; Ibar et al. 2013; Thomson et al. 2017) in order to compare consistently.

[6]Done by A. M. Swinbank up to the 'A' and 'B' datacubes generation for each OB
[7]Done by D. Sobral

TABLE 3.1: INTEGRATED GALAXY PROPERTIES

Table 3.1: Flux densities ($f_{H\alpha}$) are taken from narrow-band photometry and include contamination by [N II]. $SFR^{obs}_{H\alpha}$ are not corrected for extinction. $r_{1/2,H\alpha}$ is the Hα half-light radius and has been deconvolved by the PSF.

ID	RA (J2000)	Dec (J2000)	Strehl	$z_{H\alpha}$	$f_{H\alpha}$ ($\times 10^{-16}$ erg s^{-1}cm^{-2})	[N II]/Hα	$SFR^{obs}_{H\alpha}$ ($M_\odot$ yr^{-1})	$\log_{10}(M_\star)$ ($M_\odot$)	$r_{1/2,H\alpha}$ (kpc)	$E(B-V)$	$\Delta\log(O/H)/\Delta R$ (dex kpc^{-1})
SA22-17	22 19 36.1	+00 34 07.8	34%	0.8114	1.7±0.1	<0.1	2	9.6±0.1	4.2±0.3	0.5±0.2	...
SA22-26	22 18 22.9	+01 00 22.1	34%	0.8150	2.3±0.2	0.26±0.05	3	9.6±0.2	3.1±0.4	0.2±0.2	−0.05±0.02
SA22-28	22 15 36.3	+00 41 08.8	37%	0.8130	2.6±0.2	0.30±0.06	4	9.8±0.3	3.1±0.3	0.5±0.1	−0.03±0.02
SA22-54	22 22 23.0	+00 47 33.0	21%	0.8093	2.3±0.1	0.12±0.07	3	10.1±0.2	2.4±0.3	0.2±0.1	...
COS-16	10 00 49.0	+02 44 41.1	32%	1.3598	1.0±0.1	0.10±0.04	5	9.8±0.3	1.5±0.4	0.0±0.1	+0.08±0.02
COS-30	09 59 11.5	+02 23 24.3	21%	1.4861	1.1±0.1	0.43±0.03	7	10.0±0.1	3.5±0.3	0.5±0.1	−0.014±0.005
SA22-01	22 19 16.0	+00 40 36.1	25%	2.2390	1.0±0.1	0.42±0.13	17	10.3±0.4	2.0±0.2	0.1±0.1	...
SA22-02	22 18 58.9	+00 05 58.3	35%	2.2526	1.2±0.1	0.27±0.07	21	10.5±0.4	3.8±0.3	0.0±0.1	−0.005±0.009
UDS-10	02 16 45.8	−05 02 44.7	33%	2.2382	1.1±0.1	0.23±0.04	19	10.3±0.1	1.6±0.1	0.2±0.1	...
UDS-17	02 16 55.3	−05 23 35.5	12%	2.2395	1.8±0.2	<0.1	31	10.5±0.1	1.5±0.3	0.3±0.1	...
UDS-21	02 16 49.0	−05 03 20.6	33%	2.2391	0.8±0.1	<0.1	14	9.8±0.2	1.0±0.3	0.1±0.1	...
Median	...	...	33%	...	1.2±0.03	0.27±0.02	12±3	10.1±0.2	2.4±0.1	0.2±0.1	−0.014±0.009

3.2.5 Spatial extent

To measure the spatial extent of the galaxies, I use the procedure described in Chapter 2 and I consider a $\sim 0\farcs15$ seeing to perform the beam-smearing correction. The median $r_{1/2,H\alpha}$ for the sample is found to be 2.4 ± 0.1 kpc (Table 3.1), which is consistent with previous studies at similar redshift range (e.g. Swinbank et al. 2012b).

3.2.6 Average ISM properties

To analyse the Hα and [N II] line fluxes for the targets, I collapse each datacube into a one-dimensional spectrum (see Fig. 3.2). In eight cases, I detect the [N II]λ6583 emission line, deriving a median ratio of [N II]/H$\alpha = 0.27 \pm 0.02$, with a range between $0.10 <$ [N II]/H$\alpha < 0.43$ (Table 3.1). None of the galaxies display strong active galactic nucleus (AGN) signatures in their rest-frame optical spectra (Fig. 3.2).

To search for fainter lines and obtain the mean properties of the observed sample, I de-redshift each spectrum to rest-frame and co-add them (weighted by flux), yielding the composite spectrum shown in Fig. 3.2. Weighting by flux instead of signal-to-noise helps to smooth residual features seen in low S/N spectra (e.g. SA22-54, UDS-17 in Fig. 3.2). In this stacked spectrum, the measured [N II]/Hα ratio is 0.25±0.04, a value consistent with the median ratio derived for the sample. I also make a weak detection of the [S II]$\lambda\lambda$6716,6731 doublet and derive a flux ratio of I_{6716}/I_{6731}=1.04±0.31. If I assume a typical H II region temperature of $\sim 10^4$ K, then the measured I_{6716}/I_{6731} ratio corresponds to an electron density (n_e) in the range of 100–1000 cm^{-3} (Osterbrock, 1989), and an upper limit to the ionised gas mass in the ISM of 4–40 $\times 10^{10}$ $M_\odot$ for a disc galaxy with half-light radius of ∼2.4 kpc (Table 3.1).

For an isobaric density distribution of the ionized gas, the density is defined in terms of the mean ISM pressure 'P' and mean electron temperature ($T_e \sim 10^4$ K), through $P/k_B \sim T_e\, n_e$. Therefore, I estimate a median ISM pressure of $P/k_B \sim 10^{6-7}$ K cm^{-3} which is ∼100-1000 times higher than the typical ISM pressure in the Milky Way ($\sim 10^4$ K cm^{-3}) and consistent

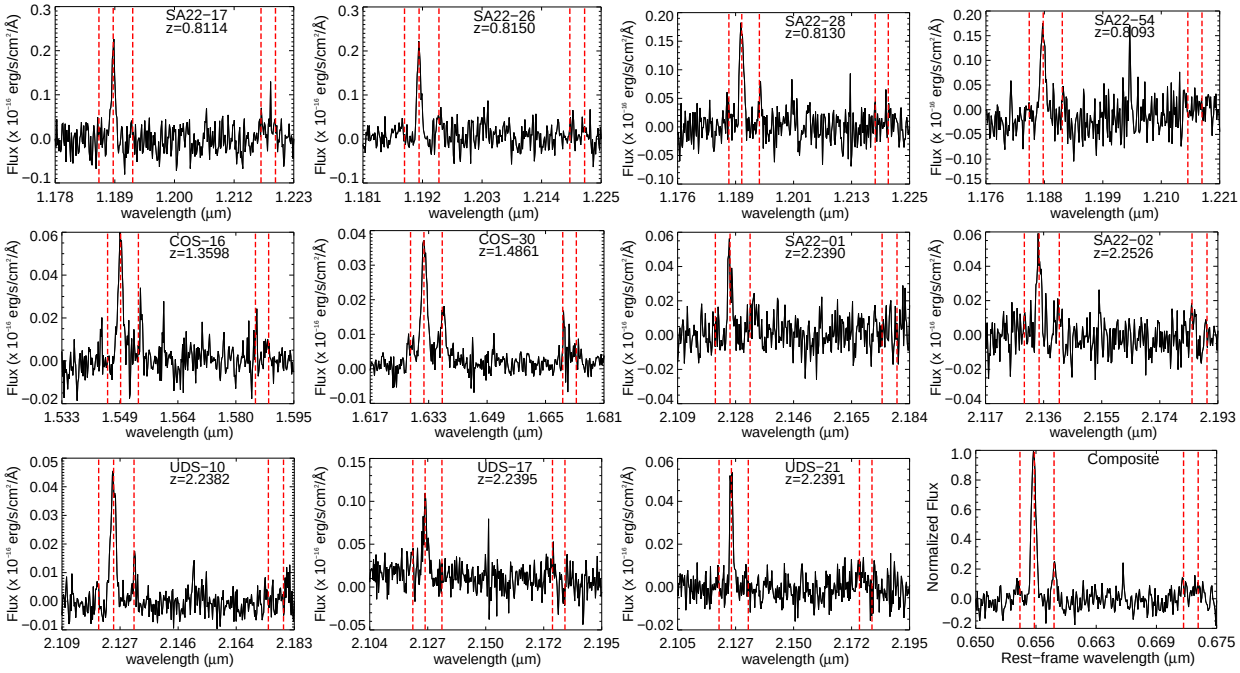

Figure 3.2: Spatially integrated one dimensional spectra around the redshifted Hα emission for each of the galaxies in the sample. Hα, [N II]$\lambda\lambda$6583,6548 and [S II]$\lambda\lambda$6716,6731 emission lines are represented by the red-dashed lines. I detect [N II] emission in eight targets within the sample and the median [N II]/Hα for the sample is 0.27$\pm$0.02, with a range of $0.10 <$ [N II]/Hα < 0.43. None of the galaxies display strong AGN signatures in their near-infrared spectra (e.g. broad lines or high [N II]/Hα ratios).

with other high-redshift galaxy ISM pressure estimates (Swinbank et al., 2015). Although this value has considerable uncertainty, the derived pressure is compatible with hydrodynamic models which suggest that typical pressure in the ISM of star-forming galaxies should increases from $\sim 10^4\,\mathrm{K\,cm^{-3}}$ at $z \approx 0.1$ to $\sim 10^{6-7}\,\mathrm{K\,cm^{-3}}$ at $z \approx 2$ (Crain et al., 2015).

The $\mathrm{I_{6716}/H\alpha}$ flux ratio reflects the ionisation strength of the ISM. I measure $\mathrm{I_{6716}/H\alpha} = 0.12 \pm 0.03$. Considering also the derived [N II]/Hα flux ratio, then I suggest an ionisation parameter of $\log_{10}(\mathrm{U/cm^3})$=$-3.6\pm0.3$ (Osterbrock, 1989; Collins & Rand, 2001), in agreement with Swinbank et al. (2012b), Stott et al. (2013b) and Sobral et al. (2013b, 2015).

3.3 ANALYSIS, RESULTS & DISCUSSION

3.3.1 Galaxy Dynamics

To measure the dynamics of each galaxy, I use the emission line fitting procedure explained in Chapter 2. The Hα and [N II]$\lambda\lambda$6548,6583 emission lines are fitted pixel by pixel. From this procedure, I obtain the Hα intensity, rotation velocity and velocity dispersion two-dimensional fields for each galaxy. I present these maps in Fig. 3.3.

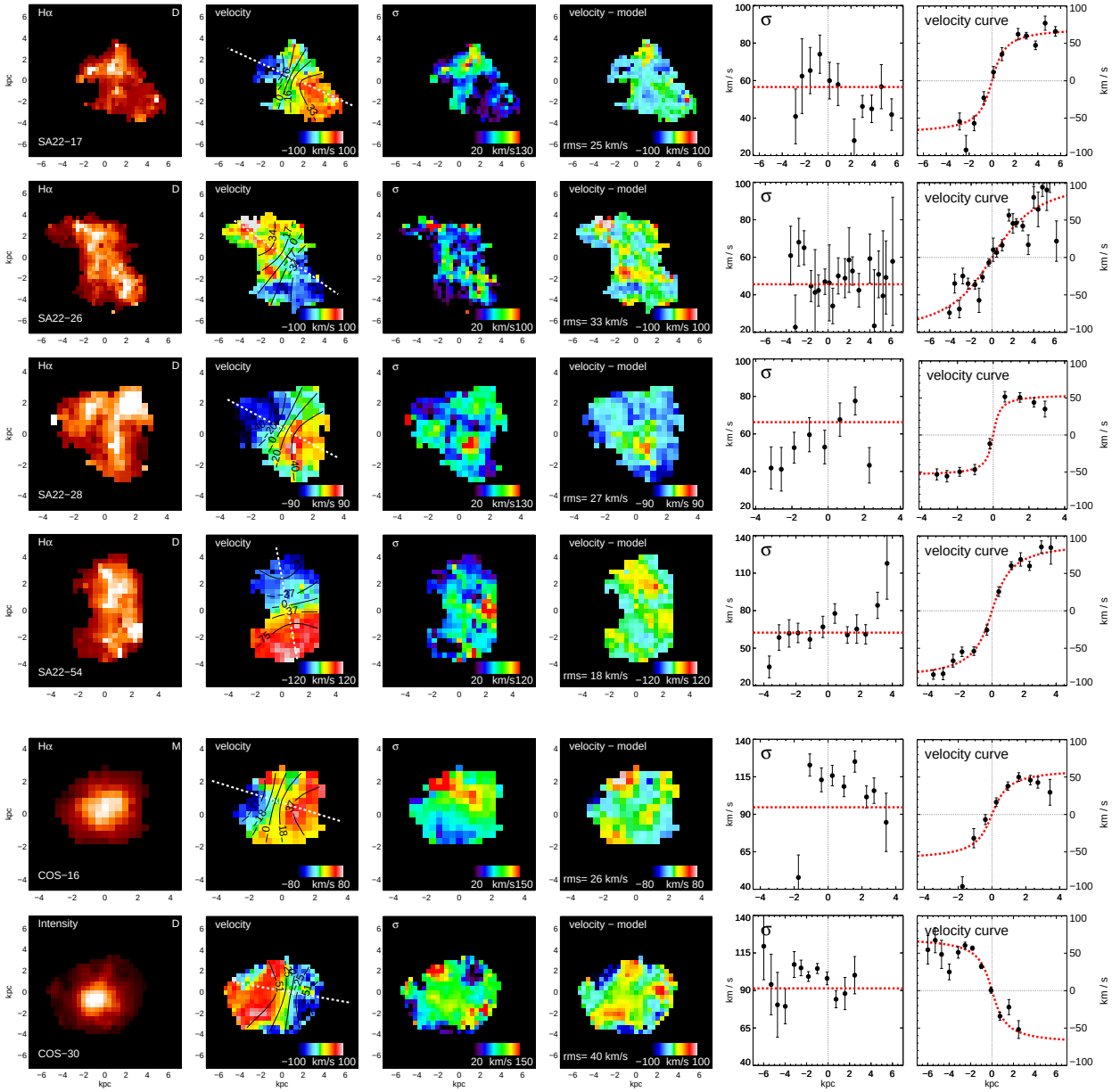

Figure 3.3: Hα intensity, rotation velocity, velocity dispersion, residual fields, one-dimensional velocity dispersion and rotation velocity profiles (columns) for the observed sample (rows). The Hα intensity maps show the classification done by *kinemetry* analysis. The unresolved/compact source (SA22-01) has no modelling. The velocity field show the kinematic centre, the mayor kinematic axis and velocity contours of the best-fit two-dimensional kinematic model. The velocity dispersion field is corrected for the local velocity gradient ($\Delta V/\Delta R$) across the PSF. The residual map is constructed by subtracting the best-fit kinematic model from the velocity map: the r.m.s. of these residuals are given in each panel. The one-dimensional velocity profiles are derived from the two-dimensional velocity field using the best-fit kinematic parameters and a slit width of $\sim$1 kpc across the major kinematic axis. The error bars shows the 1-σ uncertainty and the vertical dotted grey line represents the best-fit dynamical centre. In the velocity dispersion profile panels, the red-dashed line shows the mean galactic value ($\sigma_{v,\mathrm{H}\alpha}$). In the last column, the red-dashed line show the best arctan one-dimensional fit and The horizontal line represents the zero value.

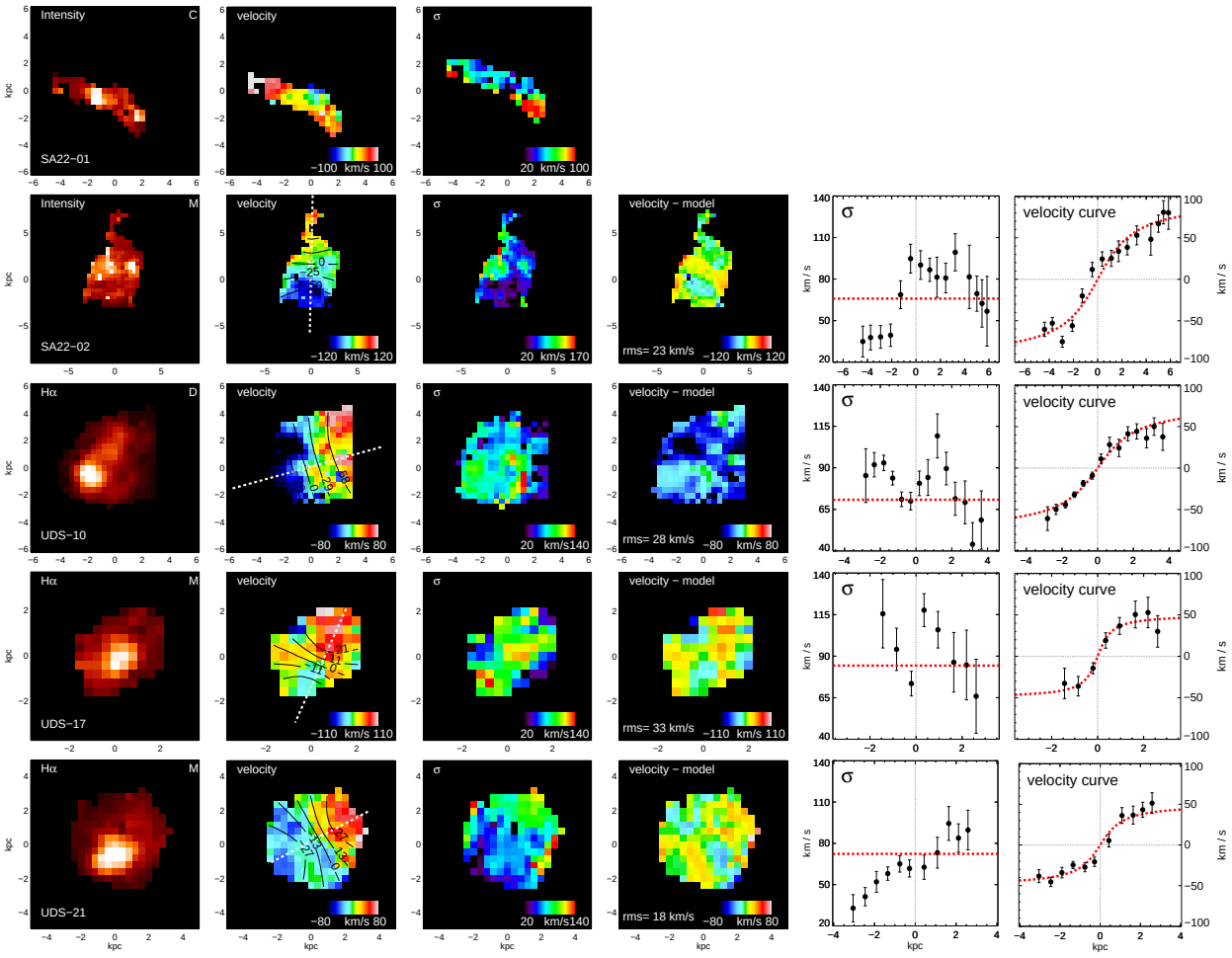

Figure 3.3 Continued.

Fig. 3.3 suggests a variety of Hα structures, including various levels of clumpiness within the sample. However, I note that resolution effects tend to smooth kinematic deviations making galaxy velocity fields appear more disc-like than they actually are (Bellocchi et al., 2012). Fig. 3.3 also shows that there are strong velocity gradients in many cases (e.g. SA22-28, SA22-54) with peak-to-peak differences ($V_{\rm max,H\alpha}\,{\rm sin(i)}$) ranging from 90–180 km s^{-1} and ratio of peak-to-peak difference to velocity dispersion of $V_{\rm max,H\alpha}\,{\rm sin(i)}/\sigma_{v,{\rm H}\alpha} = 1.1$–$3.8$. This is in concordance with previous observations of galaxies at $z \sim 2$ (e.g. Stark et al. 2008; Law et al. 2009; Gnerucci et al. 2011; Genzel et al. 2011). Assuming that the dynamics of the underlying mass distribution are coupled to the measured kinematics of the ionized gas, then these observed high-redshift galaxies are consistent with being highly turbulent systems.

Although a ratio of $V_{\rm max,H\alpha}/\sigma_{v,{\rm H}\alpha} = 0.4$ has been used to crudely differentiate rotating systems from mergers (Förster Schreiber et al., 2009), more detailed kinematic modelling is essential to reliably distinguish these two populations. Therefore, I attempt to model the two-dimensional velocity fields by first identifying the dynamical centre and the kinematic major axis. Each velocity field is modelled by implementing the single-map kinematic fitting procedure explained in Chapter 2 and without any constrain in the inclination angles. From this modelling, the best-fit kinematic maps and velocity residuals are shown in Fig. 3.3, the best-fit inclination and disc rotation speeds are given in Table 3.2. The mean deviation from the best-fit models within the sample (indicated by the typical r.m.s.) is $<{\rm data-model}> = 27\pm2$ km s^{-1} with a range of $<{\rm data-model}> = 18$–40 km s^{-1}. These off-

TABLE 3.2: DYNAMICAL PROPERTIES

Table 3.2: Dynamical properties of the galaxies in the sample. 'inc.' is the inclination angle defined by the angle between the line of sight and the plane of the galaxy disc (for a face-on galaxy, inc = 0 deg.). $\sigma_{v,{\rm H}\alpha}$ is the average velocity dispersion across the galaxy image corrected for "beam smearing" effects due to PSF. $V_{\rm asym}$ and $V_{2.2}$ are inclination corrected. The χ^2_ν of the best two-dimensional fit for each source is given in column six. $K_{\rm Tot}$ is the *kinemetry* coefficient. The classes in the final column denote Disc(D), Merger(M) and Compact(C).

ID	inc. (deg)	$\sigma_{v,{\rm H}\alpha}$ (km/s)	$V_{\rm asym}$ (km/s)	$V_{2.2}$ (km/s)	χ^2_ν	$K_{\rm Tot}$	Class
SA22-17	72	57±13	75±2	62±4	1.1	0.36±0.04	D
SA22-26	53	46±11	142±3	120±12	1.5	0.24±0.03	D
SA22-28	65	66±8	60±3	52±7	1.7	0.22±0.03	D
SA22-54	63	62±10	104±2	95±5	1.3	0.14±0.02	D
COS-16	53	95±8	77±11	59±10	1.9	0.99±0.09	M
COS-30	63	91±13	81±3	61±3	2.9	0.16±0.02	D
SA22-01	...	...	...	...	...	...	C
SA22-02	71	66±9	100±3	85±12	2.0	0.81±0.09	M
UDS-10	32	71±10	143±10	85±7	3.2	0.24±0.04	D
UDS-17	71	84±14	53±6	40±7	9.0	0.90±0.08	M
UDS-21	40	72±11	78±14	58±12	1.6	0.75±0.07	M
Mean	58	71±3	91±2	72±3	2.6	0.48±0.02	...

sets are probably the product of an un-relaxed dynamical component indicated by the high mean velocity dispersion $\sigma_{v,\mathrm{H}\alpha} = 71 \pm 1\,\mathrm{km\,s^{-1}}$ of the sample (Table 3.2), dynamical substructures, or effects of gravitational instability within the disc.

As indicated in Chapter 2, I use the dynamical centre and position angle derived from the best-fit dynamical model to extract the one-dimensional rotation curve across the major kinematic axis of each galaxy (see Fig. 3.3). Three targets (SA22-26, SA22-54 and SA22-02) do not show a flattening of the velocity curve at large radii, so V_{asym} can only be estimated using an extrapolation of the true rotational velocity for these targets.

In order to classify the galaxies as disc-like or merger system, I use the *kinemetry* procedure explained in Chapter 2 and I consider the Shapiro et al. (2008)'s K_{Tot} criterion. I note that Bellocchi et al. (2012) proposed a modified *kinemetry* criterion ($K_{\mathrm{Tot,B12}}$), which try to distinguish between post-coalescence mergers and discs. As the major merger evolves, the central region tends to relax rapidly into a disc meanwhile the outer parts remain out of equilibrium. Therefore, the outer regions retain better the memory of a merger event (Kronberger et al., 2007). In order to consider this effect, Bellocchi et al. (2012) weights more highly the outskirts of each galaxy when combining the asymmetries measured from the velocity and velocity dispersion maps.

These two *kinemetry* criteria have been compared with a visual classification scheme done at higher spatial resolution. Hung et al. (2015) observed eighteen (U)LIRGs at $z < 0.088$ with the *Hubble Space Telescope* (*HST*) Advanced Camera for Surveys (ACS) and considered another six sources from the Digitized Sky Survey (DSS). The IFS data for this galaxy sample is obtained from the Wide Field Spectrograph (WiFeS), while the morphological classification is based on optical morphology analysis (Larson et al., 2016) . They artificially redshifted their local IFS observations to $z \approx 1.5$ to make a comparison with IFU seeing-limited observations ($\sim 0\farcs6$) at high-redshift. Hung et al. (2015) concluded that Shapiro et al. (2008)'s *kinemetry* criterion (K_{Tot}) tend to underestimate the merger fraction whereas Bellocchi et al. (2012)'s *kinemetry* criterion ($K_{\mathrm{Tot,B12}}$) overestimated the number of mergers within the same sample. Hereafter, I will use the *kinemetry* criterion defined by Shapiro et al. (2008) to classify the targets, considering that the merger fraction values are likely to be lower limits at each redshift.

From the *kinemetry* criterion, I classify four targets as merger systems and six targets as rotating systems (see Table 3.2). In addition, from the *kinemetry* criterion error rate (see Shapiro et al. 2008 for more details), I expect that $\sim$1 merger is being misclassified as a disc and $\sim$1 disc is being misclassified as merger. The fraction of rotating systems within the sample is $\sim$60%, which is consistent within 1-σ with that found from other Hα IFU surveys at similar redshifts (e.g. Förster Schreiber et al. 2009; Jones et al. 2010; Wisnioski et al. 2011; Swinbank et al. 2012b). I note that most of the mergers are identified in galaxies at $z \sim 2.23$ and the large error estimates are inherent of the low statistics of the sample.

In Fig. 3.4, I plot the K_{Tot} parameter against the $V_{\mathrm{max,H}\alpha}/\sigma_{v,\mathrm{H}\alpha}$ ratio for the sample and that presented by Swinbank et al. (2012b). All of these galaxies were observed at $\sim$kpc-scale resolution using AO. I find no correlation between both quantities. Although galaxies classified as mergers by *kinemetry* tend to lie in the region with lower $V_{\mathrm{max,H}\alpha}/\sigma_{v,\mathrm{H}\alpha}$ ratio, I find that the $V_{\mathrm{max,H}\alpha}/\sigma_{v,\mathrm{H}\alpha} = 0.4$ merger criterion is not consistent with the more

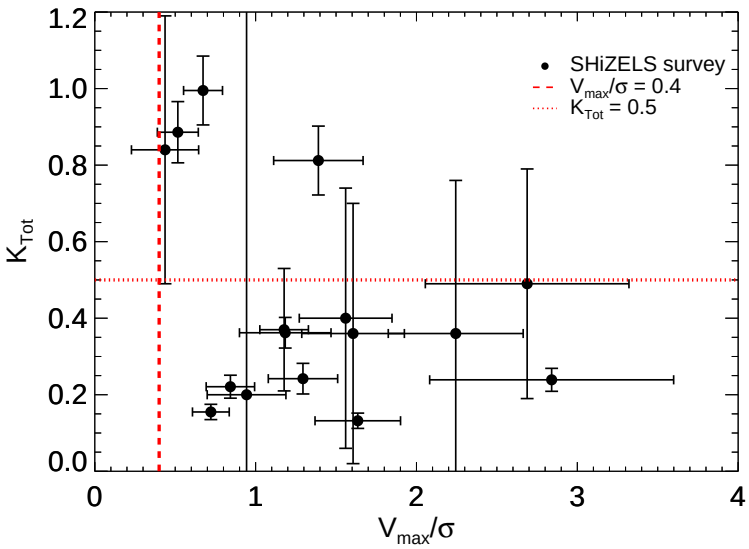

Figure 3.4: The kinematic measure $K_{\rm Tot}$ against the $V_{\rm max}/\sigma_{v,{\rm H}\alpha}$ ratio for the SHiZELS Survey. The red-dashed line shows the $V_{\rm max}/\sigma_{v,{\rm H}\alpha} = 0.4$ ratio which has been used to crudely differentiate rotating systems from mergers (Förster Schreiber et al., 2009). The red-dotted line shows the $K_{\rm Tot} = 0.5$ value which is used to distinguish between galaxy discs from mergers (Shapiro et al., 2008). Although there is no strong correlation between both quantities, it is notable that galaxies classified as mergers by *kinemetry* criterion tend to show lower $V_{\rm max,H\alpha}/\sigma_{v,{\rm H}\alpha}$ ratio, however not as low as 0.4. This suggests that the $V_{\rm max,H\alpha}/\sigma_{v,{\rm H}\alpha} = 0.4$ criterion tend to under-estimate the total number of mergers in a given galaxy sample.

sophisticated kinematic estimate $K_{\rm Tot}$, suggesting that the former criterion under-estimates the total number of mergers within a given galaxy sample. This also suggests that a detailed kinematic analysis is needed in order to classify mergers from galaxy discs.

Hereafter, I will refer to the 'SHiZELS' survey as the compilation of the observations presented in this work with the previous observations done by Swinbank et al. (2012b). In this previous campaign, they observed nine Hα-selected star-forming galaxies between $z \approx 0.84 - 2.23$ with SINFONI. This sample was also drawn from the HiZELS survey. The median $M_\star$ and SFR values are $\sim 2 \times 10^{10}\,M_\odot$ and $\sim 7\,M_\odot\,{\rm yr}^{-1}$, respectively (see Swinbank et al. 2012b for more details).

3.3.2 The Stellar-Mass Tully-Fisher and $M_\star$–$S_{0.5}$ Relations

The Tully-Fisher relation is a fundamental scaling relation describing the interdependence of luminosity or stellar mass and the maximum rotational velocities (a dark matter mass tracer) in galaxies. It allows to trace the evolution of the mass-to-luminosity ratio of populations of galaxies at different epochs. Recently, the KROSS survey (Stott et al., 2016; Tiley et al., 2016b; Harrison et al., 2017) has provided a new perspective on TFR evolution by observing $\sim$ 600 galaxies at $z \sim 0.9$. Tiley et al. (2016b) derived an evolution of the stellar-mass TFR zero-point of -0.41 ± 0.08 dex for rotationally supported galaxies defined with $V_{\rm rot,H\alpha}/\sigma_{v,{\rm H}\alpha} > 3$. However, when they analysed their data without this $V_{\rm rot,H\alpha}/\sigma_{v,{\rm H}\alpha}$ constraint, they did not

find any significant evolution of the $M_\star$-TFR zero-point. I note that the $M_\star$–TFR zero-point evolution found by Tiley et al. (2016b) is contrary to some previous studies conducted at similar redshift (Miller et al., 2011, 2012; Di Teodoro et al., 2016).

Similarly, Weiner et al. (2006) and Kassin et al. (2007) introduced the kinematic measure $S_{0.5} = (0.5V^2 + \sigma_v^2)^{0.5}$ which considers support by both rotational motions and dispersion arising from disordered motions (Weiner et al., 2006). Kassin et al. (2007) computed the $M_\star$-TFR and $M_\star$–$S_{0.5}$ relations within 544 galaxies at $0.1 < z < 1.2$. The $M_\star$–$S_{0.5}$ relationship was found to be a tighter relation compared with the $M_\star$-TFR relation, and this relation also showed no evolution with redshift in either intercept or slope.

When measuring circular velocities, to be consistent with the previous Swinbank et al. (2012b) campaign, I use velocities observed at 2.2 times the disc scale length ($V_{2.2}$) corrected for inclination effects. The disc scale length ($r_{\rm d}$) is defined as the radius at which the galaxy Hα intensity has decreased to $e^{-1}(\sim 0.37)$ times it's central value.

The Stellar Mass Tully-Fisher Relation

In Fig. 3.5, I study the $M_\star$-TFR at $z = 0.8 - 2.23$ using SHiZELS survey galaxies classified as disc-like by the *kinemetry* analysis. The stellar masses and velocities from the comparison samples have been estimated in a fully consistent way, and these values (or corrections, where necessary) are presented in Swinbank et al. (2012b). I also show the TF relations at $z = 0$ (Pizagno et al., 2005) and the best-fit relation at $z = 1 - 2$ (Swinbank et al., 2012b) from the literature. Even though I do not attempt to fit a relation to the data, Fig. 3.5 suggests that apparently the sample is consistent with no evolution in the zero-point of the $M_\star$-TFR out to $z = 0.8 - 2.23$.

As suggested by Tiley et al. (2016b) I estimated the rotational velocity to dispersion velocity ratio. This is done by calculating the $V_{2.2}/\sigma_{v,{\rm H}\alpha}$ ratio. I show this parameter colour-coded in Fig. 3.5. I find that galaxies with lower $V_{2.2}/\sigma_{v,{\rm H}\alpha}$ ratio (i.e. with greater pressure support) tend to be scattered to lower values along the rotational velocity axis: this is consistent with Tiley et al. (2016b), who found an evolution of the zero-point $M_\star$-TFR at $z = 0.9$ when they select galaxies with $V_{80}/\sigma_{v,{\rm H}\alpha} \geq 3$ within their sample (V_{80} is the velocity observed at the radius which encloses the 80% of the total Hα intensity of the galaxy), although the complete sample is consistent with no evolution in the $M_\star$-TFR zero-point.

This result suggests that the large scatter measured from the $M_\star$-TFR at high-redshift may be produced by galaxies which are supported by a combination of rotational and disordered motions. If I do not take into account this effect then this could produce misleading conclusions. I note that galaxies which have greater rotational support within the SHiZELS survey tend to lie closer to the $M_\star$-TFR at $z = 2$ derived by Swinbank et al. (2012b), whilst galaxies with strong disordered motion support tend to be have a greater offset from this relationship. This trend, perhaps, implies that galaxies may be moving onto the $M_\star$-TFR with time as the dynamics of the stars and gas in the central few kpc of the halos are yet to relax into a disc-like system.

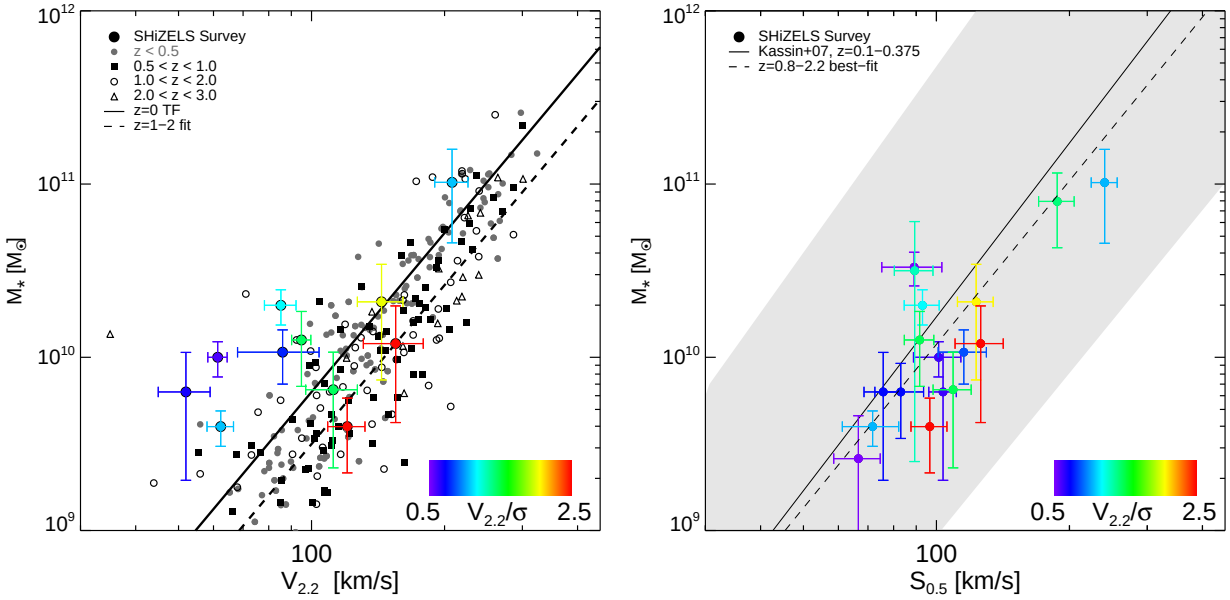

Figure 3.5: *Right*: Evolution of the stellar mass TF relation measured from the SHiZELS survey at $z = 0.8 - 2.23$ colour-coded using the $V_{2.2}/\sigma_{v,\mathrm{H}\alpha}$ ratio. I only show the galaxies consistent with rotating systems together with their 1-σ velocity and stellar mass uncertainties. The solid line denotes the TFR at $z = 0$ from Pizagno et al. (2005). The dashed line represent the best-fit TF relation at $z = 1 - 2$ from Swinbank et al. (2012b) based on the compilation of high-redshift points from (Miller et al. 2011, 2012 $z = 0.6 - 1.3$; Swinbank et al. 2006 $z = 1$; Swinbank et al. 2012b $z = 1.5$; Jones et al. 2010 $z = 2$; Cresci et al. 2009 $z = 2$and Gnerucci et al. 2011 $z = 3$). Galaxies with lower relative rotational support tend to be scattered to lower values along the velocity axis. This is consistent with the result found by Tiley et al. (2016b). *Left*: The $M_\star$–$S_{0.5}$ relationship measured from the SHiZELS survey at $z = 0.8 - 2.23$. The error bars show the 1-σ stellar mass and $S_{0.5}$ uncertainties. The data is colour-coded as in the image above. The solid line represents the relation at $z \sim 0.2$ from Kassin et al. (2007) and the shaded area represents its 1-σ uncertainty. The dashed line corresponds to the best-linear-fit to the data. The scatter is tighter than the intrinsic $M_\star$–$S_{0.5}$ scatter. The slope (0.32±0.2) and the intercept at $10^{10}\,M_\odot$(1.98±0.09) found from the best-fit are consistent with the uncertainties of the $z \sim 0.2$ relation. This is consistent with no evolution of the $M_\star$–$S_{0.5}$ relation with redshift up to $z \approx 2.23$.

The $M_\star$–$S_{0.5}$ Relation

The stellar mass TFR is found to be sensitive to which process dominates the support of the galaxy. The scatter increases when galaxies with pressure gradient support equivalent to the rotational support ($V_{2.2}/\sigma_{v,\mathrm{H}\alpha} \sim 1$) are included. Perhaps a more fundamental relation is the $M_\star$-$S_{0.5}$ relationship (Weiner et al., 2006; Kassin et al., 2007) which consider the support given by ordered and disordered motions within the galaxy.

In Fig. 3.5, I show the $M_\star$-$S_{0.5}$ relation for the SHiZELS survey using the inclination-corrected speeds, colour-coded by $V_{2.2}/\sigma_{v,\mathrm{H}\alpha}$ ratio. I also show the $z \sim 0.2$ $M_\star$-$S_{0.5}$ relationship from Kassin et al. (2007) and the best linear fit to the SHiZELS survey sample. I note that this relationship is fitted in the form $\log_{10}(S_{0.5}) = \mathrm{a} + \mathrm{b}\log_{10}(M_\star \times 10^{-10}\,M_\odot)$,

where 'a' is the interceptor. From Fig. 3.5 it can be seen that the sample agrees with the $z \sim 0.2$ $M_\star$-$S_{0.5}$ relationship within 1-σ uncertainty: this is consistent with either no evolution of interceptor or slope of the $M_\star$-$S_{0.5}$ relation with redshift (Kassin et al., 2007). Despite the low number statistics, I do not identify any dependency on $V_{2.2}/\sigma_{v,\mathrm{H}\alpha}$ for this relation, contrasting with what was previously seen in the $M_\star$-TFR (Fig. 3.5).

This relationship is consistent with a scenario of galaxy formation that begins with matter assembling into a dark-matter halo with turbulent kinematics. The baryonic component forms protodiscs that are initially supported by a combination of rotational and disordered motions ($V/\sigma \sim 1$). The material in these protodiscs settles down, probably produced by gas dissipation and the redistribution of the angular momentum of the stars, unless they undergo major mergers (Kassin et al., 2007). This traduces to the circularization of the gas and stellar orbits and the decline of the turbulent motions amplitude to the values observed in local galaxies ($V/\sigma \sim 10 - 20$, Glazebrook 2013).

3.3.3 Merger Fraction

To test whether it is galaxy mergers, secular processes or a combination of both that dominate and drive galaxy evolution at the peak era for star formation, I need to measure the merger fraction (f_{merg}) at this epoch. From a theoretical perspective in the ΛCDM paradigm, dark matter haloes merge hierarchically from the bottom up (e.g. Lacey & Cole 1993; Cole et al. 2000; Springel et al. 2005). As baryonic matter traces the underlying dark matter, I expect that galaxies merge hierarchically as well.

Stott et al. (2013b) noted that the typical sSFR for galaxies increases with redshift within the HiZELS sample. They found greater merger fractions with increasing sSFR suggesting that major mergers can lead to galaxies having unusually high sSFR. Although the targets within the SHiZELS survey have higher SFR at higher redshift, they also have higher stellar masses, maintaining the median sSFR per redshift slice roughly constant (see Fig. 3.1).

I define 'merger fraction' as the number of galaxies classified as merger by the *kinemetry* criterion divided by the total number of galaxies in the redshift slice (I do not consider the unresolved galaxy classified as 'compact' in this analysis).

In Fig. 3.6, I show the variation of the merger fraction as a function redshift for the $z = 0.8$, 1.47 and 2.23 redshift slices. From the SHiZELS survey, I find a merger fraction of $0.0^{+0.4}$, $0.3^{+0.2}_{-0.2}$ and $0.6^{+0.2}_{-0.3}$ at $z = 0.8$, 1.47 and 2.23, respectively. The error in the merger fraction are estimated by assuming binomial statistics. These values are consistent with previous IFU surveys (e.g. Shapiro et al. 2008; Förster Schreiber et al. 2009).

I compare with Stott et al. (2013b) who used the M_{20} morphological classification (Lotz et al., 2004) in the HiZELS sample, but I only consider the merger fraction calculated for those galaxies with similar sSFR values ($\sim 10^{-9}\,\mathrm{yr}^{-1}$). From Fig. 3.6, I find a clear increase in merger fraction from $z = 0.8$ to $z = 2.23$ that seems to be stronger than the increase found by Stott et al. (2013b). This suggests that methods based on surface brightness morphology classification may underestimate the number of major mergers at low sSFR and similar

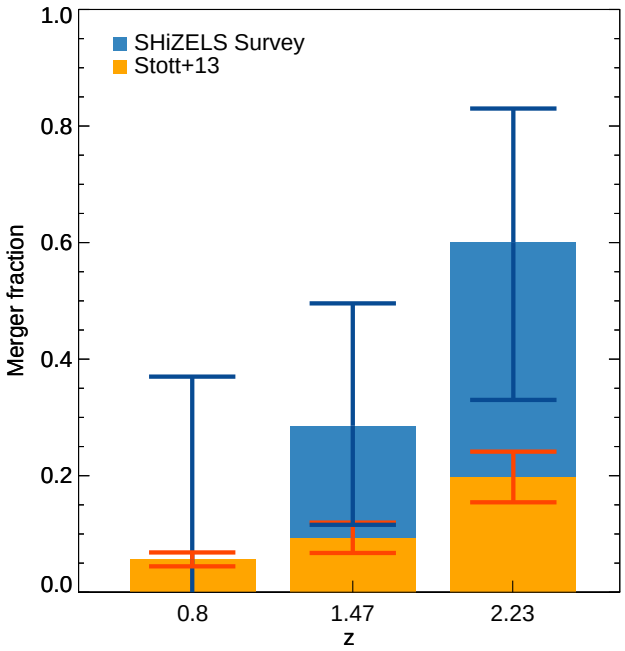

Figure 3.6: In blue are represented the kinematically selected mayor merger fractions measured from the SHiZELS survey at $z = 0.8 - 2.23$. The error bars for the SHiZELS survey are estimated by assuming binomial statistics. The orange colour correspond to the data at similar sSFR ($\sim 10^{-9}\,\mathrm{yr}^{-1}$) from Stott et al. (2013b), who use the M_{20} morphological criterion to classify mergers. I find higher merger fraction at each redshift slice.

($0\farcs2 - 0\farcs7$) spatial resolution. This result also suggests that galaxy mergers usually lie within the 'main-sequence' of star forming galaxies at $z \gtrsim 2$, being representative of the 'typical' galaxy population at these redshifts.

Taking into account that galaxy mergers are usually associated to (Ultra-)Luminous Infrared Galaxies (ULIRGs)LIRGs in the local Universe (e.g. Arribas et al. 2014) and that (U)LIRGs systems dominate the 'main-sequence' galaxy population at $z \gtrsim 1$ (Daddi et al., 2007; Sargent et al., 2012), then I suggest that most of the galaxy mergers may not produce the sufficient SFR enhancement compared to the evolution of the average SFR of all galaxies with redshift in order to produce extreme starburst episodes at $z \gtrsim 1$. I conclude that galaxy mergers may have a dominant role in the evolution of 'typical' star-forming galaxies at $z \gtrsim 2$, but I caution regarding the low number of statistics.

3.3.4 Metallicity Content

Measuring the internal enrichment and radial abundance gradients of high redshift star-forming galaxies provides a tool for studying the gas accretion and mass assembly process such as the gas exchange with the intergalactic medium. The Oxygen (O) abundance has been traditionally used as a tracer of the metal content in galaxies. Produced by massive stars, oxygen is the most common metal in terms of mass and by measuring the auroral to nebular emission line ratio, such as [OIII]λ4363/λ5007, the metal content can be easily

determined in the local Universe (e.g. Lequeux 1979). However, at higher redshifts, determine the metallicity of galaxies becomes prohibitive from Oxygen mainly due to the faintness of the [OIII] emission lines (Pettini & Pagel, 2004).

The Nitrogen (N) abundance can also be used to determine the metal content in galaxies (e.g. Denicoló et al. 2002). It is released to the ISM by low- and intermediate-mass stars as a product of the CNO cycle, and/or during the third dredge-up occurring along the asymptotic giant branch (AGB) phase (Vincenzo et al., 2016). Along with the Hα emission line, the [N II]/Hα ratio can be used to determine the metallicity of high-redshift galaxies using the conversion $12 + \log_{10}(\mathrm{O/H}) = 8.9 + 0.57\ \log_{10}([\mathrm{N\,II}]/\mathrm{H}\alpha)$ (Pettini & Pagel, 2004). The sample has a median metallicity of $12 + \log_{10}(\mathrm{O/H}) = 8.57\pm0.05$, which is slightly below but still consistent with the solar value. Also the galaxies have metallicities consistent with previous studies that derive typical metallicities of 8.66±0.05 and 8.58±0.07 for Hα-selected samples at $z \sim 0.81$ and $z \sim 0.84$–2.23, respectively (Queyrel et al., 2012; Swinbank et al., 2012b; Sobral et al., 2013b).

A relationship between mass, metallicity and SFR has been found in both the local and high-redshift Universe (Mannucci et al., 2010; Lara-López et al., 2010, 2013) and measured by Stott et al. (2013a) for a sample drawn from the HiZELS survey at $z \sim 1$. The shape of this 'Fundamental Metallicity Relationship' (FMR) is, to first order, a manifestation of the positive correlation of the metallicity and stellar mass at fixed SFR and a negative correlation of the metallicity and SFR at fixed stellar mass. The shape of the FMR can be explained as the result of the competing effects of chemical enrichment of the gas by the evolving stellar population, star-formation driven winds and the inflow of gas from the IGM.

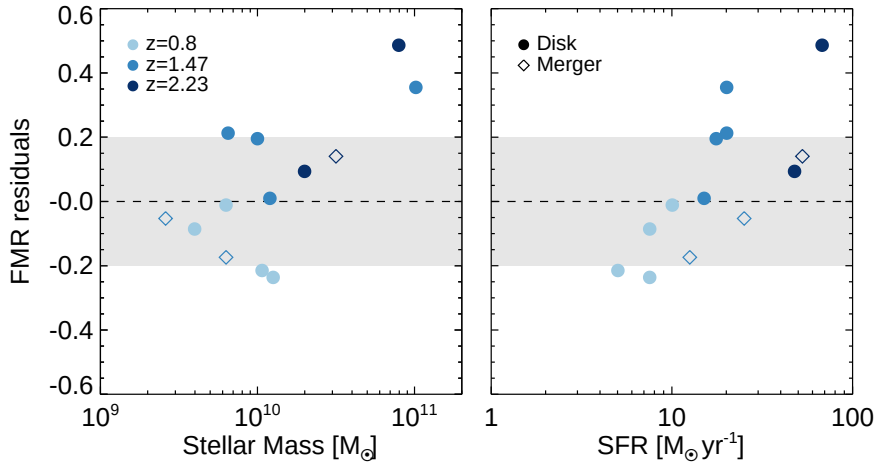

Figure 3.7: The metallicity residuals within the SHiZELS Survey calculated as the subtraction between the measured metallicities and the metallicities predicted by the FMR of Stott et al. (2013a). I plot against the stellar mass (*left*) and SFR (*right*). Negative values mean metallicities lower than expected by the FMR. The sky blue, blue and dark blue colours represent the sources at $z = 0.8$, 1.47 and 2.23 respectively. Diamonds and circles show targets classified as Merger and Discs respectively from *kinemetry* criterion. The shaded area corresponds to the scatter of the FMR of ≈ 0.2 dex (Stott et al., 2013a). The measured residuals expected from the FMR are ≈ 0.23 dex, which is consistent with the relationship. I find no trend between galaxy morphology and metallicity content within the sample.

I test this relationship and its dependence on galaxy morphology using the SHiZELS Survey. In Fig. 3.7, I show the difference between the measured metallicity of the SHiZELS Survey and the metal content predicted by the FMR at $z = 0.84 - 1.47$ (Stott et al., 2013a). The scatter is consistent within 1-σ uncertainties from the FMR. On average, I find that the metal content in the star-forming galaxies is similar to galaxies of similar $M_\star$ and SFR at $z \sim 0.1$ (Stott et al., 2013a). I find no trend between mergers and discs morphologies within the residuals from this relationship. This suggests no evolution in the FMR up to $z \sim 2.2$, indicating that the interplay between gas accretion, star formation and gas outflows have not evolved since $z \sim 2.2$ in agreement with previous studies (e.g. Mannucci et al. 2010).

In order to derive the chemical abundance gradients in the sample, I use the disc inclination and position angle (derived from the best-fit dynamical model) to define ∼1 kpc annuli centred at the dynamical centre. Within each annulus, I stack the spectrum (considering emission line offsets in each annulus) to measure the average [N II]/Hα flux ratio by fitting a double Gaussian profile with coupled Gaussian widths. For a detection, I enforce S/N > 5 thresholds at each radius and a minimum of three radial detections per target. Then, I fit a straight line as a function of galaxy radius in each case.

From the eight galaxies with measured [N II]/Hα flux ratio detected from their one-dimensional spectra, five galaxies present reliable [N II]/Hα gradients. I show this in Fig. 3.8 and the individual metallicity gradients values are reported in Table 3.1. I find a median of $\Delta \log_{10}(\mathrm{O/H})/\Delta \mathrm{R} = -0.014 \pm 0.009\,\mathrm{dex\,kpc^{-1}}$, i.e. a median gradient consistent with a negative gradient. In comparison, Swinbank et al. (2012b) found a slightly steeper median metallicity gradient ($\Delta \log_{10}(\mathrm{O/H})/\Delta \mathrm{R} = -0.027 \pm 0.006\,\mathrm{dex\,kpc^{-1}}$) from their sample at similar redshift range. Considering the combination of both studies (the full SHiZELS sample), I find a median metallicity gradient of $\Delta \log_{10}(\mathrm{O/H})/\Delta \mathrm{R} = -0.026 \pm 0.008$ dex kpc^{-1}. This result suggests that either low metallicity gas from the halo or IGM is accreted onto the outer disc, or metal enrichment is higher in the central region of the galaxy.

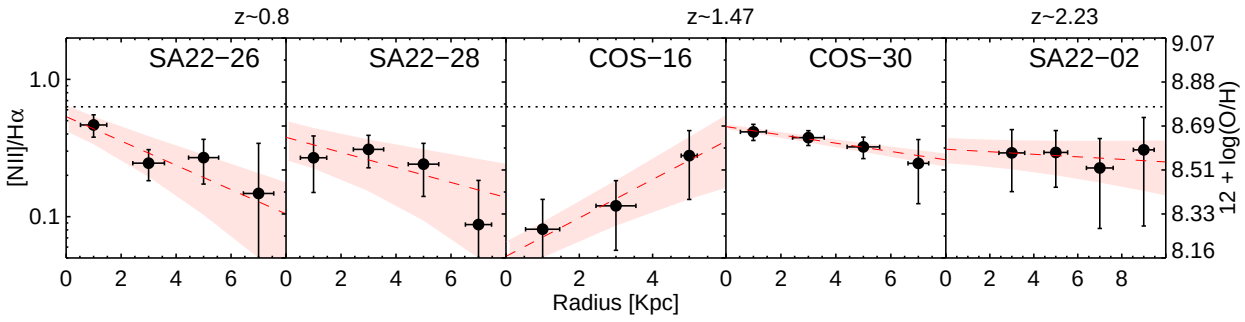

Figure 3.8: Metallicity gradients for five galaxies in the observed sample (Table 3.1) from spatially resolved measurements as function of the physical radius derived from the best kinematic model. The red dashed line represents the best linear fit and the shaded region represents 1-σ uncertainties. The dotted line shows the AGN limit of $\log_{10}([\mathrm{N\,II}]/\mathrm{H}\alpha) \approx -0.2$ at $z = 0.8$ (Kewley et al., 2013). This suggests the potential for a starting AGN activity within the central kpc in source SA22-26. Within the sample, SA22-02 has a gradient consistent with zero, SA22-26, SA22-28 and COS-30 have negative gradients and COS-16 source has positive metallicity gradient.

I do not have simultaneous access to the nebular [O III]λ5007, Hβ, Hα, [N II]λ6583 and/or [S II]$\lambda\lambda$6717, 6731 emission lines to distinguish any possible strong AGN contribution within the sample via a BPT diagram (Baldwin et al., 1981). Considering $\log_{10}([\mathrm{N\,II}]/\mathrm{H}\alpha) \approx -0.2$ flux ratio as a rough limit for identifying an AGN at $z \geq 0.8$ (Kewley et al., 2013), only the central kpc of SA22-26 might be affected by low AGN contamination. This conclusion is also supported by the lack of broad recombination lines in the spectra.

Just one galaxy (COS-16) shows a positive metallicity gradient within the SHiZELS survey – a system which is also classified as a major merger by the *kinemetry* criterion. From cosmological simulations, Tissera et al. (2016) found that galaxies with positive metallicity gradients tend to exhibit morphological perturbations and close neighbours. They suggest that those galaxies have a high probability of interactions/mergers due to a high number of surrounding satellites. They analyse the evolution of a gas-rich equal-mass merger and they found that both negative and positive metallicity gradients might be produced during different stages of the merger evolution.

I note that, I do not find any clear correlation between the asymmetries measured from the *kinemetry* coefficients defined by Shapiro et al. (2008) (K_{V}, K_{σ} and K_{Tot}) and the metallicity gradients observed within the SHiZELS survey.

3.3.5 Spatially Resolved Chemical Abundances

A tentative anti-correlation between the metallicity gradient and the global integrated metallicity was previously hinted at the MASSIV survey using star-forming galaxies at $z \sim 1.2$ (Queyrel et al., 2012). They suggest that metallicity gradients are more frequently negative in metal-rich galaxies and more frequently positive in low-metallicity galaxies. In Fig. 3.9 I show the anti-correlation suggested by Queyrel et al. (2012), adding the SHiZELS galaxies and the sample observed by Stott et al. (2014). I calculate the average and median values per $\Delta \log_{10} = 0.1$ bin. Then, I fit a straight-line to the average and median values.

The slope is 2.5-σ from being flat (2.0-σ by fitting the median values), but due to beam smearing effects and inclination angles the measured metallicity gradients are likely to be underestimated, especially those of Stott et al. (2014) and MASSIV samples which were measured on seeing-limited conditions ($\sim 0\farcs7$). Stott et al. (2014) estimated that their observed metallicity gradients reflects only $\sim$70% of the true values. This suggests that, if I alleviate inclination angle effects with higher resolution IFU observations, these results will not change. The results support the previous suggestion by Queyrel et al. (2012).

I note that positive metallicity gradients could be explained by the infall of metal-poor gas from the IGM into the centre of the galaxy, diluting the gas and lowering its metallicity in the central regions. If the funnelling of metal-poor gas into the centres of galaxies is triggered by galaxy mergers, then from the merger fraction estimated for the SHiZELS Survey (Fig. 3.6), I should expect to find more systems with positive/flat metallicity gradients at $z \sim 2$.

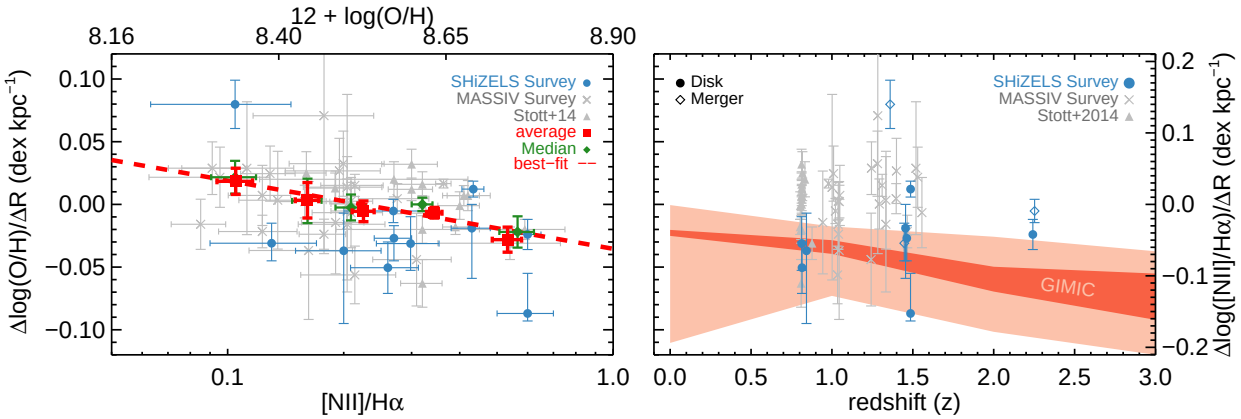

Figure 3.9: *Left*: Metallicity gradient as a function of the [N II]/Hα emission line ratio from the one-dimensional spectra of each galaxy. The blue circles are individual galaxies within the SHiZELS Survey. The grey crosses denotes the sample from the MASSIV survey (Queyrel et al., 2012) corrected for a Pettini & Pagel (2004) metallicity calibration. The grey triangles denotes the sample from Stott et al. (2014). The red squares and green diamonds show the average and median metallicity content and metallicity gradient per $\Delta \log_{10}(\mathrm{O/H})$=0.1 bin respectively. The error bars show 1-σ uncertainties. Within the literature, I only consider [N II]/Hα fluxes ratio above 1-σ detection threshold. The red-dashed line shows the best linear fit ($\Delta \log_{10}(\mathrm{O/H})/\Delta \mathrm{R} = \mathrm{a} + \mathrm{b} \times \log_{10}(\mathrm{O/H})$) to the average values with a slope value of a= -0.10 ± 0.04 and zero-point of b=0.89 ± 0.30. The SHiZELS survey supports the anti-correlation such that metallicity gradients tend to be negative in metal-rich galaxies and positive in low-metallicity galaxies (see also Queyrel et al. 2012). *Right*: Metallicity gradient as a function of redshift. I also show the theoretical evolution of the metallicity gradient with redshift from the GIMIC simulation (Crain et al., 2009; McCarthy et al., 2012). The shaded-red area shows the range of metallicity gradients for all disc galaxies in the simulation in the mass range $9.5 < \log_{10}(M/M_{\odot}) < 11.5$, whilst the shaded light-red denotes the 1-σ scatter at each epoch. Diamonds and circles show targets classified as Merger and Disc respectively from *kinemetry* criterion. The metallicity gradients measured from the SHiZELS survey do not support the evolution predicted from the GIMIC simulation from $z = 0$ to $z \approx 1.47$.

Taking into account the metallicity gradients measured for the SHiZELS Survey (Fig. 3.9), I compare its evolution with redshift with the prediction from the 'Galaxies-Intergalactic Medium Interaction Calculation' simulation (GIMIC; Crain et al. 2009; McCarthy et al. 2012; Swinbank et al. 2012b), where the metallicity gradient evolution within disc galaxies is a consequence of a decrement of gas inflow rates from $z \approx 2$ to $z = 0$ and redistribution of gas within the galaxy disc.

The observed metallicity gradients for disc galaxies within the SHiZELS survey do not support the trend predicted by the GIMIC simulation between $z \approx 0 - 2$ as this simulation predicts steeper metallicity gradients at $z \gtrsim 1.5$. However, it should be noted that GIMIC does not implement an AGN feedback 'sub-grid' model. AGN activity may help to pollute the circumgalactic medium by the injection of metals towards larger radius via the triggering of metal-rich outflows from the galactic centre. The chosen metal mixing procedure in the hydrodynamical simulation may also play a critical role as different metal diffusion prescriptions can produce different galaxy property outcomes (e.g. Wiersma et al. 2009). Nevertheless, I note that a much larger sample of disc-like galaxies at $z \gtrsim 2$ are needed to be observed to further test this.

3.4 Conclusions

I present new AO-aided SINFONI IFU observations of spatially resolved Hα kinematics of eleven mass-selected ($M_{\star} = 10^{9.5-10.5}\,M_{\odot}$) 'typical' star-forming galaxies from the wide-field narrow-band HiZELS survey in three redshift slices, $z = 0.8$, 1.47 and 2.23. All galaxies lie within $< 30''$ of bright (R<15.0) stars enabling natural guide star AO-assisted observations. Modelling the Hα dynamics along the major kinematic axis of the galaxies, I derive a median dynamical-to-dispersion support of $V_{\mathrm{max,H}\alpha}\,\mathrm{sin(i)}/\sigma_{v,\mathrm{H}\alpha} = 1.6\pm0.3$ (with a range of 1.1–3.8). I classify the galaxies using a *kinemetry* analysis (Shapiro et al., 2008) finding six disc-like galaxies and four mergers. One galaxy is unresolved. These new observations are combined with a previous similar study (nine galaxies taken from Swinbank et al. 2012b) to create a homogeneously selected sample of star-forming galaxies with dynamical characterisation at $\sim$kpc scales near the peak of the cosmic star-formation rate density.

I find a tentative increase of the merger fraction as a function of redshift ($f_{\mathrm{merg}}(z) \sim 0.0^{+0.4}$, $0.3^{+0.2}_{-0.2}$ and $0.6^{+0.2}_{-0.3}$ at $z = 0.8$, 1.47, 2.23, respectively). Nevertheless, the results are consistent with previous IFU surveys (Shapiro et al., 2008; Förster Schreiber et al., 2009), although I find higher merger fractions at a given sSFR in comparison to previous analyses by Stott et al. (2013b) who used a morphological classification from *HST* near-IR imaging.

I combine the observations with previous studies of intermediate and high-redshift galaxies (Swinbank et al., 2006; Cresci et al., 2009; Jones et al., 2010; Gnerucci et al., 2011; Miller et al., 2011, 2012; Swinbank et al., 2012b) to investigate the stellar mass Tully-Fisher relation. I find that the scatter of this relation is affected by the galaxy pressure support ($V_{2.2}/\sigma_{v,\mathrm{H}\alpha}$) – a result which is consistent with Tiley et al. (2016b) findings. On the other hand, I also investigate the $M_{\star}$-$S_{0.5}$ (Kassin et al., 2007) relation within the SHiZELS survey at

$z = 0.8 - 2.23$. The kinematic measure $S_{0.5} = (0.5V^2 + \sigma_v^2)^{0.5}$ consider support by both rotational motions and dispersion arising from disordered motions (Weiner et al., 2006). The results are consistent (within 1-σ) with the $M_\star$-$S_{0.5}$ relationship found at $z \sim 0.2$, suggesting little or no evolution of this relation as function of redshift.

I measured the residuals from the 'Fundamental metallicity relation' (Stott et al., 2013a) at $z = 0.84 - 1.47$, finding that the scatter is consistent with measurements errors, suggesting no variation in the FMR up to $z \approx 2.23$.

I measure metallicity gradients ($\Delta \log_{10}(\mathrm{O/H})/\Delta \mathrm{R}$) using the [N II]/H$\alpha$ ratio for 3, 7 and 2 galaxies at z =0.8, 1.47 and 2.23 within the SHiZELS Survey. These metallicity gradients ranges between -0.087 and $0.08\,\mathrm{dex\,kpc^{-1}}$, with a median metallicity gradient of $\Delta \log_{10}(\mathrm{O/H})/\Delta \mathrm{R} = -0.027 \pm 0.008\,\mathrm{dex\,kpc^{-1}}$. The evolution of metallicity gradients as a function of redshift in the sample do not exhibit any clear trend such as the predicted by the GIMIC simulation for galaxy discs, where gas inflow rate decreases with decreasing redshift progressively. However, larger samples at $z \approx 2$ are needed to further test this.

I show that metallicity gradients and global metallicity contents are consistent with the anti-correlation suggested by Queyrel et al. (2012). This can be explained by the scenario in which infall of metal-poor gas from the IGM into the central part of the galaxy drives the positive gradients.

3.5 Appendix

3.5.1 Appendix A: Serendipitous detection

Within the SA22-26 datacube, I found an unexpected emission line at $\lambda \sim 1.203\,\mu$m. This emission line does not coincide with any expected emission line emitted from the SA22-26 source as it would correspond to $\lambda_{\mathrm{rest}} \sim 0.663\,\mu$m in that galaxy's restframe. This unexpected emission line overlaps spatially with part of the Hα emission from SA22-26 source (Fig. 3.10-*top*). Furthermore, the kinematic behaviour of this emission line region shows a position angle (Fig. 3.10-*bottom*) which differs from the position angle derived for the SA22-26 source (Fig. 3.3). This suggests that this serendipitous emission does not come from SA22-26. In the spectrum, I did not find any other emission lines associated with this galaxy which could be used for determining the redshift of this possible new source. I call this source as SA22-26B. If I assume that this emission line is also a redshifted Hα emission line, then SA22-26B is offset redwards by $\sim 5500\,\mathrm{km\,s^{-1}}$ (in the line-of-sight direction, $z \sim 0.833$) from the SA22-26 source. The modest redshift difference (if the emission line is Hα) would be consistent with no lensing. I note that the emission from SA22-26 shows no sign of extinction by SA22-26B supporting the fact that this galaxy is background.

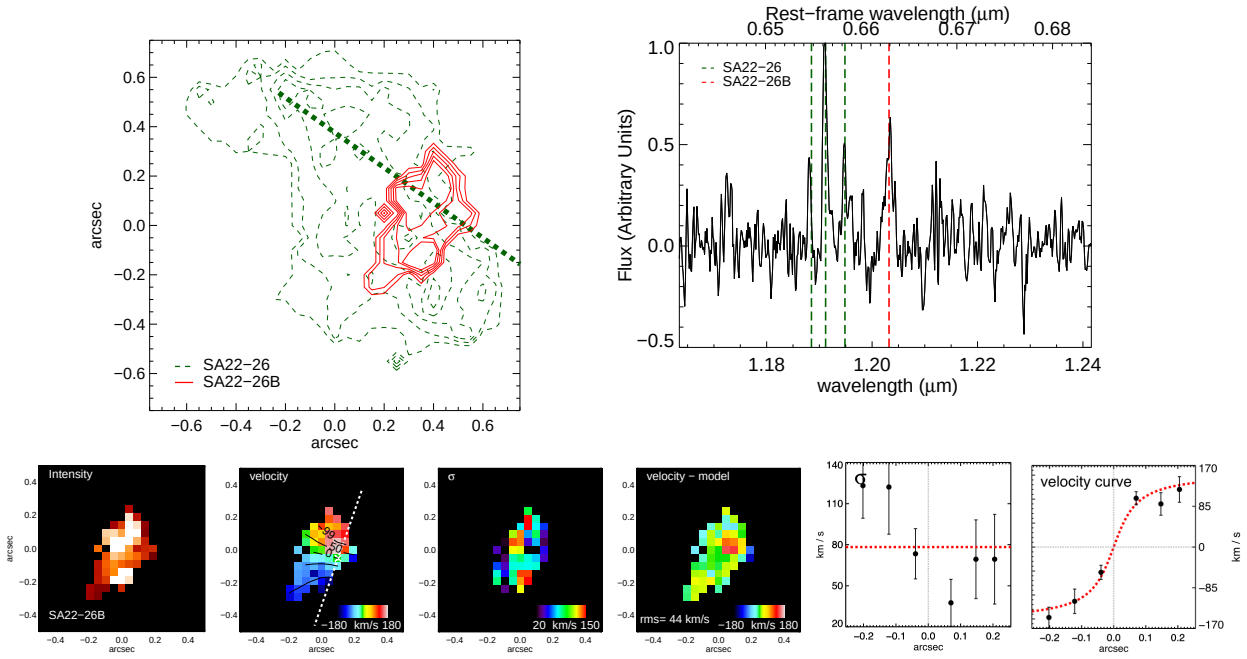

Figure 3.10: *Top Left*: Intensity contours of the serendipitous detection (red) and SA22-26 (green-dashed) sources within the SINFONI data-cube. The dashed line shows the position angle derived for SA22-26 source. There is a clear spatially overlap between both emissions. *Top Right*: Spatially integrated one-dimensional spectra of SA22-26B. The emission is integrated within the red contour showed in top-left figure. The red-dashed line shows the emission line detected at $\lambda \sim 1.203$ μm. The green-dashed lines show the Hα, [N II]$\lambda\lambda$6583,6548 emission lines for the SA22-26 source extracted from the area encircled by the green contours. *Bottom*: Intensity, rotation velocity, velocity dispersion, residual field, one-dimensional velocity dispersion profile and one-dimensional velocity profile (as in Fig. 3.3) for the serendipitous detection. The spatial scale is showed in arcseconds due to the uncertain redshift determination.

Chapter 4

The kiloparsec-scale gas kinematics in two star-forming galaxies at $z \sim 1.47$ seen with ALMA and VLT-SINFONI at matched resolution

In this Chapter[8], I present ALMA CO($J = 2 - 1$) follow-up observations of two main-sequence star-forming galaxies at $z \sim 1.47$ taken from the HiZELS survey. These two systems have been previously reported to be molecular gas rich $f_{\rm H_2} \equiv M_{\rm H_2}/(M_{\rm H_2} + M_\star) \sim 0.8$. I carried out a detailed study to resolve, at ∼kpc-scales, the CO emission. These new observations are combined with earlier ALMA observations (sensitive to diffuse CO emission) and compared with previous Hα observations with VLT-SINFONI at matched ∼kpc spatial resolution. One target is marginally detected in CO(2-1), showing complex dynamics with respect to the ionised gas traced by Hα. The other source is spatially resolved and detected at high significance, enabling a detailed exploration of its internal dynamical properties. In this system, both gaseous phases show similar spatial extension, rotation velocities and velocity dispersions ($V_{\rm rot} \sim \sigma_v \sim 100\,{\rm km\,s^{-1}}$) suggesting a rotational velocity to velocity dispersion ratio consistent with unity. By comparing the ionized and molecular gas tracers through the use of a two-dimensional kinematic model, I estimate a median depletion time $\tau_{\rm dep} = 2.3 \pm 1.2\,{\rm Gyr}$ for the galaxy as a whole. This value is in agreement with the average $\tau_{\rm dep}$ value observed in local star-forming galaxies at similar spatial scales. Using a thick-disc dynamical modelling, I derive a dynamical mass $M_{\rm dyn} \approx (1.6 \pm 0.2) \times 10^{11}\,M_\odot$ within $\approx 6\,{\rm kpc}$. This suggests a dark matter fraction ($f_{\rm DM} \equiv M_{\rm DM}/M_{\rm dyn}$) of 0.6 ± 0.1 at $\approx 6\,{\rm kpc}$ ($\approx 6 r_{\rm d}$), in agreement with the average $f_{\rm DM}$ value derived from stacked rotation curve analysis of galaxies at similar redshift range.

[8]These results were published in Molina, et al. 2019b, MNRAS, 487, 4856

4.1 Introduction

Understanding how galaxies form and evolve over cosmic time is a major goal in modern astrophysics. Surveys have shown that there is a decline in the overall cosmic star-formation rate density since $z \sim 2$ (e.g. Madau et al. 1996; Sobral et al. 2013b; Khostovan et al. 2015) which coincides with the decrease of the average fraction of molecular gas mass in galaxies (e.g. Tacconi et al. 2010; Geach et al. 2012; Carilli & Walter 2013). This behaviour is thought to match the cosmic evolution of the mass in stars, and the molecular gas content ($M_{\rm H_2}$) of the Universe, hence it provides a logical interpretation for the interplay between, perhaps, the main actors controlling the growth of galaxies (e.g. Madau & Dickinson 2014).

At the peak epoch of the cosmic star formation activity ($z \sim 2-3$), spatially-resolved observations of galaxies have mostly come from large *Hubble Space Telescope* (*HST*) and IFU surveys (e.g. Koekemoer et al. 2011; Brammer et al. 2012; Law et al. 2012). The latter trace the ionized gas content in seeing limited conditions ($\sim 0\farcs6$ in $K-$band, e.g. Sobral et al. 2013b; Wisnioski et al. 2015; Stott et al. 2016; Turner et al. 2017; Johnson et al. 2018). Although adaptive optics aided IFU observations have delivered $\sim 0\farcs15$ ($\sim$kpc-scale) spatial resolution data on smaller galaxy samples (e.g. Förster Schreiber et al. 2009; Swinbank et al. 2012b; Molina et al. 2017; Förster Schreiber et al. 2018; Gillman et al. 2019). Deep observations have focused mainly in sampling the 'main-sequence' of star-forming galaxies, i.e., those galaxies that are part of the bulk of the galaxy population in terms of stellar mass, and SFR (e.g. Noeske et al. 2007; Whitaker et al. 2012).

High-redshift ($z \sim 1-3$) IFU surveys targeting the Hα emission have revealed that most of the main-sequence star-forming galaxies (hereafter, 'typical' star-forming galaxies), present: (1) highly turbulent galactic disks with high surface brightness, indicating that the interstellar medium is highly pressurized with $P_{\rm tot} \sim 10^{3-4}$ times higher than the typical ISM pressure in the Milky Way (Swinbank et al., 2015; Molina et al., 2017); (2) the star-formation activity is partly triggered by gravitational fragmentation of dynamically unstable gas potentially leading to the formation of massive clumps which could be up to $\sim 1000\times$ more massive ($\sim 10^9\,M_\odot$) than star-forming complexes seen in local galaxies (e.g. Genzel et al. 2011; Swinbank et al. 2012a).

Although the physical conditions that produce these extreme ISM properties remain poorly understood, one possible explanation may be related to the high molecular gas densities that may arise from the high molecular gas fractions (e.g. Escala & Larson 2008). In the local Universe galaxies have typical $f_{\rm H_2}$ values of ~ 0.1, while on the other hand galaxies at $z \sim 1-3$ have reported molecular gas fractions up to ~ 0.8 (e.g. Tacconi et al. 2010; Daddi et al. 2010; Hughes et al. in prep.). The molecular gas content seems to dominate the baryonic mass budget in the central parts of these high-redshift 'typical' star-forming systems, but there is little or almost no information about their spatial distribution and kinematics.

Spatially-resolved morpho-kinematic studies of the molecular gas content in galaxies are critical to understand the physical processes that control the star formation activity. Nevertheless, observations of high-redshift galaxies with direct spatially resolved molecular gas detections have remained a challenge. Beyond the local Universe, resolved CO detections are limited to the most massive/luminous yet rare galaxies or highly magnified gravitationally

Table 4.1: ALMA Cycle-5 observations. These data have been concatenated with the data shown in Hughes et al. (in prep.). 'PWV' is the average precipitable water vapour estimate for the observations

Source	Project ID	Observation Date	Flux Calibrator	Bandpass Calibrator	Phase Calibrator	PWV (mm)	Number of antennas	Time on Target (min)
SHiZELS-8	2017.1.01674.S	14 November 2017	J0238+1636	J0238+1636	J0217-0820	3.17	43	47.05
		15 Nov. 2017	J0238+1636	J0238+1636	J0217-0820	2.05	43	45.78
		16 Nov. 2017	J0006-0623	J0006-0623	J0217-0820	1.44	43	45.82
COS-30 / SHiZELS-19	2017.1.01674.S	14 Nov. 2017	J1058+0133	J1058+0133	J0948+0022	3.56	43	43.67
		14 Nov. 2017	J1058+0133	J1058+0133	J0948+0022	3.92	43	44.12
		16 Nov. 2017	J1058+0133	J1058+0133	J0948+0022	0.89	43	44.23
		18 Nov. 2017	J1058+0133	J1058+0133	J0948+0022	0.60	43	44.50
		20 Nov. 2017	J1058+0133	J1058+0133	J0948+0022	0.48	50	44.02

lensed sources (e.g. Saintonge et al. 2013; Swinbank et al. 2015; Chen et al. 2017; Calistro Rivera et al. 2018; Motta et al. 2018). With ALMA, now is possible to study the physical conditions of the cold molecular gas in 'typical' star-forming galaxies at $z > 1$ and test if the actual cosmological models successfully explain the characteristics of the high-redshift ISM.

4.2 Observations & Data Reduction

4.2.1 The SHiZELS Survey

In this work, I take advantage of galaxies with previous Hα VLT-SINFONI IFU AO-aided imaging taken from the SHiZELS survey (Swinbank et al. 2012b; Molina et al. 2017; Gillman et al. 2019). This is based on a sub-sample of sources taken from the HiZELS near-infrared narrow-band imaging project (Sobral et al., 2012, 2013b, 2015) and is one of the largest IFU-AO survey observing the Hα emission in 'typical' star-forming galaxies on $\sim$kpc-scales in three narrow redshift slices $z = 0.86$, 1.47 & 2.23 ($M_\star \sim 3 - 30 \times 10^{10}\,M_\odot$; SFR$\sim 2 - 30\,M_\odot\,\mathrm{yr}^{-1}$). All galaxies have a deep multi-wavelength coverage from the UDS, COSMOS or SA22 fields. From SHiZELS, I select two galaxies, COS-30 and SHiZELS-8, which have been previously detected in CO($J = 2 - 1$) with ALMA at $\sim 1\farcs6 - 2\farcs5$ resolution (Hughes et al. in prep.).

The global stellar masses and SFRs are taken from Gillman et al. (2019). Briefly, the stellar masses were computed by using the Bayesian SED fitting code, MAGPHYS (da Cunha et al., 2008) to the rest-frame UV, optical and near-infrared data available ($FUV - 8.0\,\mu$m photometry collated in Sobral et al. 2014, and references therein), assuming a Chabrier (2003) IMF and a Calzetti et al. (2000) extinction law.

The SFRs are calculated from the $M_\star$-based extinction-corrected Hα emission line fluxes (Garn & Best, 2010; Sobral et al., 2012; Ibar et al., 2013) and adopting the Kennicutt (1998a) calibration $\mathrm{SFR}_{\mathrm{H}\alpha}\,(M_\odot\,\mathrm{yr}^{-1}) = 4.6 \times 10^{-42}\ L_{\mathrm{H}\alpha}\,(\mathrm{erg\,s}^{-1})$ with a Chabrier (2003) IMF. The total Hα emission line fluxes are taken from the HiZELS narrow-band survey and are corrected for [NII] flux contamination by considering the [NII]/Hα ratio measured from the SINFONI observations. I note that the extinction corrected SFR values presented in this work are consistent with the values reported in Gillman et al. (2019), i.e, with the intrinsic SFR values estimated by MAGPHYS. The COS-30 galaxy is referred to as 'SHiZELS-19' in Gillman et al. (2019). Hereafter I use this name to refer to this galaxy.

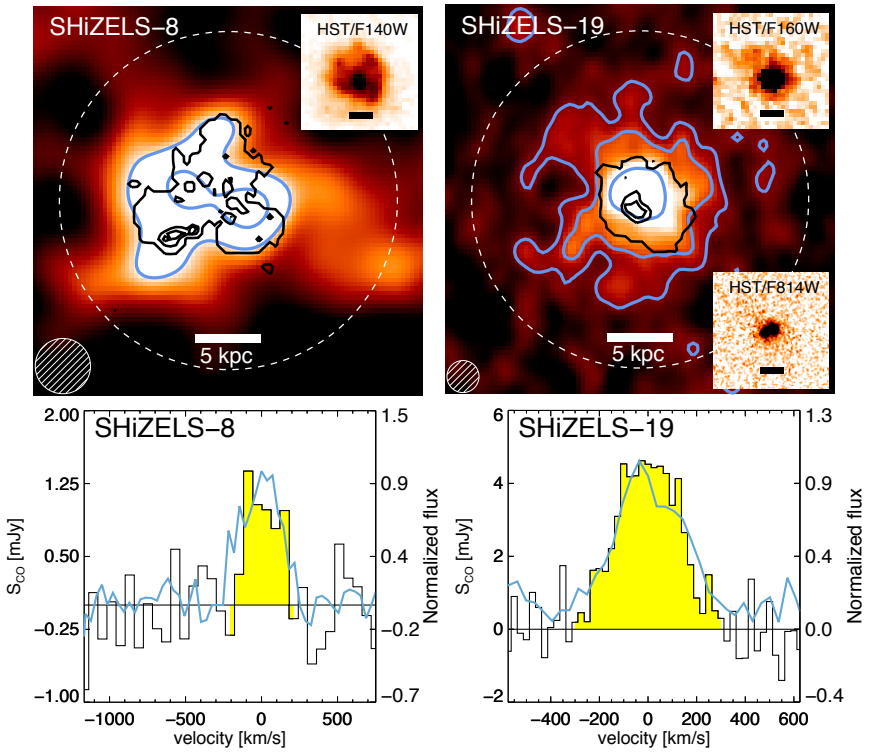

Figure 4.1: *Top*: Spectrally integrated 2000 kλ datacubes encompassing the CO(2-1) emission line for each galaxy in a 3.″56 ($\approx$ 30 kpc) squared sky region. The synthesized beam size ($\theta_{\rm BMAJ}$ = 0.″50, 0.″29 for SHiZELS-8 and SHiZELS-19, respectively) is showed in the bottom-left corner in each map. The blue contours represent the 3-, 5- and 10-σ levels the image noise. The black contours show the Hα emission detected in the SINFONI-AO observations. For SHiZELS-19, I align both intensity maps by using their best-kinematic centres (see § 4.3.3). In contrast, as I lack the detailed kinematic information for SHiZELS-8, I just align its intensity maps by eye in order to improve visualization. The dashed line represents the sky-aperture defined as 2$\times$ FWHM of the best-fitted two-dimensional Gaussian in each map. If available, I also show the *HST* broad-band images over the same sky region in the right side of the map. In each *HST* cut-out, the black bar represents the 5 kpc scale. *Bottom*: Spatially-collapsed spectra extracted within the sky-aperture for each galaxy showing the CO(2-1) emission line. The yellow colour indicates the 2$\times$ FWHM region for the CO emission line. The blue line shows the Hα emission line flux density normalized to the CO emission line peak and extracted from the SINFONI-AO IFU observations using the same sky aperture (Swinbank et al., 2012b; Molina et al., 2017; Gillman et al., 2019). I find good agreement between the CO and Hα linewidths.

I adopt the Whitaker et al. (2012)'s definition of the 'main-sequence' of star-forming galaxies, and by using the redshift, $M_\star$ and the specific star formation rate (sSFR$\equiv$SFR$/M_\star$) estimates, I calculate the 'distance' to the main-sequence ΔMS$\equiv$sSFR/sSFR$_{\rm MS}(z,M_\star)$ for each source. The $\log_{10}(\Delta{\rm MS})$ values are presented in Table 4.2. These values are lower than the 0.6 dex upper limit usually adopted to define the main-sequence (Genzel et al., 2015).

4.2.2 ALMA observations & data reduction

Cycle-5 ALMA Band-3 observations (2017.1.01674.S; P.I. Molina J.; see Table 4.1) are used to detect and resolve the redshifted CO(2–1) emission line ($\nu_{\rm rest} = 230.538$ GHz) for SHiZELS-8 (Swinbank et al., 2012b) and SHiZELS-19 (presented as COS-30 in Molina et al. 2017). Those observations were carried during November 2017, reaching a root-mean-squared (r.m.s.) noise of 120–150 μJy beam^{-1} at 0.″15 angular resolution using a channel width of 60 km s^{-1}.

The Cycle-5 observations were taken in an extended configuration (synthesized beam FWHM of $\approx$ 0.″15), thus being more sensitive to more compact emission. These are combined them with previous 2″ resolution Cycle-1 and -3 ALMA data (see Hughes et al. in prep. for more details) to obtain sensitive and high-fidelity imaging of the CO(2-1) emission.

Data were reduced[9] using Common Astronomy Software Applications[10] (casa) considering a standard ALMA pipeline up to calibrated u-v products. The task tclean was used to deconvolve the data to produce datacubes for both galaxies. In each datacube the regions where emission is identified down to 3-σ were cleaned using the tclean casa task, allowing multi-scale cleaning (multiscale=[0.5,5,15,45], where image pixel size is fixed at 0.″04). The high-resolution datacubes are produced by using Briggs weighting with robust parameter at 0.5, obtaining synthesized beam FWHMs of $\approx$ 0.″15 ($\sim$kpc-scale at $z \sim 1.47$). By taking advantage of the Cycle-1 and -3 data, datacubes with different spatial scales are produced by tapering at 2000 kλ and reducing the spatial resolution using a circular restoring synthesized beam (0.″29 $\approx$ 2.5 kpc at $z \sim 1.47$). These combined tapered datacubes are produced with the aim to recovering as much as the low surface brightness CO(2-1) emission as possible from the outskirts of each galaxy (Fig. 4.1).

In the case of SHiZELS-8, I am unable to detect the CO emission in the high-resolution datacube or the $\approx$ 2.5 kpc resolution map. Therefore, for this galaxy, the spectral and spatial resolutions are reduced in order to boost the CO emission signal-to-noise (S/N). The spectral channel width is set to 60 km s^{-1} and the spatial resolution is degraded to 0.″50 by performing an additional smoothing step.

In the case for SHiZELS-19, the source is easily detected in the high-resolution datacube. Thus, for this galaxy, the spectral channel width is set to 25 km s^{-1} aiming to minimize spectral resolution effects in the derivation of the kinematic parameters.

[9]Done by E. Villard and E. Ibar due to computational hardware limitations
[10]http://casa.nrao.edu/index.shtml

TABLE 4.2: SPATIALLY-INTEGRATED GALAXY PROPERTIES

Table 4.2: The integrated Hα flux densities ($f_{H\alpha}$) are taken from narrow-band photometry and corrected for [NII] contamination. The $SFR_{H\alpha}$ values are corrected for Hα extinction ($A_{H\alpha}$) following the $M_\star - A_{H\alpha}$ parametrization presented by Garn & Best (2010). ΔMS is the offset of each galaxy with respect to the main-sequence of star-forming galaxies. $\alpha_{CO,A+17}$ and $\alpha_{CO,N+12}$ are the CO-to-H_2 conversion values calculated by following the Accurso et al. (2017) and Narayanan et al. (2012) parametrizations. The M_{H_2} and f_{H_2} quantities are computed by using $\alpha_{CO,N+12}$ (see § 4.3.4).

ID	SHiZELS-8	SHiZELS-19
RA (J2000)	02:18:21.0	09:59:11.5
Dec (J2000)	−05:19:07.8	+02:23:24.3
z_{spec}	1.4608	1.4861
$f_{H\alpha}/10^{-17}$ (erg s^{-1} cm^{-2})	10.9±1	7.6±1
$A_{H\alpha}$	1.1±0.2	1.1±0.2
[NII]/Hα	<0.1	0.43±0.03
$SFR_{H\alpha}$ ($M_\odot$ yr^{-1})	16±2	13±2
$\log_{10} M_\star$ ($M_\odot$)	10.3±0.2	10.3±0.2
$\log_{10}\Delta$MS (dex)	0.53	0.41
$S_{CO(2-1)}\Delta v$ (Jy km s^{-1})	0.38±0.08	0.64±0.03
$\log_{10} L'_{CO(2-1)}$ (K km s^{-1} pc^2)	10.04±0.04	10.27±0.04
$\alpha_{CO,A+17}$ ($M_\odot$(K km s^{-1} pc^2)$^{-1}$)	21±8	3.9±1.5
$\alpha_{CO,N+12}$ ($M_\odot$(K km s^{-1} pc^2)$^{-1}$)	5.0±1.0	1.5±0.2
$\log_{10} M_{H_2}$ ($M_\odot$)	10.81±0.10	10.51±0.07
f_{H_2}	0.76±0.24	0.62±0.16

I show the spatially integrated spectrum for each galaxy in Fig. 4.1. Those were extracted by considering a sky-aperture defined in diameter as 2× FWHM of the best-fitted two-dimensional Gaussian in each map ($\sim 1\farcs3 - 1\farcs2$ for SHiZELS-8 and SHiZELS-19).

In summary, for SHiZELS-19, the Cycle-1, -3 and -5 data were combined to generate a high resolution ($\approx 0\farcs15$ ∼kpc-scale) and a 'low resolution' ($\approx 0\farcs29 \sim 2.5$ kpc) datacubes, while for SHiZELS-8, I use a $\approx 0\farcs5$ resolution map (~ 4.3 kpc), optimizing the flux sensitivity to the compact and diffuse emission.

4.3 ANALYSIS, RESULTS & DISCUSSION

4.3.1 CO emission & CO-to-H_2 conversion factor

The global CO(2-1) velocity-integrated flux densities ($S_{CO(2-1)}\Delta v$) are taken from Hughes et al. (in prep.) and presented in Table 4.2. Those are estimated by fitting a 2D Gaussian profile to the spectrally-integrated datacube (moment 0). The CO(2-1) luminosities ($L'_{CO(2-1)}$) are calculated by following Solomon & Vanden Bout (2005);

$$L'_{\rm CO(2-1)} = 3.25 \times 10^7 \, S_{\rm CO(2-1)} \Delta v \, \nu_{\rm obs}^{-2} \, D_{\rm L}^2 \, (1+z)^{-3} \, [{\rm K \, km \, s^{-1} \, pc^2}], \quad (4.1)$$

where $S_{\rm CO(2-1)}\Delta v$ is in Jy km s^{-1}, $\nu_{\rm obs}$ is the observed frequency of the emission line in GHz, $D_{\rm L}$ is the luminosity distance in Mpc, and z is the redshift. Then, I estimate the CO(1-0) luminosity for each galaxy by assuming a $L'_{\rm CO(2-1)}/L'_{\rm CO(1-0)} = 0.85$ ratio (e.g. Danielson et al. 2011).

To derive molecular gas masses, I need to assume a CO-to-H_2 conversion factor. By considering a dynamical model, I constrain the $\alpha_{\rm CO}$ value in the galaxies (see § 4.3.4). However, I also use different prescriptions in the literature to calculate tentative CO-to-H_2 conversion factor values. Unfortunately, as I lack of dust masses for SHiZELS-8 and SHiZELS-19 (see Cheng et al. in prep), I am unable to use a dust-to-gas ratio motivated $\alpha_{\rm CO}$ value (e.g. Leroy et al. 2013). Thus, from the literature, I use the Accurso et al. (2017) and Narayanan et al. (2012) $\alpha_{\rm CO}$ prescriptions as I have direct estimates of the input observables and these parametrizations do not require a minimum observational spatial resolution (e.g. Feldmann et al. 2012).

Briefly, Accurso et al. (2017)'s prescription considers the effect of the ISM metallicity and the strength of the UV radiation field in the estimation of the CO-to-H_2 conversion factor. I note that in this parametrization, the strength of the UV field is traced by the offset of the galaxy with respect to the main-sequence of star-forming galaxies (see Accurso et al. 2017, for more details). However, this prescription does not consider deviations of the $\alpha_{\rm CO}$ value due to high gas surface density ($\Sigma_{\rm gas}$) values (e.g. Bolatto et al. 2013). In contrast, the Narayanan et al. (2012)'s prescription takes into account the effect of the ISM metallicity and gas surface density in the estimation of the $\alpha_{\rm CO}$ value. This is, however, a numerical prediction for $\Sigma_{\rm gas}$ and its effect is parametrized via the luminosity-weighted CO surface brightness quantity ($\Sigma_{\rm CO}$; see Narayanan et al. 2012, for more details).

In order to apply these two $\alpha_{\rm CO}$ parametrizations, I use the ΔMS values calculated by assuming the Whitaker et al. (2012)'s definition of the main-sequence of star-forming galaxies and presented in Table 4.2. The metallicities are estimated from the [NII]/Hα ratio and assuming the Pettini & Pagel (2004) metallicity prescription. The inclination corrected $\Sigma_{\rm CO}$ values are calculated from the ALMA observations. Based on these assumptions, the global $\alpha_{\rm CO}$ values are listed for each galaxy in Table 4.2.

I find little agreement between the two parametrizations. By considering the Accurso et al. (2017)'s prescription, I find higher CO-to-H_2 conversion values than the obtained from the Narayanan et al. (2012)'s parametrization (Table 4.2). This is expected as Accurso et al. (2017)'s prescription does not consider the effect of $\Sigma_{\rm gas}$ in their estimation of the $\alpha_{\rm CO}$, and it has a steeper dependence on metallicity. In the case of the Narayanan et al. (2012)'s parametrization, the low $\alpha_{\rm CO}$ value obtained for SHiZELS-19 is mainly dominated by its high galactic $\Sigma_{\rm CO}$, which is reflected by its high $\Sigma_{\rm H_2}$ value (Table 4.4). On the other hand, SHiZELS-8 has an $\alpha_{\rm CO}$ value closer to that found in Galactic GMCs (Table 4.2). This is produced by its low metal content. Although variations of the CO-to-H_2 conversion factor within galactic discs have been reported (e.g. Sandstrom et al. 2013), I note that a global $\alpha_{\rm CO}$ value seems to be a good approximation for the SHiZELS-19 galaxy (Appendix 4.5.1).

4.3.2 The SHiZELS-8 galaxy

The SHiZELS-8 Hα observation (Swinbank et al., 2012b) suggests that this galaxy is consistent with being a turbulent rotating disc hosting three kpc-sized clumps (Swinbank et al., 2012a). Unfortunately the SHiZELS-8 CO(2-1) observations have too low S/N to allow a detailed dynamical characterization. This galaxy has $\sim$50% lower velocity-integrated CO(2-1) flux density than SHiZELS-19, but its emission seems more extended, i.e, it has a lower CO surface brightness. On the other hand, the estimated low metallicity for SHiZELS-8 ($12+\log_{10}(\mathrm{O/H}) < 8.12$) suggests a lack of dust content which could indicate an efficiently CO molecule photo-dissociation by the far-ultraviolet (far-UV) photons and a higher CO-to-H_2 conversion factor (Bolatto et al., 2013). This implies that SHiZELS-8 could have a larger molecular gas content than SHiZELS-19, albeit similar SFR and $M_\star$ (see Table 4.2).

From the high-resolution (0$''$.15 $\sim$kpc-scale) datacube, I obtain a velocity-integrated peak flux density r.m.s of $3.4\,\mathrm{mJy\,km\,s^{-1}\,beam^{-1}}$, corresponding a $\Sigma_{\mathrm{H_2}}$ upper limit of $\sim 1.6 \times 10^3\,M_\odot\,\mathrm{pc^{-2}\,beam^{-1}}$ based on the Narayanan et al. (2012)'s CO-to-H_2 conversion factor (see § 4.3.4). Thus, by considering the beam angular size, I estimate a molecular gas mass 5-σ upper limit of $\sim 2.8 \times 10^8\,M_\odot$ to the three $\sim$kpc-scale gaseous clumps detected in the Hα observation and reported by Swinbank et al. (2012a) for this galaxy.

From the 0$''$.5 smoothed map, I obtain a velocity-integrated peak flux density r.m.s of $2.5\,\mathrm{mJy\,km\,s^{-1}\,beam^{-1}}$. The lower image noise allows to marginally detect the CO(2-1) emission in four spectral channels ($\Delta v = 240\,\mathrm{km\,s^{-1}}$). I show the SHiZELS-8 marginally detection in Fig. 4.2. I clearly observe the CO emission line spatial and spectral shifts produced by the internal galactic dynamics. Thus, I estimate a rough major kinematic axis PA of ~ 140 deg, with a peak-to-peak rotational velocity of $\sim$145 $\mathrm{km\,s^{-1}}$ (non-corrected by inclination).

SHiZELS-8: a dynamically-perturbed system?

Two pieces of evidence support the idea that SHiZELS-8 is a dynamically complex system. Firstly, the Hα and CO dynamics show that both components rotate roughly in the same direction but have position angles offset by $\sim 100-120$ deg (see Fig. 4.2), which is in contrast to the negligible offset in the Hα and CO dynamics seen in SHiZELS-19 (Fig. 4.3). Second, the previous SINFONI observation shows a flat radial [N II]/Hα metallicity gradient (Swinbank et al., 2012b).

I am possibly witnessing a massive reservoir of gas fuelling the star formation seen in Hα in a similar way to that previously seen in more violent sub-millimetre galaxies (SMGs; Tacconi et al. 2008). Indeed, the complex dynamics evidenced for the different ISM states might be mixing the gas producing the flat metallicity gradient. I conclude that while SHiZELS-8 is a 'typical' galaxy that resides in the upper range of the main sequence for star-forming galaxies, which follows the Kennicutt-Schmidt law (see Hughes et al. in prep.), it is probably experiencing torques that will eventually drive a flow of gas into the central regions. The SHiZELS-8 case demonstrates the wide variety of galaxy kinematics within the main-sequence (Elbaz et al., 2018). Given the impossibility to describe this source as a virialized rotating disc, in the remaining of this work, I focus on the analysis of the SHiZELS-19 galaxy.

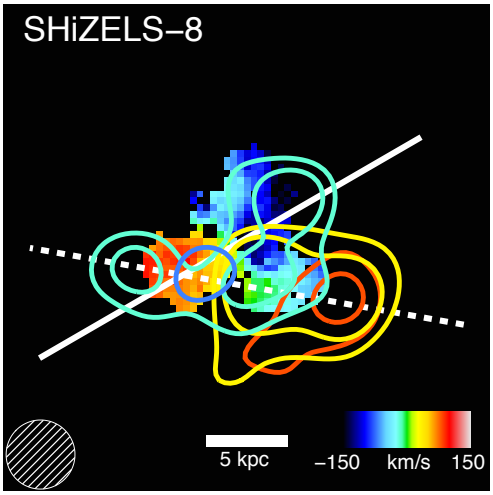

Figure 4.2: Hα velocity map at $\sim$kpc-scale for the SHiZELS-8 galaxy. The solid and dashed white lines represent the ionized and molecular gas major kinematic axis, respectively. The coloured contours represent the 3- and 5-σ CO(2-1) emission from the 2000 kλ tapered datacube in four spectral channels (Δv = 240 km s^{-1}). The synthesized beam size of this tapered observation ($\theta_{\rm BMAJ} = 0\farcs50 \sim 4.3$ kpc) is showed in the bottom-left corner. I note that the apparent shift between the two maps may be produced by the astrometry inaccuracies of the SINFONI observations. Nevertheless, both observations suggest that the CO(2-1) and Hα major kinematic axes are misaligned by $\sim$100-120 deg, which is indicative of a kinematic complex system.

4.3.3 The SHiZELS-19 galaxy

I derive the two-dimensional intensity and kinematic maps for SHiZELS-19 by analysing the CO(2-1) emission line using the line-fitting procedure explained in Chapter 2. The CO(2-1) emission line is fitted pixel-by-pixel using a χ^2 minimization technique. From this procedure I obtain the CO intensity, rotation velocity and velocity dispersion two-dimensional fields for each galaxy. I highlight that for this galaxy, the Hα emission line properties were derived and presented in an analogous manner in Molina et al. (2017).

I show the CO(2-1) intensity, rotation velocity and velocity dispersion maps for SHiZELS-19 in Fig. 4.3, whilst the best-fitted kinematic parameters are listed in Table 4.3. I observe a smooth CO(2-1) intensity map with no apparent clumpiness, which is consistent with the morphology observed in the Hα intensity map (Molina et al., 2017) and the *HST* F160W-band (reft-frame optical) image. However, this galaxy presents an irregular morphology in the *HST* F814W-band map (rest-frame UV, Fig. 4.1). The discrepancy between the galaxy morphology seen in the *HST* images suggests that the irregular morphology seen in the *HST* F814W-band image may just reflect a complex dust distribution through the galactic disc (e.g. Genzel et al. 2013).

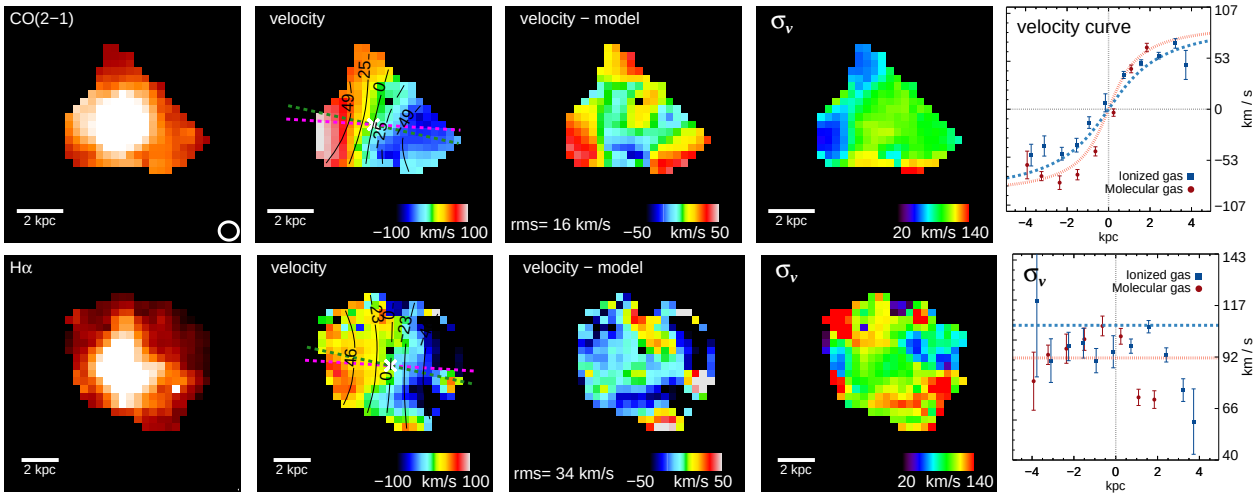

Figure 4.3: Intensity, velocity, residual and velocity dispersion maps (1st to 4th columns) for the COS-30 galaxy obtained from the Hα (bottom) and CO(2-1) (top) emission lines. In the 5th column, I show an example of the one-dimensional rotational velocity (top) and velocity dispersion (bottom) profiles across each major kinematic axis for both observations. The spatial scale for each observation is showed in each moment map. The CO(2-1) intensity map also shows the synthesized beam size. The velocity maps have over-plotted the kinematic centre and the velocity contours from their best-fit disc model. The green- and pink-dashed lines represent the molecular and ionized gas major kinematic axis, respectively. The residual fields are constructed by subtracting the velocity disc model from the velocity maps: the r.m.s. of these residuals are given in each panel. The velocity dispersion maps are corrected for beam-smearing effects. The one-dimensional profiles are constructed by using the best-fit kinematic parameters and a slit width equal to half of the synthesized beam/PSF FWHM. In each one-dimensional profile, the error bars show the 1-σ uncertainty and the vertical dashed grey line represents the best-fit dynamical centre. In the velocity profile panel, the red- and blue-dashed curves show the velocity curve extracted from the beam-smeared CO and Hα two-dimensional best-fit models, respectively. In the σ_v one-dimensional profile panel, the red- and blue-dashed lines show the average galactic value for the CO and Hα observations, respectively.

Global Dynamical Properties

In order to characterise the dynamical properties of SHiZELS-19, I fit the two-dimensional velocity fields for the ionized and molecular gas jointly. To do this, I use the double-map kinematic fitting procedure explained in Chapter 2. In this procedure, the inclination angle parameter is coupled, an assumption that seems appropriate since the CO and Hα velocity fields are consistent (Fig. 4.3). I remind that the 'disc thickness' is modelled by considering the galaxy as an oblate spheroid system with intrinsic minor-to-major axis ratio of 0.2 (Law et al., 2012). The dynamical centres are not locked through RA−DEC coordinates as the SINFONI astrometry is not accurate enough to allow it.

In Molina et al. (2017), the kinematic model for SHiZELS-19 was performed without any constraint on the inclination angle value. This adds an additional source of uncertainty as the inclination angle is poorly constrained from the velocity field modelling alone (Glazebrook,

2013). In order to deal with this uncertainty, I constrain the inclination angle by fitting a two-dimensional Sérsic model (Sérsic, 1963) to the CO intensity map (moment 0) using `GALFIT` (Peng et al., 2010). I obtain an observed minor-to-major axis ratio of $\sim 0.90 \pm 0.05$, which corresponds to an inclination angle value of $\sim 26 \pm 6\,\mathrm{deg}$. However, as `GALFIT` tends to underestimate the parameter errors, I consider a more conservative inclination angle uncertainty of $\pm 10\%$ in the fitting procedure (Epinat et al., 2012).

As indicated in Chapter 2, I use the dynamical centres and position angles derived from the best-fit dynamical models to extract the one-dimensional rotation curve and velocity dispersion profile across the major kinematic axes of the ionized and molecular gas. The extracted one-dimensional rotational curves and dispersion velocity profiles are presented in Fig. 4.3.

The half-light radius ($r_{1/2,\mathrm{CO}}$,$r_{1/2,\mathrm{H}\alpha}$), the rotational velocity ($V_{\mathrm{rot,H}\alpha}$, $V_{\mathrm{rot,CO}}$) and the global velocity dispersion for the ionized and molecular gas component ($\sigma_{v,\mathrm{CO}}$, $\sigma_{v,\mathrm{H}\alpha}$) are calculated by using the procedures described in Chapter 2. I remind that the Hα and CO rotation velocity is defined as the inclination-corrected velocity observed at two times the Hα and CO half-light radii, respectively. The velocity dispersion values are calculated as the median of the pixel values from a zone beyond three times the size of the angular resolution of each map centred at the kinematic centre. These values are reported in Table 4.3.

The best-fit kinematic maps and velocity residuals for the Hα and CO derived maps are shown in Fig. 4.3. The best-fit inclination, position angle and half-light radius values are given in Table 4.3. The mean deviation from the best-fit model (indicated by the typical r.m.s) is given in each residual map.

The molecular and ionized gas components show similar scale sizes $r_{1/2,\mathrm{H}\alpha}/r_{1/2,\mathrm{CO}} \approx 1.07 \pm 0.09$. I stress that the CO and Hα analyses are obtained from images created at matched spatial resolution ($0\farcs15$; corresponding to $\sim$kpc-scale at $z \sim 1.47$). Possible loss of the extended CO flux in the high-resolution observation may reduce the $r_{1/2,\mathrm{CO}}$ value in its calculation. Nevertheless, the estimation of the half-light radius for both ISM components are slightly smaller than the half-light radius value measured from the *HST* F160W-band image $r_{1/2,\mathrm{HST-F160W}} = 2.1 \pm 0.5\,\mathrm{kpc}$ (Gillman et al., 2019).

The CO(2-1) velocity map shows a clear rotational pattern, roughly matching the rotational motions traced by the ionized gas component. From the two-dimensional modelling, I find that the kinematic position angles agree ($\Delta\mathrm{PA} \equiv \mathrm{PA}_{\mathrm{H}\alpha} - \mathrm{PA}_{\mathrm{CO}} = 9 \pm 23\,\mathrm{deg}$) within the 1-$\sigma$ error range. The velocity curves roughly agree, except in the blueshifted zone where the CO traced rotation curve drops to lower velocity values. However, I note that the ionized gas velocity map is noisier than the molecular gas velocity map, especially in the galaxy outskirts. This may be partly produced by OH sky-line features present in the $H-$band spectra, whilst the ALMA observation is free from sky-line residuals. I find that, the ionized gas component shows a slightly lower rotational velocity value when compared to that from the molecular gas observations ($V_{\mathrm{rot,H}\alpha}/V_{\mathrm{rot,CO}} \approx 0.88 \pm 0.10$). This might be due to differences in the spatial distribution between the two ISM components.

TABLE 4.3: KINEMATIC PROPERTIES

Table 4.3: Best-fit kinematic parameters for SHiZELS-19 galaxy. 'inc.' is the inclination angle defined by the angle between the line-of-sight and the plane perpendicular to the galaxy disc (for a face-on galaxy, inc. = 0 deg.). The velocity dispersion and half-light radii values are corrected for beam-smearing effects (see § 4.3.3 for more details). The last row shows the reduced chi-squared (χ^2_ν) of the best-fit two-dimensional model.

ID	SHiZELS-19
$PA_{H\alpha}$ (deg)	176±18
$\sigma_{v,H\alpha}$ ($km\,s^{-1}$)	107±13
$V_{rot,H\alpha}$ ($km\,s^{-1}$)	106±9
$r_{1/2,H\alpha}$ (kpc)	1.80±0.16
PA_{CO} (deg)	167 ± 14
$\sigma_{v,CO}$ ($km\,s^{-1}$)	91±6
$V_{rot,CO}$ ($km\,s^{-1}$)	121±10
$r_{1/2,CO}$ (kpc)	1.68±0.03
inc. (deg)	27.5±0.6
χ^2_ν	3.51

In terms of velocity dispersion, the CO observation shows a slightly lower average velocity dispersion value than the mean value observed from the ionized gas component ($\sigma_{v,H\alpha}/\sigma_{v,CO} \approx 1.18 \pm 0.16$). The difference between the ALMA ($25\,km\,s^{-1}$) and the $H-$band SINFONI ($50\,km\,s^{-1}$) spectral resolutions should not produce such differences as the intrinsic CO and Hα linewidths are significantly broader. The high σ_v values observed at the outskirts of the Hα velocity dispersion map may increase the ionized gas average value. In a similar way as the comparison between the velocity maps, the ionized gas velocity dispersion map is noisier than the molecular gas map at larger radii. By considering all the pixels in the mean σ_v estimation, I obtain an average $\sigma_{v,H\alpha}$ value of $91 \pm 13\,km\,s^{-1}$ (Molina et al., 2017), in agreement with the measured $\sigma_{v,CO}$ value (Table 4.3). Thus, I suggest that both ISM tracers show similar supersonic turbulence values.

I derive rotational velocity to dispersion velocity ratio (V_{rot}/σ_v) values of 0.99±0.14 and 1.33±0.14 for the ionized and molecular gas ISM phases, respectively. This suggests that the disordered motions of both ISM phases are playing an important role in the galactic support against self-gravity (Burkert et al., 2010).

Kinematic Asymmetry Characterization

In order to obtain a detailed characterization of the ionized and molecular gas kinematics, I quantify the kinematic deviations from the ideal rotating disc case by performing the '*kinemetry*' analysis (Krajnović et al., 2006) explained in Chapter 2. I remind that, *kinemetry* proceeds to analyse the two-dimensional kinematic maps using azimuthal profiles in an outward series of best fitting tilted rings. The kinematic profile as a function of the cosine of the azimuthal angle parametrized by $k_{n,v}$ and $k_{n,\sigma}$ at each tilted ring for the velocity and velocity dispersion maps, respectively. In the velocity map, the first order decomposition '$k_{1,v}$'

is equivalent to the rotational velocity value. The high-order terms describe the kinematic anomalies with respect to the ideal rotating disc case (see Krajnović et al. 2006 for more details). The inclination and position angles are restricted within the 1-σ error range given by the best-fit two-dimensional model. The $k_{n,v}$ and $k_{n,\sigma}$ errors are derived by bootstrapping via Monte-Carlo simulations the errors in measured velocities, velocity dispersions, and estimated dynamical parameters.

The kinematic deviations from the ideal disc case are characterized by computing the three different estimators mentioned in Chapter 2: (1) the $k_{5,v}/k_{1,v}$ ratio (Krajnović et al., 2006); (2) the $(k_{2,v}+k_{3,v}+k_{4,v}+k_{5,v})/4k_{1,v}$ and $(k_{1,\sigma}+k_{2,\sigma}+k_{3,\sigma}+k_{4,\sigma}+k_{5,\sigma})/5k_{1,v}$ fractions (Shapiro et al., 2008); and (3) the $(k_{3,v}+k_{5,v})/2k_{1,v}$ and $(k_{2,\sigma}+k_{4,\sigma})/2k_{1,v}$ ratios (Bloom et al., 2018).

In Fig. 4.4, I show the different estimators of the kinematic deviations for the CO and Hα velocity and velocity dispersion maps as a function of the de-projected radius. I note that the shorter CO radial profiles compared to the Hα radial profiles are produced by the stop of the 'kinemetry' procedure at shorter radius due to the lack of roundness of the CO two-dimensional maps derived from the observations.

In the case of the velocity map, the $k_{5,v}/k_{1,v}$ (Krajnović et al., 2006) ratio gives lower values along the galactic disc compared with the other two estimators. I obtain an average $k_{5,v}/k_{1,v}$ ratio of 0.04±0.01 and 0.09±0.05 for the CO and Hα velocity map respectively. This difference is mainly produced by the higher $k_{5,v}/k_{1,v}$ values found in the Hα velocity map at longer radius ($\gtrsim 2\,$kpc). This gradient suggests that SHiZELS-19 suffered a merger event in the past as the outer regions retain better the kinematic perturbations by remaining out of equilibrium while the central region tends to relax faster to a disc-like system (Kronberger et al., 2007).

If I follow the kinematic classification performed to the ATLAS^{3D} (Krajnović et al., 2011) and SAMI local galaxy surveys (van de Sande et al., 2017) and I consider their $k_{5,v}/k_{1,v} = 0.04$ limit value to classify systems as regular rotators, this would imply that SHiZELS-19 corresponds to a 'non-regular' rotator, i.e, the velocity field presents significant kinematic deviations that make it not well-described by the cosine law.

In the case of the velocity dispersion map, I found that the Bloom et al. (2018)'s estimator is higher than the Shapiro et al. (2008)'s estimator at all radii. The additional $k_{n,\sigma}$ coefficients considered in the latter case contribute little to the kinematic asymmetry estimator. This may also suggests that SHiZELS-19 is a 'moderate disturbed' system (Bloom et al., 2018). I also note that, as a difference from the velocity map, the kinematic asymmetries in the CO and Hα velocity dispersion map tend to be nearly constant along the galactic disc. The kinematic deviations measured from the CO map tend to be lower than the ones measured from the Hα map, however, they agree between the 1-σ error range.

The rough agreement between the molecular and ionized gas kinematics suggests that, at ∼kpc-scales, both phases of the ISM are tracing the galactic dynamics instead of peculiar kinematics (e.g. gas inflows/outflows). This is in agreement with previous studies of massive galaxies (at $\sim 0.4-2.4\times10^{11}\,M_{\odot}$) at similar redshift (e.g. Übler et al. 2018; Calistro Rivera et al. 2018).

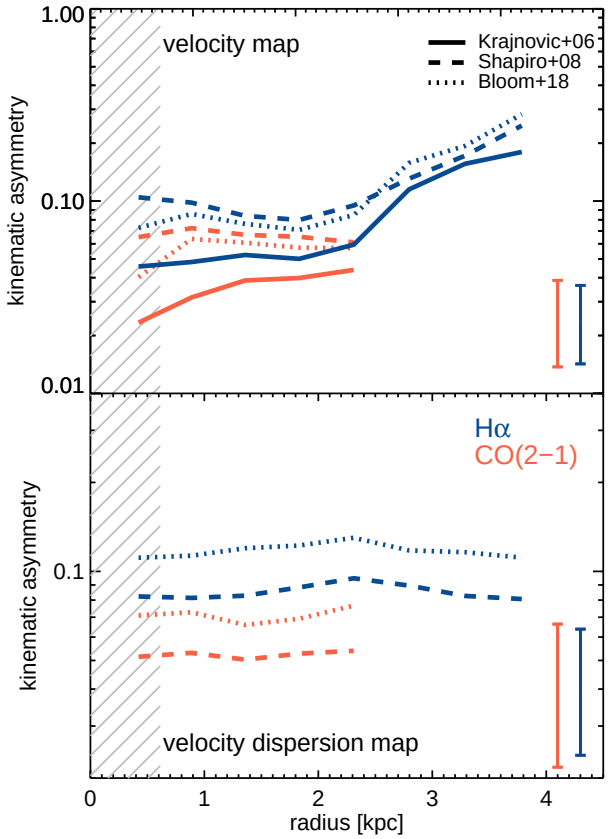

Figure 4.4: Kinematic asymmetry radial profiles measured from the SHiZELS-19 velocity (*top*) and velocity dispersion (*bottom*) maps. The solid line, dashed-line and dotted-line represent the kinematic asymmetry estimators presented in Krajnović et al. (2006); Shapiro et al. (2008) and Bloom et al. (2018) for each map (see § 4.3.3 for more details). The colour-coded error bars show the median 1-σ uncertainties in each panel. The grey-dashed area represents the resolution element radial extent. Despite of the estimator used, the ionized gas two-dimensional maps tend to show slightly higher kinematic deviations from the ideal rotating disc case than the molecular gas kinematic maps. Although, the measurements agree within 1-σ error range.

4.3.4 Dynamical Mass & Dark Matter content

The dynamical mass estimate is a useful tool that allows to measure the total galactic mass enclosed as a function of radius. It provides a simple way to probe the existence of dark matter haloes (e.g. Gnerucci et al. 2011) or to constrain the CO-to-H_2 conversion factor (e.g. Motta et al. 2018; Calistro Rivera et al. 2018).

By measuring the global kinematics of a galaxy, the dynamical mass can be easily estimated from the rotational velocity (e.g. Genzel et al. 2011) considering a thin-disc dynamical mass approximation ($M_{\rm dyn,thin}$). However, if the supersonic turbulence across the galactic disc is comparable to the ordered motions amplitude, then, an additional pressure gradient support against self-gravity has to be considered. The galactic disc height is not negligible and a thick-disc approximation ($M_{\rm dyn,thick}$) should be considered (Burkert et al., 2010).

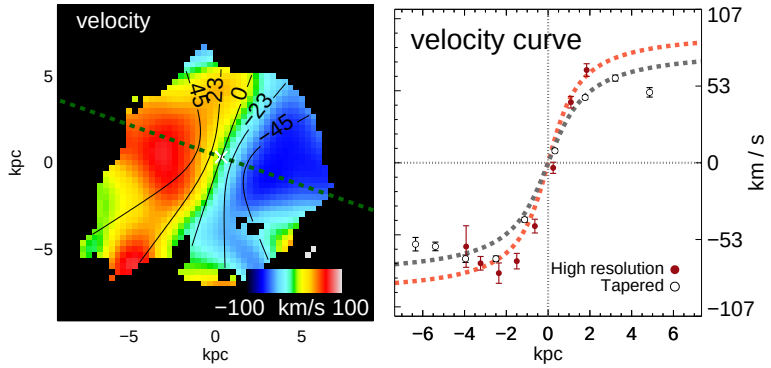

Figure 4.5: Velocity map, and velocity profile for the CO(2-1) 2000 kλ tapered datacube for SHiZELS-19. I use the same colour-coding presented in Fig. 4.3. In this case, the one-dimensional velocity profile is constructed by using the best-fit kinematic parameters for the tapered datacube and a slit-width equal to half of the tapered synthesized beam FWHM. I also show the data taken from the ∼kpc-scale high-resolution observations. The tapered rotation curve extends up to ≈6 kpc.

I calculate the dynamical mass for the SHiZELS-19 galaxy by using the kinematic information from the CO observations as its velocity map shows lower kinematic asymmetry amplitudes compared to the Hα velocity map (§ 4.3.3). Since the CO ∼kpc-scale observations are more sensitive to the denser and compact emission, I use a tapered version (2000 kλ) of the ALMA observations that allows to trace the diffuse and more extended CO emission (at 0.″29 resolution). This allows to observe a rotation curve up to a radial distance of ≈6 kpc or ∼3.5 times the CO half-light radius (Fig. 4.5).

Taking into account that the Sérsic index derived from the *HST* image is consistent with unity for this galaxy (Gillman et al., 2019), I assume an exponential disc surface density profile. This implies that, in terms of the disc scale length ($r_{\rm d}$), I observe the rotation curve up to $\approx 6r_{\rm d}$ ($r_{1/2} \approx 1.67r_{\rm d}$ for an exponential disc).

By using the inclination-corrected rotational velocity value derived from the tapered rotation curve at radius of ≈6 kpc ($V_{\rm rot,tap} = 112 \pm 6\,{\rm km\,s^{-1}}$), I would obtain a total enclosed mass of $M_{\rm dyn,thin}(r \lesssim 6\,{\rm kpc}) = (1.75 \pm 0.19) \times 10^{10}\,M_{\odot}$ assuming a thin disc approximation. This dynamical mass estimate is lower but consistent within 1-σ range with the estimated stellar mass for this galaxy scaled at the same radius; $M_{\star}(r \lesssim 6\,{\rm kpc}) \approx 0.98 M_{\star} \approx (1.96 \pm 0.90) \times 10^{10}\,M_{\odot}$. However, this 'thin disc' dynamical mass value would suggest that this galaxy has almost no gaseous mass content, evidencing an apparent discrepancy with the CO and Hα emission line measurements. On the other hand, as the $V_{\rm rot}/\sigma_v$ ratio is consistent with unity for both ISM components, this suggests that the $M_{\rm dyn,thin}$ quantity may be underestimating the total mass of this galaxy. Additional support against self-gravity needs to be considered.

I follow the analysis by Burkert et al. (2010), and I consider a possible additional pressure support by calculating the dynamical mass in the thick disc approximation. In the 'thick-disc' dynamical mass modelling, the radial pressure gradient term in the hydrostatic equation can not be neglected and it is parametrized by the galactic velocity dispersion and the mass density radial profiles. This approximation further assumes that σ_v is independent of the galaxy disc radius and height. I use Burkert et al. (2010)'s Eq.11 with $\sigma_{v,\rm CO}$ and $r_{1/2,\rm CO}$ as

input values and I obtain $M_{\rm dyn,thick} = (1.59 \pm 0.19) \times 10^{11}\,M_{\odot}$. This dynamical mass value is ~ 8 times higher than $M_{\star}$, erasing any discrepancy between both quantities, but allowing the possibility of a non-negligible amount of dark matter content in this galaxy.

In order to test this, I calculate the dark matter fraction by comparing the total mass budget derived from the dynamical analysis with the luminosity-based total mass content. I consider the total $M_{\star}$ value estimated for the SHiZELS-19 galaxy as its difference with the scaled value at $\approx 6\,$kpc ($M_{\star} - M_{\star}(r \lesssim 6\,{\rm kpc}) \approx 0.02 M_{\star}$) is negligible compared to the stellar mass uncertainty (see Table 4.2). Therefore, by considering the $M_{\star}$, $M_{\rm H_2}$ and $M_{\rm dyn}$ quantities, I define the dark matter fraction as,

$$f_{\rm DM} \equiv 1 - \frac{M_{\star} + M_{\rm H_2}}{M_{\rm dyn,thick}} = 1 - \frac{\alpha_{\rm CO} L'_{\rm CO} + M_{\star}}{M_{\rm dyn,thick}}, \tag{4.2}$$

where the molecular mass content is estimated via the CO luminosity ($M_{\rm H_2} = \alpha_{\rm CO} L'_{\rm CO}$). However, this mass sum approach needs additional information about the CO-to-H_2 conversion factor in order to overcome the degeneracy between $\alpha_{\rm CO}$ and $f_{\rm DM}$. I also note that strong dependence on the assumptions behind $M_{\star}$, $M_{\rm dyn}$ and $L'_{\rm CO}$ may also affect the result from Eq. 4.2.

In order to properly consider the $M_{\star}$, $M_{\rm dyn}$ and $L'_{\rm CO}$ uncertainties and the degeneracy between $\alpha_{\rm CO}$ and $f_{\rm DM}$, I reproduce the parameter space built up in Eq. 4.2 by applying a Markov Chain Monte Carlo (MCMC) technique following Calistro Rivera et al. (2018). Briefly, based on the likelihood of the measured $L'_{\rm CO}$, $M_{\star}$ and $M_{\rm dyn}$ values, I sample the posterior probability density function (posterior PDF) for $\alpha_{\rm CO}$ and $f_{\rm DM}$ parameters using the EMCEE algorithm (Foreman-Mackey et al., 2013).

I note that SED fitting techniques based on unresolved flux observations may lead to the underestimation of the galactic stellar mass values (Sorba & Sawicki, 2018). Thus, I consider an additional case in which I assume that the stellar mass content is being underestimated by a factor of two. This is likely to be an extreme case as suggested by Sorba & Sawicki (2018) for galaxies with similar sSFR than SHiZELS-19.

In Fig.4.6, I show the one- and two- dimensional posterior PDFs of the $\alpha_{\rm CO}$ and $f_{\rm DM}$ parameters. I also show the CO-to-H_2 conversion factor values suggested by following Accurso et al. (2017) and Narayanan et al. (2012). From the two-dimensional posterior PDF, I observe the strong degeneracy between both parameters regardless of the $M_{\star}$ value assumed. Lower $\alpha_{\rm CO}$ values imply higher dark matter fractions. I note that if I assume the Accurso et al. (2017)'s $\alpha_{\rm CO}$ value, I obtain $f_{\rm DM} \sim 0.3 \pm 0.13$.

Although SHiZELS-19 has a metallicity consistent with being solar, its ISM morphology and kinematics departs strongly from the ISM conditions observed in local galaxies. The high molecular gas velocity dispersion values (Table 4.3) observed for this system suggest that SHiZELS-19 should have a dense ISM (Papadopoulos et al., 2012) which may lower its CO-to-H_2 conversion factor value (Bolatto et al., 2013). As the Accurso et al. (2017)'s parametrization does not consider the ISM density effects, its $\alpha_{\rm CO}$ value should be considered as an upper limit. This is also consistent with the $\alpha_{\rm CO}$ upper limit derived from the dynamical

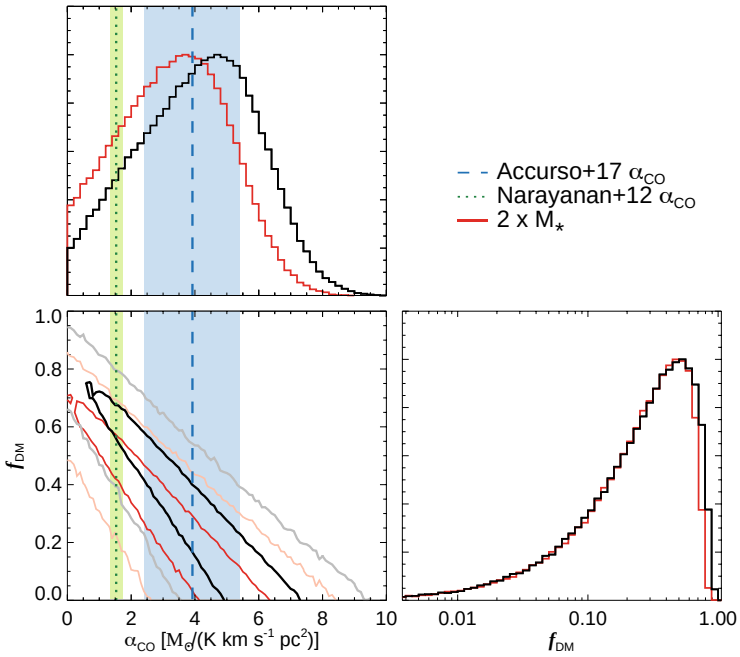

Figure 4.6: One- and two-dimensional posterior PDFs of the $f_{\rm DM}$ and $\alpha_{\rm CO}$ parameters for SHiZELS-19. The one-dimensional PDFs are represented by the black line in the *top-left* and *bottom-right* panels. The red line represents the inference assuming 2× the stellar-mass value derived from the spatially unresolved SED fitting, thus I consider a possible underestimation of $M_\star$ as suggested from spatially-resolved studies (Sorba & Sawicki, 2018). In *bottom-left* panel I show the two-dimensional PDFs, i.e., the covariance between both parameters. The black and grey lines show the 1- and 3-σ regions of the PDF derived by using the stellar mas value obtained from the spatially-unresolved SED fitting. The red and orange lines show the 1- and 3-σ regions by assuming a stellar mass correction factor of two. In the *bottom-* and *top-left* panels, the dashed and dotted lines show the CO-to-H_2 conversion factors calculated by following the Accurso et al. (2017) and Narayanan et al. (2012) parametrizations, respectively. The blue- and green- shaded regions show the 1-σ uncertainties for each parametrization.

mass estimate within the CO half-light radius (see Appendix 4.5.2, for more details.). Thus, in the remaining of this work, I use the Narayanan et al. (2012)'s parametrization as it does consider the ISM density effect in the estimation of $\alpha_{\rm CO}$.

I find $f_{\rm DM} \approx 0.59 \pm 0.10$ for SHiZELS-19. This value is consistent with the dark matter fraction predicted for disc-like galaxies at similar redshift range and stellar mass content from hydrodynamical simulations (Lovell et al., 2018). From the Bayesian approach, I find 3-σ range boundaries of $\sim 0.31 - 0.70$ for the $f_{\rm DM}$ value. On the other hand, if I consider the extreme case of a stellar mass underestimated by a factor of two (Sorba & Sawicki, 2018), then the 3-σ range boundaries correspond to $\sim 0.20 - 0.64$.

To determine if I need to include the HI content in the analysis, I note that in local spirals the transition between a H_2- to HI-dominated ISM ($\Sigma_{\rm H_2} \approx \Sigma_{\rm HI}$) occurs at a gas surface density of $\Sigma_{\rm gas} \sim 12 \pm 6\, M_\odot\, {\rm pc}^{-2}$ (Leroy et al., 2008). In contrast, from the spatially resolved CO(2-1) observations, I derive an average $\Sigma_{\rm H_2} \sim 220 \pm 166\, M_\odot\, {\rm pc}^{-2}$ value from a tilted ring centred at the the same radius at which $V_{\rm rot,tap}$ was calculated. This suggests that the HI mass

TABLE 4.4: SHiZELS-19 FINAL PARAMETERS

Table 4.4: Summary of the SHiZELS-19 galaxy parameters derived in this work using the kinematic modelling. The $f_{\rm DM}$, $\Sigma_{\rm H_2}$ and $\tau_{\rm dep}$ values are computed by considering the Narayanan et al. (2012)'s CO-to-H_2 conversion factor (see § 4.3.4).

$f_{\rm DM}$	0.59 ± 0.10
$\log_{10}\Sigma_{\rm SFR}$ $(M_\odot\,{\rm kpc}^{-2})$	-0.5 ± 0.3
$\log_{10}\Sigma_{\rm H_2}$ $(M_\odot\,{\rm pc}^{-2})$	3.0 ± 0.6
$\tau_{\rm dep}$ (Gyr)	2.3 ± 1.2

content within a radius of ≈6 kpc is likely to be negligible compared to $M_{\rm H_2}$ and therefore, the estimated $f_{\rm DM}$ value may be a good approximation. Thus, I suggest that SHiZELS-19 is a 'typical' star-forming galaxy which may have a considerable dark matter content.

The dark matter fraction obtained for SHiZELS-19 is consistent with the values reported by Tiley et al. (2019), but in tension with the conclusions reported from Genzel et al. (2017) and Lang et al. (2017). These three studies rely primarily on the analysis of the stacked rotation curve constructed from normalized individual velocity curves from galaxies in the $0.6 \lesssim z \lesssim 2.6$ redshift range. However, the discrepancy between the obtained $f_{\rm DM}$ values from these studies seems to be driven by the way in which the velocity curves are normalized.

In Genzel et al. (2017) and Lang et al. (2017) works they normalize the individual velocity curves in both, radial extension through the turn-over radius and velocity amplitude through the velocity at the turn-over radius (see Lang et al. 2017 for more details). This normalization procedure tends to favour the contribution of the systems with low $V_{\rm rot}/\sigma_v$ values to the stacked rotation curve at longer radii. This bias seems to be produced by the smaller turn over radius values presented in those galaxies which acts as a 'zoom-in' scaling factor (Tiley et al., 2019). On the other hand, Tiley et al. (2019) normalize the individual velocity curves by the stellar light disc-scale radius and also velocity. In this case, galaxies with different $V_{\rm rot}/\sigma_v$ values contribute more uniformly to the shape of the stacked rotation curve. Taking this into account, I note that SHiZELS-19 is a galaxy with $V_{\rm rot}/\sigma_v \sim 1.0 - 1.3$, favouring the scenario in which the conclusions presented in Genzel et al. (2017) and Lang et al. (2017) studies may be biased.

4.3.5 The Kennicutt-Schmidt law at ∼kpc-scales

Proposed by Schmidt (1959) and extended by Kennicutt (1998a,b), the Kennicutt-Schmidt law is an observational power-law relationship between the star formation rate surface density and the gas surface density. It describes how efficiently galaxies turn their gas content into stars. For local galaxies, this relation is fitted by an exponent $N = 1.4$ (Kennicutt, 1998b).

Since then, latter studies have found that $\Sigma_{\rm SFR}$ is better correlated with the molecular gas surface density ($\Sigma_{\rm H_2}$) rather than $\Sigma_{\rm gas}$ (e.g. Bigiel et al. 2008; Leroy et al. 2008). At first order, local disc-like galaxies show a linear correlation between both surface density quantities ($\Sigma_{\rm SFR} \propto \Sigma_{\rm H_2}$), with a median depletion time ($\tau_{\rm dep} \equiv \Sigma_{\rm H_2}/\Sigma_{\rm SFR}$) of $\sim 2.2 \pm 0.3$ Gyr (e.g. Leroy et al. 2013). Second order departures from this relationship have also been found

(e.g. Saintonge et al. 2012; Utreras et al. 2016), although these effects may be related to systematic errors behind the estimation of the molecular gas content and/or local nuclear starburst activity (Leroy et al., 2013).

In Fig. 4.7, I present the star formation activity of SHiZELS-8 and SHiZELS-19 in the context of the $\Sigma_{\rm SFR} - \Sigma_{\rm H_2}$ relation. I compare with several local galaxy samples observed at similar spatial scales and galactic averages of galaxies observed at similar redshifts. Briefly, the '$z \sim 0$ spirals' sample is composed by high spatial resolution ($\sim 0.2-1\,$kpc) observations of small galactic regions taken from Kennicutt et al. (2007); Blanc et al. (2009); Rahman et al. (2011, 2012). The '$z \sim 0$ LIRGs' sample consists in observations of the NGC3110 and NGC232 galaxies observed at $\sim 1\,$kpc scale (Espada et al., 2018). Both starburst systems have SFR$\sim 20\,M_{\odot}\,{\rm yr}^{-1}$, i.e. comparable with the value reported for SHiZELS-19 (SFR$_{\rm H\alpha} \approx 23\,M_{\odot}\,{\rm yr}^{-1}$). NGC3110 is a barred Sb galaxy interacting with a minor companion (mass ratio ∼14:1), whilst NGC232 corresponds to a barred Sa galaxy which presents a bright compact nuclear region (see Espada et al. 2018, for more details). I also compare with the median trend observed for a sub-sample of 30 local galaxies taken from the HERACLES survey (Leroy et al., 2013)). These data also consist in $\sim 1\,$kpc scale observations of the galactic ISM.

The high-redshift observations consist in galaxy-integrated estimates from ULIRGs ($z \sim 0.4-1$; Combes et al. 2013), four SMGs taken from the ALESS survey ($z \sim 2.0-2.9$; Calistro Rivera et al. 2018), 'typical' star-forming galaxies observed at $z \sim 1-2.5$ taken from the PHIBSS survey (Tacconi et al., 2013) and five BzK galaxies ($z \sim 1.5$) presented in Daddi et al. (2010). For the ALESS SMGs, I calculate the surface density quantities following Tacconi et al. (2013).

Given the marginally-detected CO observation for SHiZELS-8, I just plot a galactic average estimation ($\log_{10}\Sigma_{\rm SFR} \approx -0.61 \pm 0.07\,M_{\odot}\,{\rm yr}^{-1}\,{\rm kpc}^{-2}$; $\Sigma_{\rm H_2} \sim 2.23 \pm 0.08\,M_{\odot}\,{\rm pc}^{-2}$). However, I caution that in this particular case, $\Sigma_{\rm H_2}$ is an upper limit as I can not constrain the SHiZELS-8's CO spatial distribution accurately.

For SHiZELS-19, I use the IDL procedure HASTROM to align the two-dimensional fields using as a reference point the kinematic centre (left panel) and the luminosity peak position (right panel) from the Hα and CO ∼kpc-scale observations. For this galaxy, I derive a median $\log_{10}\Sigma_{\rm SFR} = -0.5 \pm 0.3\,M_{\odot}\,{\rm yr}^{-1}\,{\rm kpc}^{-2}$ and $\log_{10}\Sigma_{\rm H_2} = 3.0 \pm 0.6\,M_{\odot}\,{\rm pc}^{-2}$ values. These estimations indicate that SHiZELS-19 has a somewhat denser ISM compared with local star-forming galaxies in terms of surface density quantities. On the other hand, the median $\Sigma_{\rm H_2}$ value is consistent with molecular surface density estimations from galaxy-integrated observations of BzK and 'typical' star-forming galaxies at similar redshifts (Daddi et al., 2010; Tacconi et al., 2013), but SHiZELS-19 presents lower $\Sigma_{\rm SFR}$ values compared to these systems.

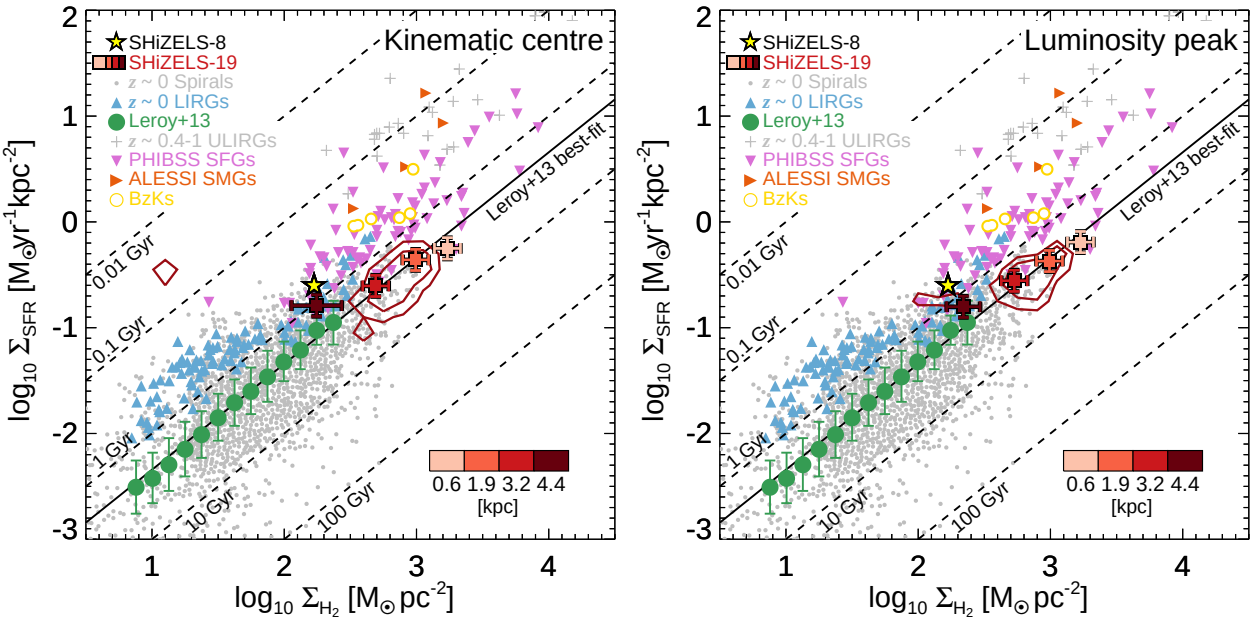

Figure 4.7: *Left:* $\Sigma_{\rm SFR}$ against $\Sigma_{\rm H_2}$ for SHiZELS-8 and SHiZELS-19 galaxies compared with spatially-resolved local galaxy observations in the literature. For SHiZELS-8, I just show a global estimate given the limitations of the marginally-detected CO observation. For SHiZELS-19, I centre the CO(2-1) and Hα two-dimensional intensity maps by using the best-fit kinematic centre. The red contours show the 50th and 90th percentile levels of the pixel-by-pixel distribution. The colour-coded squares represent the $\Sigma_{\rm SFR} - \Sigma_{\rm H_2}$ values calculated within tilted rings of 0.″15 ($\sim$ 1.2 kpc) thickness at the radius indicated by the colour bar. The '$z \sim 0$ Spirals' sample consist in observations of local discs taken from Kennicutt et al. (2007); Blanc et al. (2009); Rahman et al. (2011, 2012) at spatial resolutions between $\sim 0.2 - 1$ kpc. The '$z \sim 0$ LIRGs' values consist in $\sim$ 1 kpc scale observations of two galaxies (Espada et al., 2018). The green circles show the median trend observed in the HERACLES survey (Leroy et al., 2013) at $\sim$kpc-scales and the black line represents the best-fit for those median values. The error bars represent the 1-σ uncertainty. I also present galaxy-integrated estimates of ULIRGs ($z \sim 0.4 - 1$; Combes et al. 2013), four SMGs taken from the ALESS survey ($z \sim 2.0 - 2.9$; Calistro Rivera et al. 2018), 'typical' star-forming galaxies observed at similar redshifts (Tacconi et al., 2013) and five BzK galaxies ($z \sim 1.5$; Daddi et al. 2010). The dashed lines indicate fixed $\tau_{\rm dep}$ values. *Right:* The same plot as the showed in left panel, but now the CO(2-1) and Hα two-dimensional intensity maps are centred by using the CO and Hα luminosity peaks.

I derive a median $\tau_{\rm dep} = 2.3 \pm 1.2\,{\rm Gyr}$ for this galaxy, with the pixel-by-pixel distribution between $\sim 0.003 - 5\,{\rm Gyr}$. SHiZELS-19 presents a median depletion time consistent with the best-fit $\tau_{\rm dep} = 2.2 \pm 0.3\,{\rm Gyr}$ reported in Leroy et al. (2013) for the median trend observed in local galaxies at similar spatial resolution.

In the left panel of Fig. 4.7, I show the $\tau_{\rm dep}$ values calculated from tilted rings constructed from the two-dimensional best-fit model and centred at the kinematic centre. At first order, I find the same trend suggested from the average $\tau_{\rm dep}$ values. But, at second order, I note that the depletion times vary from $\sim 1.0 \pm 0.3\,{\rm Gyr}$ in the outer ring ($\approx 4.4\,{\rm kpc}$) to $\sim 2.9 \pm 0.2\,{\rm Gyr}$ in the central kpc of this galaxy, suggesting an apparent decrease in the star formation efficiency (SFE$\equiv \tau_{\rm dep}^{-1}$) towards the galactic centre in SHiZELS-19. This is in contradiction with second order effects found in galaxies in the local Universe. Possible variations of the CO-to-H_2 conversion factor through a radial dependence of the dust-to-gas ratio optical depth or gas excitation or nuclear starburst activity in galactic centres favour the opposite $\tau_{\rm dep}$ correlation with galactic radius (e.g. Sandstrom et al. 2013; Leroy et al. 2013). However, by using the [NII/Hα] ratio as a proxy of the metallicity gradient (Pettini & Pagel, 2004), I find a $\alpha_{\rm CO}$ radial profile consistent with being flat (see Appendix 4.5.1).

Although the CO and Hα maps show smooth spatial distributions, the Hα best-fit kinematic centre does not coincide exactly with the Hα luminosity peak as it does in the CO observations. Indeed, the projected distance between both centres is $\sim 0\farcs11$, i.e, slightly lower than the spatial resolution of the observations ($\approx 0\farcs15$). Thus, possible inaccuracies of the best-fit kinematic centres given by the limited spatial resolution of the observations may lead to the apparent outward decrease of the $\tau_{\rm dep}$ values obtained from the tilted rings. In order to explore this possibility, in the right panel of Fig. 4.7, I show the $\tau_{\rm dep}$ values calculated from tilted rings constructed from the two-dimensional best-fit model, but centred at the luminosity peak. For this case, the $\tau_{\rm dep}$ values vary from $\sim 1.3 \pm 0.3\,{\rm Gyr}$ in the outer ring to $\sim 2.5 \pm 0.1$ in the inner ring. The increase of the $\tau_{\rm dep}$ values towards the galactic centre still remains.

The suppression of the star formation in the molecular gas by dynamical effects is a possibility. For example, a morphological quenching scenario in which the bulge stabilises the molecular gas, preventing the star-formation activity but not destroying the gas may explain the observed $\tau_{\rm dep}$ trend with galactocentric radius (e.g. Martig et al. 2009; Saintonge et al. 2011). However, this scenario is unlikely as the Sérsic index measured for SHiZELS-19 ($n \sim 1$; Gillman et al. 2019) indicates that this galaxy is consistent with being a disc-like galaxy with no prominent bulge component. Galaxies with a prominent bulge component tend to show Sérsic index values deviated from unity (Lang et al., 2014). On the other hand, Schreiber et al. (2016) found that the increase of $\tau_{\rm dep}$ towards the central galactic zone in massive systems ($M_\star \sim 10^{11}\,M_\odot$) seems to be independent of the possible mass growth of the bulge component as disc-dominated galaxies tend to present the same $\tau_{\rm dep}$ trend with radius.

Another possible effect that adds uncertainty to the calculated $\tau_{\rm dep}$ values is a potential spatial variation of the Hα extinction. I have used an $A_{\rm H\alpha}$ correction constant across the galactic disc, but an underestimated galactic extinction in the galactic centre may lower the observed $\tau_{\rm dep}$ values in the central kpc zone therefore, producing the observed trend. An increase of the Hα extinction towards the galactic centre is consistent with findings of $A_{\rm H\alpha}$

being correlated with stellar mass surface density (Hemmati et al., 2015) or the presence of compact density starbursts (e.g. Simpson et al. 2015; Hodge et al. 2016, 2018)

In order to explore the effects of the global galaxy kinematics in the global star formation activity, I compute the orbital timescale ($\tau_{\rm orb} = 2\pi R/V_{\rm rot,CO}$) to be compared it with the median depletion timescale (e.g. Kennicutt 1998b; Daddi et al. 2010). By following the analysis of Daddi et al. (2010), I choose R to be equal to three times the half-light radius. Although this assumes that the rotation curve remains flat beyond two half-light radius (the radius at which $V_{\rm rot,CO}$ was estimated), this seems to be a reasonable assumption (see Fig. 4.5 & Tiley et al. 2019). Thus, I obtain $\tau_{\rm orb} = 256 \pm 22\,{\rm Myr}$ and $\tau_{\rm dep}/\tau_{\rm orb} \sim 9 \pm 5$. I find that SHiZELS-19 converts $\sim$10% of its available gas into stars per orbit. This is consistent with the average value found for local galaxies by Kennicutt (1998b) and with galaxy-integrated studies of BzK galaxies at similar redshifts (Daddi et al., 2010). Therefore, on average, SHiZELS-19 is a galaxy which follows a similar star formation law to that seen in local spiral galaxies, although in environments with higher gas surface density.

I should stress, however, that these conclusions are highly dependent on the assumed $\alpha_{\rm CO}$ value (Table 4.4) and its variation with radius. I have used the CO-to-H_2 conversion suggested by Narayanan et al. (2012) in order to consider possible variations in the average ISM metallicity and density (see also Appendix 4.5.1). A higher $\alpha_{\rm CO}$ value may imply a lower star formation efficiency, indicating a higher galactic depletion time compared to local galaxies (e.g. $\tau_{\rm dep} \sim 7 \pm 4\,{\rm Gyr}$ for $\alpha_{\rm CO} = 4.6\,M_{\odot}\,({\rm K\,km\,s^{-1}\,pc^2})^{-1}$). Spatially-resolved observations of the dust content are desirable as these may help to constrain the $\alpha_{\rm CO}$ value through a dust-to-gas-to ratio based approach (Leroy et al., 2013; Sandstrom et al., 2013).

Our work opens the possibility to perform morpho-kinematic analysis of high-redshift galaxies at $\sim$kpc-scales using two different ISM tracers, but I stress that more observations of 'typical' galaxies are needed to understand the impact of local or global galactic properties on the star formation activity in high-redshift systems.

4.4 Conclusions

I present new ALMA Cycle-5 observations tracing the CO(2-1) emission line from two 'typical' star-forming galaxies at $z \sim 1.47$. The ALMA observations were designed to deliver spatially-resolved observations of the molecular gas content on $\sim$kpc-scales. Combined with the previous Hα VLT-SINFONI AO-aided observations (Swinbank et al. 2012b; Molina et al. 2017; Gillman et al. 2019), I study the ionized and molecular gas dynamics jointly.

One of the targets, SHiZELS-8, is marginally detected only in the 2000kλ tapered datacube ($0\farcs5 \sim 4.3\,{\rm kpc}$ spatial resolution). For this system, the Hα and CO dynamics show that both ISM components rotate roughly in the same direction but have position angles offset by $100 - 120\,{\rm deg}$. This suggests that SHiZELS-8 is a dynamically perturbed system consistent with its previously observed flat metallicity gradient (Swinbank et al., 2012b). This finding suggests that main-sequence galaxies at high-redshift are not exclusively part of a well-behaved morpho-kinematic disc-like population (e.g. Elbaz et al. 2018).

For the second target, SHiZELS-19, I find a good agreement between the CO and Hα spatial extent ($r_{1/2,\mathrm{H}\alpha}/r_{1/2,\mathrm{CO}} \sim 1.07 \pm 0.09$) and dynamics at ∼kpc-scales (Fig. 4.3). From both ISM phases, I derive $V_{\mathrm{rot}}/\sigma_v \sim 1$ (Table 4.3). By performing a kinemetry analysis, I classify SHiZELS-19 as a 'non-regular rotator' (van de Sande et al., 2017). The kinematic analysis suggests that the CO and Hα observations are tracing the same galactic kinematics in agreement with previous studies of massive galaxies at similar redshift range (e.g. Übler et al. 2018; Calistro Rivera et al. 2018).

I estimate the total mass budget of the SHiZELS-19 galaxy by assuming a galactic thick-disc geometry (Burkert et al., 2010) and Narayanan et al. (2012)'s CO-to-H_2 conversion factor. From the SHiZELS-19 2000kλ datacube, I am able to trace the CO emission up to $\approx 6\,$kpc (Fig. 4.5), finding a dark matter fraction of $f_{\mathrm{DM}} = 0.6 \pm 0.1$ within this aperture. By applying a MCMC technique to sample the posterior PDF and take into account the parameter uncertainties (Fig. 4.6; e.g. Calistro Rivera et al. 2018), I estimate a f_{DM} 3-σ error range of ∼0.3−0.7. The dark matter fraction value is in agreement with hydrodynamical simulations of disc-like galaxies with similar stellar mass (Lovell et al., 2018) and the average dark matter fraction suggested by the stacked rotation curve analysis of galaxies at similar redshift range (Tiley et al., 2019). Thus, I conclude that SHiZELS-19 is a 'typical' star-forming galaxy at $z \sim 1.47$ harbour in a non-negligible amount of dark matter.

By using two-dimensional modelling, I study the star formation activity observed in the SHiZELS-19 galaxy at ∼kpc-scales. I derive a median $\tau_{\mathrm{dep}} = 2.3 \pm 1.2\,$Gyr. This median value is consistent with the typical value observed in local galaxies at similar spatial scales ($\tau_{\mathrm{dep}} = 2.2 \pm 0.3\,$Gyr; Leroy et al. 2013) and consistent with the the large scatter presented in the $z \sim 0$ spirals galaxy observations (Fig. 4.7), suggesting that 'typical' high-redshift galaxies (at $z \sim 1.47$) with higher gas surface density still follow the same star-formation law.

4.5 Appendix

4.5.1 Appendix A: α_{CO} RADIAL PROFILE

Throughout this work, I have used a simple CO-to-H_2 conversion factor to estimate the molecular gas content in SHiZELS-8 and SHiZELS-19 galaxies (§ 4.3.1). Thus, I have assumed that there is no significant radial variation of the α_{CO} value across each galactic disc. In order to test this assumption, I calculate the CO-to-H_2 conversion factor radial profile. This can only be done for the SHiZELS-19 galaxy since I was not able to obtain spatially resolved CO observations for SHiZELS-8. In Fig. 4.8, I show the α_{CO} as a function of the galactocentric radius. It was calculated by using the Narayanan et al. (2012)'s parametrization with the CO surface brightness radial profile and metallicity gradient as input values. I find an α_{CO} gradient consistent with being flat. This is mainly produced by the sub-linear dependence of the CO-to-H_2 conversion factor with respect to Σ_{CO} and metallicity in the Narayanan et al. (2012)'s parametrization. Although SHiZELS-19 has a negative metallicity gradient (Molina et al., 2017) it does not vary enough in order to increase the α_{CO} value at larger radii.

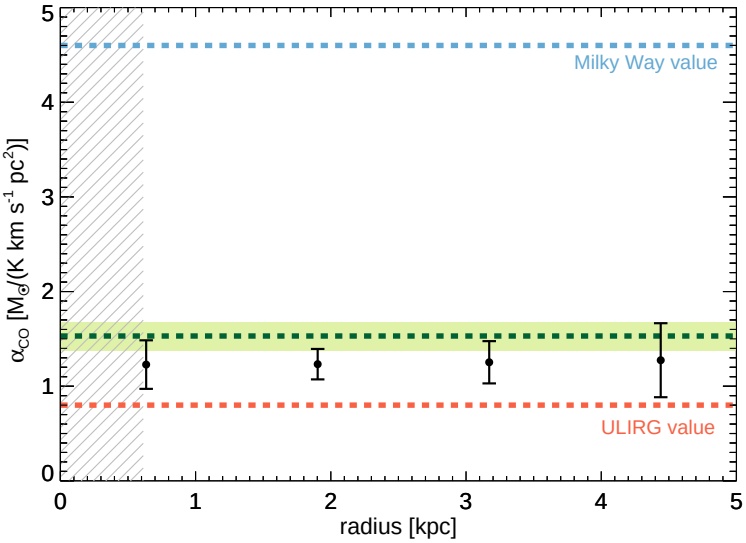

Figure 4.8: CO-to-H_2 conversion factor gradient across SHiZELS-19 from spatially-resolved measurements and as a function of the galactocentric radius derived from the best-fit kinematic model. The green-dashed line represent the galactic α_{CO} value derived from the tapered (2000 kλ) map and the green-shaded region show the 1-σ uncertainty. The blue- and red-dashed lines indicate the α_{CO} values usually adopted for the Milky Way and ULIRG like systems. The grey-dashed area represents the resolution element radial extent. I find a flat α_{CO} profile.

I note that the α_{CO} radial profile values are slightly lower but still consistent within 1-σ uncertainties with the galactic average CO-to-H_2 conversion factor value calculated from the tapered (2000 kλ) map. This is expected as the low spatial resolution datacube is able to trace CO(2-1) emission from the outskirts of the galaxy where the CO surface brightness is lower and the molecular gas has low metallicity compared to the inner parts. Both effects favour the increase of the average α_{CO} value.

It is worth to mention that by considering the large variety of metallicity gradients observed in high-redshift galaxies (e.g. Queyrel et al. 2012; Swinbank et al. 2012b; Molina et al. 2017), this result may be particularly applicable to SHiZELS-19 and it might not be used as typical property for the bulk population.

4.5.2 Appendix B: α_{CO} UPPER LIMIT FROM DYNAMICS

In § 4.3.4, I have assumed the Narayanan et al. (2012)'s parametrization to estimate the CO-to-H_2 conversion factor. Using this α_{CO} value coupled with the dynamical mass calculus, I have constrained the dark matter content in the SHiZELS-19 galaxy. I have used the Narayanan et al. (2012)'s parametrization in detriment of Accurso et al. (2017)'s parametrization as the second is likely to be an upper limit for the CO-to-H_2 conversion factor as it does not consider the gas surface density effects (Bolatto et al., 2013). In order to confirm this assumption, I use the dynamical mass calculus to constrain the CO-to-H_2 conversion factor (e.g. Tacconi et al. 2008).

I repeat the analysis done in § 4.3.4, but now I calculate the total and stellar mass content within one CO half-light radius. The stellar mass within this radius is estimated by assuming an exponential stellar surface density profile, as suggested by the best-fitted Sérsic profile presented in Gillman et al. (2019) for the *HST*-F160W broad-band image. I caution, however, that this calculus also assumes a constant mass-to-light ratio across the SHiZELS-19 galactic disc. I estimate the total mass by calculating the thick-disc dynamical mass within one $r_{1/2,\mathrm{CO}}$ by using the ∼kpc-scale kinematic CO observations (Fig. 4.3).

Initially, I just constrain the α_{CO} lower limit value by imposing that the CO emission should be optically thick ($\alpha_{\mathrm{CO}} \gtrsim 0.34$; Bolatto et al. 2013). I do not assume any dark matter content as I allow that the MCMC technique samples $\alpha_{\mathrm{CO}} - f_{\mathrm{DM}}$ phase-space and fully considers the parameter degeneration introduced in Eq. 4.2.

In Fig.4.9, I show the one- and two- dimensional posterior PDFs of the α_{CO} and f_{DM} parameters. As in § 4.3.4, I find that higher α_{CO} values imply lower dark matter fractions. In the case of negligible central dark matter content within $r_{1/2,\mathrm{CO}}$, I find an α_{CO} upper limit of $1.3(2.4)\,M_{\odot}\,(\mathrm{K\,km\,s^{-1}\,pc^{2}})^{-1}$ by considering 1-(3-)$\,\sigma$ uncertainties.

This analysis suggests that the Accurso et al. (2017)'s parametrization overestimates the CO-to-H_2 conversion factor in SHiZELS-19 as this value is beyond the 3-σ range derived from the α_{CO} PDF. Meanwhile, the CO-to-H_2 conversion factor estimated by assuming the Narayanan et al. (2012)'s parametrization is consistent within 1-σ uncertainties. I note that an assumed $\alpha_{\mathrm{CO}} \gtrsim 1$ implies that SHiZELS-19 may be baryon dominated ($f_{\mathrm{DM}} < 0.5$) in its central zone, albeit dark matter dominated in its outskirts (§ 4.3.4; see also Tiley et al. 2019). This is consistent with the 'compaction' scenario (e.g. Dekel & Burkert 2014; Zolotov et al. 2015) in which the baryonic matter can cool and condense more efficiently than the collisionless dark matter, and thus, falling into the centre of the dark matter halo where they concentrate.

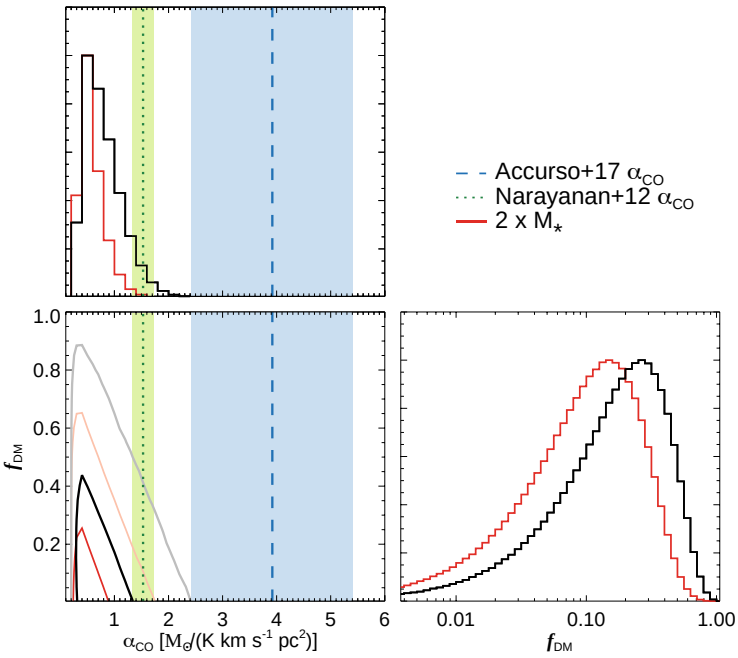

Figure 4.9: One- and two- dimensional posterior PDFs of the $f_{\rm DM}$ and $\alpha_{\rm CO}$ parameters estimated by considering the total mass content within one CO half-light radius for SHiZELS-19. The data is colour coded in the same way as Fig. 4.6. This suggests an $\alpha_{\rm CO}$ upper limit of $2.4\,M_\odot\,({\rm K\,km\,s^{-1}\,pc^2})^{-1}$ in the case of negligible dark matter content within this radius. This result rules out the Accurso et al. (2017)'s CO-to-H_2 conversion factor suggested for SHiZELS-19 by the 3-σ.

Chapter 5

A kinematic analysis of the molecular gas content in dusty galaxies at $z \sim 0.03 - 0.35$ using ALMA

In this Chapter[11], I present spatially-resolved observations of the molecular gas content traced by the CO($J = 1 - 0$) emission line ($\nu_{\rm rest} = 115.271\,{\rm GHz}$) in galaxies up to $z \approx 0.35$. Aided by auxiliary data, I characterise the role of galactic dynamics on the interstellar medium properties. These observations consist of ALMA observations for a sub-sample of 39 'typical' star-forming and starburst galaxies taken from the Valparaíso ALMA Line Emission Survey (VALES). By modelling the galactic-scale dynamics of the molecular gas content, I study the correlations between the kinematic state of galaxies with respect to different luminosity tracers. I find a dependence between $V_{\rm rot}/\sigma_v$ and the [CII]/IR ratio, suggesting that the so-called '[CII] deficit' is related to the dynamical state of the galaxies. I find that global pressure support is needed to reconcile the dynamical mass estimates with the stellar masses in systems with low $V_{\rm rot}/\sigma_v$ values. The star formation rate is weakly correlated with the molecular gas fraction in the sample, suggesting that the release of gravitational energy from cold gas may not be the main source of energy to explain the turbulent motions seen in the VALES galaxies. Finally, by defining a proxy of the 'star formation efficiency' parameter, given by SFR divided by the CO luminosity (SFE$' \equiv$SFR/L$'_{\rm CO}$), I find a constant SFE$'$ per radial crossing time ($t_{\rm cross}$), where $t_{\rm cross}$ is defined as the CO half-light radius $r_{1/2,{\rm CO}}$ divided by velocity dispersion. This suggests that $t_{\rm cross}$ may be the characteristic controlling timescale in which the star formation occurs in 'typical' and starburst dusty $z \sim 0.03 - 0.35$ galaxies. The assumed ΛCDM cosmology implies a spatial resolution, determined by typical major axis of the synthesized beam, of $3" - 4"$ that correspond to a physical scale between ≈ 2 and $\approx 17\,{\rm kpc}$ for the sample.

[11]These results were published in Molina, et al. 2019a, MNRAS, 482, 1499

5.1 Introduction

The star formation activity is one of the main processes that drives cosmic evolution of galaxies. Stars produce heavy elements via nucleosynthesis, which are expelled into the ISM during their late stages of evolution, enriching the gas with metals and dust (e.g. Nozawa & Kozasa 2013). Thus, star formation is directly involved in the processes the growth and evolution of galaxies to the formation of planets through cosmic time. Nevertheless, the knowledge about the physical processes that dominate the formation of stars starting from pristine gas is far from complete, mainly because of the wide range of physical processes are involved.

Schmidt (1959) was the first to propose a power-law relationship between the star formation activity of galaxies and their gas content. This relationship was confirmed later by Kennicutt (1998a,b), who revealed a clear relationship between the disc-averaged total galaxy gas (atomic plus molecular) surface density and the rate of star formation per surface area, the Kennicutt-Schmidt relationship (hereafter, KS law). The KS law describes how efficiently galaxies turn their gas into stars.

Since Kennicutt (1998a,b)'s work, the KS law has been tested in numerous spatially-resolved surveys on local galaxies during the last decades (e.g. Wong & Blitz 2002; Kennicutt et al. 2007; Bigiel et al. 2008; Villanueva et al. 2017). One of the first conclusions extracted from these observations was that star formation in galaxies is more strongly correlated with $\Sigma_{\rm H_2}$ than $\Sigma_{\rm HI}$ (especially at $\Sigma_{\rm gas} > 10\,M_\odot\,{\rm pc}^{-2}$). However, when additional data from high star-forming galaxies are included, the KS law shows an apparent bimodal behaviour where 'discs' and 'starburst' galaxies appear to fill the $\Sigma_{\rm H_2} - \Sigma_{\rm SFR}$ plane in different loci (Daddi et al., 2010).

Significant efforts have been made to unify both sequences, principally by comparing $\Sigma_{\rm SFR}$ with $\Sigma_{\rm H_2}$ per galaxy free-fall time ($t_{\rm ff}$) and/or orbital time ($t_{\rm orb}$), i.e. the gas dynamics. The $\Sigma_{\rm SFR} - \Sigma_{\rm H_2}/t_{\rm ff}$ relation can be interpreted as dependence of the star formation law on the local volume density of the gas (Daddi et al., 2010), whilst the $\Sigma_{\rm SFR} - \Sigma_{\rm H_2}/t_{\rm orb}$ relation suggests that the star formation law is affected by the global rotation of the galaxy (Krumholz et al., 2012). Therefore, the relevant timescale gives us critical information about the physical processes that may control the formation of stars. However, it is not clear whether the bimodality seen in the KS law may be the result of the assumptions and uncertainties behind the estimates of the molecular gas mass (Cheng et al., 2018).

Direct detections of cold H_2 gas are difficult to be obtained (e.g. Papadopoulos & Seaquist 1999; Bothwell et al. 2013), implying that observations of molecular gas tracers are essential. The use of the carbon monoxide ($^{12}C^{16}O$, hereafter CO) line luminosity of rotational low-J transitions (e.g. $J = 1 - 0$ or $J = 2 - 1$) is one of the main methods to estimate the H_2 mass content (e.g. Solomon et al. 1987; Downes & Solomon 1998; Solomon & Vanden Bout 2005; Bolatto et al. 2013). In this method, the mass of one self-gravitating entity, such as a molecular cloud, is related to the CO emission linewidth, which reflects the velocity dispersion of the gas (Bolatto et al., 2013). The molecular gas to CO luminosity relation is expressed as $M_{\rm H_2} = \alpha_{\rm CO} L'_{\rm CO}$, where $M_{\rm H_2}$ represents the whole gas mass (hence, the virial mass) for GMCs (Solomon & Vanden Bout, 2005) and $\alpha_{\rm CO}$ is the CO-to-H_2 conversion factor.

If the entire CO galaxy emission comes from a non-overlapping ensemble of molecular gas clouds with similar physical properties, the $M_{\rm H_2} - L'_{\rm CO}$ relationship can be applied to estimate the molecular gas content for the entire galaxy. This is the so-called 'mist' model (Dickman et al., 1986) and it yields $\alpha_{\rm CO} \approx 4.6\,M_{\odot}\,({\rm K\,km\,s^{-1}\,pc^2})^{-1}$ for local galaxies (Bolatto et al., 2013). However, as mist model is sensitive to the underlying distribution of the CO emitting gas on galaxies, it overestimates the gas mass in more dynamically disrupted systems, such as ULIRGs (Downes & Solomon 1998).

In those systems, CO emission maps show that the molecular gas is contained in dense rotating discs or rings, suggesting that the CO emission may not come from individual virialized clouds, but from a filled inter-cloud medium. The CO linewidth is determined by the total dynamical mass ($M_{\rm dyn}$) in the region (gas and stars, Downes et al. 1993; Solomon et al. 1997). Downes & Solomon (1998) used kinematic and radiative transfer models to derive $M_{\rm H_2}/L'_{\rm CO}$ ratios in ULIRGs. The models yielded $\alpha_{\rm CO} \approx 0.8\,M_{\odot}\,({\rm K\,km\,s^{-1}\,pc^2})^{-1}$, a ratio which is roughly six times lower than the standard $\alpha_{\rm CO}$ value for local galaxies. This $\alpha_{\rm CO}$ value is usually adopted to estimate the molecular gas content in other non-virialized environments such as galaxy mergers.

On the other hand, from numerical simulations, galaxies that have similar physical conditions seems to have similar CO-to-H_2 factors (Narayanan et al., 2012). This seems to be independent of galaxy morphology or evolutionary state. Thus, rather than a bimodal distribution of 'disc' and 'ULIRG' $\alpha_{\rm CO}$ values, simulations suggest that there is a continuum of conversion values that vary with galactic environment (Narayanan et al., 2012).

Spatially-resolved studies of the molecular gas content and its kinematics in galaxies are critical to understand the physical processes that determine the CO-to-H_2 conversion factor and the star formation activity as these two quantities seem to be dependant on the galactic dynamics. However, the construction of large samples of intermediate/high-redshift galaxies with spatially-resolved molecular gas detections (via CO emission) has remained a challenge. Beyond the local Universe, resolved CO detections are limited to the most massive/luminous yet rare galaxies or highly magnified objects (e.g. Saintonge et al. 2013). With ALMA, the study of the physical conditions of the cold molecular gas in statistically modest galaxy samples at these redshifts can be achieved by using moderate observing times. This enables to test if the actual models can successfully explain the characteristics of the intermediate/high-redshift ISM.

5.2 SAMPLE SELECTION & OBSERVATIONS

5.2.1 VALES Survey

The VALES sample (Villanueva et al. 2017, hereafter V17) is taken from the *Herschel* Astrophysical TeraHertz Large Area Survey (*H*-ATLAS; Eales et al. 2010; Bourne et al. 2016; Valiante et al. 2016), which is one of the largest infra-red and submillimetre surveys covering $\sim$600 deg^2 of the sky taken by the *Herschel* Space Observatory (Pilbratt et al.,

2010). The VALES survey covers a redshift range of $0.02 < z < 0.35$, and IR-luminosity range of $L_{8-1000\mu m} \approx 10^{10-12}\,L\odot$, thus it is an excellent galaxy sample to study the molecular gas dynamics of star-forming and 'midly' starburst galaxies at low-redshift.

The VALES survey is composed of ALMA observations targeting the CO(1-0) emission line in band 3 for 67 galaxies during Cycle-1 and Cycle-2, from which 49 sources were spectroscopically detected. The observations, data reduction and analysis are presented in detail for the complete sample in V17, whilst the [C II] luminosity data for some VALES galaxies are presented in Ibar et al. (2015).

I use the V17's far-infrared (FIR; 8–1000 μm) luminosities, $L_{\rm FIR}$, which were derived from SEDs constructed with photometry from the Infrared Astronomical Satellite (IRAS; Neugebauer et al. 1984), Wide-field Infrared Survey Explorer (WISE; Wright et al. 2010), and the *Herschel* Photoconductor Array Camera and Spectrometer (PACS; Poglitsch et al. 2010) and the Spectral and Photometric Imaging REceiver (SPIRE; Griffin et al. 2010) instruments. By assuming a Chabrier (2003) initial mass function (IMF), the SFRs are calculated following $\mathrm{SFR}(M_\odot\,\mathrm{yr}^{-1}) = 10^{-10}\times L_{\rm IR}(L\odot$; Kennicutt 1998b). Those values are systematically higher than the rates estimated from fitting the SEDs with the Bayesian code MAGPHYS (da Cunha et al., 2008) by a factor of two. However, the two estimates are well correlated despite this systematic discrepancy (see V17 for more details).

The stellar masses for the sample were calculated by modelling the SEDs from the photometry provided by the GAMA Panchromatic Data Release (Driver et al., 2016) –in which *all* of the galaxies are present–in 21 bands extending from the far-ultraviolet to far-infrared ($\sim 0.1 - 500\,\mu$m). These observed SEDs have all been modelled with the Bayesian SED fitting code MAGPHYS and presented in V17.

The analysis presented in V17 shows ALMA cubes binned at different spectral resolutions (from 20 to 100 $\mathrm{km\,s^{-1}}$) in order to boost the signal-to-noise for spectral detectability. However, the use of low or variable spectral resolution observations to derive and/or analyse galactic kinematics may lead to erroneous conclusions (see § 5.3.3). Thus, I kept the spectral resolution fixed at 20 $\mathrm{km\,s^{-1}}$ despite of the degrade of S/N in order to minimize spectral resolution effects in the dynamical analysis[12].

Out of the 49 galaxies that were spectroscopically detected in CO(1-0) by V17, I find that only 39 of them are spectroscopically detected at a 5-σ significance after fixing the spectral resolution at 20 $\mathrm{km\,s^{-1}}$ to all sources. The ten non-detected galaxies correspond preferentially to high-redshift ($z \sim 0.15 - 0.35$) massive systems ($M_\star \approx 10^{11}\,M_\odot$) with considerable SFRs ($\gtrsim 15 M_\odot\,\mathrm{yr}^{-1}$), suggesting a CO sensitivity limitation for the VALES survey. I show the 39 detected galaxies in the SFR$-M_\star$ plane in Fig. 5.1. The systems sample the SFRs and stellar masses in the range of $1 - 84\,M_\odot\,\mathrm{yr}^{-1}$ and $1 - 15 \times 10^{10}\,M_\odot$, respectively. I note that the galaxies with high SFR also tend to have high $M_\star$.

Out of these 39 galaxies, 20 are considered as 'spatially resolved' (R) by following these criteria; (1) that the observed CO(1-0) emission extends for more than $\sqrt{2}$ times the major axis of the synthesized beam; and (2) the observations should have been taken with a pro-

[12]Done by V. Villanueva

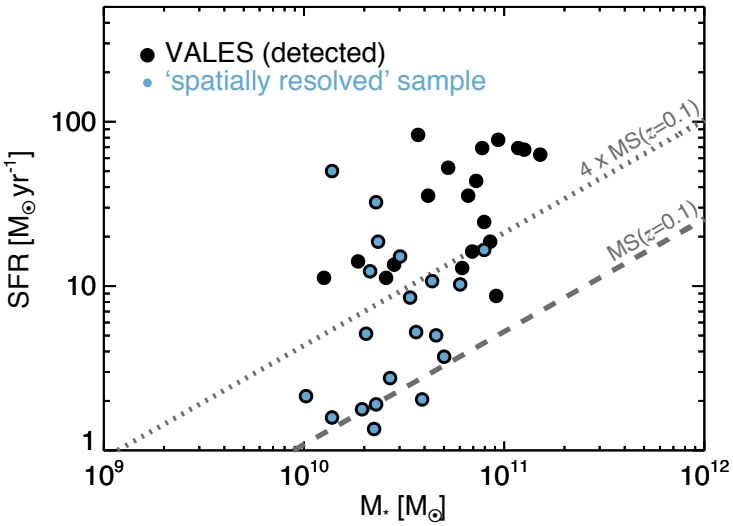

Figure 5.1: The SFR against the $M_\star$ for the 39 galaxies which were spectroscopically detected at >5-σ in datacubes with $20\,\mathrm{km\,s^{-1}}$ fixed spectral resolution from the VALES survey (V17). In blue circles I highlight the 20 sources classified as 'spatially resolved' (see § 5.2.1, for more details). The dashed line represents the SFR-$M_\star$ relationship for main-sequence star-forming galaxies at $z = 0.1$ following Genzel et al. (2015). The dotted line represents $4\times$ the SFR value expected for a main-sequence star-forming galaxy at a given stellar mass at $z = 0.1$.

jected synthesized beam smaller than 8 kpc. The other 19 sources are classified as 'compact' (C). I show the corresponding galaxy classification in the top-right of each CO(1-0) intensity map (Fig. 5.14). In the forthcoming of this work, in order to guarantee enough independent pixels to be fitted within each galaxy map, I just analyse and model the kinematics of the galaxies considered as 'resolved'.

To classify the sources as main-sequence star-forming or starburst galaxies, I use the parametrization defined by Genzel et al. (2015) in terms of the specific star formation rate (sSFR$\equiv$SFR$/M_\star$; $\log[\mathrm{sSFR}(z, M_\star)] = -1.12 + 1.14z - 0.19z^2 - (0.3 + 0.13z) \times (\log M_\star - 10.5)\,\mathrm{Gyr}^{-1}$). Galaxies with $|\,\mathrm{sSFR}/\mathrm{sSFR}(z, M_\star)\,| \leq 4$ are classified as 'normal' star-forming galaxies, whilst all the galaxies with $\mathrm{sSFR} > 4\,\mathrm{sSFR}(z, M_\star)$ are labelled as 'starburst'. I use the SFR, stellar mass and redshift of each source to perform this classification. In Fig. 5.1, the dashed line shows the main-sequence of star-forming galaxies at $z = 0.1$. As an example, the dotted line in Fig. 5.1 represents the chosen sSFR criterion for galaxies at $z = 0.1$.

I also use V17's morphological classification scheme to assume a bimodal CO-to-H_2 conversion factor of 0.8 or $4.6\,M_\odot\,(\mathrm{K\,km\,s^{-1}\,pc^2})^{-1}$ depending on whether a galaxy is classified as a 'merger' or 'disc', respectively. This classification is based on visual inspection of the galaxy images extracted by using the GAMA Panchromatic Swarp Imager tool[13]. I note that, in this case, just three galaxies (HATLASJ084630.7+005055, HATLASJ085748.0+004641, HATLASJ090750.0+010141) are classified as 'mergers' by the morphological criterion. I do not attempt to perform a kinematic classification of mergers (e.g. Shapiro et al. 2008; Förster

[13]http://gama-psi.icrar.org/psi.php

Schreiber et al. 2009; Swinbank et al. 2012b) given that the low spatial resolution tends to smooth the emission and kinematic deviations, making galaxy intensity and velocity fields appear more disc-like than they actually are (Bellocchi et al., 2012).

The mean molecular gas fraction [$f_{\rm H_2} \equiv M_{\rm H_2}/(M_{\rm H_2} + M_*)$] of the 'resolved' sample is 0.22 ± 0.15 within a range of $0.06 - 0.44$ with a typical relative error for each measurement of $\sim$12%. The use of a constant $\alpha_{\rm CO} = 4.6\,M_\odot\,({\rm K\,km\,s^{-1}\,pc^2})^{-1}$ conversion factor for all the resolved galaxies do not change this mean $f_{\rm H_2}$ value as just three galaxies are classified as 'mergers'. We note that any trend with $f_{\rm H_2}$ would be exacerbated by the choose of a constant Milky-Way CO-to-H_2 conversion factor value as the molecular gas mass may be overestimated for systems with IR luminosities values comparable to the seen for ULIRGs systems ($L_{\rm IR} \gtrsim 10^{12} L_\odot \approx 100 M_\odot\,{\rm yr^{-1}}$). On the contrary, the use of a bimodal $\alpha_{\rm CO}$ parametrization may flatten any trend with respect to $f_{\rm H_2}$ as $M_{\rm H_2}$ could be underestimated for such systems.

5.2.2 Galaxy Dynamics

To measure the dynamics of each galaxy, I fit the CO(1-0) emission line pixel-by-pixel following the procedure presented in Chapter 2. Considering that I have not applied any spectral filtering to these ALMA data for imaging purposes, the fitted linewidths correspond to the intrinsic linewidths (no deconvolution needed). Nevertheless, in order to consider if an emission line is sufficiently sampled, I only take into account those fits in which the fitted linewidth is larger than $\sqrt{2}$ times the channel width ($\approx 28\,{\rm km\,s^{-1}}$, e.g. Fig. 5.14). The spectral resolution impedes narrower velocity dispersion measurements. I caution that, this masking procedure may lead an overestimated average velocity dispersion value for each galaxy.

5.3 METHODS

5.3.1 GAMA's morphological models

I support the kinematic analysis by taking into account previous Sérsic photometry models (Sérsic, 1963) available for the GAMA survey data (Table 5.1; Liske et al. 2015). Those models are produced by using SIGMA (Structural Investigation of Galaxies via Model Analysis; Kelvin et al. 2012) on Sloan Digital Sky Survey (SDSS) and UKIRT Infrared Deep Sky Survey (UKIDSS) imaging data. By following the procedure explained in Chapter 2, I use the K-band image models to characterise stellar component of each galaxy through the half-light radius ($r_{1/2,K}$), the position angle (PA$_K$), and the inclination angle derived from the projected minor-to-major axis ratio (b/a) on the sky. I use this inclination value to constraint the galactic inclination of the molecular gas content in the kinematic modelling. I note, however, that the error estimates produced by SIGMA are determined from the covariance matrix used in the fitting procedure. As a result, the uncertainty of the inclination value tend to be underestimated (Häussler et al., 2007; Bruce et al., 2012). Therefore, I adopt the more reasonable error estimates to the galactic inclination given by the procedure explained in Chapter 2.

TABLE 5.1 $K-$band BROADBAND PROPERTIES

Table 5.1: GAMA's morphological $K-$band photometric parameters for the 'resolved' galaxy sub-sample from VALES. $\mu_{0,K}$ is the central surface brightness value. $r_{1/2,K}$ and n_S are the half-light radius and the Sérsic photometric index, respectively. PA_K is the position angle of the major axis. The ellipticity 'e' is derived from the semi-major and minor axis ratio ($\mathrm{e} \equiv 1 - b/a$). The chi-square of the best two-dimensional fitted photometric model is given in the last column.

ID	$\mu_{0,K}$ mag/″^{2}	$r_{1/2,K}$ ″	n_S	PA_K deg	e	χ^2_ν
(1)	(2)	(3)	(4)	(5)	(6)	(7)
HATLASJ083601.5+002617	15.5	5.09	1.93	2.1	0.61	1.09
HATLASJ083745.1-005141	15.5	6.26	2.46	62.8	0.19	0.92
HATLASJ084217.7+021222	12.3	0.63	2.47	168.3	0.22	0.54
HATLASJ084350.7+005535	13.5	1.38	2.61	0.0	0.57	1.12
HATLASJ084428.3+020349	4.2	23.49	8.92	101.1	0.38	1.57
HATLASJ084428.3+020657	15.6	2.04	1.28	58.6	0.77	1.63
HATLASJ084630.7+005055	0.6	0.67	8.44	141.5	0.19	1.05
HATLASJ084907.0-005139	9.7	1.06	4.95	136.4	0.34	1.11
HATLASJ085111.5+013006	11.6	5.20	3.82	114.8	0.77	1.42
HATLASJ085112.9+010342	13.6	2.68	2.82	115.6	0.53	1.16
HATLASJ085340.7+013348	16.9	6.68	2.18	27.4	0.13	1.17
HATLASJ085346.4+001252	14.9	3.31	1.93	46.0	0.77	1.07
HATLASJ085356.5+001256	17.8	4.56	1.56	57.4	0.29	1.08
HATLASJ085450.2+021207	14.0	3.62	2.58	150.3	0.52	1.48
HATLASJ085616.0+005237	13.9	0.97	2.54	78.1	0.10	1.05
HATLASJ085748.0+004641	10.1	0.72	3.48	125.3	0.10	1.28
HATLASJ085828.5+003815	8.8	7.51	5.93	121.0	0.25	1.19
HATLASJ085836.0+013149	–	–	–	–	–	–
HATLASJ090004.9+000447	12.5	1.85	2.84	47.6	0.22	1.47
HATLASJ090750.0+010141	8.2	1.49	5.40	66.3	0.28	1.89
HATLASJ091205.8+002655	9.8	0.97	4.04	52.2	0.07	1.24

Out of the 20 resolved galaxies analysed in this work,19 sources have this morphological GAMA modelling. I do not use the inclination value derived for HATLASJ085836.0+013149 from its morphological model as it implies an unrealistic central surface brightness magnitude value of $-18\,\mathrm{mag\,arcsec^{-2}}$. This galaxy was analysed without constraint on the kinematic parameters. I remind that the adopted intrinsic minor-to-major ratio for this work is $\mathrm{q_0} = 0.14$, which is the mean b/a ratio found in edge-on disc galaxies at low-redshift ($z < 0.05$; Mosenkov et al. 2015).

Table 5.2: Properties of the galaxies with resolved emission from VALES. The FIR luminosities are calculated across the 8–1000 μm wavelength range. $\theta_{\rm FWHM}$ is the synthesized beam major axis size. The CO(1-0) half-light radii ($r_{1/2,\rm CO}$) are deconvolved by the synthesized beam size. The inclination angle is defined as the angle between the line-of-sight and the plane perpendicular to the galactic disc (for a face-on galaxy, inc = 0 deg.). σ_v is the median velocity dispersion corrected for "beam smearing" effects. $V_{\rm rot}$ is the inclination corrected rotational velocity at 2 times the CO(1-0) half-light radius. χ^2_ν is the reduced chi-square of the best two-dimensional fit. The galaxy classification in the final column denotes 'Resolved' (R) or 'Compact' (C).

*H*ATLAS-DR1 ID	RA	Dec	$z_{\rm spec}$	$\log M_\star$	$\log L_{\rm FIR}$	$L_{\rm [C\,II]}$	$L'_{\rm CO}$	$\theta_{\rm FWHM}$	$r_{1/2,\rm CO}$	inc.	σ_v	$V_{\rm rot}$	χ^2_ν	Class
	J2000	J2000		$M_\odot$	$L_\odot$	$\times10^8\,L_\odot$	$\times10^{10}\,L_\odot$	kpc	kpc	deg	km/s	km/s		
(1)	(2)	(3)	(4)	(5)	(6)	(7)	(8)	(9)	(10)	(11)	(12)	(13)	(14)	(15)
HATLASJ083601.5+002617	08:36:01.6	+00:26:18.1	0.03322	10.59±0.1	10.31±0.02	0.97±0.02	0.104±0.004	2.22	3.4±0.1	80.8±0.1	24±2	180±3	0.13	R
HATLASJ083745.1−005141	08:37:45.2	−00:51:40.9	0.03059	10.35±0.1	10.13±0.03	0.73±0.01	0.034±0.003	2.06	4.4±0.3	57.2±0.1	25±1	115±1	0.14	R
HATLASJ083831.9+000045	08:38:31.9	+00:00:45.0	0.07806	10.27±0.1	11.15±0.01	2.43±0.10	0.250±0.019	6.05	–	–	–	–	–	C
HATLASJ084217.7+021222	08:42:17.9	+02:12:23.4	0.09602	10.53±0.1	10.93±0.04	2.28±0.11	0.249±0.020	5.58	12.0±3.1	77.5±0.2	35±7	75±3	0.16	R
HATLASJ084305.0+010858	08:43:05.1	+01:08:56.0	0.07770	10.41±0.2	11.05±0.03	–	0.166±0.017	6.13	–	–	–	–	–	C
HATLASJ084350.7+005535	08:43:50.8	+00:55:34.8	0.07294	10.64±0.1	11.03±0.01	1.70±0.09	0.191±0.016	5.52	4.2±0.3	67.3±0.7	70±8	58±3	0.71	R
HATLASJ084428.3+020349	08:44:28.4	+02:03:49.8	0.02538	10.29±0.1	10.25±0.01	0.33±0.01	0.041±0.003	1.76	2.4±0.4	80.0±0.2	59±14	69±6	0.86	R
HATLASJ084428.3+020657	08:44:28.4	+02:06:57.4	0.07864	10.78±0.1	11.01±0.03	4.51±0.14	0.392±0.051	6.22	6.3±0.5	83.5±0.2	39±2	162±3	2.50	R
HATLASJ084630.7+005055	08:46:30.9	+00:50:53.3	0.13232	10.36±0.1	11.51±0.02	6.22±0.63	0.463±0.042	7.51	4.5±0.5	33.3±0.1	37±28	215±8	20.6	R
HATLASJ084907.0−005139	08:49:07.1	−00:51:37.7	0.06979	10.48±0.1	11.18±0.01	2.28±0.09	0.279±0.022	5.27	4.7±1.3	45.9±0.3	54±3	108±4	0.33	R
HATLASJ085111.5+013006	08:51:11.4	+01:30:06.9	0.05937	10.56±0.1	10.72±0.02	2.66±0.07	0.198±0.007	4.63	6.5±0.4	76.2±0.1	31±8	207±4	0.22	R
HATLASJ085112.9+010342	08:51:12.8	+01:03:43.7	0.02669	10.14±0.1	10.20±0.01	0.24±0.01	0.020±0.003	1.85	1.1±0.3	58.0±0.9	43±19	81±4	0.74	R
HATLASJ085234.4+013419	08:52:33.9	+01:34:22.7	0.19500	10.57±0.1	11.92±0.01	–	1.999±0.012	14.9	–	–	–	–	–	C
HATLASJ085340.7+013348	08:53:40.7	+01:33:47.9	0.04101	10.36±0.1	10.28±0.03	0.95±0.02	0.061±0.003	2.95	3.6±0.3	39.0±0.2	24±3	181±14	0.13	R
HATLASJ085346.4+001252	08:53:46.3	+00:12:52.4	0.05044	10.31±0.1	10.71±0.01	2.18±0.04	0.076±0.002	3.57	6.4±0.4	89.7±0.2	33±5	134±4	0.26	R
HATLASJ085356.5+001256	08:53:56.3	+00:12:56.3	0.05084	10.01±0.1	10.33±0.03	1.41±0.04	0.068±0.002	3.60	2.6±0.2	52.2±0.1	25±4	109±2	0.14	R
HATLASJ085450.2+021207	08:54:50.2	+02:12:08.3	0.05831	10.66±0.1	10.70±0.02	2.30±0.08	0.202±0.019	4.66	3.9±0.1	70.4±0.1	39±16	287±6	1.52	R
HATLASJ085616.0+005237	08:56:16.0	+00:52:36.2	0.16916	10.96±0.1	10.94±0.01	–	0.443±0.076	10.4	–	–	–	–	–	C
HATLASJ085748.0+004641	08:57:48.0	+00:46:38.7	0.07177	10.37±0.1	11.27±0.01	4.69±0.09	0.276±0.014	5.57	4.6±0.3	70.2±0.1	51±5	43±3	0.10	R
HATLASJ085828.5+003815	08:58:28.6	+00:38:14.8	0.05236	10.43±0.1	10.44±0.02	0.94±0.03	0.043±0.005	3.72	2.6±0.2	52.3±0.1	22±2	159±2	0.16	R
HATLASJ085836.0+013149	08:58:36.0	+01:31:49.0	0.10677	10.90±0.1	11.22±0.01	5.30±0.21	0.554±0.011	6.17	11.1 ±0.8	80.0±0.1	27±4	91±1	0.19	R
HATLASJ090004.9+000447	09:00:05.0	+00:04:46.8	0.05386	10.70±0.1	10.57±0.02	1.86±0.06	0.153±0.022	3.80	2.7±0.1	42.5±0.2	25±2	193±10	0.22	R
HATLASJ090750.0+010141	09:07:50.1	+01:01:41.8	0.12808	10.14±0.1	11.70±0.01	9.33±0.40	0.535±0.045	7.36	10.3 ±0.6	44.8±1.4	58±6	35±5	0.12	R
HATLASJ090949.6+014847	09:09:49.6	+01:48:46.0	0.18186	10.89±0.1	11.84±0.02	13.8±0.68	1.364±0.093	12.7	–	–	–	–	–	C
HATLASJ091157.2+014453	09:11:57.2	+01:44:53.9	0.16945	10.90±0.2	11.39±0.01	–	0.737±0.072	11.0	–	–	–	–	–	C
HATLASJ091205.8+002655	09:12:05.8	+00:26:55.6	0.05446	10.33±0.1	11.09±0.01	1.45±0.05	0.187±0.011	3.94	2.6±0.3	21.0±0.5	79±24	116±12	0.11	R
HATLASJ091420.0+000509	09:14:20.0	+00:05:10.0	0.20216	10.62±0.1	11.55±0.01	–	0.667±0.114	13.0	–	–	–	–	–	C
HATLASJ091956.9+013852	09:19:57.0	+01:38:51.6	0.17635	10.45±0.1	11.13±0.01	–	0.365±0.048	11.7	–	–	–	–	–	C
HATLASJ113858.4−001629	11:38:58.5	−00:16:30.2	0.16370	10.84±0.1	11.21±0.01	–	0.546±0.129	8.94	–	–	–	–	–	C
HATLASJ114343.9+000203	11:43:44.1	+00:02:02.5	0.18716	10.10±0.1	11.05±0.01	–	0.485±0.089	10.1	–	–	–	–	–	C
HATLASJ114625.0−014511	11:46:25.0	−01:45:13.0	0.16450	10.72±0.1	11.72±0.01	–	0.861±0.084	8.91	–	–	–	–	–	C
HATLASJ121141.8−015730	12:11:41.8	−01:57:29.7	0.31704	11.18±0.1	11.80±0.01	–	0.210	15.1	–	–	–	–	–	C
HATLASJ121253.5−002203	12:12:53.5	−00:22:04.4	0.18548	10.79±0.1	11.11±0.01	–	0.447±0.065	9.71	–	–	–	–	–	C
HATLASJ121427.3+005819	12:14:27.4	+00:58:18.3	0.18045	10.93±0.1	11.27±0.01	–	0.460±0.069	9.63	–	–	–	–	–	C
HATLASJ121446.4−011155	12:14:46.5	−01:11:55.6	0.17971	10.82±0.1	11.55±0.01	–	0.765±0.094	9.45	–	–	–	–	–	C
HATLASJ140912.3−013454	14:09:12.5	−01:34:54.9	0.26492	10.97±0.1	11.89±0.01	–	1.494±0.231	9.17	–	–	–	–	–	C
HATLASJ141008.0+005106	14:10:08.0	+00:51:06.9	0.25641	11.10±0.1	11.83±0.01	–	1.311±0.295	8.80	–	–	–	–	–	C
HATLASJ142057.9+015233	14:20:58.0	+01:52:32.1	0.26462	10.86±0.1	11.64±0.01	–	1.238±0.231	9.55	–	–	–	–	–	C
HATLASJ142517.1+010546	14:25:17.1	+01:05:46.6	0.28069	11.07±0.1	11.84±0.01	–	1.714±0.237	9.98	–	–	–	–	–	C

5.3.2 Kinematic model

The CO(1-0) velocity field is modelled by implementing the single-map kinematic fitting procedure explained in Chapter 2. From this modelling, an example of the best-fit kinematic maps and velocity residuals are shown in Fig. 5.2, whilst the full sample maps are presented in the appendix (Fig. 5.14). The best-fit inclination values are given in Table 5.2. The mean deviation from the best-fit models within the sample (indicated by the typical root-mean-squared; r.m.s) is $\langle \text{data} - \text{model} \rangle = 17 \pm 9\,\text{km}\,\text{s}^{-1}$ with a range of $\langle \text{data} - \text{model} \rangle = 7$–$48\,\text{km}\,\text{s}^{-1}$. I show this value for each galaxy in its residual map.

The CO(1-0) half-light radii are calculated by following the procedure explained in Chapter 2 and are corrected for beam-smearing effects by subtracting the synthesized beam major axis width in quadrature. The median $r_{1/2,\text{CO}}$ for the sample is $4.4 \pm 3\,\text{kpc}$ (Table 5.2).

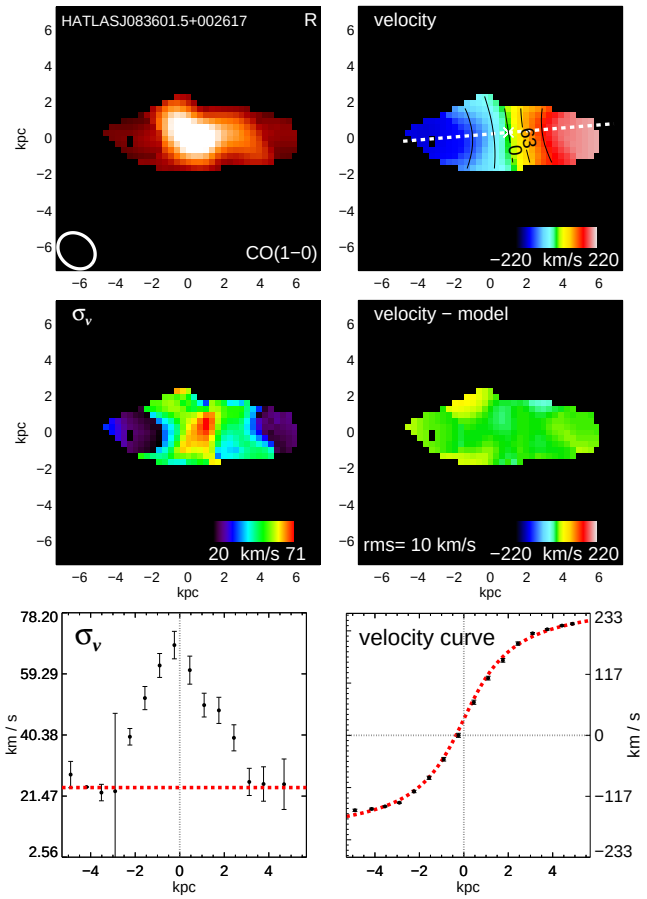

Figure 5.2: Example of the two dimensional maps and one dimensional velocity profiles for one target within the survey. The full sample maps, profiles figures and their explanation are shown in the appendix (Fig. 5.14). *Left*: From top to bottom; CO(1-0) intensity map, velocity dispersion map and one dimensional velocity dispersion profile. *Right*: From top to bottom; rotational velocity map, residual map, and one dimensional rotational velocity profile.

I define the rotational velocity corrected for inclination ($V_{\rm rot}$) as the velocity observed at two half-light radii. I note, however, that I analyse the CO(1-0) emission line, thus the radius at which is defined the representative rotational velocity of each source may not be directly related to the radius at which, for example, IFS surveys might extract rotational velocities using ionized gas dynamics (e.g. Förster Schreiber et al. 2009; Swinbank et al. 2012b; Green et al. 2014; Wisnioski et al. 2015; Stott et al. 2016).

The global molecular gas velocity dispersion value (σ_v) for each galaxy is calculated by using procedure written in Chapter 2. In this case, I calculate this value as the median value of the pixels at an angular distance 2 times greater than the angular extension of the synthesized beam from the best-fitted dynamical centre. This procedure usually calculates σ_v by considering 71 pixels on average with a range of 6-256 pixels. In the case of HATLASJ083601.5+002617, I increased the skipped area to 3 times the synthesized beam size as the method failed due to the high galaxy inclination angle (∼80 deg.) plus a beam size not large enough to avoid the zone where velocity gradients were contributing to the emission linewidths.

5.3.3 Spatial and spectral resolutions effects

In order to estimate the effect of the spatial and spectral resolution for the VALES sample on the kinematic parameters, I use ALMA Band-3 observations with higher resolution of $\sim 0\farcs5$ ($\sim$ kpc scale at $z \sim 0.1-0.2$) and $12\,{\rm km\,s^{-1}}$ towards three VALES galaxies (Chapter 6). The high resolution of those observations allows to study in detail how spectral resolution and beam-smearing effects affect the derived kinematic parameters.

I create mock-observations by spatially degrading the images using two-dimensional Gaussian kernel, while also re-binning the spectral channels to mimic lower spectral resolutions. The channel width is increased by $12\,{\rm km\,s^{-1}}$ per step between $\sim 12-84\,{\rm km\,s^{-1}}$, whilst the spatial resolution is degraded by 1 kpc per step between $\sim 1-7$ kpc (up to ~ 3 times the 'fiducial' half-light radius). From those mock datacubes, I fit the CO(1-0) emission line, I derive its best-fit kinematic model and I calculate the $V_{\rm rot}$, σ_v and $r_{1/2,{\rm CO}}$ following the procedures described in Chapter 2, but I keep the position angle fixed to the value obtained for the data-cube with higher spatial and spectral resolutions.

In Fig. 5.3, I show how the fitted kinematic parameters (rows) depend on spectral resolution (left column) at fixed ∼1 kpc scale and spatial resolution (right column) at fixed $12\,{\rm km\,s^{-1}}$ for the three sources. I consider the 'fiducial' value of each kinematic parameter for each source as the values derived for the datacubes with higher spectral and spatial resolutions ($12\,{\rm km\,s^{-1}}$ and ∼1 kpc), and are represented by the horizontal dashed lines in each plot. The fiducial values for the three galaxies are; $V_{\rm rot} = 56$, 200 and $226\,{\rm km\,s^{-1}}$; $\sigma_v = 54$, 53 and $76\,{\rm km\,s^{-1}}$; and $r_{1/2,{\rm CO}} = 1.2$, 4.2 and 4.6 kpc.

From this figure, I see how the measured galactic velocity dispersion remains constant when the spectral resolution is degraded. I also see an increase of the velocity dispersion when I spatially degrade the datacubes, however, I note that the galaxy with the lowest 'fiducial' rotational velocity value is also the galaxy less affected by spatial resolution effect.

This is consistent with the picture in which the velocity gradient within the beam area contributes to the emission linewidth represented by the velocity dispersion. I note also that galaxy mass and inclination may also affect the σ_v estimation (e.g. Burkert et al. 2016).

In the second row of Fig. 5.3, I measure $V_{\rm rot}$ for each datacube. Although I can recover nearly the same $V_{\rm rot}$ value regardless of the spectral resolution, the $V_{\rm rot}$ values vary when I spatially degrade the datacubes. At poor spatial resolution, lower rotational velocity values are recovered. This effect is expected as the observed emission line is the result of the convolution of the emission lines within the beam area. This convolution flavour brighter emission lines which are mainly produced in the galaxy central part where $V_{\rm rot}$ is lower.

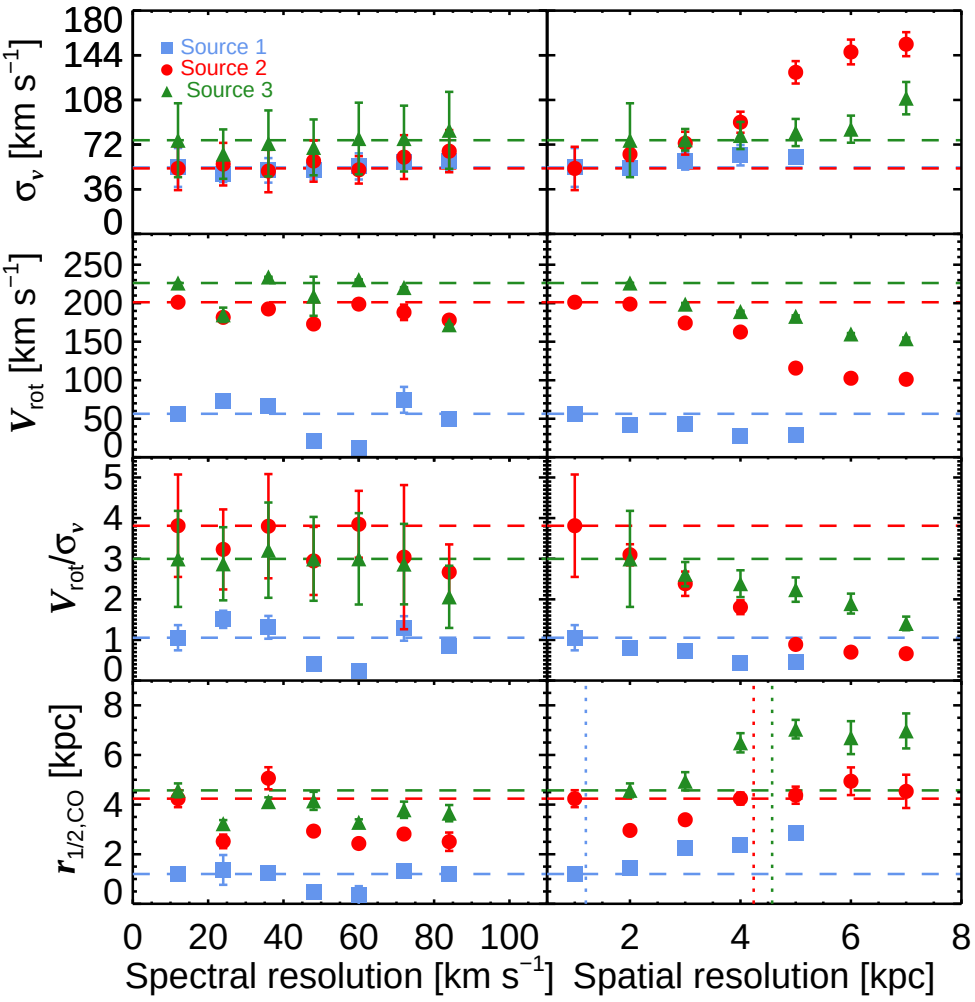

Figure 5.3: Velocity dispersion, rotational velocity, rotational velocity to velocity dispersion ratio ($V_{\rm rot}/\sigma_v$) and CO(1-0) intensity half-light radius (rows) as a function of the spectral and spatial resolution (columns). Those values were derived from mock datacubes produced by the convolution of a three dimensional gaussian kernel with the original observations. The spatial resolution corresponds to the projected major axis (FWHM) of the synthesized beam. The blue, red and green horizontal dashed lines represent the kinematic 'fiducial' values for each source. The blue, red and green vertical dotted lines represent the 'fiducial' $r_{1/2,\rm CO}$ values for each galaxy (see § 5.3.3 for more details).

In the third row of Fig. 5.3, I show the variation of the $V_{\rm rot}/\sigma_v$ ratio as a function of spectral and spatial resolutions. I see how this ratio is not affected by the increase of the channel width. However, I observe a decrease of the $V_{\rm rot}/\sigma_v$ ratio with lower spatial resolution. This is produced by a combination of both effects, the underestimation and overestimation of the $V_{\rm rot}$ and σ_v values, respectively. However the way in which the $V_{\rm rot}/\sigma_v$ ratio decreases seems to be different for each target, suggesting that the internal kinematics of each galaxy may affect the derived $V_{\rm rot}/\sigma_v$ ratio through the convolution with the synthesized beam.

In the four row of Fig. 5.3, I see how $r_{1/2,\rm CO}$ does not vary significantly with spectral resolution in any source. The gain of flux from the outskirts of each target seems to be marginal compared to the total flux of the source. On the other hand, I see a clear increase of $r_{1/2,\rm CO}$ when I lower the spatial resolution. I note that the derived half-light radii tend to suffer an appreciable increase of their value when the synthesized beam size becomes comparable to the 'fiducial' $r_{1/2,\rm CO}$ value for each galaxy (dotted vertical lines).

As a summary, the velocity dispersion and half-light radius parameters seem to be saturated to a minimum value limited by the spatial resolution. The $V_{\rm rot}/\sigma_v$ ratio tend to decrease towards low spatial resolution. However, dispersion dominated sources seem to be less affected by this effect. Thus, high spatial resolution data is required to obtain reliable estimates of those parameters. I find no trend between the spectral resolution and the kinematic estimates from the observations.

Taking into account the resolution effects discussed above, the spectral resolution is set to $20\,{\rm km\,s^{-1}}$, the maximum spectral resolution possible for the observations. I expect that spectral resolution effects do not strongly influence the conclusions of this work. The spectral resolution is set regardless of the spatial resolution effects inherent in the observations which may imply an overestimation of the observed σ_v and $r_{1/2,\rm CO}$ values and an underestimation of the $V_{\rm rot}$ value for the sources.

5.4 RESULTS & DISCUSSION

5.4.1 Morphological and kinematic properties

I show the CO(1-0) intensity, rotation velocity and velocity dispersion maps for the galaxies in this sample in the appendix (Fig. 5.14). The intensity maps show smooth distributions of emission with no level of clumpiness except for HATLASJ085340.7+013348 source. Despite the low resolution data, most of the sources show a rotational pattern in their velocity maps (Fig. 5.14), with the larger rotational velocity values being preferentially measured in galaxies at lower redshifts. I note that this bias effect may be mainly produced by the IR flux selection criteria used within the VALES sample. In particular, for the resolved sample, the flux criterion selects $0.02 < z < 0.2$ 'normal' star-forming rotating disc-like galaxies, whilst it also selects $0.1 < z < 0.35$ starburst galaxies with high velocity dispersion (Table 5.2).

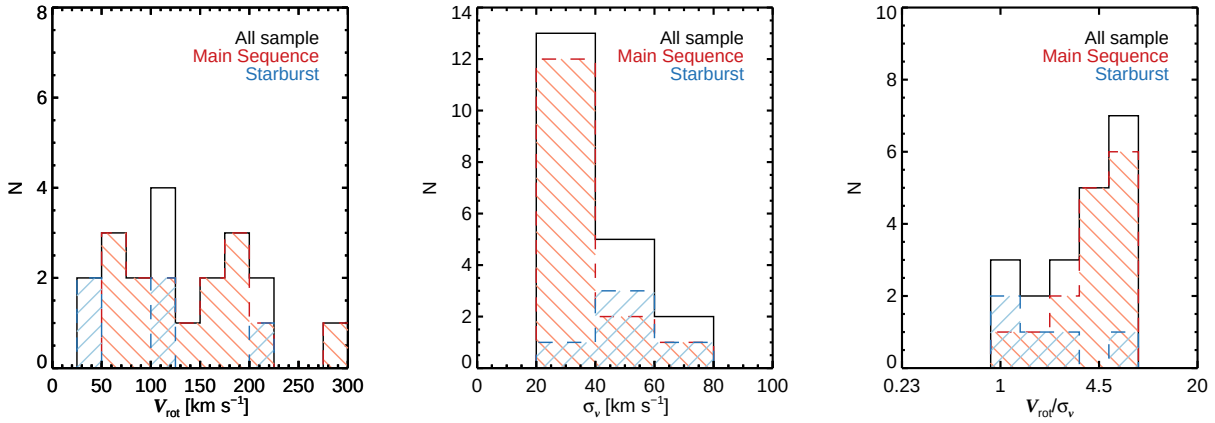

Figure 5.4: The distribution of the rotational velocity ($V_{\rm rot}$; *Left*), velocity dispersion (σ_v; *middle*) and $V_{\rm rot}/\sigma_v$ (*Right*) within the sample. In the three panels I also show the distributions for the 'normal' star-forming galaxies (dashed-red) and 'starburst' galaxies (dashed-blue). This classification was done by following the same procedure adopted by V17 for the VALES survey (see § 5.2.1). The resolved sample shows a wide ride of rotation velocities and velocity dispersions.

I note that, I find a median $r_{1/2,K}/r_{1/2,\rm CO}$ ratio of ~ 1, i.e., the molecular gas component shows an spatial extension comparable to stellar component in the galaxies. This is consistent with molecular gas observations of galaxies in the local universe (e.g. Bolatto et al. 2017). I note that the $r_{1/2,K}/r_{1/2,\rm CO}$ median ratio is lower than the median value (~ 1.6) reported by V17 for the VALES sample. I note that this difference could be explained by considering that the emission line fitting routine is able to find CO emission at larger radius than the V17's procedure. Nevertheless, I calculate the CO and $K-$band half-light radius by taking into account the projection effects (i.e. galactic PA and inclination angles), whilst V17 do not consider for such effects.

In Fig. 5.4, I show the distribution of $V_{\rm rot}$, σ_v, and the $V_{\rm rot}/\sigma_v$ ratio for the resolved sample. The $V_{\rm rot}$ values vary in the range of 35-287 km s^{-1}. The starburst and 'normal' star-forming galaxies show rotational velocities across the full range of the $V_{\rm rot}$ distribution. The velocity dispersion values ranges from 22-79 km s^{-1}. I find median velocity dispersion values of 31$\pm$20 and 53$\pm$13 km s^{-1} for the 'normal' star-forming and starburst galaxies, respectively. However, the σ_v values are susceptible to the procedure used to estimate them. Different methods can lead inconsistent results even when the same sample is analysed (e.g. Stott et al. 2016). Thus, I perform the method developed by Wisnioski et al. (2015) to calculate the velocity dispersion values ($\sigma_{v,\rm W}$) in the sample and to compare with the σ_v values. This method calculates the velocity dispersion values across the major axis of the galaxy, but far from the galactic centre where velocity gradients contribute to the observed linewidths (see Wisnioski et al. 2015, for more details).

I found a median $\sigma_{v,\rm W}$ value of 36$\pm$20 km s^{-1}, and $\sigma_{v,\rm W}$ ranges between $19-70$ km s^{-1}. This median value is in agreement with the median σ_v value (37$\pm$22 km s^{-1}) derived by the procedure implemented in this work. The derived velocity dispersion ranges are also consistent for both methods. This suggests that the procedure implemented in this work do not systematically overestimates the velocity dispersion values. I caution that, I can not

neglect overestimation of the velocity dispersion values produced by spatial resolution effects from this analysis.

The $V_{\rm rot}/\sigma_v$ ratio range between $0.6 - 7.5$, with the starburst galaxies preferentially to showing the lower values. The median $V_{\rm rot}/\sigma_v$ ratio for the sample is $4.1^{+3.5}_{-2.9}$, and the median $V_{\rm rot}/\sigma_v$ values for the 'normal' star-forming and starburst sub-samples are $4.3^{+3.2}_{-2.3}$ and $1.6^{+4.3}_{-1.0}$, respectively. The sample shows a large variety of $V_{\rm rot}/\sigma_v$ ratios, from high values comparable to local thin disc galaxies ($V/\sigma_v \sim 10 - 20$ Epinat et al. 2010; Bershady et al. 2010), to low values comparable to the $V_{\rm rot}/\sigma_v$ ratios observed in $z \sim 1$ systems (e.g. $V/\sigma_v \sim 2 - 5$ Förster Schreiber et al. 2009; Wisnioski et al. 2015; Stott et al. 2016).

In Fig. 5.5, I study the evolution of the $V_{\rm rot}/\sigma_v$ ratio at $z = 0.10 - 1.0$. I compare with the median $V_{\rm rot}/\sigma_v$ values estimated for the GHASP (Epinat et al., 2010), CARMA-EDGE (Bolatto et al., 2017), DYNAMO (Green et al., 2014), KMOS3D (Wisnioski et al., 2015), and KROSS (Stott et al., 2016) surveys. The continuous line and the grey-shaded area represent the best-fit relation and the 1-σ region estimated from the DEEP2 survey (Kassin et al., 2012) at $z = 0.2 - 1.0$, respectively. The dashed line represents an extrapolation of this relation at low-redshift. DEEP2 is the only long-slit survey considered in Fig. 5.5. I just consider the galaxies with stellar masses between $M_\star = 10^{10-11}\,M_\odot$, approximately the same stellar mass range covered by the sample (see Fig. 5.1). I also plot the median $V_{\rm rot}/\sigma_v$ values for the galaxies classified as 'starburst' and 'normal' galaxies within the sample and the DYNAMO sample as both surveys study star-forming galaxies the same epoch. However, the DYNAMO SFRs are based on dust-corrected Hα emission line measurements, whilst the SFR estimates for the sample are estimated by applying SED fitting. I also note that the sample and the CARMA-EDGE survey observe molecular gas kinematics, whilst GHASP, DYNAMO, KMOS3D and KROSS surveys study ionized gas kinematics.

The median $V_{\rm rot}/\sigma_v$ value for the sample is slightly lower but still consistent with the expected value at $z \sim 0.06$. This value is also comparable with the median value found for the KMOS3D sample of main-sequence rotating discs star-forming galaxies at $z \sim 1$. However, the median $V_{\rm rot}/\sigma_v$ value of the survey is highly influenced by the low $V_{\rm rot}/\sigma_v$ ratios measured for the starburst galaxies (Fig 5.4). If I do not consider those starburst systems, I find that the median $V_{\rm rot}/\sigma_v$ value for the 'normal' star-forming galaxies in the sample is consistent with the expected value for local galaxies. It is also consistent with the median $V_{\rm rot}/\sigma_v$ value measured for DYNAMO 'normal' star-forming galaxies.

Nevertheless, the median $V_{\rm rot}/\sigma_v$ for the starburst galaxies is $\sim 2.7\times$ lower than the median value observed for the DYNAMO starburst galaxies at the same redshift, but consistent within 1-σ error. A difference between the spatial extension of the ionized gas compared to the molecular gas across the galaxy may explain this discrepancy. An extended ionized gas component would allow to measure $V_{\rm rot}$ in the flat part of the rotation curve whilst the molecular gas observations would not allow to do it (e.g. HATLASJ084217.7+021222). Different procedures used to calculate σ_v may also explain this discrepancy. However, the different spatial resolution at which both surveys were made is likely to be producing the discrepancy between both $V_{\rm rot}/\sigma_v$ ratios. The DYNAMO galaxies were observed in natural seeing conditions ($\theta_{\rm FWHM} = 0\farcs9 - 4''$), whilst the sample was observed at $\theta_{\rm FWHM} = 3$" $- 4$".

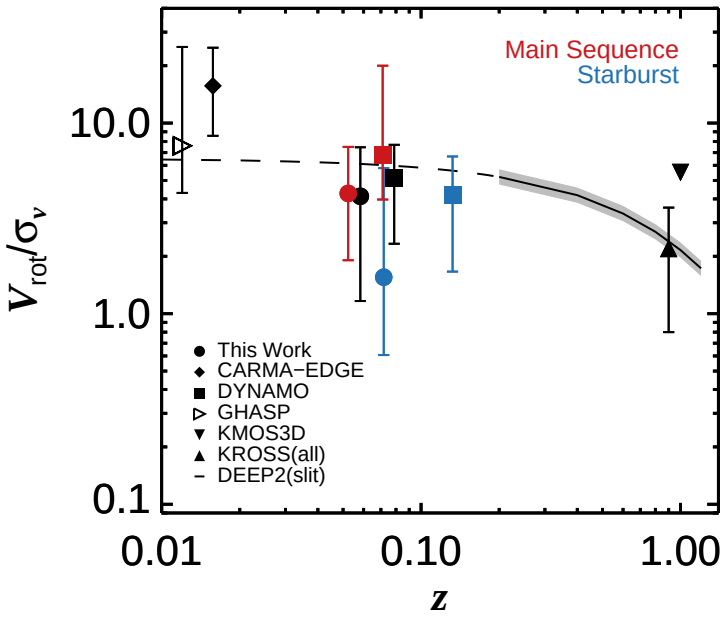

Figure 5.5: Evolution of the $V_{\rm rot}/\sigma_v$ ratio at $z \approx 0.01 - 1.0$. The symbols represent the median values for each survey and the error bars correspond to the 1-σ region calculated from the 16th and 84th percentiles for each population. The CARMA-EDGE kinetic data are extracted by using the same procedure explained in Chapter 2, but assuming thin disc geometry (see Appendix 5.6.3, for more details). I classify the sample sources and the DYNAMO galaxies as 'starburst' or 'normal' star-forming galaxy following the same procedure done by V17 for the VALES survey (see § 5.2.1). The KMOS3D data correspond to the median value for main sequence rotationally supported star-forming disc galaxies at $z \sim 1$, whilst the KROSS data correspond to the median value for all sample, i.e., including main sequence dispersion dominated galaxies. The solid line and the shaded area represent the best-fit and 1-σ region measured for the single slit DEEP2 survey. The dashed line represents the extrapolation of the best-fit to the DEEP2 survey data to lower redshifts

Regardless of the discrepancy of the median $V_{\rm rot}/\sigma_v$ value measured for the sample and the DYNAMO survey, Fig 5.5 shows that starburst galaxies at $z \sim 0.1 - 0.2$ present typical $V_{\rm rot}/\sigma_v$ ratios which are consistent with median the $V_{\rm rot}/\sigma_v$ values presented for the KMOS3D and KROSS surveys at $z \sim 1$ (Wisnioski et al., 2015; Stott et al., 2016).

5.4.2 Luminosity dependence on galactic kinematics

CO(1-0) luminosity

The CO(1-0) luminosity has been widely used as an estimator of the H_2 mass (Bolatto et al., 2013). Through a dynamically calibrated CO-to-H_2 conversion factor, reliable molecular mass estimates can be achieved (e.g. Solomon et al. 1987; Downes & Solomon 1998). Thus, depending on the dynamical model, I may expect some dependence of the CO luminosity on the galactic dynamics.

In the top panel of Fig. 5.6, I show the galactic $L'_{\rm CO}$ as a function of the rotational velocity to dispersion velocity ratio ($V_{\rm rot}/\sigma_v$). The Spearman's rank correlation coefficient ($\rho_{\rm Spearman}$) is -0.23 with a probability of 32% that the correlation is produced by chance, i.e, $\sim$ 1-σ of significance. Thus, the data suggest a tentative weak correlation between $L'_{\rm CO}$ and $V_{\rm rot}/\sigma_v$, where the CO luminosity tend to decrease at higher $V_{\rm rot}/\sigma_v$ values. Considering that $V_{\rm rot}/\sigma_v$ measures the level of support given by ordered versus disordered motion support within a galaxy, then it suggests that turbulence supported galaxies tend to have greater $L'_{\rm CO}$.

The high $L'_{\rm CO}$ values may reflect high molecular gas masses in systems with low $V_{\rm rot}/\sigma_v$ values. On the other hand, I may also expect that systems with high SFRs produce more UV photons (SFR($M_\odot\,{\rm yr}^{-1}$)$\approx 8.2 \times 10^{-29} L_{\rm UV}({\rm erg\,s^{-1}\,Hz^{-1}})$ for a Chabrier IMF, Kennicutt 1998b) which heats the gas through the photoelectric effect on dust grains. This change of gas temperature may also affect the CO-to-H_2 conversion factor (Bolatto et al., 2013). However, I lack of the adequate observations to test this.

I also note that low $V_{\rm rot}/\sigma_v$ ratios can be present in both, disc-like galaxies and major-merger systems (Chapter 3). Thus, a weak correlation between $L'_{\rm CO}$ and the $V_{\rm rot}/\sigma_v$ ratio suggests that the increase of the CO(1-0) luminosity may not be associated only to major merger events in agreement with previous results from numerical simulations (Shetty et al., 2011; Narayanan et al., 2012; Papadopoulos et al., 2012). This tentative weak correlation also suggests that turbulence may play a role in the enhancement of $L'_{\rm CO}$ in galaxies.

[C II] luminosity

The [C II] $\lambda 157.74\,\mu$m emission line ($\nu_{\rm rest} = 1900.54\,$GHz) is a far-infrared fine-structure line with a low ionization potential (11.26 eV) that makes it a key participant in the cooling of the warm and diffuse ISM to the cold and dense clouds (Dalgarno & McCray, 1972). This emission line is a tracer of all the different stages of evolution of the ISM and detailed characterisation of its emergence has been made for the Milky Way and local galaxies (e.g.

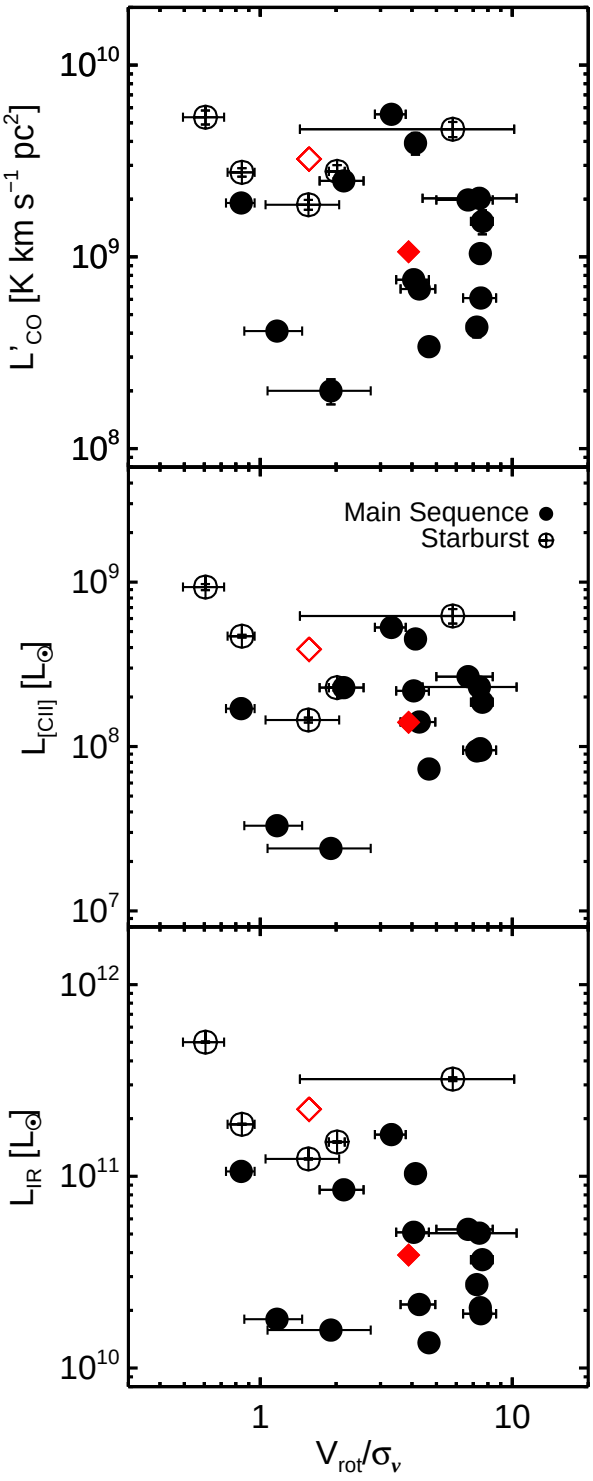

Figure 5.6: From *top* to *bottom*: CO(1-0), [C II] and IR luminosities as a function of the $V_{\rm rot}/\sigma_v$ ratio. I also classify the sources as 'starburst' or 'normal' star-forming galaxy. The red open and filled diamonds represent the mean value (in log-space) for the 'starburst' and 'normal' star-forming galaxies in each panel, respectively. Galaxies with low $V_{\rm rot}/\sigma_v$ ratio tend to show higher CO(1-0), [C II] and $L_{\rm IR}$ luminosities. The tentative anti-correlations may suggest a smooth transition between 'starburst' and 'normal' star-forming galaxies within the VALES sample.

Kramer et al. 2013; Pineda et al. 2013, 2014) suggesting that different ISM phases produce roughly comparable contributions to the [C II] luminosity (Madden et al., 1993). However, such detailed characterisations are impeded by observational limitations in distant galaxies which are typically detected in a single telescope beam. Thus, the [C II] line intensity is related to an average quantity that arises from a mix of the ISM phases (e.g. Gullberg et al. 2015, and references therein). Nevertheless, physical properties of the gaseous components of the ISM may be characterised by studying correlations between the [C II] emission with various galaxy properties (e.g. CO(1-0), $L_{\rm IR}$; Ibar et al. 2015; Hughes et al. 2017).

In the middle panel of Fig 5.6, I show the [C II] luminosity as a function of the $V_{\rm rot}/\sigma_v$ ratio for the galaxies in the sample. I measure a $\rho_{\rm Spearman} = -0.16$ with a probability of 50% that the correlation is produced by chance. The data do not support any trend between [C II] luminosity and the $V_{\rm rot}/\sigma_v$ ratio. I do not attempt to fit the data as I just have two galaxies measured [C II] luminosity at $L_{\rm [C\,II]} < 7\times10^7 L\odot$. I need more [CII] luminosity measurements, especially at $L_{\rm [C\,II]} < 7 \times 10^7 L\odot$, in order to discard or validate the possible trend between [CII] luminosity and $V_{\rm rot}/\sigma_v$. [CII] spatially resolved observations would be also useful in order to account for extended and/or nuclear emission effects (e.g. Díaz-Santos et al. 2013).

IR luminosity & the $L_{\rm [C\,II]}/L_{\rm IR}$ deficit

Infrared luminosities are commonly used as a tracer of the star formation activity in galaxies. It can be understood as the emitted UV radiation from young stars which is re-processed by dust. In the limit of complete obscuration, the re-emitted $L_{\rm IR}$ will effectively provide a bolometric measure of the SFR (Kennicutt, 1998a). However, if the attenuation of the stellar light is not completely re-processed, then the IR emission may underestimate the SFR. Applying SED fitting methods, the IR emission can be also used as a tracer of dust temperature ($T_{\rm dust}$) and mass ($M_{\rm dust}$; e.g. Draine et al. 2007; Ibar et al. 2015).

In the bottom panel of Fig 5.6, I show the $L_{\rm IR}$ compared to the $V_{\rm rot}/\sigma_v$ ratio for the sources. The data present an anti-correlation with $\rho_{\rm Spearman} = -0.44$ with a probability of 5% that the correlation is produced by chance. Sources with greater $L_{\rm IR}$ have lower $V_{\rm rot}/\sigma_v$ values, indicating that high IR-luminosities are likely to be present in systems where pressure support becomes comparable and even greater than rotational support. I note that $L_{\rm IR}$ show strong anti-correlation with the $V_{\rm rot}/\sigma_v$ ratio than the CO luminosity. This suggests that the $\rm L_{IR}/L'_{CO}$ ratio correlates with the $V_{\rm rot}/\sigma_v$ values. I will discuss this further in § 5.4.7.

The IR luminosity has also been traditionally compared to the [CII] luminosity (e.g Stacey et al. 1991). The [CII] luminosity to IR luminosity ratio ($L_{\rm [C\,II]}/L_{\rm IR}$) is found to be roughly constant for local star-forming galaxies with $L_{\rm IR} < 10^{11}\,L\odot$, but decreases at higher luminosities (e.g. Stacey et al. 1991; Malhotra et al. 1997). This is the so-called '[CII] deficit'. However, the intricate decomposition of the [CII] emission into the different ISM phases complicates the interpretation of this correlation (e.g. Ibar et al. 2015). Therefore, additional comparisons with other galactic properties are needed. Considering that the 'resolved' VALES sample covers the $10^{10-12}\,L\odot$ IR luminosity range, it is an ideal sample to study the '[CII] deficit' from a kinematic point of view.

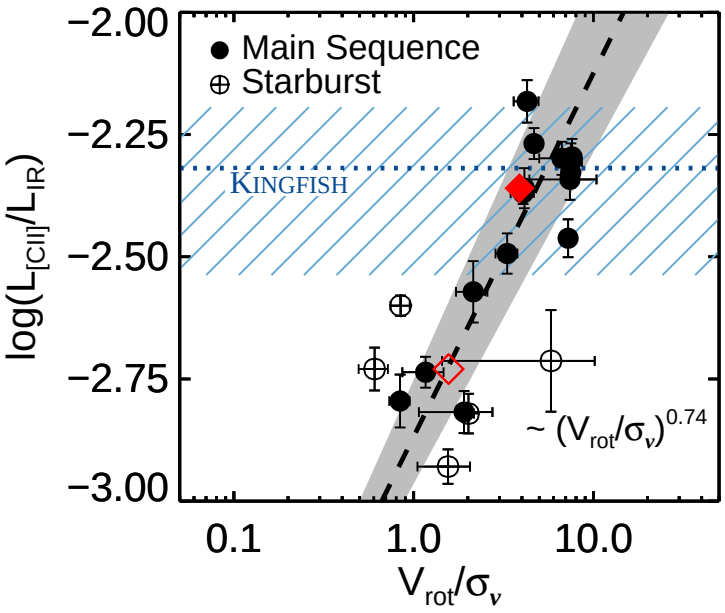

Figure 5.7: $L_{[\mathrm{C\,II}]}/L_{\mathrm{IR}}$ ratio as a function of the $V_{\mathrm{rot}}/\sigma_v$ ratio for the sample. I also classify the sources as 'starburst' or 'normal' star-forming galaxy. The dashed line represents the best power-law fit to the data and the grey-shaded area represents its 1-σ error. The best-fit slope is presented in the plot. The red open and filled diamond represent the mean value (in log-space) for the 'starburst' and 'normal' star-forming galaxies, respectively. The horizontal dotted blue line and the blue-dashed area represent the median $L_{[\mathrm{C\,II}]}/L_{\mathrm{IR}}$ ratio and its 1-σ region for the KINGFISH survey data regardless of the kinematics, respectively (Smith et al., 2017). I find an increase of the [C II]/IR ratio when the $V_{\mathrm{rot}}/\sigma_v$ ratio increases.

In Fig. 5.7, I show the $L_{[\mathrm{C\,II}]}/L_{\mathrm{IR}}$ as a function of the $V_{\mathrm{rot}}/\sigma_v$ ratio. I find that $L_{[\mathrm{C\,II}]}/L_{\mathrm{IR}}$ increases at high $V_{\mathrm{rot}}/\sigma_v$ ratios, but shows a significant scatter at low $V_{\mathrm{rot}}/\sigma_v$ values. This correlation has $\rho_{\mathrm{Spearman}} = 0.76$ with a probability of 0.0001% that the correlation is produced by chance. I note that this probability is significantly lower than the $L_{[\mathrm{C\,II}]} - V_{\mathrm{rot}}/\sigma_v$ and $L_{\mathrm{IR}} - V_{\mathrm{rot}}/\sigma_v$ Spearman correlation's probabilities. The data are well-represented by a power-law with best-fit slope of 0.74±0.14. Considering that a high $V_{\mathrm{rot}}/\sigma_v$ value suggests a host galaxy with a dominant disc geometry, then the finding is consistent with Ibar et al. (2015), who found that galaxies presenting a prominent disc show higher $L_{[\mathrm{C\,II}]}/L_{\mathrm{IR}}$ ratios than those that do not present disc-like morphologies.

In Fig. 5.7 ,I also compare the measured $L_{[\mathrm{C\,II}]}/L_{\mathrm{IR}}$ ratios with the values derived for the KINGFISH survey (Kennicutt et al., 2011)). These $L_{[\mathrm{C\,II}]}/L_{\mathrm{IR}}$ ratios are measured from over ∼15000 resolved regions within 54 nearby ($d \leq 30$ Mpc) galaxies (Smith et al., 2017) and I represent the median $L_{[\mathrm{C\,II}]}/L_{\mathrm{IR}}$ ratio of the sample and its 1-σ region with the dotted blue line and the blue dashed-area, respectively.

A sub-sample of eight galaxies from the KINGFISH survey have measured molecular gas dynamics from the HERACLES survey (Leroy et al., 2009; Mogotsi et al., 2016), and accurate rotation curves derived through H I observations from The H I Nearby Galaxy Survey (THINGS; Walter et al. 2008; de Blok et al. 2008). Those observations suggest $V_{\mathrm{rot}}/\sigma_v \gtrsim 10$

for this sub-sample. However, as I can not assume that this sub-sample is representative from the complete survey, I do not assume any constraint in the $V_{\rm rot}/\sigma_v$ ratio for the KINGFISH data.

I find that the VALES galaxies with $V_{\rm rot}/\sigma_v \gtrsim 3$ present similar $L_{[\rm C\,II]}/L_{\rm IR}$ ratios compared to the KINGFISH data. However, the VALES galaxies with $V_{\rm rot}/\sigma_v \lesssim 3$ tend to show even lower $L_{[\rm C\,II]}/L_{\rm IR}$ values. This is independent whether the galaxy was classified as 'normal' star-forming galaxy or 'starburst'.

I note that the sample is not significantly contaminated by AGNs (V17) and the [CII] emission is likely to be optically thin ($\tau_{[\rm C\,II]} \sim 0.1$) within the galaxies of the sample as based on photodissociation region (PDR) modelling (Hughes et al., 2017), suggesting that these two possible effects are not substantially affecting the trend observed in Fig. 5.7. As the $L_{[\rm C\,II]}/L'_{\rm CO}$ ratio seems to be constant for the VALES galaxies (Hughes et al., 2017), another possibility is that the [CII] deficit may just reflect the $L'_{\rm CO}/L_{\rm IR}$ variation within the galaxy sample. However, we note that this may not to be the case as the $L'_{\rm CO}/L_{\rm IR}$ ratio is nearly constant for the VALES galaxies with detected CO emission (see Fig. 5 in V17).

5.4.3 PDR modelling & molecular gas kinematics

PDR modelling has been traditionally used to derive the physical properties of the gaseous components of the ISM (e.g. Tielens & Hollenbach 1985). Although each PDR code has its own unique model setup and output, it usually determines the physical parameters by solving chemical and energy balance while also solving the respective radiative transfer equations (Röllig et al., 2007).

For the VALES survey, Hughes et al. (2017) applied the PDR model of Kaufman et al. (1999, 2006), which is an updated version of the PDR model of Tielens & Hollenbach (1985). The model treats PDR regions as homogeneous infinite plane slabs of hydrogen with physical conditions characterised by the hydrogen nuclei density (n_H) and the strength of the incident FUV radiation field, G_0, which is normalised to the Habing Field (Habing, 1968). The model covers a density range of $10 < n_H < 10^7\,{\rm cm}^{-3}$ and FUV radiation field strength range of $10^{0.5} < G_0 < 10^{6.5}$. In this model, the gas is assumed to be collisionally heated via the ejection of photoelectrons from dust grains and polycyclic aromatic hydrocarbon (PAH) molecules by FUV photons, and gas cooling from line emission is predicted by simultaneously solving the chemical and energy equilibrium in the slab.

Hughes et al. (2017) assumed that the galactic emission comes from a single PDR. They compared the predicted $L_{[\rm C\,II]}/L_{\rm IR}$ and $L'_{\rm CO}/L_{\rm IR}$ luminosity ratios with the observed quantities. However, since the fragment of the [C II] emission produced in PDRs with respect to the total galactic emission is observed to vary between 0.5–0.7 (e.g. Stacey et al. 1991; Malhotra et al. 2001; Oberst et al. 2006; Stacey et al. 2010), they also consider two additional models in which they adjust the parameters to match to the 50% and 70% values of the total [C II] luminosity for each galaxy. In these two models, they also consider the missing CO(1-0) flux emitted along different line-of-sight by multiplying their observed CO(1-0) emission by a factor of two (see Hughes et al. 2017 for more details). Although these assumptions can modify

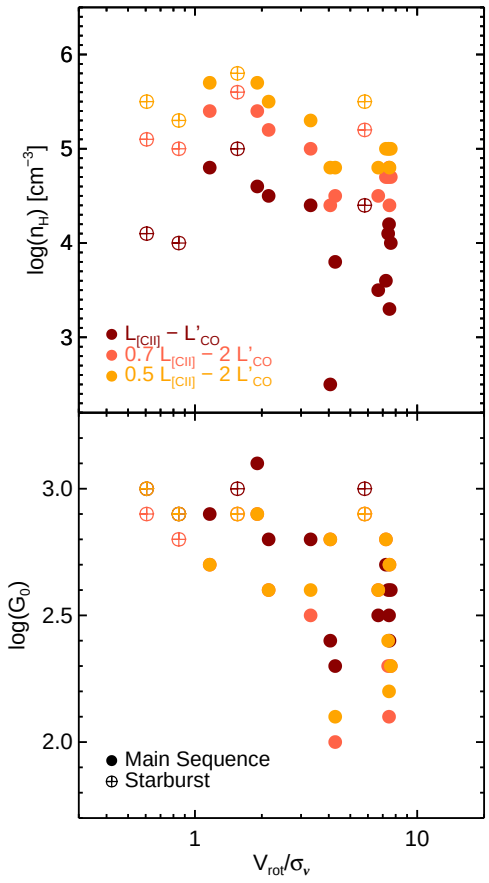

Figure 5.8: Hydrogen nuclei density (n_H, *top*) and incident FUV radiation strength (G_0, *bottom*) as a function of $V_{\rm rot}/\sigma_v$ ratio for the sample. I colour-code the data depending on the [C II] and CO(1-0) luminosities used to constrain the physical parameters through the PDR modelling (see § 5.4.3 for more details). I also classify the sources as 'starburst' or 'normal' star-forming galaxy. Regardless of the PDR model, galaxies with low $V_{\rm rot}/\sigma_v$ ratio tend to show higher hydrogen nuclei density and G_0 values. I note that G_0 seems to be insensitive to the [C II] and CO(1-0) luminosities assumed to constrain the PDR model within the sample.

the values of the derived PDR parameters, in the remaining analysis, I will only consider the possible trends seen between n_H and G_0 with respect to the molecular gas kinematics regardless the absolute value for each quantity in each model.

In Fig. 5.8, I compare n_H and G_0 as a function of the $V_{\rm rot}/\sigma_v$ ratio for each model within the sample. I do not consider the galaxies with $n_H \lesssim 10^2\,{\rm cm}^{-3}$ due to the high degeneracy of the model parameters (Hughes et al., 2017). In the top panel, I see how the hydrogen nuclei density may increase at low $V_{\rm rot}/\sigma_v$ for each PDR modelling. This is consistent with the picture in which higher density environments usually show higher velocity dispersions (Papadopoulos et al., 2012). In the bottom panel, the incident FUV radiation strength also increases at low $V_{\rm rot}/\sigma_v$ for each PDR modelling. G_0 seems to be nearly independent of the assumed [C II] and CO(1-0) luminosities to constrain the PDR model, the variation of G_0 across the sample may reflect the variation of SFR through the IR-luminosity. Therefore, the trend between G_0 and $V_{\rm rot}/\sigma_v$ may reflect the $L_{\rm IR} - V_{\rm rot}/\sigma_v$ correlation (§ 5.4.2).

If systems with high G_0 – i.e. high SFR (or $L_{\rm IR}$) and low $V_{\rm rot}/\sigma_v$ – have ionized most of their atomic carbon content within the PDRs, then this should result in an inefficient gas cooling through the [C II] emission line and a lack of the observed [C II] luminosity compared to the IR luminosity. This may explain the '[C II] deficit' correlation with galactic dynamics found in § 5.4.2.

5.4.4 Dynamical Masses of Turbulent Thick Galactic Discs

The dynamical mass estimate ($M_{\rm dyn}$) is a major tool that allows to measure the mass of galaxies, and a simple way to probe the existence of dark matter haloes (e.g. Gnerucci et al. 2011). By considering galaxies as thin discs, in which all the material is supported by rotation [$M_{\rm dyn,thin}(r) = \frac{V^2_{\rm rot}(r)r}{G}$], the dynamical mass can be easily derived from the two-dimensional kinematic modelling (e.g. Genzel et al. 2011). However, galaxies with low $V_{\rm rot}/\sigma_v$ ratio are believed to be well-represented by galactic thick discs (e.g. Glazebrook 2013). In those galaxies, a considerable pressure gradient support is needed to be taken into account in order to calculate reliable dynamical mass estimates (Burkert et al., 2010).

In order to test whether the galaxies in the sample are better represented by galactic thick discs rather than thin discs, I calculate their dynamical masses and compare with their stellar masses (Table 5.2). Following Burkert et al. (2010), I model the galaxies as turbulent galactic gas discs in which pressure gradient support cannot be neglected. In this model, the *observable* rotational velocity is given by:

$$V^2_{\rm rot} = V^2_0 + 2\sigma^2_v \frac{{\rm d}\ln\Sigma}{{\rm d}\ln r}, \tag{5.1}$$

where V_0 is the zero-pressure velocity curve ($V^2_0 \equiv r \times {\rm d}\Phi/{\rm d}r$), which traces the gravitational potential of the galaxy; σ_v is the one-dimensional velocity dispersion of the gas, and Σ is the total mass surface density profile of the galaxy. In order to derive an explicit model from of Eq. 5.1, I need to make some assumptions about the total mass surface density distribution $\Sigma(r)$. Assuming both, that Σ follows the stellar mass surface density profile ($\Sigma_\star$) and a constant $K-$band mass-to-light ratio across the galactic disc (Υ_K), then Σ can be approximated by the K-band surface brightness distribution (μ_K), i.e., $\Sigma(r) \approx \Sigma_\star(r) \approx \Upsilon_K \mu_K(r)$. Considering that μ_K is well-described by a Sérsic profile (Sérsic, 1963), Eq. 5.1 can be written as:

$$V^2_{\rm rot} = V^2_0 - \frac{2\sigma^2_v b_{n_S}}{n_S}\left(\frac{r}{r_{\rm e}}\right)^{1/n_S}, \tag{5.2}$$

where n_S is the Sérsic index and b_{n_S} is the Sérsic coefficient, which sets $r_{\rm e}$ as the half-light radius. I note that the case $n_S = 1$ is equivalent to an exponential profile. In this model, the dynamical mass is traced by V^2_0 rather than $V^2_{\rm rot}$:

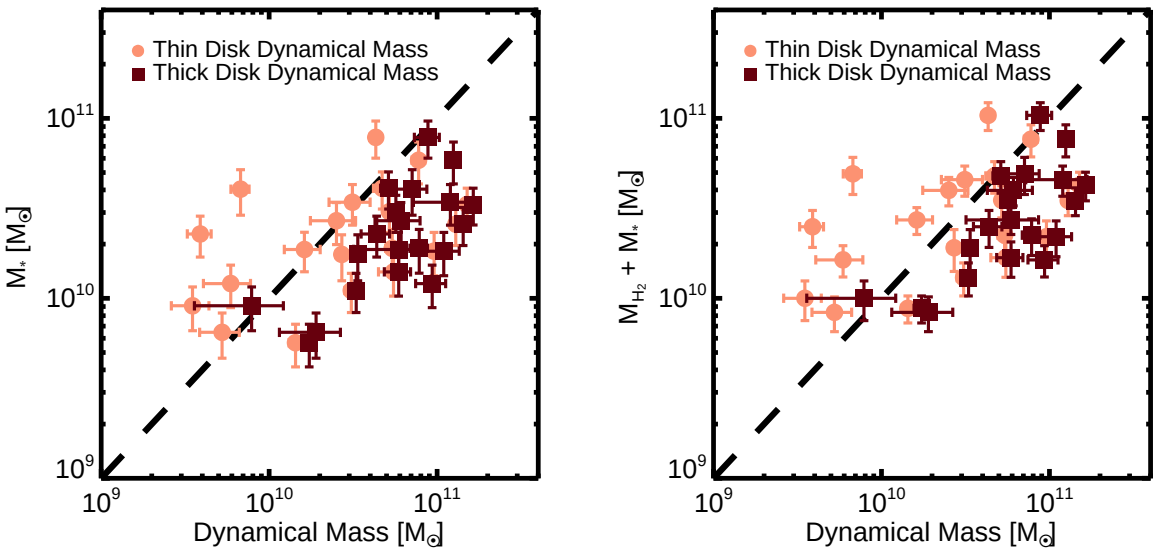

Figure 5.9: *Left:* Encircled stellar masses at the radii at which $V_{\rm rot}$ is extracted ($2\,r_{1/2,\rm CO}$) as a function of the dynamical masses encircled at the same radius. The light-red circles show the dynamical masses assuming a thin disc model, i.e. the total mass is traced just by the observed rotational velocity. The dark red squares show the dynamical masses assuming a thick disc model in which the surface density profile of each galaxy is traced by the $K-$band surface brightness also assuming a constant mass-to-light ratio. The encircled stellar mass content is calculated by considering the μ_K profile (see Eq. 5.4). The dashed line corresponds to the 1:1 ratio. *Right:* Molecular gas mass plus encircled stellar mass as a function of the dynamical masses encircled at the same radius. This panel is colour-coded as the same as left panel. I clearly see how the thin disc approximation fails to estimate the total mass in five systems as their truncated stellar masses have greater values, a trend that seems exacerbated up to nine galaxies when I also consider their molecular gas content.

$$M_{\rm dyn,thick}(r) = \frac{V_0^2(r) r}{G}. \tag{5.3}$$

I note that the $K-$band Sérsic model parameters for the resolved sample are listed in Table 5.1 for each galaxy. For the galaxy without $K-$band modelling, I assume an exponential $\Sigma_\star$ profile.

In Fig. 5.9, I show the dynamical masses calculated by assuming a thin disc model and a thick disc model (Eq. 5.3) within $r \leq 2r_{1/2,\rm CO}$. I note that, I have considered the radius at which I extracted $V_{\rm rot}$. I compare these dynamical masses with the stellar masses truncated at the same radius and normalized to the stellar mass values derived in V17 (Table 5.2):

$$M_\star(r) \equiv M_\star \frac{\int_{S(<r)} \Sigma_\star(r) {\rm d}S}{\int_S \Sigma_\star(r) {\rm d}S} \approx M_\star \frac{\int_0^r \mu_K(r) r {\rm d}r}{\int_0^\infty \mu_K(r) r {\rm d}r}. \tag{5.4}$$

The dashed line in Fig. 5.9 represents the 1:1 ratio between both quantities. Clearly, the thin disc dynamical mass model underestimates the total mass for five of the systems, as it predicts masses lower than the encircled stellar masses. On the other hand, the thick disc dynamical mass model estimates masses greater than the stellar masses, with just one target showing encircled stellar mass nearly equal to their estimated dynamical mass within 1-σ error. This suggests that these five VALES galaxies with lower $V_{\rm rot}/\sigma_v$ ratio may be better represented by thick galactic disc, while the rest of the sample is best described by thin galactic disc.

This trend is exacerbated when I add the molecular gas mass content measured for the VALES galaxies. Up to nine galaxies show greater gas plus stellar mass content than the estimated thin-disc dynamical mass, but again, this problem alleviates when thick-disc dynamical modelling is considered. The mass gap between the thick-disc dynamical masses and the mass traced by light suggests that VALES galaxies have considerable amount of dark matter. However, it should be noted that the estimation of dark matter masses by using this method are highly sensitive to the chosen CO-to-H_2 conversion factor (see Chapter 4). I note that the existence of gaseous thick discs at the observed redshift range may indicate a late assembly of the thick disc stellar component in those systems (Bournaud et al., 2009).

The validity of this result depends on the assumption that the $K-$band surface brightness traces $\Sigma_\star$ by considering a mass-to-light ratio which does not vary as a function of galactocentric radius. I explore the effect produced by a different mass distribution in Appendix 5.6.2, where I show that it has a negligible effect when considering, for example, an exponential disc mass profile. I conclude that the considerable pressure gradient support predicted by the high velocity dispersion values is a key ingredient to obtain reliable conclusions from the modelling. This may be especially important in the systems which present the highest gas fractions (see § 5.4.6).

I caution, however, that spatial resolutions effects may produce an overestimation or underestimation of the dynamical mass values derived from the thin and thick disc models. The $V_{\rm rot}$ values can be underestimated by beam-smearing, especially in cases when the rotation curve beyond the turn-over radius is not observed (e.g. HATLASJ084217.7+021222). On the other hand, overestimated $r_{1/2,\rm CO}$ and σ_v values are expected to be calculated due to the same effect. The result of the competition between both effects is uncertain.

5.4.5 Gravitationally stable discs

Gravitational stability analysis is usually used to explain the formation and growth of internal galactic sub-structures at low- (e.g. Lowe et al. 1994) and high-redshift (Swinbank et al., 2012a; Wisnioski et al., 2012), between other major topics (e.g. Kennicutt 1998b). In thin galactic discs, one of the first studies was done by Toomre (1964), who derived a simple gravitational stability criterion that can be quantified through the parameter:

$$Q_{\rm Toomre} \equiv \frac{\kappa \sigma_v}{\pi G \Sigma_{\rm gas}}, \tag{5.5}$$

where, $\kappa \equiv (2\Omega/r)\,\mathrm{d}(r^2\Omega)/\mathrm{d}r = av_c/r$ is the epicyclic frequency, usually expressed as a function of orbital frequency (Ω) or the circular velocity v_c at some radius r with $a = \sqrt{2}$ for a flat rotational curve; σ_v is the measure of the random motions of the gas; $\Sigma_{\rm gas}$ is the gas surface density; and G is the gravitational constant. If $Q_{\rm Toomre} < 1$, then the system is prone to develop local gravitational instabilities. Otherwise, the system is not susceptible to local gravitational collapse ($Q_{\rm Toomre} > 1$).

Since the Toomre (1964)'s earlier work, the $Q_{\rm Toomre}$ parameter has been generalized to include different physical effects such as galactic disc thickness ($Q_{\rm thick}$, e.g. Goldreich & Lynden-Bell 1965; Romeo 1992) and/or multiple galactic components (Q_M, e.g. Jog & Solomon 1984; Jog 1996; Rafikov 2001; Romeo & Wiegert 2011):

$$Q_{\rm thick} = TQ_{\rm Toomre}, \tag{5.6}$$

$$\frac{1}{Q_M} = \sum_{k=1}^{M} \frac{W_k}{Q_{{\rm Toomre},k}}, \tag{5.7}$$

where, T represents the stabilizing effect of the disc thickness, and ranges between 1–1.5 depending on the velocity dispersion anisotropy ($\sigma_{v,z}/\sigma_{v,R}$; Romeo & Wiegert 2011). $Q_{{\rm Toomre},k}$ is the Toomre parameter of the galactic component k, M is the total number of different galactic components considered in the analysis, and W_k is a weighting factor that is higher for the component with smallest $Q_{\rm Toomre}$ value (see Romeo & Falstad 2013 for more details). Other physical effects such as gas dissipation (e.g. Elmegreen 2011), and supersonically turbulence (e.g. Romeo et al. 2010) can be included to derive other generalized Q parameters, however they require assumptions on how the gas dissipates energy across different scales and its beyond the scope of this work test those assumptions. Thus, in order to maintain simplicity, I just test the $Q_{\rm Toomre}$, $Q_{\rm thick}$ and the Q_M stability parameters and for the Q_M parameter, I just consider the stellar and molecular gas galactic components ($M = 2$).

In order to proceed further, by assuming that; (1) the system is supported by rotation; (2) the galactic mass budget is dominated by the gas and stars at the radii in which $V_{\rm rot}$ is derived; and (3) the gas within that radii is principally in the form of molecular gas; then the $Q_{\rm Toomre}$ (hereafter, $Q_{\rm gas}$) can be rewritten as a function of the molecular gas kinematics and the molecular gas fraction (Genzel et al., 2011):

$$Q_{\rm gas} \approx \sqrt{2}\frac{\sigma_v}{v_c} f_{\rm H_2}^{-1}. \tag{5.8}$$

By following an analogous procedure, I find similar formulas for the $Q_{\rm thick}$ and Q_M (hereafter, Q_2) parameters:

$$Q_{\rm thick} \approx T\sqrt{2}\frac{\sigma_v}{v_c} f_{\rm H_2}^{-1}, \tag{5.9}$$

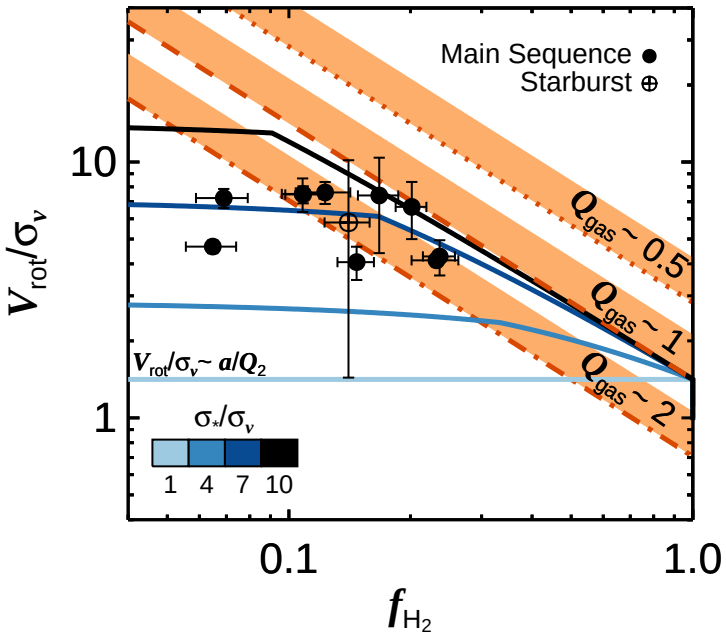

Figure 5.10: $V_{\rm rot}/\sigma_v$ as a function of the molecular gas fraction. The $f_{\rm H_2}$ values are calculated from the $M_{\rm H_2}$ and $M_\star$ estimates for each galaxy. The orange dotted-dashed, dashed and dotted lines represent the Toomre (1964)'s $Q_{\rm gas}$ values of 2, 1 and 0.5 for thin disc galaxies, respectively. The orange-shaded areas represent the possible $Q_{\rm thick}$ values given the mentioned $Q_{\rm gas}$ values. The black, dark-blue, blue and light-blue lines shows the $Q_2 = 1$ values for different σ_*/σ_v ratios listed in the colour-bar. I also classify the sources as 'starburst' or 'normal' star-forming galaxy.

$$Q_2 \approx \begin{cases} \sqrt{2}\frac{\sigma_v}{v_c}[f_{\rm H_2} + \frac{2}{1+s^2}(1-f_{\rm H_2})]^{-1} & \text{if } s > \frac{1}{f_{\rm H_2}} - 1; \\ \sqrt{2}\frac{\sigma_v}{v_c}[\frac{2s}{1+s^2} f_{\rm H_2} + \frac{1}{s}(1-f_{\rm H_2})]^{-1} & \text{otherwise,} \end{cases} \tag{5.10}$$

where 's' is the stellar to molecular gas velocity dispersion ratio ($s \equiv \sigma_*/\sigma_v \geq 1$) and the conditioning represents the $Q_{\rm stars} > Q_{\rm gas}$ requirement (see Romeo & Falstad 2013, for more details).

In order to fulfil assumption (1), I choose $M_{\rm dyn,thin}/M_{\rm dyn,thick} > 0.5$ as a somewhat crude criterion to select galaxies that are mainly supported by rotation. Regardless of the density profile of the galaxies, this criterion can be traduced into a threshold to the measured $V_{\rm rot}/\sigma_v$ ratio ($V_{\rm rot}/\sigma_v \gtrsim 2$ in the case). Thus, within the resolved sample, I just find eleven galaxies consistent with being rotationally supported.

In Fig. 5.10, I show $f_{\rm H_2}$ as a function of $V_{\rm rot}/\sigma_v$ for the rotationally supported galaxies in the sample. The orange dot-dashed, dashed and dotted lines represent the $Q_{\rm gas} = 2$, 1, 0.5 values, respectively. Three galaxies are consistent with $Q_{\rm gas} \sim 1$ (within 1-σ range), whilst eight galaxies have $Q_{\rm gas} \gtrsim 2$. The majority of the rotationally supported systems seems to be gravitationally unstable within the thin disc single component approximation. Although the poor spatial resolution of the observations smooth the CO intensity maps, I note that

the unique source that shows some degree of clumpiness in its CO intensity map (HATLASJ085340.7+013348) is consistent with being susceptible to gravitational instabilities.

The next step is to include the disc thickness effect in the analysis. In order to do that, I use Eq. 5.6 to compute $Q_{\rm thick}$ from the $Q_{\rm gas}$ = 2, 1, 0.5 values. As I do not have velocity dispersion anisotropy estimates for the sample to determine the T factor, I assume T values between the limit ranges ($1 \leq T \leq 1.5$; Romeo & Wiegert 2011) and I present the possible $Q_{\rm thick}$ values as the orange-shaded areas in Fig. 5.10. From the sample, is clearly that I can not differentiate the disc thickness effect as the $V_{\rm rot}/\sigma_v$ ratios are not enough accurate.

As a final step, I consider a two-component gravitational stability analysis in which the main components are the molecular gas and the stars. I note that the two-component system is more unstable than either component in the system by itself (Jog, 1996). However, in order to use the two-component gravitational stability criterion (Q_2), I must measure σ_*, the velocity dispersion of the stars, or in equivalence the σ_*/σ_v ratio.

As I lack of that information for the rotationally supported galaxies, I just assume four different values of σ_*/σ_v between the range indicated in the colour-bar in Fig. 5.10. I note that $\sigma_*/\sigma_v = 1$ is the minimum value that can be assumed within this model (see Romeo & Falstad 2013 for more details). On the other hand, a maximum range value of $\sigma_*/\sigma_v = 10$ may be appropriate for local spiral galaxies. For example, the expected value for the Milky Way is in the range of $4 < \sigma_*^{\rm MW}/\sigma_v^{\rm MW} < 8$, whether I consider the stellar velocity dispersion of the thin or thick disc as the representative $\sigma_*^{\rm MW}$ value (Glazebrook, 2013). In the remaining of this analysis I kept fixed Q_2 to the unity value.

At high σ_*/σ_v ratio, the molecular gas component is more susceptible to gravitational instabilities than stars, and therefore, the gravitational stability of the system is dictated by the gaseous component alone ($Q_2 \approx Q_{\rm gas}$) at least if $f_{\rm H_2}$ is not low enough. The latter case implies $Q_2 \approx Q_{\rm stars}$. In Fig. 5.10, the $Q_2 \approx Q_{\rm gas}$ case is better represented by the black line, which approach to the orange-dashed line ($Q_{\rm gas} = 1$) at $f_{\rm H_2} \gtrsim 0.1$. For molecular gas fractions below that value, the gravitational stability of the system is dictated mainly by the stellar component from which I do not have any information. I also note that when the σ_*/σ_v ratio decreases, Q_2 approximates to $Q_{\rm gas}$ at higher $f_{\rm H_2}$ values as the gravitational effect of the stellar component becomes more significant.

At $\sigma_*/\sigma_v \sim 1$, from Eq. 5.10, I can see that the Q_2 parameter does not depends on $f_{\rm H_2}$. In this limit, the two-component system behave as a single component fluid in which the gravitational criterion is dictated by the total surface density of the system. In Fig. 5.10 it is better represented by the light-blue line. In this limit, the Q_2 value can be recovered by measuring the kinematics of the galaxy and the shape of the rotation curve (accounted by the factor a) at a given radii. Nevertheless, if the dark matter component is not negligible, i.e. assumption (2) is incorrect, then an additional baryonic mass fraction needs to be accounted.

Within two-fluid component framework, two of the rotationally supported galaxies are consistent with being gravitational unstable systems (within 1-σ range). The seven galaxies with the lower $f_{\rm H_2}$ values are likely to be in the $Q_2 \approx Q_{\rm stars}$ regime. Thus, I can not determine if these systems are gravitationally stable or not. I also note that the remaining galaxies can be consistent with being gravitationally unstable or not depending on its σ_* value.

Therefore, from the gravitational stability analysis, I conclude that two galaxies are consistent with being marginally gravitationally unstable disc, but observations of the stellar dynamics are required to determine the gravitational stability for the remaining nine cases.

This result disagrees with White et al. (2017) who found a $Q_{\rm gas} \sim 1$ trend (but with considerable scatter) in their sample of local star-forming galaxies taken from the DYNAMO survey ($z \sim 0.06 - 0.08$ & $z \sim 0.12 - 0.16$). They found this trend by fitting the Eq. 5.8 (their Eq. 10) to their sample, but by considering ionized gas kinematics instead molecular gas kinematics. This disagreement may be produced by two reasons: (1) the no consideration of galactic thickness and/or the stellar component in the Q parameter analysis done by White et al. (2017); and (2) the non quantification of the scatter which may imply that they can not determine accurately the $Q_{\rm gas}$ values (at least in the $Q_{\rm gas} = 1 - 2$ range).

I note that the conservative choice of $\alpha_{\rm CO}$ values (see § 5.2.2) tends to overestimate the molecular gas reservoir for most of the galaxies within the sample. Using a lower CO-to-H_2 conversion factor would imply greater $Q_{\rm gas}$, $Q_{\rm thick}$ and Q_2 values in these galaxies. Nevertheless, I have analysed the galaxies in which the assumption (1) is likely to be correct, however I can not determine if assumptions (2) and (3) are correct. I stress that HI observations are required in order to test assumptions (2) and (3).

5.4.6 Energy sources of turbulent motions

The origin of the energy sources of the random motions in galactic discs are unclear, low- and high-redshift galaxy observations show a positive correlation between the ionized gas turbulence with the measured $\Sigma_{\rm SFR}$, with larger scatter at high-redshift (e.g. Lehnert et al. 2009; Johnson et al. 2017; Zhou et al. 2017). These observations favour a models in which stellar feedback is driving those random motions. However, observations also suggest that other energy sources may contribute to produce turbulence in the ISM (Zhou et al., 2017).

From a theoretical perspective, two possible scenarios have been proposed. In the first scenario, the star-formation is determined by the requirement to maintain hydrostatic balance through the input of energy from supernovae feedback. In this model, stars are produced efficiently by the gravitational collapse of gas within GMCs and the GMCs are treated as bound entities that are hydrodynamically decoupled from the galactic disc (Faucher-Giguère et al., 2013). Therefore, the production of stars is limited by the formation of GMCs and this process is driven by the self-gravity of the gas, and not by a combination of the gravitational potential of gas and stars from the galactic disc. Thus, in the feedback-driven model, it is expected that SFR$\propto \sigma_v^2$.

In the second scenario, the turbulence is expected to be driven by the release of gravitational energy of the gas which is accreted through the disc (Krumholz & Burkhart, 2016). The accretion of the gas is ultimately powered by gravitational instabilities through the galactic disc that are regulated by the gravitational potential of stars and gas. This model also assumes a star formation law in which the star formation rate per molecular gas mass is represented by $\varepsilon_{\rm ff}/t_{\rm ff}$, the efficiency per free-fall time ($\varepsilon_{\rm ff} \approx 0.01$, e.g. Krumholz & Tan 2007; Krumholz et al. 2012). The $t_{\rm ff}$ is estimated by assuming that the star-forming gas

density is set by the total gravitational potential of the ISM, rather than by the properties of hydrodynamically decoupled GMCs (Krumholz et al., 2012). In this gravity-driven model, the SFR vary as SFR$\propto \sigma_v f_{\rm gas}^2$, where $f_{\rm gas}$ is the mid-plane galactic gas fraction.

With the aim to test both models, in the top and bottom panels of Fig 5.11, I show $f_{\rm H_2}$ and σ_v as a function of the SFR, for the VALES survey and the EDGE-CALIFA survey (Bolatto et al., 2017). The VALES data are colour-coded in each panel by the velocity dispersion and the molecular gas fraction, respectively. The EDGE-CALIFA data are represented by the dark-grey triangles. The EDGE-CALIFA data were modelled using the same procedure described for the VALES data (see § 5.6.3 for more details). In top panel, I also show the median $f_{\rm H_2}$ and SFR values per $\log_{10}(f_{\rm H_2})= 0.4$ bin combining the data from both surveys. The median values suggest that the SFR is weakly correlated with $f_{\rm H_2}$. Systems with high molecular gas fraction may tend to have high SFR, although the scatter is considerable. On the other hand, in the bottom panel, I observe that systems with high SFRs also tend to present high σ_v values. I note that, I do not find any correlation between inclination angles and velocity dispersions within Fig 5.11.

I represent the best-fitted gravity-driven and feedback-driven models by the dashed and dotted lines in Fig. 5.11, respectively. The gravity-driven model gives a poor description to the data. At high molecular gas fractions ($f_{\rm H_2} \gtrsim 0.1$), galaxies tend to present a large variety of SFRs than the predicted by this model. This suggests that the release of the gravitational energy from the molecular gas may not be the main source of energy that support the σ_v values observed in the VALES and EDGE-CALIFA surveys. The feedback-driven model may also not explain the loci of the galaxies in the SFR$-f_{\rm H_2}-\sigma_v$ phase space as it tends to overestimate the σ_v values for most of the systems with SFR$\gtrsim 2\,M_\odot\,{\rm yr}^{-1}$. The distribution of the VALES and EDGE-CALIFA galaxies in Fig. 5.11 suggest that different energy sources may sustain the observed supersonic turbulence.

I stress that the scatter behind Fig. 5.11 might be induced by a handful of effects, including the bimodal CO-to-H_2 conversion factor (see § 5.2.1) used to calculate the molecular gas masses and, therefore, the molecular gas fractions. On the other hand, poor spatial resolution could potentially bias σ_v towards higher values. It may contribute to the high velocity dispersion values seen in the VALES galaxies with higher SFRs. Spatial resolution effects may favour models which accounts for a higher dependence of the SFR with σ_v.

Despite of the weakness of the median trend observed between SFR and $f_{\rm H_2}$, I note that this result is in contradiction with Green et al. (2010) results. They found that velocity dispersion values measured from a sample of 65 star-forming galaxies at $z \sim 0.1$ seems to be correlated with their SFRs but not with the gas fraction. However, as a difference with this work, they estimated the velocity dispersion values from the ionized gas kinematics traced by the Hα emission line, whist I measure the molecular gas kinematics. Moreover, Green et al. (2010) calculated the gas mass content for their sample by converting the measured $\Sigma_{\rm SFR}$ through the application of the KS law, this assumes that the molecular and ionized gas are spatially correlated, but also that the galaxies in their sample follow the KS law, which is not straightforward to assume (see § 5.4.7). On the other hand, I measure the molecular gas content from the CO line emission by applying the CO-to-H_2 conversion factor.

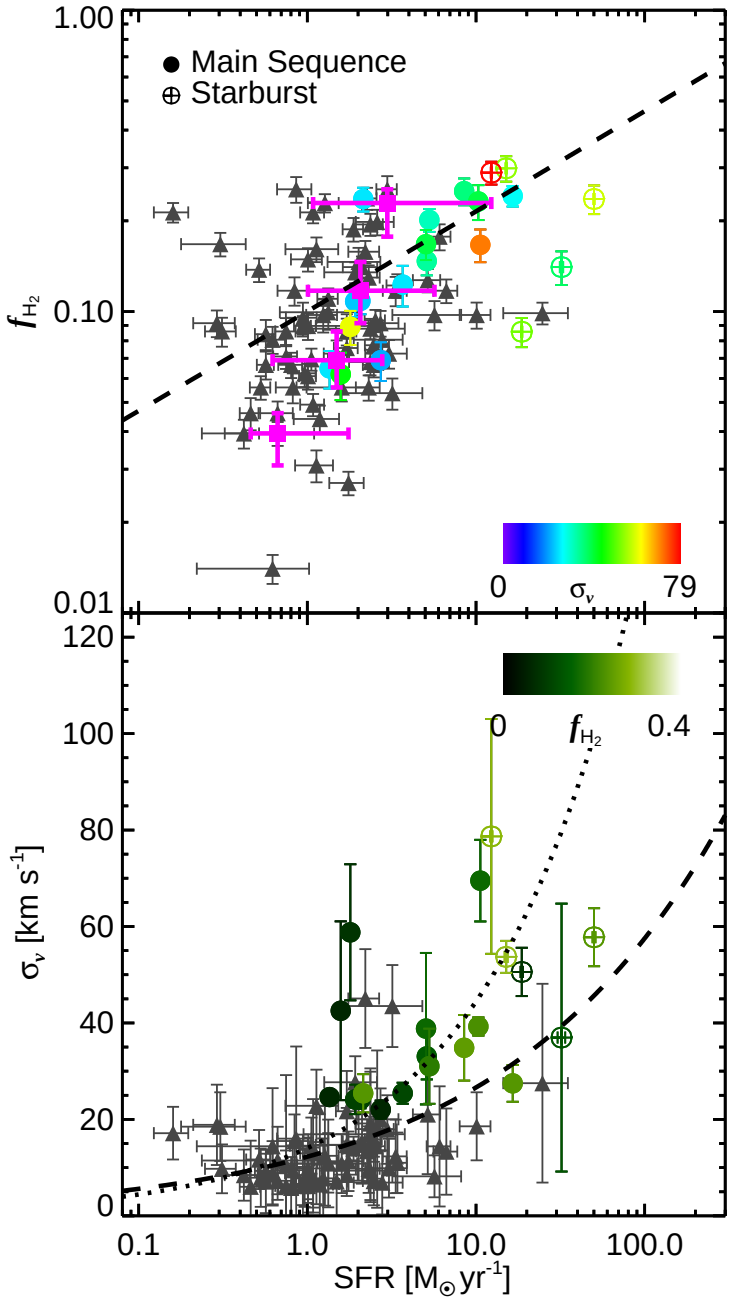

Figure 5.11: *Top:* Molecular gas fraction as a function of SFR, colour-coded by velocity dispersion value. *Bottom:* Velocity dispersion as a function of SFR and colour-coded by the observed molecular gas fraction. In both panels the VALES galaxies are classified as 'normal' (filled circles) and 'starburst' (circles with plus sign) star-forming galaxies. The dark grey triangles represent the galaxies from the EDGE-CALIFA survey (Bolatto et al., 2017). In the top panel, the magenta squares represent the median f_{H_2} and SFR values per $\log_{10}(f_{H_2})$= 0.4 bin. The dashed line represents the best-fitted gravity-driven model (SFR$\propto \sigma_v f_{gas}^2$) for the VALES galaxies; Krumholz & Burkhart 2016), assuming $f_{gas} \approx f_{H_2}$. The dotted line in the bottom panel represents the best-fitted feedback-driven model for the VALES galaxies (SFR$\propto \sigma_v^2$; Faucher-Giguère et al. 2013).

A possible selection bias may also explain the discrepancy with Green et al. (2010)'s results. The VALES galaxies are selected by a applying IR-luminosity threshold, i.e., they are likely to be dusty redder systems. As a difference, Green et al. (2010) select their galaxy sample from the SDSS survey based on the optical light properties, i.e., they are choosing bluer star-forming systems. This may imply that Green et al. (2010)'s criterion favour the selection of interacting systems compared to VALES as galaxy mergers tend present bluer colours than the underlying galaxy population (Kampczyk et al., 2007). Galaxy interactions increase the star formation activity of the systems, but also the ISM turbulence, hence the velocity dispersions, favouring the correlation between SFR and σ_v but probably erasing any trend with respect to $f_{\rm H_2}$. Nevertheless, I stress that spatially-resolved observations of gas-rich systems ($f_{\rm H_2} \gtrsim 0.3$) are needed to test possible trends between SFR and $f_{\rm H_2}$.

It should be mentioned that the model developed by Krumholz & Burkhart (2016) relates the SFR with the mid-plane galactic gas fraction and its velocity dispersion rather than the molecular gas fraction and the molecular gas velocity dispersion which are shown in Fig 5.11. I note that it is not straightforward to expect that those quantities are related between each other. The model also assumes that the stellar velocity dispersion should be comparable with the velocity dispersion of the gas. Taking into account these caveats, in order to produce a more complete observational test, atomic gas (HI) and stellar kinematic observations are needed.

5.4.7 Kennicutt-Schmidt Law Efficiency & Depletion Times

The Kennicutt-Schmidt law (Kennicutt, 1998a,b) describes the power-law relationship between the galaxy star formation rate surface density and the disc-averaged total gas surface density. It describes how efficiently galaxies turn their gas into stars. For local galaxies, this correlation is well-fitted by $\Sigma_{\rm SFR} \propto \Sigma_{\rm gas}^{1.4}$ (Kennicutt, 1998b). Although a tight relation can be found when $\Sigma_{\rm SFR}$ is compared with the molecular gas surface density $\Sigma_{\rm H_2}$ rather than $\Sigma_{\rm gas}$ (e.g. Bigiel et al. 2008; Leroy et al. 2008, 2013), also the slope is changed ($\Sigma_{\rm SFR} \propto \Sigma_{\rm H_2}$).

However, the KS law shows an apparent bimodal behaviour where 'discs' and 'starburst' galaxies fill the $\Sigma_{\rm H_2} - \Sigma_{\rm SFR}$ plane in two parallel sequences (Daddi et al., 2010). Nevertheless, by computing $\Sigma_{\rm H_2}/t_{\rm ff}$ and/or $\Sigma_{\rm H_2}/t_{\rm orb}$ relationships, a single power-law relation can be obtained (e.g. Daddi et al. 2010; Krumholz et al. 2012). The $\Sigma_{\rm SFR} - \Sigma_{\rm H_2}/t_{\rm ff}$ relation can be interpreted as dependence of the star formation law on the local volume density of the gas, whilst the $\Sigma_{\rm SFR} - \Sigma_{\rm H_2}/t_{\rm orb}$ relation suggests that the star formation law is affected by the global rotation of the galaxy. Thus, the relevant timescale gives critical information about the physical processes that may control the formation of stars.

As I consider just galaxies where their CO luminosity is spatially resolved (see 5.2.1), I do not have any information of the spatial extent of the IR luminosity, i.e. the SFR. Therefore, to study the KS law and its dependence on different timescales, I need to assume the spatial extent of the SFR within each galaxy. However, in order to avoid the need of this assumption, instead of using the surface density quantities $\Sigma_{\rm H_2}$ and $\Sigma_{\rm SFR}$, I use the spatially integrated variables. I also avoid to assume a specific CO-to-H_2 conversion factor, thus, I finally use the SFR (from $L_{\rm IR}$) and $L'_{\rm CO}$ galactic quantities (Table. 5.2).

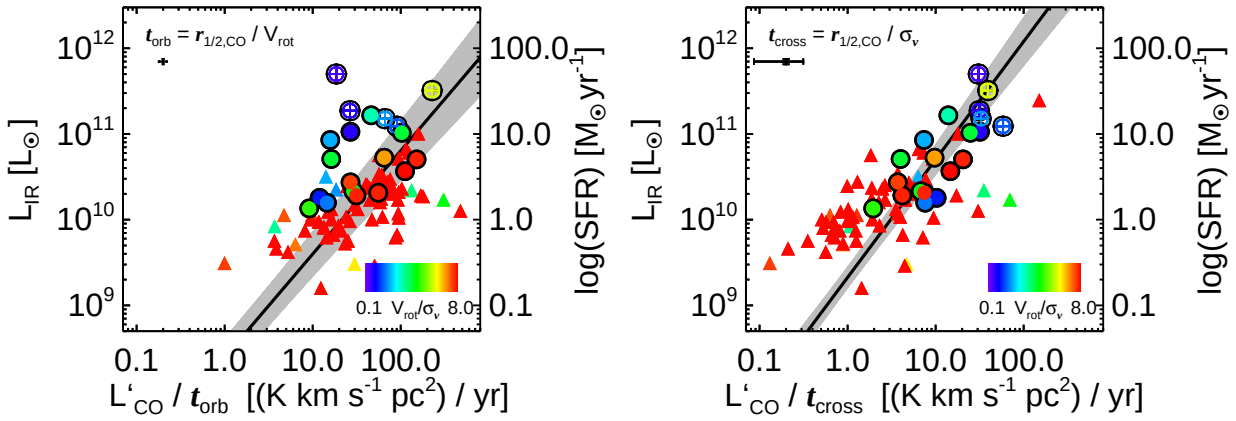

Figure 5.12: The IR luminosity as a function of the CO luminosity divided by the orbital timescale (left panel) and the crossing time (right panel). In both panels the VALES galaxies are classified as 'normal' (filled circles) and 'starburst' (circles with plus sign) galaxies as in Fig. 5.6. The triangles represent the EDGE-CALIFA galaxies (Bolatto et al., 2017). The VALES and CARMA-EDGE data presented in both panels are colour-coded by the observed $V_{\rm rot}/\sigma_v$ ratio. The line and the grey shaded area represent the best-fitted power-law function and its 1-σ error respectively in each panel. For the SFR-$L'_{\rm CO}/\tau_{\rm orb}$ plot I find a best-fit slope of 1.21±0.14, whilst for the SFR-$L'_{\rm CO}/\tau_{\rm cross}$ plot I find a best-fit slope of 1.38±0.13.

In Fig. 5.12, I investigate whether the star formation activity occurs on a timescale set by the orbital time ($t_{\rm orb} \equiv r_{1/2,\rm CO}/V_{\rm rot}$; left panel) or the radial crossing time ($t_{\rm cross} \equiv r_{1/2,\rm CO}/\sigma_v$; right panel) by studying the SFR$-L'_{\rm CO}/t_{\rm orb}$ and SFR$-L'_{\rm CO}/t_{\rm cross}$ correlations, respectively. I just consider these two timescales as they can be calculated directly from the molecular gas ALMA observations. I also include the data presented in the EDGE-CALIFA survey (Bolatto et al., 2017). These data were modelled using the same procedure described for the VALES data (see § 5.6.3 for more details).

In the left panel of Fig. 5.12, I find that galaxies with high SFRs also tend to present high $L'_{\rm CO}/t_{\rm orb}$ ratios. The Spearman's rank correlation coefficient is 0.52 with a significance of its deviation from zero of 1.3×10^{-7}. Thus, I find a correlation between SFR and $L'_{\rm CO}/t_{\rm orb}$. The data are fitted by a power-law function with best-fit slope of 1.21±0.14. As the $L'_{\rm CO}/L_{\rm IR}$ ratio seems to be constant for the detected VALES galaxies (V17), then this correlation is likely to be produced by low $t_{\rm orb}$ estimates measured for systems with higher $L'_{\rm CO}$ and $L_{\rm IR}$ values. However, I note that the VALES galaxies with low $V_{\rm rot}/\sigma_v$ ratio tend to lie above the best-fit, suggesting an enhanced star-formation efficiency per orbital time in these systems, in contradiction with Daddi et al. (2010). Although this correlation is often used to suggest that global galactic rotation may affect the star formation process (e.g. Silk 1997), I note that, perhaps, this explanation may not be the unique.

Galaxies with higher SFRs are expected to be more massive and have large gas content. Also, a massive galaxy is expected to rotate faster in order to balance its self-gravity. Therefore, the SFR-$L'_{\rm CO}/t_{\rm orb}$ correlation may reflect the mass-velocity trend in galaxies. I note that the location of the galaxies with low $V_{\rm rot}/\sigma_v$ ratio in the SFR-$L'_{\rm CO}/t_{\rm orb}$ plane can also be explained by the same kind of argument, but by considering a more sophisticated hydrodynamical balance against the gravitational force.

In § 5.4.4, I found that five systems are better represented by thick galactic discs than thin galactic discs. In thick discs, the gravitational force is balanced by both, negative radial pressure gradients and rotational support. Thus, thick galactic discs present lower $V_{\rm rot}$ values compared to thin galactic discs with equivalent mass. Therefore, the apparently enhanced star formation efficiency per orbital time observed in the SFR-$L'_{\rm CO}/t_{\rm orb}$ plane for galaxies with low $V_{\rm rot}/\sigma_v$ ratio may be produced by a relative reduction of the rotational velocity as pressure gradient support is not negligible across the galactic disc.

Within the thick disc model (Burkert et al., 2010), the relevance of the pressure gradient support is reflected by the velocity dispersion value (Eq. 5.1). Thus, one possible way to test the pressure support influence on the star formation is to test dependence of the SFR on the timescale given by σ_v, the crossing time. I remind that the velocity dispersion range observed in the sample is $\sigma_v \sim 22 - 79\,{\rm km\,s^{-1}}$ (Table 5.2). In the right panel of Fig. 5.12 I plot the SFR as a function of $L'_{\rm CO}/t_{\rm cross}$. I also find that galaxies with high SFR tend to have greater $L'_{\rm CO}/t_{\rm orb}$ ratio. The Spearman's rank correlation coefficient is 0.69 with a significance of 5.6×10^{-13}, also suggesting a correlation between both quantities. The best-fit power law function is 1.38±0.13. The SFR-$L'_{\rm CO}/t_{\rm cross}$ represents a reasonably better fit to data. However, I caution that the fitting procedures are highly sensitive on whether I include the starburst galaxies or not in the data, i.e., the parameter errors may be underestimated.

Another way to study the star-formation law is by defining the 'star formation efficiency' parameter as the star formation rate divided by the CO(1-0) luminosity (SFE$' \equiv$SFR/L$'_{\rm CO}$), i.e. a proxy of the molecular depletion time without assuming any $\alpha_{\rm CO}$ factor can be obtained by calculating L$'_{\rm CO}$/SFR (Cheng et al., 2018). This depletion time proxy can be compared with other timescales 't' by calculating the (L$'_{\rm CO}$/SFR)/t ratio. If the star formation efficiency can be expressed as SFE$'$ =SFE$'_t/t$, with the star-formation efficiency per timescale (SFE$'_t$) being constant, then the quantity (L$'_{\rm CO}$/SFR)/t should also be constant for the timescale 't' regardless of the SFR of the system. This can be understood as a constant depletion time per timescale unit. I test this in Fig 5.13 by showing the proxy of the depletion time divided by the orbital time [(L$'_{\rm CO}$/SFR)/$t_{\rm orb}$] and the crossing time [(L$'_{\rm CO}$/SFR)/$t_{\rm cross}$]. Both panels are plotted against the SFR.

I can see in the left panel of Fig 5.13 how the proxy of depletion time per orbital time varies with SFR. The Spearman's rank correlation coefficient is -0.30 with a significance of 0.004. I also get a best-fit power-law slope of -0.64±0.09. As mentioned before, this trend may be enhanced by pressure support effects which increase the observed orbital time (by decreasing $V_{\rm rot}$) as σ_v becomes comparable to $V_{\rm rot}$. On the other hand, in the right panel of Fig 5.13, I can see that the proxy of depletion time per crossing time appears to be independent of the SFR. The Spearman's rank correlation coefficient is -0.003 with a significance of 0.98, suggesting not correlation between both quantities. This plot also suggests that L$'_{\rm CO}$/SFR$\approx t_{\rm cross}$, with a median value of ∼1.7 and the 1-σ region between ∼0.8 and 4.8. This suggests SFE$'_{t_{\rm cross}} \sim 1$.

I note that a constant star formation efficiency per crossing time found in this work departs from the fixed efficiency per free-fall time suggested by Krumholz et al. (2012), as their estimation of the free-fall time for their extragalactic data set varies with the rotational velocity ($t_{\rm ff,T} \propto \Omega^{-1} \propto V_{\rm rot}^{-1}$). Nevertheless, in the $V_{\rm rot}/\sigma_v \approx 1$ limit, the free-fall time calculated by Krumholz et al. (2012) becomes comparable with the crossing time ($t_{\rm cross} \approx$

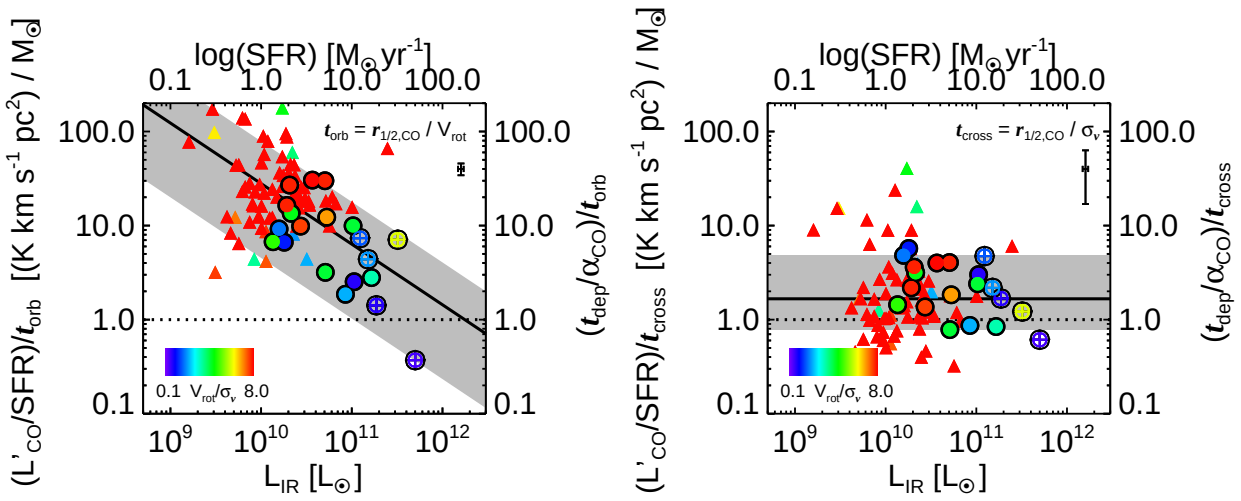

Figure 5.13: The $L'_{\rm CO}/L'_{\rm IR}$ ratio (SFE$'^{-1}$) divided by the orbital time (*left*) and crossing time (*right*) as a function of the IR-luminosity (SFR). This can be interpreted as the molecular gas depletion time divided by the respective timescale (orbital or crossing time) as a function of the SFR, without any assumption of the CO-to-H_2 conversion value. The data presented in both panels are coded in the same way as Fig. 5.12). The dotted lines represent a 1:1 ratio. In the left panel, the black line shows the best-fitted power-law function and the 1-σ error is represented by the grey-shaded region. In the right panel, the black line shows the median value and the grey shaded region also represents the 1-σ region. Interestingly, the data is consistent with a star formation law in which SFE$'^{-1}$ is fixed per crossing time.

Ω^{-1}). Thus, both laws fit the extragalactic data as a simple linear function in the $V_{\rm rot}/\sigma_v \gtrsim 1$ range. A possible way to differentiate both laws would be by performing spatially-resolved molecular gas observations in star-forming galaxies with $V_{\rm rot}/\sigma_v < 1$, where $t_{\rm ff,T} > t_{\rm cross}$.

This finding agrees with numerical simulations in which it is found that the star formation efficiency is well-represented by an exponentially decreasing function of the angular velocity of the disc (Utreras et al., 2016).

Before finalising this study, I would like to caution that spatial resolution effects may affect the analysis of Fig. 5.12 and Fig 5.13. Indeed, the low spatial resolution of the observations may lead to an overestimation of $t_{\rm orb}$ through possible overestimated CO half-light radii and underestimated $V_{\rm rot}$ (see § 5.3.3). This effect might decrease the estimated gas consumption rate per orbital time, especially on the sources observed at lower spatial resolution, which also are the galaxies with greater pressure gradient support and higher $r_{1/2,\rm CO}$ values within the sample. I note that the slope of the best-fit for the SFR-$L'_{\rm CO}/\tau_{\rm orb}$ correlation gets lower ($N = 0.87 \pm 0.09$) if I just consider galaxies observed with a projected beam size lower than 5 kpc within the sample. This spatial resolution limit is, for example, the value obtained for the current seeing limited ($\sim$0.″6) IFS observations at $z \sim 1$. I also note that this spatial resolution threshold selects 'normal' star-forming galaxies, but just one starburst galaxy with $V_{\rm rot}/\sigma_v \approx 2$ at $z < 0.06$ within the resolved sample. In this case, all of the selected galaxies have SFR$\lesssim$12 $M_\odot\,{\rm yr}^{-1}$. Thus, the conclusion remains unchanged.

On the other hand, $t_{\rm cross}$ may be less affected by spatial resolution effects as both, σ_v and $r_{1/2,\rm CO}$ values tend to be overestimated. If I consider the galaxies observed with a projected beam size lower than 5 kpc within the sample, I found a best-fit slope for the SFR-$L'_{\rm CO}/\tau_{\rm cross}$ correlation of 1.13 ± 0.17. However, as I mentioned earlier, this threshold just include one starburst galaxy with low $V_{\rm rot}/\sigma_v$ ratio and SFR. When I include galaxies observed with a spatial resolution up to 7 kpc (six more galaxies; $V_{\rm rot}/\sigma_v \sim 1$; SFR$\lesssim$20 $M_\odot\,{\rm yr}^{-1}$), I obtain a slope of 1.23 ± 0.12. In summary, the results are dependent whether I consider the systems with high SFRs and lower $V_{\rm rot}/\sigma_v$ ratios. Regardless of the spatial resolution effects discussed recently, the variable $\alpha_{\rm CO}$ factor should also have an affect on the analysis.

5.5 Conclusions

I present ALMA observations of 39 flux-selected ($S_{160\mu m} \geq 100$ mJy; $L_{\rm IR} \approx 10^{10-12}\,L_\odot$) galaxies with detected CO($J = 1 - 0$) emission, comprising 'starburst' and 'normal' star-forming galaxies drawn from the VALES survey (V17), at the redshift range of $0.02 < z < 0.35$. I incorporate the exquisite multi-wavelength coverage from the GAMA survey. I found 20 galaxies with extended ('resolved') emission whilst 19 have 'compact' (or 'unresolved') emission. The spatial resolution of the sample ranges from ≈2 to ≈8 kpc, with a fixed spectral resolution of 20 km s^{-1}. I model the CO(1-0) kinematics by using a two-dimensional disc model with an arctan velocity profile and consider disc thickness effects on the projection of the galactic disc in the observed plane. These new observations represent one of the largest samples of molecular gas kinematics traced by the CO of 'typical' and 'starburst' star-forming galaxies at intermediate redshifts.

The median $V_{\rm rot}/\sigma_v$ ratio for the sample is 4.1 and the $V_{\rm rot}/\sigma_v$ values range between $0.6 - 7.5$. I found median $V_{\rm rot}/\sigma_v$ ratios of 4.3 and 1.6 for the 'normal' star-forming and starburst sub-samples, respectively. The median $V_{\rm rot}/\sigma_v$ value for the 'normal' galaxies in the sample is consistent with the expected evolution with redshift for this ratio.

I find a tentative correlation between the $L_{\rm IR}$ luminosity with the rotation-to-pressure support ratio ($V_{\rm rot}/\sigma_v$). That anti-correlation suggest a smooth transition of the star formation efficiency on terms of the kinematic state for 'starburst' and 'normal' star-forming galaxies.

I find that the [CII]/IR luminosity ratio decreases at low $V_{\rm rot}/\sigma_v$ ratio. The data are well-represented by a power-law with best-fit slope of 0.74±0.14. This finding is consistent with Ibar et al. (2015), who found that galaxies presenting a prominent disc show higher $L_{\rm [C_II]}/L_{\rm IR}$ ratios than those which do not present disc-like morphologies. The VALES galaxies with $V_{\rm rot}/\sigma_v \gtrsim 3$ tend to show $L_{\rm [C_II]}/L_{\rm IR}$ comparable with the values measured in the KINGFISH survey for nearby galaxies (Smith et al., 2017), whilst galaxies with $V_{\rm rot}/\sigma_v \lesssim 3$ tend to show lower $L_{\rm [C_II]}/L_{\rm IR}$ values.

I compare the physical parameters derived by PDR modeling for the sample (Hughes et al., 2017) with the $V_{\rm rot}/\sigma_v$ ratio. I find that high hydrogen nuclei densities and high strength of the FUV radiation field are likely to be found in systems with low $V_{\rm rot}/\sigma_v$ ratio, with the latter quantity being almost independent of the CO and [CII] luminosities.

By calculating dynamical masses following both, thin and thick turbulent disc models, I find that the thin disc model tends to underestimate the galactic total mass as its values are lower than the estimated stellar masses for five of the galaxies (up to nine systems when molecular gas masses are also considered). On the other hand, the thick turbulent disc model tends to alleviate this conflict, suggesting that these sources with low $V_{\rm rot}/\sigma_v$ values are better represented by thick galactic discs. This also suggests that pressure gradient support effects should not be neglected in high velocity dispersion galactic discs.

I test if the rotationally supported galaxies are prone to develop gravitational instabilities. This is done by analysing the sources in the $f_{\rm H_2} - V_{\rm rot}/\sigma_v$ plane and comparing with expected values for a marginally stable gaseous thin disc ($Q_{\rm gas} = 1$), a gaseous thick disc ($Q_{\rm thick} = 1$) and a two component disc (stars plus gas; $Q_2 = 1$). From eleven galaxies classified as rotationally supported systems, I find that three galaxies are consistent with $Q_{\rm gas} \approx 1$, i.e., are prone to develop gravitational instabilities. The other eight systems have measured $Q_{\rm gas} \gtrsim 1$. This conclusion is not changed if I apply the thick disc gravitational stability analysis as the kinematic estimates are not enough accurate. The gravitational analysis considering a galactic disc with a gaseous and stellar component may change this result by increasing the number of galaxies consistent with being susceptible to develop gravitational instabilities, however stellar dynamic measurements are needed to corroborate this result.

I explore the possible origin of the energy sources of those high turbulent motions seen in the galaxies by comparing the SFRs with $f_{\rm H_2}$ and σ_v. I find that the SFR is weakly correlated with $f_{\rm H_2}$. By comparing the data with two theoretical models in the literature, the feedback-driven and gravity-driven models, I find that both models give a poor description of the data. This suggests that the main energy source of the supersonic turbulence observed in the VALES galaxies seem to be neither the gravitational energy released by cold gas accreted through the galactic disc nor the energy injected into the ISM by supernovae feedback.

I study the spatially-integrated star formation law dependence on galactic dynamics, avoiding assumptions about the the CO-to-H_2 conversion factor by studying the SFR$-L'_{\rm CO}/t_{\rm orb}$ and SFR$-L'_{\rm CO}/t_{\rm cross}$ relations. I find a correlation between SFR and $L'_{\rm CO}/t_{\rm orb}$, with a best-fit power-law slope of 1.21$\pm$0.13. Galaxies with higher SFRs are expected to be more massive, having large gas content and, hence to rotate faster in order to balance its self-gravity. Therefore, the SFR-$L'_{\rm CO}/t_{\rm orb}$ correlation may reflect the mass-velocity trend in galaxies. I also conclude that the SFR$-L'_{\rm CO}/t_{\rm orb}$ correlation is affected by the decrease of $V_{\rm rot}$ (thus, an increase of $t_{\rm orb}$) due to extra pressure gradient support to the gravitational potential as systems with low $V_{\rm rot}/\sigma_v$ ratio tend to lie above the best-fitted linear trend observed for galaxies with dominant rotational support.

I find that the proxy of the 'star formation efficiency' (SFE$' \propto$SFR$/L'_{\rm CO}$) is correlated with the crossing time, suggesting an efficiency per crossing time of $\sim$0.6. This correlation implies that an enhancement of the turbulent motions traduces to an increase of the star formation activity beyond the expectation from just the higher gas density. By considering the better correlation between SFE$'$ and $t_{\rm cross}$, I propose that the radial crossing time may be the timescale in which the star formation occurs in these systems. Therefore, by knowing the size, SFR, and mean velocity dispersion of a galaxy, I can estimate its molecular gas mass. However, a different assumption of the CO-to-H_2 conversion factor may change this result.

Obtain deeper and higher resolution observations of the molecular gas in a large sample of highly turbulent systems is critical to confirm or refute the findings reported in this work. It will allow to overcome spatial resolution effects which bias the velocity dispersion to higher values and to characterise the rotational velocity of the systems by observing the flat part of the velocity curve. This will be done in future work.

5.6 Appendix

5.6.1 Appendix A: KINEMATIC MAPS AND VELOCITY PROFILES

In Fig. 5.14, I plot the kinematic maps (1st to 3rd columns), residual maps (4th column) and one-dimensional velocity profiles (5th and 6th columns) for the sample taken from the VALES survey. Full information for the panels in the figure is given in its caption.

5.6.2 Appendix B: DYNAMICAL MASS ESTIMATES FOR DIFFERENT DENSITY PROFILES

In § 5.4.4, I show that roughly half of the galaxies within this sample are best described by a thick disc model rather than a thin disc model. The thick disc dynamical model predicts total masses greater than the stellar masses at the same radii, unlike the thin disc dynamical model. However, in order to implement the thick disc model, the surface density of the source needs to be known.

For the galaxies, I assumed a surface density profile given by the observed surface density brightness in the $K-$band, but I also assume a constant mass-to-light ratio and light extinction over the galactic disc. This is likely not to be true since I expect a major concentration of dust (thus extinction) in the central part of galaxies compared to their outskirts. With the aim to show that the choice of surface density distribution should not affect the conclusions of § 5.4.4, in Fig. 5.15, I plot the ratio between the dynamical masses assuming an exponential surface density profile and the observational Sérsic-like surface density profile as a function of the $V_{\rm rot}/\sigma_v$ ratio. When assuming an exponential surface density profile, I obtain greater dynamical mass values on average compared to the observational Sérsic-like surface density profiles. However, the median ratio of ~ 1.5 indicates that the conclusions should not be sensitive to the chosen surface density profiles.

I note that the possible trend between the dynamical mass ratio and the $V_{\rm rot}/\sigma_v$ ratio observed in Fig. 5.15 is consistent with the finding of increasing Sérsic indices above unity at galaxies with $\log(M_*/M_\odot) > 10.5$ (Wuyts et al., 2011; Bell et al., 2012; Lang et al., 2014). I also note that disc truncation is expected to be enhanced in galaxies with considerable turbulent pressure gradient support (Burkert et al., 2016).

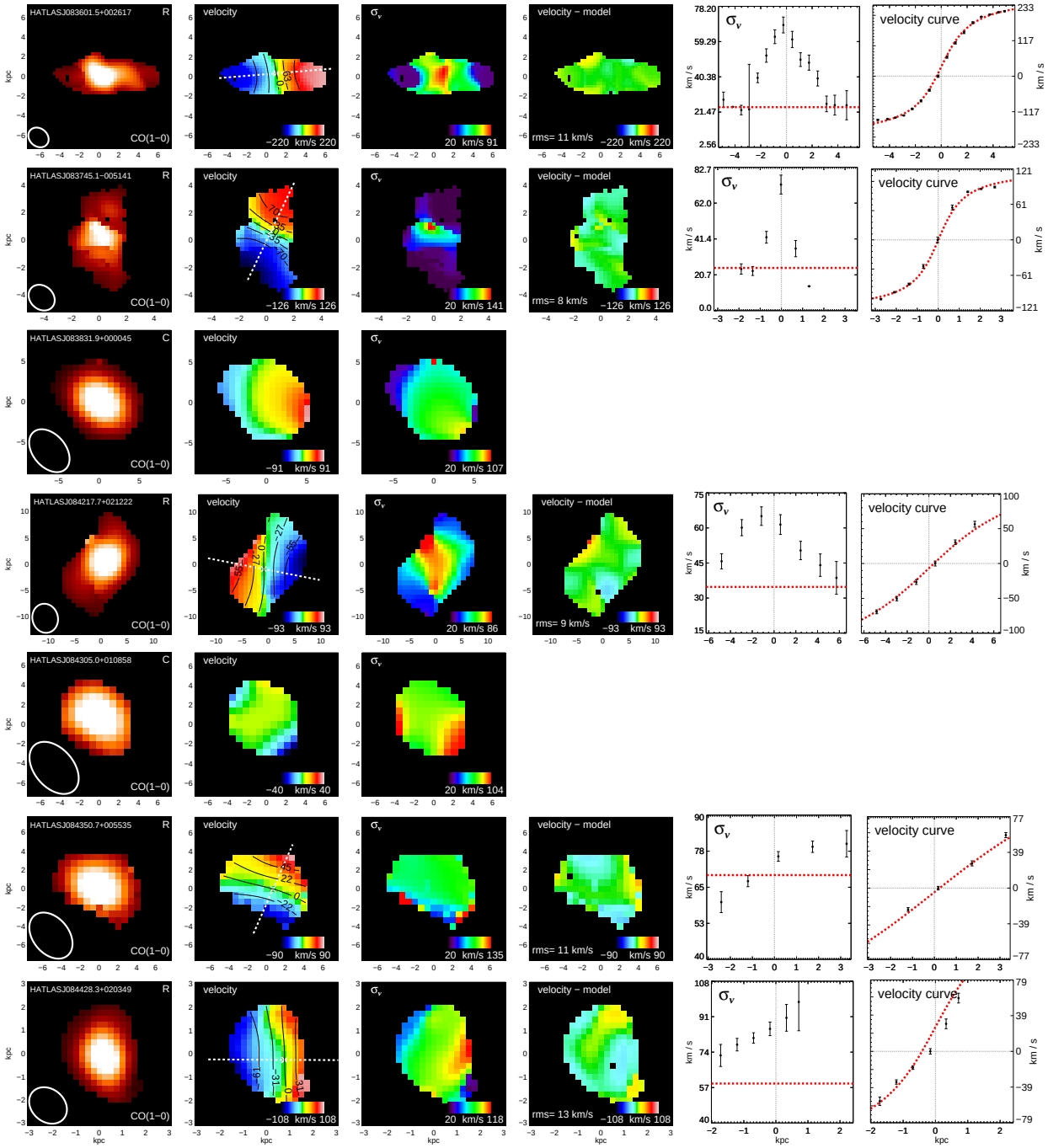

Figure 5.14: CO(1-0) intensity, rotation velocity, velocity dispersion and residual maps, along with the one-dimensional dispersion and rotation velocity profiles (columns) for each target (rows). The 'resolved' (R) or 'compact' (C) labels are showed in the intensity map. 'Compact' galaxies are not modelled. The intensity map also shows the synthesized beam size. Each velocity field show the kinematic centre, the major kinematic axis and best-fit disc model contours. The residual maps show the r.m.s. values. The one-dimensional profiles are derived by using a slit-width with size equal to half of the beam FWHM across the major kinematic axis. In each one-dimensional profile, the vertical dashed grey line represents the best-fit dynamical centre. In the σ_v profile panels, the red-dashed line shows the mean galactic value. In the last column, the red-dashed curve shows the best-fit rotation curve.

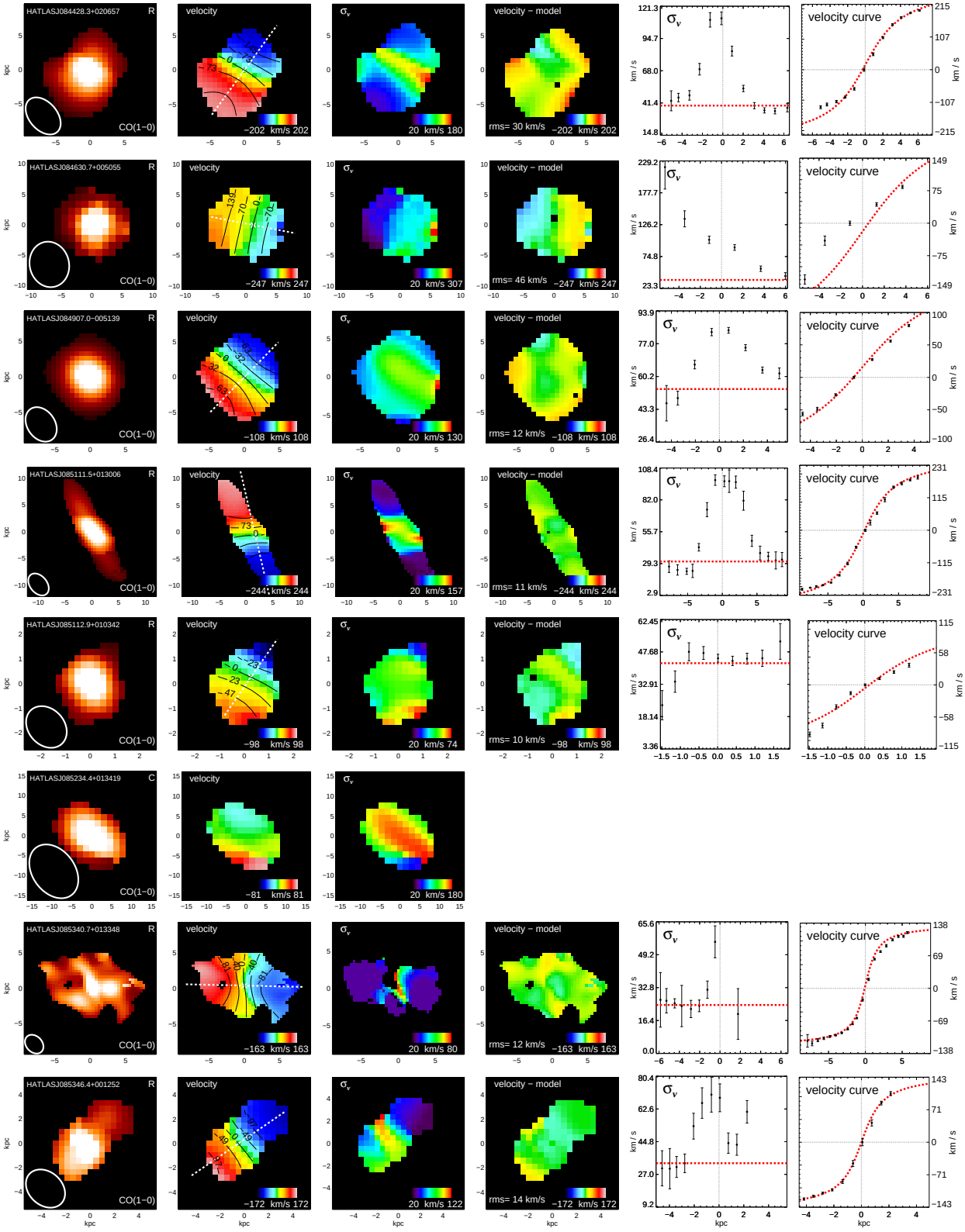

Figure 5.14 Continued.

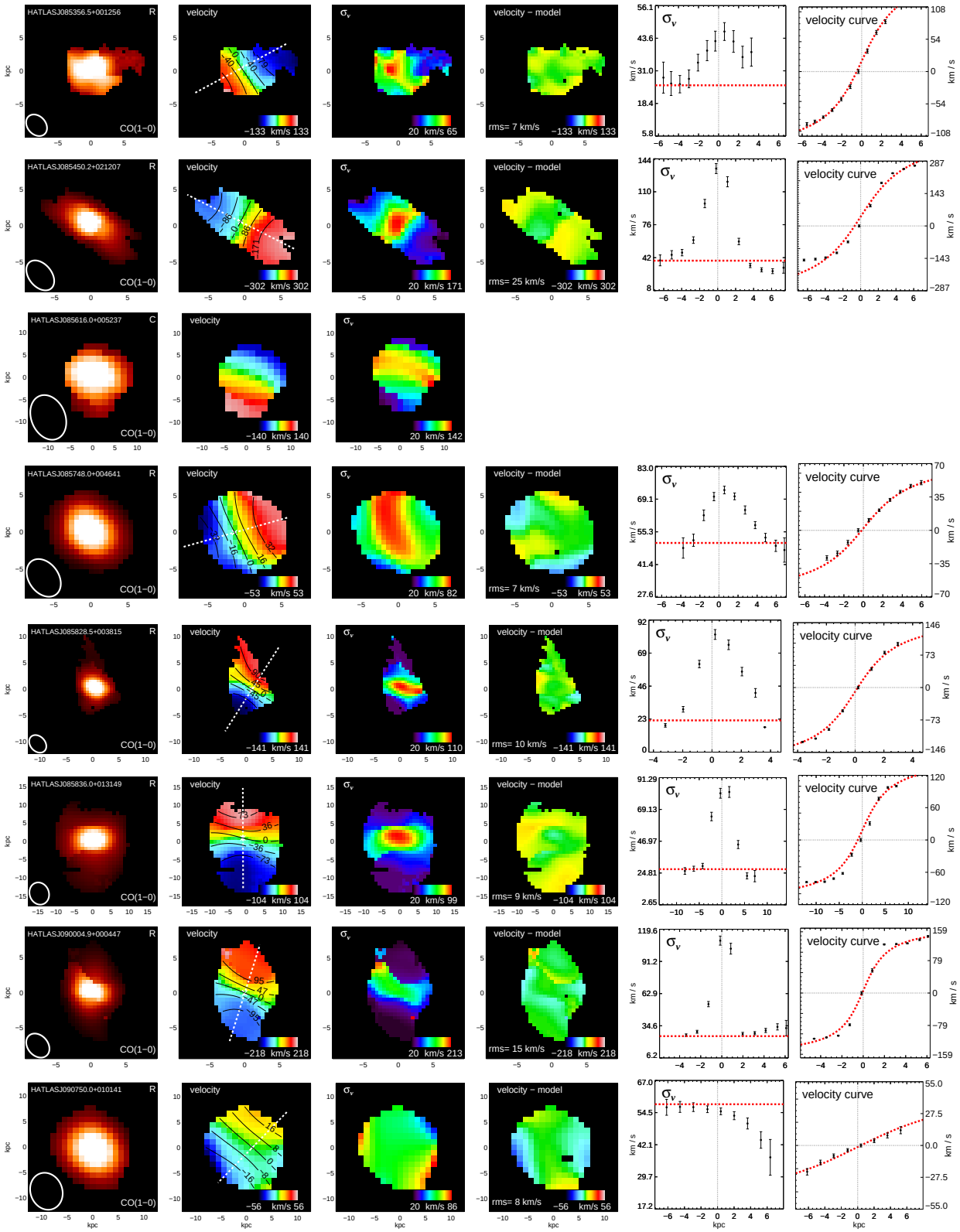

Figure 5.14 Continued.

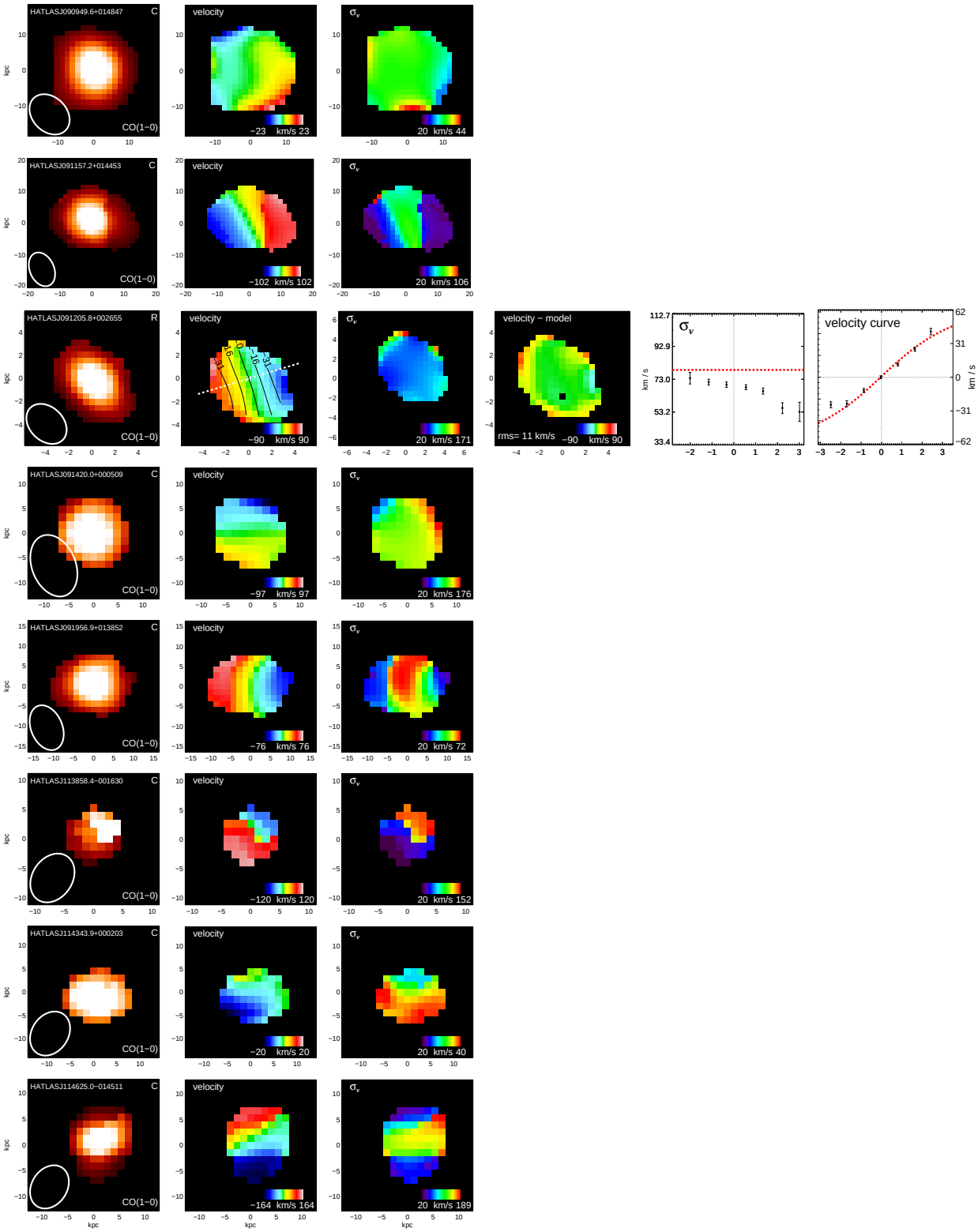

Figure 5.14 Continued.

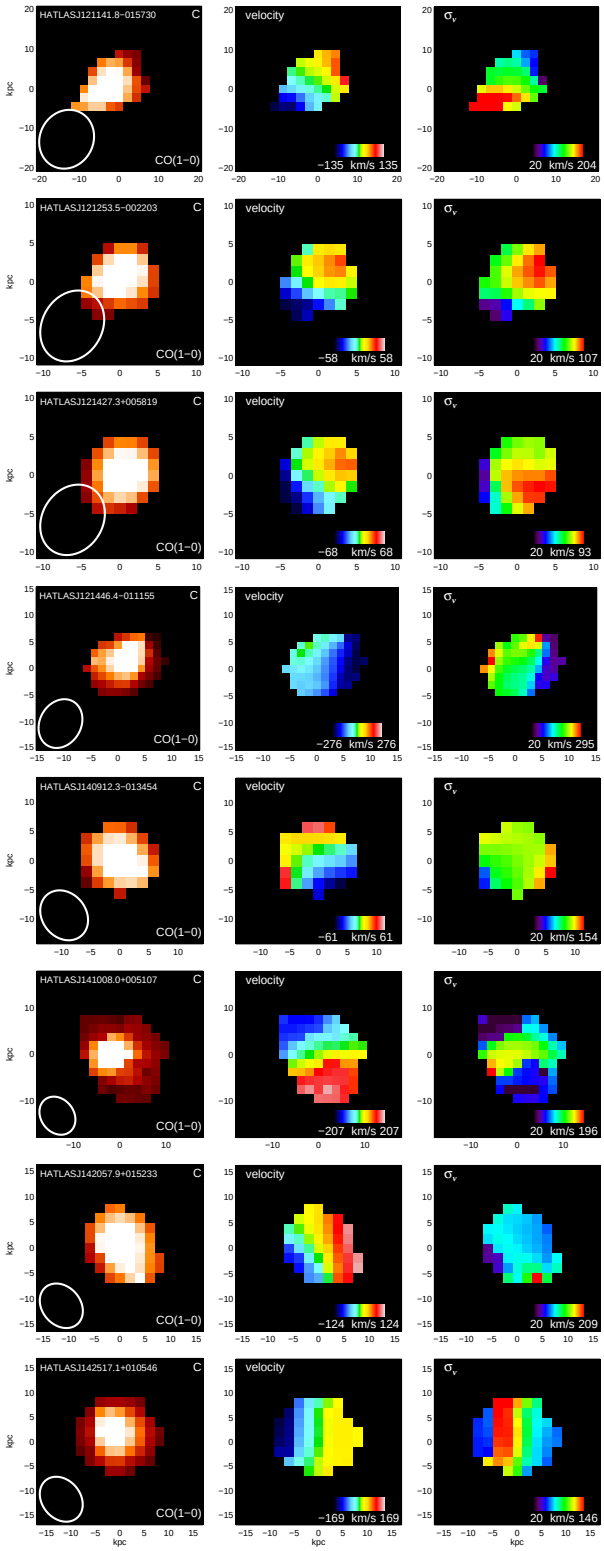

Figure 5.14 Continued.

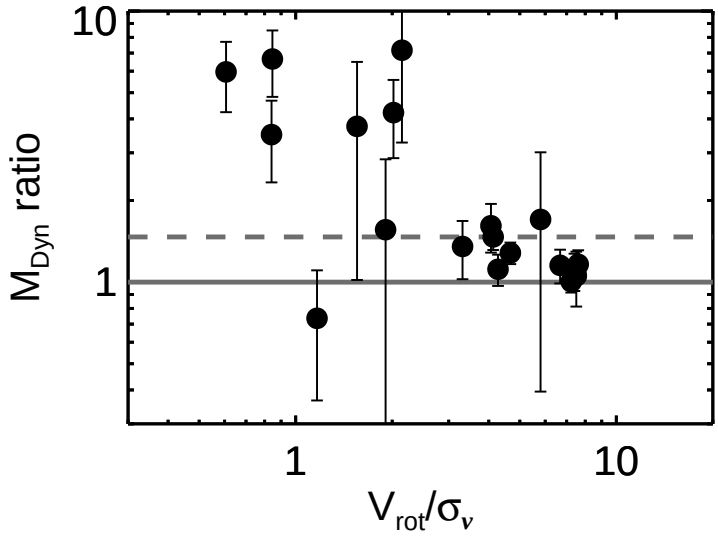

Figure 5.15: Ratio between the thick disc dynamical masses assuming an exponential surface density profile and the $K-$band converted surface density profile as a function of the $V_{\rm rot}/\sigma_v$ ratio for the sample. The grey line represents equality between both quantities. The dashed line represents the median value of ~ 1.5. By assuming an exponential surface density profile, I obtain greater dynamical mass estimates. This seems to be dependent of the observed $V_{\rm rot}/\sigma_v$ ratio.

5.6.3 Appendix C: EDGE-CALIFA SURVEY

In § 5.4.6, § 5.4.6 and § 5.4.7, I support the analysis by adding the EDGE-CALIFA survey data (Bolatto et al., 2017) to the VALES data. The EDGE-CALIFA survey is based on interferometric CO(1-0) observations made with CARMA of 126 nearby ($\rm d = 23 - 130\,Mpc$) galaxies from the EDGE survey. This sample is selected from the CALIFA survey and it has on average spectral and spatial resolutions of $\sim 10\,\rm km\,s^{-1}$ and $\sim$1.4 kpc, respectively. These spectral and spatial resolutions are higher than the used in this survey (Table 5.2).

From the EDGE-CALIFA survey, I analyse the galactic kinematics of the galaxies which have available their CO intensity, velocity and dispersion velocity maps with the additional requirement that the velocity map must sample the galactic centre given from the SDSS 'igu' multi-color image. Thus, I 'just' analyse 70 galaxies from the EDGE-CALIFA survey. The kinematic analysis is done in the same manner than I did for the VALES survey, but with two differences; (1) I constrain the inclination angles by using the values presented in Bolatto et al. (2017); and (2) I model these galaxies as thin galactic discs, i.e., $\rm q_0 = 0.0$. Finally, I correct the gas mass content by using the chosen CO-to-H_2 conversion factor, and I correct the stellar masses and SFRs for a Chabrier IMF.

Future Work

Even though the work done in this thesis can be considered as a progress into the understanding of the gaseous ISM morpho-kinematics in galaxies at different redshifts, there is many questions that are needed to be answered in order to have a more complete knowledge about the evolution of galaxies over cosmic time. For example, in Chapter 4, I studied the ∼kpc-scale kinematics of the molecular gas content for the SHiZELS-19 galaxy at $z \sim 1.47$. Furthermore, by comparing with the available ionized gas IFU observations at matched spatial resolution, I presented a spatially-resolved study of the star formation activity on this galaxy. Although this galaxy is representative of the star-forming galaxy bulk population in terms of stellar mass and SFR (Chapter 3), its morpho-kinematics may not be representative of the majority of main-sequence star-forming systems seen at nearly the same redshift (e.g. Stott et al. 2016).

SHiZELS-19 presents a smooth spatial distribution of the ionized and molecular ISM gaseous phases. This galaxy also has a $V_{\rm rot,CO}/\sigma_{v,\rm CO} \approx V_{\rm rot,H\alpha}/\sigma_{v,\rm H\alpha} \sim 1$. On the contrary, the average $V_{\rm rot,H\alpha}/\sigma_{vH\alpha}$ ratio for main-sequence star-forming galaxies if found to be $\sim 2-5$ at the same cosmic epoch (Wisnioski et al., 2015; Stott et al., 2016), with some galaxies presenting a clumpy substructure seen in the ionized gas emission (e.g. Swinbank et al. 2012a). Therefore, observe the molecular gas content in larger galaxy samples is fundamental in order to fully characterize the ISM properties and the star-formation activity for the bulk of the galaxy population at high-redshift.

In order to expand the study of the molecular gas content on galaxies at $z \sim 1.5$, for the ALMA Cycle-7, I proposed to carry on observations to spatially-resolve the CO(2-1) emission on another three main-sequence galaxies (proposal under review process). These galaxies are part of the KMOS Galaxy Evolution Survey (KGES; Tiley et al. in prep.), with exquisite multi-wavelength coverage and including ionized gas IFU observations from KMOS. For these three galaxies, I plan to perform a similar analysis than the one presented for SHiZELS-19 in Chapter 4. If the clumpy structure of the ISM is detected in the CO emission, then I will also be able to study the Larson's relations (Larson, 1981) on these ∼kpc-sized molecular clouds and test if their properties are consistent with the predicted from the gravitational instability theory (e.g. Escala & Larson 2008; Toomre 1964).

Another line of future research is to study galaxies at intermediate redshifts ($z \sim 0.1-0.7$). These systems have been generally ignored within the picture of dynamical evolution of galaxies across cosmic time (e.g. Stott et al. 2016). Recently, the VALES survey (Villanueva et al., 2017) has observed the molecular gas content of normal star-forming and starburst

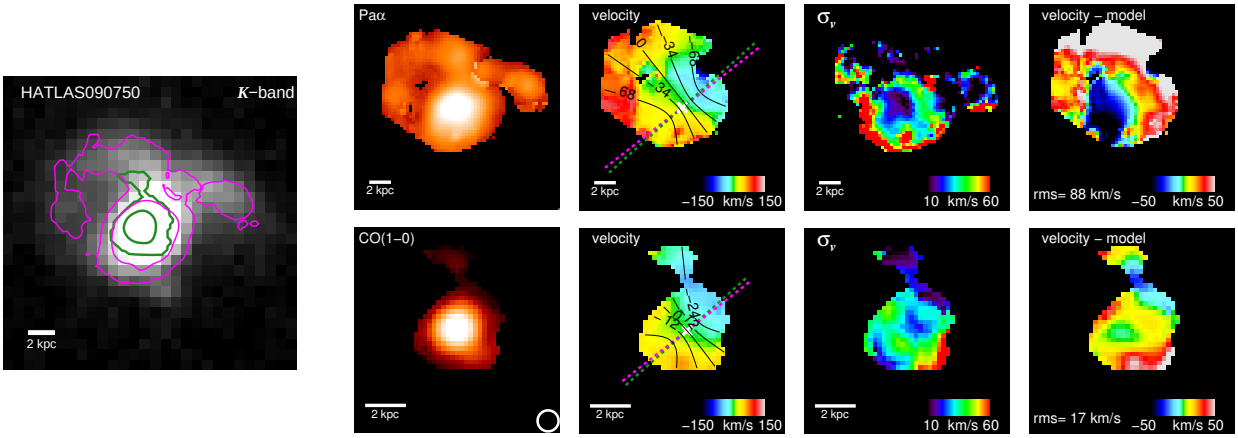

Figure 5.16: An early view to the K-band, intensity, velocity, residual and velocity dispersion maps for the HATLAS90750.0+010141 galaxy taken from the VALES survey (Villanueva et al., 2017). *Left:* The K-band map has over-plotted the CO(1-0) and Paα emissions in green and pink contours, respectively. *Right:* I show the two-dimensional maps derived from the CO(1-0) (bottom) and Paα (top) emission lines. The spatial scale for each observation is showed in each map. The CO(1-0) intensity map shows the synthesized beam size. The velocity maps have over-plotted the kinematic centre and the velocity contours from the best-fit disc model. The green- and pink-dashed lines represent the molecular and ionized gas major kinematic axis, respectively. The residual fields are constructed by subtracting the velocity disc model from the velocity maps. As revealed by the images, the galaxy shows features of a recent interaction, with tidal tail-like structures present in the upper-zone of the datacube.

dusty galaxies at $z = 0.03 - 0.35$. In terms of dynamical properties, these main-sequence and starburst galaxies are also consistent with being highly turbulent rotating discs on global scales (Chapter 5), but a detailed characterisation of their dynamics was impeded by the poor spatial resolution observations ($\sim 17\,$kpc at $z \approx 0.35$). Another way to study the galaxy dynamics is by observing the ionized gas phase (e.g. Swinbank et al. 2012b; Green et al. 2014; Wisnioski et al. 2015). Through the observation of the Paschen-α (Paα; $\lambda = 1.875\mu$m) emission line, I can measure the ionized gas morpho-kinematics in those galaxies with minimal extinction effects. I note that Paα can be observed in K-band with SINFONI up to $z \lesssim 0.3$.

Hence, pursuing this line, I am exploiting the synergy between the ALMA and VLT-SINFONI observations by carrying on a pilot study of the ionized and molecular gas morpho-kinematics on three galaxies at $z \sim 0.1$ taken from VALES. I am using the SINFONI instrument to observe the ionized gas through the Paα emission line (Project 099.B-0479(A); P.I. J.Molina). I note that, these K-band seeing-limited observations ($\approx 0\farcs6$) deliver $\sim$kpc-scale spatial resolution at $z \sim 0.1$. These observations are already reduced and will be complemented with available CO(1-0) emission line observations tracing the molecular gas content at matched spatial resolution (e.g., Fig. 5.16). I plan to compare the kinematics of the ionized and molecular gas ISM phases along with the spatially-resolved star formation activity in these three galaxies in a similar way as I did for SHiZELS-19 (Chapter 4). As a pilot study, the success of this project will enable the future exploration of the ionized and molecular gas kinematics for larger galaxy samples at intermediate redshifts, specially for the highly dust-obscured star-forming galaxy population (e.g. Calabrò et al. 2018).

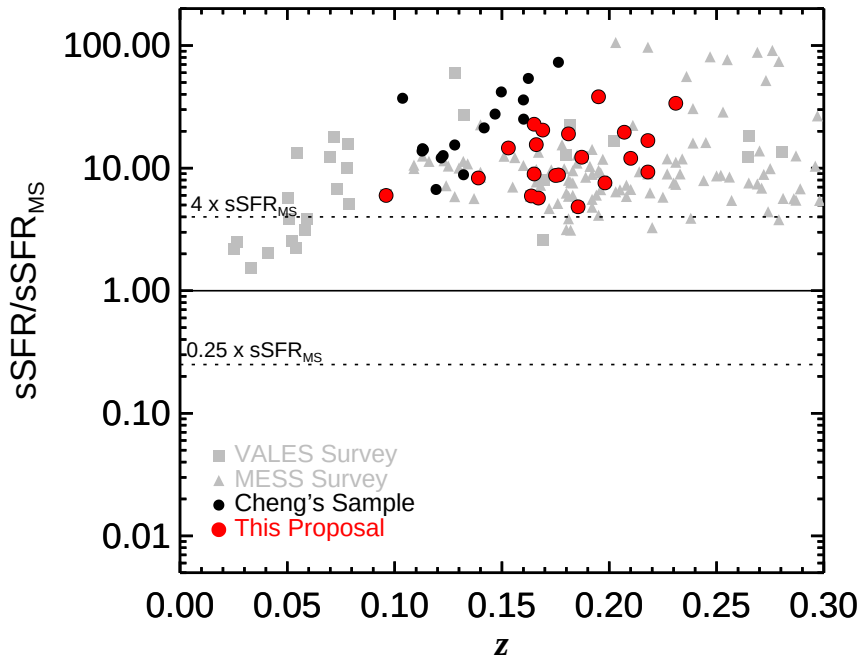

Figure 5.17: The sSFR over the main sequence sSFR value ($\mathrm{sSFR_{MS}}$) as proposed by Genzel et al. (2015) as a function of redshift. The upper and bottom dashed lines represent the $4\times$ and $0.25\times$ the $\mathrm{sSFR_{MS}}$ value respectively, separating starburst and quiescent galaxies from the 'typical' SFGs. All of the galaxies are classified as starburst systems following the criteria $\mathrm{sSFR/sSFR_{MS}} > 4.0$ (e.g. Villanueva et al. 2017) and complement with the sample of starburst galaxies presented in Cheng et al. (2018).

Finally, my latest future research project is to further test one of the main results derived from the VALES campaign. Recently, Cheng et al. (2018) have studied the proxy of the star formation efficiency ($\mathrm{SFE'} = \mathrm{SFR}/L'_{\mathrm{CO}}$) without assuming a CO-to-H_2 conversion factor by using the VALES data and APEX/SEPIA Band-5 detections of 16 starburst galaxies at $z = 0.1 - 0.2$. They have provided evidence that the SFE$'$ seems to increase smoothly with the Far-Infrared luminosity (L_{FIR}), i.e., SFR. This may imply that the bi-modality seen in the Kennicutt-Schmidt law (Daddi et al., 2010; Genzel et al., 2010) may be produced by the assumptions, as thus, the uncertainties behind the estimates of the molecular gas content on galaxies (Cheng et al., 2018).

However, the VALES galaxies (including Cheng et al. 2018's sample) were selected by applying a flux density threshold in the Far-IR. These galaxies are likely to be massive and metal rich dusty obscured systems (Ibar et al., 2015). Thus, the characteristics of this sample may not reflect an unbiased picture of the starburst galaxy population at $z = 0.1 - 0.3$. Therefore, one of my future projects is to make use of the Multi-wavelength Extreme Starburst Sample (MESS; Laag et al. 2010) to include optically-selected starburst galaxies in order to create a sample of starburst galaxies which is less affected by selection effects at $0.1 < z < 0.3$ (Fig. 5.17). By using APEX-SEPIA/Band-5 targeting the CO(2-1) emission line, this project has been already observed (C-0102.F-9713B-2018, P.I. J. Molina; C-0103.F-9712B-2019; P.I. E. Ibar).

Complemented with Cheng et al. (2018)'s galaxy sample, I aim to create one of the largest sample of starburst galaxies with measured molecular gas masses at $0.1 < z < 0.3$. The main advantages of using the MESS-selected star-forming galaxies are: (1) provides an optically selected starburst galaxy sample at $z = 0.1 - 0.3$ in which the SFRs are calculated by using a Bayesian fitting approach to their SED (Brinchmann et al., 2004). Therefore, those galaxies were selected by considering that the entire spectrum indicates an unusually high level of star-forming activity (Laag et al., 2010); (2) this sample is not contaminated by AGN as indicated by the 'BPT diagram' analysis (Baldwin et al., 1981); and (3) this sample has multi-band imaging photometer (MIPS; 24, 70, and 160μm) on the Spitzer Space Telescope which indicates that MESS galaxies have IR luminosities similar to those of LIRGs observed in Cheng et al. (2018).

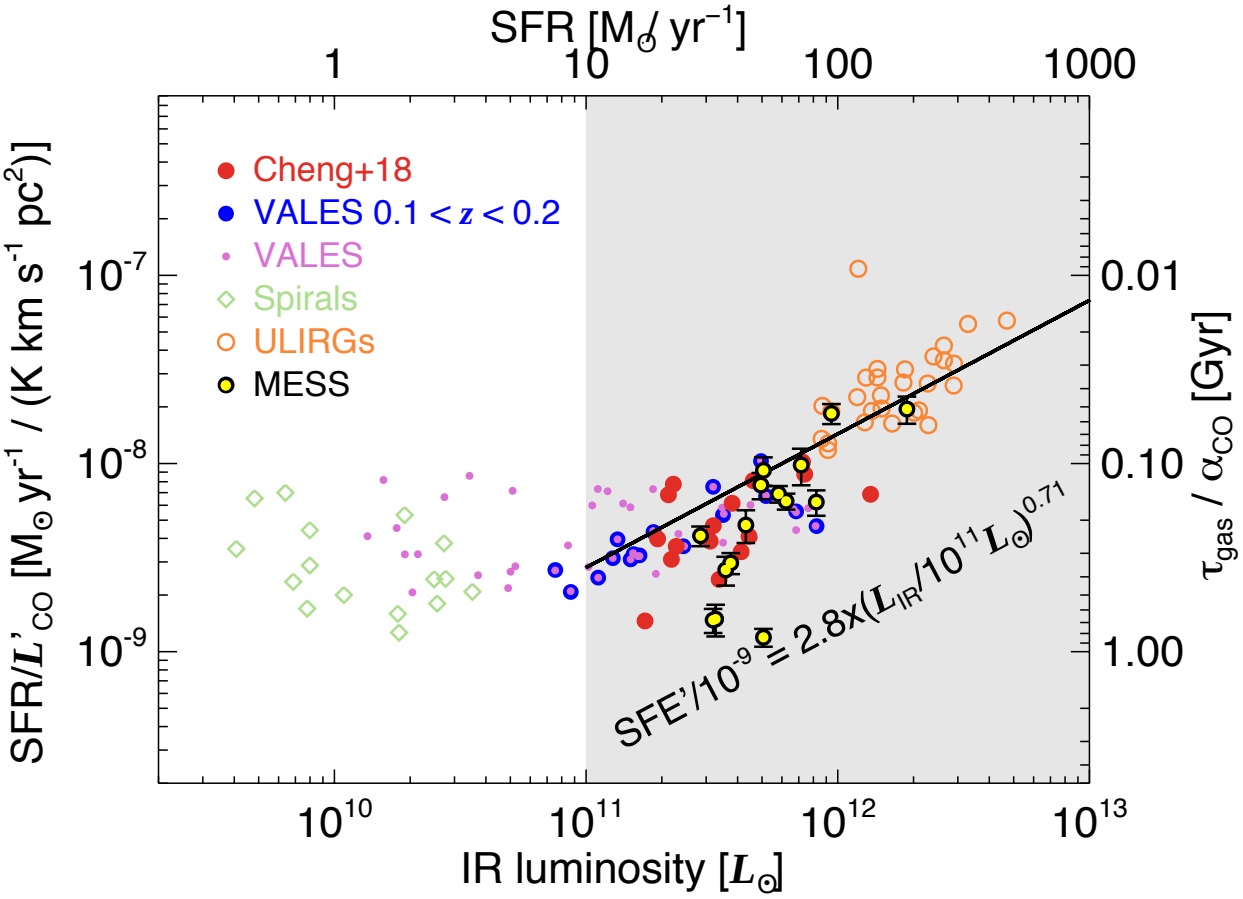

Figure 5.18: The SFR/$L'_{\rm CO}$ vs $L_{\rm IR}$ for the MESS galaxies with detected CO(2-1) emission (yellow circles). The MESS data are added to the panel by using the inverse relation between SFR and $L_{\rm IR}$ adopting a Chabrier (2003)'s IMF [SFR($M_\odot\,{\rm yr}^{-1}$) = $10^{-10} L_{\rm IR}(L_\odot)$]. The top label shows the SFR scale. The right Y-axis is the gas depletion time-scale normalised by $\alpha_{\rm CO}$. The literature data is colour-coded in the same way as are presented in Cheng et al. (2018); the VALES sample (purple/blue/red dots); local spirals (green diamonds; Leroy et al. 2009) and the local ULIRGs (orange circles; Solomon et al. 1997). I also show the best-fit linear function presented by Cheng et al. (2018) for galaxies with $L_{\rm IR} > 10^{11}\,L_\odot$ (grey-shaded region). The MESS data support the increasing SFE′ trend with respect to SFR.

From this campaign, the early results are promising (Fig. 5.18). Preliminary CO(2-1) fluxes for the MESS galaxies seem to confirm the trend suggested by Cheng et al. (2018). Indeed, as the MESS galaxies were added by using the SFR values measured from Brinchmann et al. (2004)'s SED fitting, it suggests that the $\mathrm{SFR}/L'_{\mathrm{CO}}$ quantity tend to increase with SFR for the hole starburst galaxy population (dusty or not) and not driven by undetected AGN activity. Nevertheless, I note that those CO(2-1) fluxes obtained for the MESS galaxies will be critical to obtain future secure spatially-resolved molecular gas observations with ALMA. Even though the details of these observations are not yet fully analysed, the availability of these recent data will facilitate upcoming publications which will be carried on in a future post-doctoral position already granted in a foreign country.

Summary & Conclusion

Understanding how galaxies form and evolve over cosmic time is a major goal in modern extragalactic astrophysics. Surveys have shown that there is a decline in the overall cosmic star-formation rate density since $z \sim 2$ (e.g. Madau et al. 1996; Sobral et al. 2013a; Khostovan et al. 2015) which coincides with the decrease of the average fraction of molecular gas mass in galaxies (e.g. Tacconi et al. 2010; Geach et al. 2012; Carilli & Walter 2013). This behaviour is thought to match the cosmic evolution of the mass in stars, and the molecular gas content ($M_{\rm H_2}$) of the Universe, hence it provides a logical interpretation for the interplay between, perhaps, the main actors controlling the growth of galaxies (e.g. Madau & Dickinson 2014). One possible scenario is that the high levels of star formation at those redshifts may be promoted and maintained by the continuously fed gas from the intergalactic medium (IGM) and therefore, the star-formation activity may be driven by internal dynamical processes within the interstellar medium (ISM; Kereš et al. 2005; Bournaud et al. 2007; Dekel et al. 2009b). In this case, secular processes drive the galaxy evolution and spatially-resolved observations of the morpho-kinematics of galaxies are critical to measure their internal dynamical properties.

In the present work I studied the morpho-kinematic properties galaxy samples at high-redshifts ($z \sim 0.8 - 2.2$; Chapter 3 and 4) and low-redshift ($z \sim 0.02 - 0.35$; Chapter 5). I have analysed the internal kinematics of these galaxies with the aim to find possible correlations between the kinematic state of the interstellar medium (ISM) and its physical properties, including the study of the star formation activity and its possible evolutionary trends with cosmic time. Through the observation of the H$\alpha\lambda$6562.8 hydrogen recombination emission line, I have characterized the ionized ISM gaseous phase of galaxies. This is done by analysing adaptive optics (AO) assisted Integral Field Unit (IFU) observations using the Spectrograph for INtegral Field Observations in the Near Infrared (SINFONI) instrument mounted on the Very Large Telescope (VLT). These observations deliver ∼kpc-scale spatial resolution for galaxies at $z \sim 0.8 - 2.2$. In parallel, I used the Atacama Large Millimetre/-submillimetre Array (ALMA) interferometer to observe the molecular gas content of galaxies via the observation of the Carbon Monoxide (CO) molecule low-J ($J = 1 - 0; 2 - 1$) rotation emission lines.

The characterization of the galaxy dynamics through the construction of the collapsed moment two-dimensional maps is done by modelling the emission line in each pixel of the datacubes as a simple Gaussian profile. The intensity, rotation velocity and velocity dispersion values in each pixel of the two-dimensional maps are derived from Gaussian fitted profiles. In the particular case of the high-redshift ($z \sim 0.8 - 2.2$) SINFONI observations, I perform a multiple emission line fitting using my own developed computing codes.

The kinematic modelling of the galaxies is done by applying a χ^2 minimization procedure adopted from Swinbank et al. (2012b) to search for the best-fit solution of the model parameters. In general, I characterise the velocity profiles assuming an 'arctan' profile, where the main kinematic parameters are the radius at which the rotation curve flattens (r_t) and the asymptotic amplitude of the rotational motions observed at the galaxy outskirts ($V_{\rm asym}$). The spatial resolution of the observations is accounted by convolving model velocity maps with the synthesized beam or Point Spread Function (PSF), accordingly. In my analyses, I have also used photometric models from broad-band galaxy images to aid the kinematic modelling and overcome parameter degeneracy, especially with the inclination angle.

In the redshift range of $0.8 - 2.2$, I present natural guide star AO-aided SINFONI IFU observations of spatially-resolved Hα kinematics of eleven mass-selected ($M_\star = 10^{9.5-10.5}\,M_\odot$) 'typical' star-forming galaxies from the wide-field narrow-band High-Z Emission Line Survey (HiZELS). I characterized the dynamics of this galaxy sample and I derived a median peak-to-peak velocity to velocity dispersion support of $V_{\rm max,H\alpha}\sin({\rm i})/\sigma_{v,{\rm H}\alpha} = 1.6{\pm}0.3$ (with a range of 1.1–3.8). These observations are combined with a previous study (nine galaxies taken from Swinbank et al. 2012b) to create an homogeneously selected sample of star-forming galaxies with dynamical characterisation at $\sim$kpc scales near the peak of the cosmic star-formation rate density.

By implementing a tilted ring kinematic decomposition in the azimuthal angle ('*kinemetry*'), I find a tentative increase of the merger fraction as a function of redshift ($f_{\rm merg}(z) \sim 0.0^{+0.4}$, $0.3^{+0.2}_{-0.2}$ and $0.6^{+0.2}_{-0.3}$ at $z = 0.8$, 1.47, 2.23, respectively). These results are consistent with previous IFU surveys (Shapiro et al., 2008; Förster Schreiber et al., 2009), although I find higher merger fractions at a given specific star formation rate (sSFR) in comparison to previous analyses by Stott et al. (2013b) who used a morphological classification from Hubble Space Telescope (*HST*) near-IR imaging. I combine the observations with previous studies of intermediate and high-redshift galaxies (Swinbank et al., 2006; Cresci et al., 2009; Jones et al., 2010; Gnerucci et al., 2011; Miller et al., 2011, 2012; Swinbank et al., 2012b) to investigate the stellar mass Tully-Fisher relation. I find that the scatter of this relation is affected by the galaxy pressure gradient support represented by the $V_{2.2}/\sigma_{v,{\rm H}\alpha}$ ratio – a result which is consistent with Tiley et al. (2016b) findings.

The evolution of the stellar mass TFR from $z \sim 0$ to $z \sim 2$ is consistent with the secular evolution of galaxies, where the dynamics of the gas and stellar components are still relaxing into a disc-like system. This finding is also consistent with the decrease of the merger fraction since $z \sim 2$ derived from the kinematic analysis for this galaxy sample, suggesting that the evolution of galaxies may be driven by the accretion of cold gas inflows from the IGM since $z \lesssim 2$.

I measure metallicity gradients ($\Delta\log_{10}({\rm O/H})/\Delta R$) using the [N II]/H$\alpha$ ratio for 3, 7 and 2 galaxies at z =0.8, 1.47 and 2.23 within the SINFONI-HiZELS (SHiZELS) survey. These metallicity gradients ranges between -0.087 and $0.08\,{\rm dex\,kpc^{-1}}$, with a median metallicity gradient of $\Delta\log_{10}({\rm O/H})/\Delta R = -0.027{\pm}0.008\,{\rm dex\,kpc^{-1}}$. The evolution of metallicity gradients as a function of redshift in the sample does not exhibit any clear trend such as the predicted by the 'Galaxies-Intergalactic Medium Interaction Calculation' (GIMIC) simulation for galaxy discs (Crain et al., 2009; McCarthy et al., 2012), where gas inflow rate

decreases with decreasing redshift progressively. This may be partly produced by the lack of AGN feedback and/or strong nuclear outflows in the GIMIC simulation 'sub-grid' model which produces a lower metal yield in the circumgalactic medium than the expected.

I find that metal-rich galaxies tend to show negative gradients, whereas metal-poor galaxies tend to exhibit positive metallicity gradients. This correlation may be explained by the infall of metal-poor gas from the IGM into the central part of galaxies lowering the global galactic metallicity, but especially diluting the gas in the galactic centre. This result suggests that the accretion of pristine gas in the periphery of galaxies plays an important role in replenishing the gas in 'typical' star-forming galaxies.

As a follow-up campaign of the previous SHiZELS studies, I present new ALMA Cycle-5 observations tracing the CO(2-1) emission line from two 'typical' star-forming galaxies at $z \sim 1.47$. These observations were designed to deliver spatially-resolved observations of the molecular gas content on ∼kpc-scales, i.e., the same spatial scale that the previous AO-aided Hα SINFONI observations reached. Using both set of observations, I study the ionized and molecular gas dynamics jointly on these galaxies with special focus to measure the total baryonic mass content and the star formation activity on ∼kpc-scales. One of the targets, SHiZELS-8, is just marginally detected. For this system the Hα and CO(2-1) dynamics show that both ISM components rotate roughly in the same direction but have kinematic position angles offset by $100-120$ deg., suggesting that SHiZELS-8 is a dynamically perturbed system consistent with its previously observed flat metallicity gradient (Swinbank et al., 2012b).

For the second target, SHiZELS-19, I find a good agreement between the CO(2-1) and Hα spatial extent and dynamics at ∼kpc-scales. For both ISM phases I derive $V_{\rm rot}/\sigma_v \sim 1$. The kinematic analysis suggests that the CO(2-1) and Hα observations are tracing the same galactic dynamics. This may imply that he Hα observations of some galaxies at high-redshift are tracing the dynamical state of these systems instead of an extra-planar diffuse ionized gas component or out-flowing gas motions. On the other hand, this result may also imply that the CO emission may not be a good tracer, in terms of rotational velocity, of the gravitational potential well of galaxies as the molecular gas ISM component should be also susceptible to pressure gradient support. Therefore, at this redshift, the CO emission may not be a good tracer to study the TFR. The 'CO-TFR' may suffer from the same scatter than Hα-based studies present at high-redshift (e.g. Tiley et al. 2016b), in contrast with local galaxy studies (e.g. Tiley et al. 2016a; Topal et al. 2018).

For this galaxy, I am able to trace the CO(2-1) emission up to ≈ 6 kpc from the galactic centre, finding a dark matter fraction of $f_{\rm DM} = 0.6 \pm 0.1$ within this aperture. The dark matter fraction value is in agreement with those expected from hydrodynamical simulations of disc-like galaxies with similar stellar mass (Lovell et al., 2018), and the average dark matter fraction suggested by a stacking rotation curve analysis of galaxies at a similar redshift range (Tiley et al., 2019). By using the two-dimensional kinematic modelling, I study the internal star formation activity observed in the SHiZELS-19 galaxy at ∼kpc-scales. I derive a median gas depletion time $\tau_{\rm dep} = 2.3 \pm 1.2$ Gyr. This median value is consistent with the typical value observed in local galaxies at similar spatial scales ($\tau_{\rm dep} = 2.2 \pm 0.3$ Gyr; Leroy et al. 2013), suggesting that 'typical' high-redshift galaxies (at $z \sim 1.47$) with high $\Sigma_{\rm H_2}$ values still follow the Kennicutt-Schmidt law.

In the redshift range of $0.02 < z < 0.35$, I study the kinematic of 39 flux-selected ($S_{160\mu m} \geq 100\,\mathrm{mJy}$; $L_{\mathrm{IR}} \approx 10^{10-12}\,L_{\odot}$) galaxies observed with ALMA in CO($J = 1-0$) emission. These galaxies comprise 'starburst' and 'normal' star-forming galaxies drawn from the Valparaíso ALMA/APEX Emission Line Survey (VALES) (Villanueva et al., 2017). The kinematic analysis is aided by the exquisite multi-wavelength coverage from the Gas And Mass Assembly (GAMA) survey and the *Herschel* Astrophysical Terahertz Large Area Survey (*H*-ATLAS). For this galaxy sample, I found 20 galaxies with extended ('resolved') emission whilst 19 have 'compact' (or 'unresolved') emission. The median CO-based rotational velocity to velocity dispersion ($V_{\mathrm{rot}}/\sigma_v$) ratio for the sample is $\approx 4.1^{+3.5}_{-2.9}$ and the $V_{\mathrm{rot}}/\sigma_v$ values range between $\sim 0.6 - 7.5$. Assuming that galaxies can be separated in two different populations using the so-called 'main-sequence' (e.g. Brinchmann et al. 2004; Noeske et al. 2007; Whitaker et al. 2012),I found median $V_{\mathrm{rot}}/\sigma_v$ ratios of $\approx 4.3^{+3.2}_{-2.3}$ and $\approx 1.6^{+4.3}_{-1.0}$ for the 'normal' star-forming and starburst sub-samples, respectively. The median $V_{\mathrm{rot}}/\sigma_v$ value for the 'normal' galaxies in the sample is consistent with the observed evolution of this ratio derived from the ionized gas component, suggesting that the molecular turbulence also increases with cosmic time.

In this work, I find a tentative anti-correlation between the L_{IR} luminosity with the $V_{\mathrm{rot}}/\sigma_v$ ratio. This suggests a smooth transition of the star formation efficiency in terms of the kinematic state for 'starburst' and 'normal' star-forming galaxies. Although it is not possible to conclude that the [CII] deficit is controlled by the dynamical state, I find that the [CII]/IR luminosity ratio decreases at low $V_{\mathrm{rot}}/\sigma_v$ values. This implies that in certain galaxies, where dynamics tend to be dominated by dispersion, the amount of $L_{[\mathrm{C_{II}}]}/L_{\mathrm{IR}}$ decreases. This finding is consistent with Ibar et al. (2015) who found that galaxies presenting a prominent disc show higher $L_{[\mathrm{C_{II}}]}/L_{\mathrm{IR}}$ ratios than those which do not present disc-like morphologies.

PDR analysis suggests that these disturbed galaxies, which probably have more violent star formation episodes, have higher gas densities and radiation fields. The large amount of free electrons (from dust grains via photoelectric effect) in these systems may ionize most of their atomic Carbon content within the PDRs, resulting in an inefficient gas cooling through the [C II] emission line and a lack of the observed [C II] luminosity compared to the IR luminosity.

To test if rotationally supported galaxies are prone to develop gravitational instabilities, I performed an analysis the sources in the $f_{\mathrm{H_2}} - V_{\mathrm{rot}}/\sigma_v$ phase plane in which I compare with expected values for a marginally stable gaseous thin disc ($Q_{\mathrm{gas}} = 1$), a gaseous thick disc ($Q_{\mathrm{thick}} = 1$) and a two component disc (stars plus gas; $Q_{\mathrm{gas+stars}} = 1$). From eleven galaxies classified as rotationally supported systems, I find that three galaxies are consistent with $Q_{\mathrm{gas}} \approx 1$, i.e., are prone to develop gravitational instabilities. The other eight systems have measured $Q_{\mathrm{gas}} \gtrsim 1$. This conclusion is not changed if I apply the thick disc gravitational stability analysis as the kinematic estimates are not enough accurate. However, within the two component disc gravitational framework, more VALES galaxies may be classified as gravitational unstable discs ($Q_2 < 1$) depending on their stellar dynamics. Thus, stellar dynamics measurements are critical to study the gravitational stability in galaxies, except for gas-rich galaxies where the self-gravity is mainly dictated by the gaseous ISM phase alone.

One of the main results in the analysis is that I have been able to characterize the star formation activity in terms of galactic dynamics, avoiding assumptions about the CO-to-H_2 conversion factor. This allows to put confident constraints on the SFR$-L'_{\rm CO}/t_{\rm orb}$ and SFR$-L'_{\rm CO}/t_{\rm cross}$ relations, where $t_{\rm orb}$ and $t_{\rm cross}$ are the orbital and crossing times. I find a correlation between SFR and $L'_{\rm CO}/t_{\rm orb}$, with a best-fit power-law slope of 1.21±0.13. I suggest that the SFR$-L'_{\rm CO}/t_{\rm orb}$ correlation is affected by the decrease of $V_{\rm rot}$ (thus, an increase of $t_{\rm orb}$) due to pressure gradient support to the gravitational potential in systems with low $V_{\rm rot}/\sigma_v$ ratio. I find that the proxy of the 'star formation efficiency' (SFE$' \propto$ SFR$/L'_{\rm CO}$) is correlated with crossing time, suggesting a constant efficiency per crossing time of ∼0.6. Therefore, by knowing the size, SFR, and mean velocity dispersion of a galaxy, my studies reveal that it is possible to estimate its molecular gas mass. This correlation may also imply an apparent evolution star formation efficiency (when it is not normalized by $t_{\rm cross}$) with cosmic time as galaxies at higher redshifts tend to show higher velocity dispersion values. By considering the better correlation between SFE$'$ and $t_{\rm cross}$, I propose that the radial crossing time may be the characteristic timescale in which the star formation occurs in these systems (see Chapter 5 for details).

In this thesis, I have found that the molecular gas in galaxies beyond the local Universe seems to be turbulent, with velocity dispersion values comparable to that seen from the ionized gas ISM phase. However, due to the limited spatial resolution of the galaxy observations at low-redshift and the low number statistics at high-redshift traduce to the need of more spatially-resolved observations of the cold H_2 gas. This seems to be critical as large-scale near-IR and optical IFS surveys of hundreds and thousands of objects are currently being observed at high- and low-redshifts (e.g. SAMI and KROSS surveys). Carry on large molecular gas galaxy surveys is now possible with ALMA and NOEMA, allowing observations with sub-arcsecond resolution and delivering kpc-scale kinematic and morphology data for 'typical' star-forming galaxies across cosmic time. Is common that the molecular gas kinematics is correlated to the ionized gas kinematics on high-redshift galaxies?. The super-giant HII regions seen in galaxies at high-redshift have their corresponding super-GMC counterparts?. It will be a though task as even with the full ALMA array it is needed nearly ∼7 hours to observe the CO emission at kpc-scales from just one 'typical' star-forming galaxy at $z \sim 1$.

These molecular gas observations will also enable the exploration of the star-formation law on turbulent galaxy environments at low- and high-redshifts. They will allow to determine whether the star formation efficiency depends on the global or local galactic dynamics (e.g. Daddi et al. 2010; Krumholz et al. 2012). Is the star formation efficiency enhanced by turbulence? Its depends on $t_{\rm cross}$?. This is a very important research area as the star formation process is key to determine how galaxies have evolved across cosmic time. Nevertheless it is also a key theoretical ingredient added to numerical galaxy formation simulations (often named 'sub-grid physics'). However, it should be noted that the IFS surveys trace the star formation activity by observing the optical and near-IR emisson lines, i.e. the non-obscured star formation activity. In these surveys, the extinction correction rely on SED fitting techniques or prescriptions based on stacked IR luminosity profiles (e.g. Garn & Best 2010). These techniques also assume a very idealized dust distribution across the galactic discs. With ALMA is now possible to study the dust extinction in an spatially-resolved approach. This may help to characterize the dust extinction and the obscured star-formation activity on dusty galaxies.

Future AO surveys will also be important. The merger fraction values estimated in Chapter 3 are very uncertain, principally as the number statistics is low. More kpc-scale observations are needed to better constrain the merger fraction for 'typical' star-forming galaxies and its evolution with cosmic time. However, AO observations require for bright guide stars (even with the laser guide star mode) near the observing target in order to correct the wavefront, a limitation that ALMA does not suffer. Moreover, imperfect optical corrections lead to very low Strehl ratio values, i.e. low observational sensitivity, producing the need of long exposure times to overcome this effect. Next generation AO systems will deliver higher Strehl ratios, with sensitive near-IR wavefront sensors which will allow the use of fainter stars as guide stars (Max et al., 2008). The advent of 20-40 m class telescopes during the next decade will also help by increasing the light gathering power and the AO resolution (from the diffraction limit), overcoming the kpc-scale spatial resolution limit and allow the study of very compact galaxies at high-redshifts (e.g. van Dokkum et al. 2008; Wuyts et al. 2011). Nevertheless, ALMA and IFS observations of gravitationally-lensed galaxies may also be common as the Large Synoptic Sky Telescope (LSST, Tyson 2002) will deliver thousands of tens of thousands of new strong-lens candidates to be studied.

As a future work, I am leading one ALMA Cycle-7 proposal to expand the morpho-kinematic study of the molecular gas content on galaxies at high-redshift. I am aiming to spatially-resolve the CO(2-1) emission on ∼kpc-scales for three 'main-sequence' star-forming galaxies selected from the KGES survey at $z \sim 1.5$. This will allow me to compare the ionized and molecular gas kinematics along with the study of the star formation activity in a similar manner to the presented for the SHiZELS-19 galaxy. At $z \sim 0.1$, I'm carrying on a similar joint analysis between the ionized and molecular gas kinematics by observing the CO(1-0) and Paα emission lines for three galaxies taken from the VALES survey. The observation of the Paα emission line allows the study of the ionized gas phase with minimal extinction effects. Also, I'm observing the molecular gas content in optically-selected starburst galaxies at $z \sim 0.2$ taken from the MESS survey. These systems will complement the VALES and APEX/SEPIA dusty obscured starburst galaxy sample in order to test whether the proxy of the star formation efficiency increases with SFR or not.

Bibliography

Abazajian, K. N., Adelman-McCarthy, J. K., Agüeros, M. A., et al. 2009, ApJS, 182, 543

Accurso, G., Saintonge, A., Catinella, B., et al. 2017, MNRAS, 470, 4750

Alaghband-Zadeh, S., Chapman, S. C., Swinbank, A. M., et al. 2012, MNRAS, 424, 2232

Allen, J. T., Croom, S. M., Konstantopoulos, I. S., et al. 2015, MNRAS, 446, 1567

Allen, R. J. 1975, in La Dynamique des galaxies spirales, ed. L. Weliachew, Vol. 241, 157

Allington-Smith, J. 2006, NewAR, 50, 244

Andersen, D. R., Bershady, M. A., Sparke, L. S., et al. 2006, ApJS, 166, 505

Argyle, E. 1965, ApJ, 141, 750

Arribas, S., Colina, L., Bellocchi, E., Maiolino, R., & Villar-Martín, M. 2014, A&A, 568, A14

Asplund, M., Grevesse, N., Sauval, A. J., & Scott, P. 2009, Annual Review of Astronomy and Astrophysics, 47, 481

Babcock, H. W. 1941, Ciel et Terre, 57, 91

Baldry, I. K., Glazebrook, K., Brinkmann, J., et al. 2004, ApJ, 600, 681

Baldwin, J. A., Phillips, M. M., & Terlevich, R. 1981, PASP, 93, 5

Belfiore, F., Maiolino, R., Maraston, C., et al. 2016, MNRAS, 461, 3111

Bell, E. F., van der Wel, A., Papovich, C., et al. 2012, ApJ, 753, 167

Bellocchi, E., Arribas, S., & Colina, L. 2012, A&A, 542, A54

Bershady, M. A., Verheijen, M. A. W., Swaters, R. A., et al. 2010, ApJ, 716, 198

Best, P., Smail, I., Sobral, D., et al. 2013, in Thirty Years of Astronomical Discovery with UKIRT, Vol. 37, 235

Bigiel, F., Leroy, A., Walter, F., et al. 2008, AJ, 136, 2846

Binney, J., & Tremaine, S. 2008, Galactic Dynamics: Second Edition

Blanc, G. A., Heiderman, A., Gebhardt, K., Evans, Neal J., I., & Adams, J. 2009, ApJ, 704, 842

Blanton, M. R., & Moustakas, J. 2009, ARA&A, 47, 159

Bloom, J. V., Croom, S. M., Bryant, J. J., et al. 2018, MNRAS, 476, 2339

Bluck, A. F. L., Conselice, C. J., Bouwens, R. J., et al. 2009, MNRAS, 394, L51

Blumenthal, G. R., Faber, S. M., Primack, J. R., & Rees, M. J. 1985, Nature, 313, 72

Bolatto, A. D., Leroy, A. K., Rosolowsky, E., Walter, F., & Blitz, L. 2008, ApJ, 686, 948

Bolatto, A. D., Wolfire, M., & Leroy, A. K. 2013, Annual Review of Astronomy and Astrophysics, 51, 207

Bolatto, A. D., Wong, T., Utomo, D., et al. 2017, ApJ, 846, 159

Bothwell, M. S., Smail, I., Chapman, S. C., et al. 2013, MNRAS, 429, 3047

Bournaud, F., Elmegreen, B. G., & Elmegreen, D. M. 2007, ApJ, 670, 237

Bournaud, F., Elmegreen, B. G., & Martig, M. 2009, ApJ, 707, L1

Bourne, N., Dunne, L., Maddox, S. J., et al. 2016, MNRAS, 462, 1714

Bouwens, R. J., Illingworth, G. D., Oesch, P. A., et al. 2011, ApJ, 737, 90

Brammer, G. B., van Dokkum, P. G., Franx, M., et al. 2012, ApJS, 200, 13

Bridge, C. R., Appleton, P. N., Conselice, C. J., et al. 2007, ApJ, 659, 931

Brinchmann, J., Charlot, S., White, S. D. M., et al. 2004, MNRAS, 351, 1151

Brown, R. L., & Vanden Bout, P. A. 1991, AJ, 102, 1956

Bruce, V. A., Dunlop, J. S., Cirasuolo, M., et al. 2012, MNRAS, 427, 1666

Bruzual, G. 2007, in Astronomical Society of the Pacific Conference Series, Vol. 374, From Stars to Galaxies: Building the Pieces to Build Up the Universe, ed. A. Vallenari, R. Tantalo, L. Portinari, & A. Moretti, 303

Bruzual, G., & Charlot, S. 2003, MNRAS, 344, 1000

Bryant, J. J., Owers, M. S., Robotham, A. S. G., et al. 2015, MNRAS, 447, 2857

Bundy, K., Bershady, M. A., Law, D. R., et al. 2015, ApJ, 798, 7

Burkert, A., Genzel, R., Bouché, N., et al. 2010, ApJ, 725, 2324

Burkert, A., Förster Schreiber, N. M., Genzel, R., et al. 2016, ApJ, 826, 214

Calabrò, A., Daddi, E., Cassata, P., et al. 2018, ApJL, 862, L22

Calistro Rivera, G., Hodge, J. A., Smail, I., et al. 2018, ApJ, 863, 56

Calzetti, D., Armus, L., Bohlin, R. C., et al. 2000, ApJ, 533, 682

Cappellari, M., Emsellem, E., Bacon, R., et al. 2007, MNRAS, 379, 418

Carilli, C. L., & Walter, F. 2013, ARA&A, 51, 105

Chabrier, G. 2003, PASP, 115, 763

Charbonneau, P. 1995, ApJS, 101, 309

Chen, C.-C., Hodge, J. A., Smail, I., et al. 2017, ApJ, 846, 108

Cheng, C., Ibar, E., Hughes, T. M., et al. 2018, MNRAS, 475, 248

Cole, S., Lacey, C. G., Baugh, C. M., & Frenk, C. S. 2000, MNRAS, 319, 168

Colina, L., Arribas, S., & Monreal-Ibero, A. 2005, ApJ, 621, 725

Collins, J. A., & Rand, R. J. 2001, ApJ, 551, 57

Combes, F., García-Burillo, S., Braine, J., et al. 2013, A&A, 550, A41

Conselice, C. J., Bershady, M. A., Dickinson, M., & Papovich, C. 2003, AJ, 126, 1183

Conselice, C. J., Gallagher, John S., I., & Wyse, R. F. G. 2002, AJ, 123, 2246

Conselice, C. J., Rajgor, S., & Myers, R. 2008, MNRAS, 386, 909

Conselice, C. J., Yang, C., & Bluck, A. F. L. 2009, MNRAS, 394, 1956

Contini, T., Garilli, B., Le Fèvre, O., et al. 2012, A&A, 539, A91

Cortese, L., Fogarty, L. M. R., Bekki, K., et al. 2016, MNRAS, 463, 170

Courteau, S. 1997, AJ, 114, 2402

Crain, R. A., Theuns, T., Dalla Vecchia, C., et al. 2009, MNRAS, 399, 1773

Crain, R. A., Schaye, J., Bower, R. G., et al. 2015, MNRAS, 450, 1937

Cresci, G., Hicks, E. K. S., Genzel, R., et al. 2009, ApJ, 697, 115

da Cunha, E., Charlot, S., & Elbaz, D. 2008, MNRAS, 388, 1595

Daddi, E., Alexander, D. M., Dickinson, M., et al. 2007, ApJ, 670, 173

Daddi, E., Bournaud, F., Walter, F., et al. 2010, ApJ, 713, 686

Dalgarno, A., & McCray, R. A. 1972, ARA&A, 10, 375

Danielson, A. L. R., Swinbank, A. M., Smail, I., et al. 2011, MNRAS, 410, 1687

Davies, R., Förster Schreiber, N. M., Cresci, G., et al. 2011, ApJ, 741, 69

de Blok, W. J. G., Walter, F., Brinks, E., et al. 2008, AJ, 136, 2648

de Vaucouleurs, G. 1958, ApJ, 128, 465

—. 1959, ApJ, 130, 728

de Zeeuw, T., & Franx, M. 1991, ARA&A, 29, 239

Dekel, A., & Burkert, A. 2014, MNRAS, 438, 1870

Dekel, A., Sari, R., & Ceverino, D. 2009a, ApJ, 703, 785

Dekel, A., Birnboim, Y., Engel, G., et al. 2009b, Nature, 457, 451

Denicoló, G., Terlevich, R., & Terlevich, E. 2002, MNRAS, 330, 69

Di Teodoro, E. M., Fraternali, F., & Miller, S. H. 2016, A&A, 594, A77

Díaz-Santos, T., Armus, L., Charmandaris, V., et al. 2013, ApJ, 774, 68

Dickman, R. L., Snell, R. L., & Schloerb, F. P. 1986, ApJ, 309, 326

Downes, D., & Solomon, P. M. 1998, ApJ, 507, 615

Downes, D., Solomon, P. M., & Radford, S. J. E. 1993, ApJ, 414, L13

Draine, B. T., Dale, D. A., Bendo, G., et al. 2007, ApJ, 663, 866

Drew, P. M., Casey, C. M., Burnham, A. D., et al. 2018, ApJ, 869, 58

Driver, S. P., Wright, A. H., Andrews, S. K., et al. 2016, MNRAS, 455, 3911

Eales, S., Dunne, L., Clements, D., et al. 2010, PASP, 122, 499

Eisenhauer, F., Abuter, R., Bickert, K., et al. 2003, in Proc. SPIE, Vol. 4841, Instrument Design and Performance for Optical/Infrared Ground-based Telescopes, ed. M. Iye & A. F. M. Moorwood, 1548–1561

Elbaz, D., Dickinson, M., Hwang, H. S., et al. 2011, A&A, 533, A119

Elbaz, D., Leiton, R., Nagar, N., et al. 2018, A&A, 616, A110

Elmegreen, B. G. 2011, ApJ, 737, 10

Elmegreen, B. G., Morris, M., & Elmegreen, D. M. 1980, ApJ, 240, 455

Epinat, B., Amram, P., Balkowski, C., & Marcelin, M. 2010, MNRAS, 401, 2113

Epinat, B., Contini, T., Le Fèvre, O., et al. 2009, A&A, 504, 789

Epinat, B., Tasca, L., Amram, P., et al. 2012, A&A, 539, A92

Escala, A., & Larson, R. B. 2008, ApJL, 685, L31

Espada, D., Martin, S., Verley, S., et al. 2018, ApJ, 866, 77

Faucher-Giguère, C.-A., Quataert, E., & Hopkins, P. F. 2013, MNRAS, 433, 1970

Feldmann, R., Gnedin, N. Y., & Kravtsov, A. V. 2012, ApJ, 747, 124

Finkelstein, S. L., Papovich, C., Ryan, R. E., et al. 2012, ApJ, 758, 93

Fisher, D. B., Glazebrook, K., Bolatto, A., et al. 2014, ApJ, 790, L30

Fisher, D. B., Glazebrook, K., Damjanov, I., et al. 2017, MNRAS, 464, 491

Fisher, K. B., Bahcall, J. N., Kirhakos, S., & Schneider, D. P. 1996, ApJ, 468, 469

Foreman-Mackey, D., Hogg, D. W., Lang, D., & Goodman, J. 2013, PASP, 125, 306

Förster Schreiber, N. M., Genzel, R., Lehnert, M. D., et al. 2006, ApJ, 645, 1062

Förster Schreiber, N. M., Genzel, R., Bouché, N., et al. 2009, ApJ, 706, 1364

Förster Schreiber, N. M., Renzini, A., Mancini, C., et al. 2018, The Astrophysical Journal Supplement Series, 238, 21

Freeman, K. C. 1970, ApJ, 160, 811

Garn, T., & Best, P. N. 2010, MNRAS, 409, 421

Geach, J. E., Smail, I., Best, P. N., et al. 2008, MNRAS, 388, 1473

Geach, J. E., Smail, I., Moran, S. M., et al. 2011, ApJ, 730, L19

Geach, J. E., Sobral, D., Hickox, R. C., et al. 2012, MNRAS, 426, 679

Genzel, R., Burkert, A., Bouché, N., et al. 2008, ApJ, 687, 59

Genzel, R., Tacconi, L. J., Gracia-Carpio, J., et al. 2010, MNRAS, 407, 2091

Genzel, R., Newman, S., Jones, T., et al. 2011, ApJ, 733, 101

Genzel, R., Tacconi, L. J., Kurk, J., et al. 2013, ApJ, 773, 68

Genzel, R., Tacconi, L. J., Lutz, D., et al. 2015, ApJ, 800, 20

Genzel, R., Schreiber, N. M. F., Übler, H., et al. 2017, Nature, 543, 397

Gilbank, D. G., Bower, R. G., Glazebrook, K., et al. 2011, MNRAS, 414, 304

Gillman, S., Swinbank, A. M., Tiley, A. L., et al. 2019, MNRAS, 727

Gilmore, G., King, I. R., van der Kruit, P. C., & Buser, R. 1990, Science, 250, 703

Girard, M., Dessauges-Zavadsky, M., Schaerer, D., et al. 2018, A&A, 613, A72

Glazebrook, K. 2013, PASA, 30, e056

Gnerucci, A., Marconi, A., Cresci, G., et al. 2011, A&A, 528, A88

Goddard, D., Thomas, D., Maraston, C., et al. 2017, MNRAS, 466, 4731

Goldreich, P., & Lynden-Bell, D. 1965, MNRAS, 130, 97

González Delgado, R. M., García-Benito, R., Pérez, E., et al. 2015, A&A, 581, A103

Green, A. W., Glazebrook, K., McGregor, P. J., et al. 2010, Nature, 467, 684

—. 2014, MNRAS, 437, 1070

Griffin, M. J., Abergel, A., Abreu, A., et al. 2010, A&A, 518, L3

Gullberg, B., De Breuck, C., Vieira, J. D., et al. 2015, MNRAS, 449, 2883

Guo, Y., Rafelski, M., Bell, E. F., et al. 2018, ApJ, 853, 108

Habing, H. J. 1968, Bulletin of the Astronomical Institutes of the Netherlands, 19, 421

Harrison, C. M., Alexander, D. M., Mullaney, J. R., & Swinbank, A. M. 2014, MNRAS, 441, 3306

Harrison, C. M., Johnson, H. L., Swinbank, A. M., et al. 2017, MNRAS, 467, 1965

Häussler, B., McIntosh, D. H., Barden, M., et al. 2007, ApJS, 172, 615

Helfer, T. T., Thornley, M. D., Regan, M. W., et al. 2003, ApJS, 145, 259

Hemmati, S., Mobasher, B., Darvish, B., et al. 2015, ApJ, 814, 46

Heyer, M., Krawczyk, C., Duval, J., & Jackson, J. M. 2009, ApJ, 699, 1092

Ho, I. T., Kewley, L. J., Dopita, M. A., et al. 2014, MNRAS, 444, 3894

Ho, I. T., Medling, A. M., Bland-Hawthorn, J., et al. 2016, MNRAS, 457, 1257

Hodge, J. A., Carilli, C. L., Walter, F., et al. 2012, ApJ, 760, 11

Hodge, J. A., Swinbank, A. M., Simpson, J. M., et al. 2016, ApJ, 833, 103

Hodge, J. A., Smail, I., Walter, F., et al. 2018, arXiv e-prints, arXiv:1810.12307

Holmberg, E. 1958, Meddelanden fran Lunds Astronomiska Observatorium Serie II, 136, 1

Hughes, T. M., Ibar, E., Villanueva, V., et al. 2017, A&A, 602, A49

Hung, C.-L., Rich, J. A., Yuan, T., et al. 2015, ApJ, 803, 62

Ibar, E., Sobral, D., Best, P. N., et al. 2013, MNRAS, 434, 3218

Ibar, E., Lara-López, M. A., Herrera-Camus, R., et al. 2015, MNRAS, 449, 2498

Jog, C. J. 1996, MNRAS, 278, 209

Jog, C. J., & Solomon, P. M. 1984, ApJ, 276, 114

Johnson, H. L., Harrison, C. M., Swinbank, A. M., et al. 2018, MNRAS, 474, 5076

Johnson, T. L., Rigby, J. R., Sharon, K., et al. 2017, ApJ, 843, L21

Jones, T. A., Swinbank, A. M., Ellis, R. S., Richard, J., & Stark, D. P. 2010, MNRAS, 404, 1247

Kampczyk, P., Lilly, S. J., Carollo, C. M., et al. 2007, ApJS, 172, 329

Karim, A., Schinnerer, E., Martínez-Sansigre, A., et al. 2011, ApJ, 730, 61

Kassin, S. A., Weiner, B. J., Faber, S. M., et al. 2007, ApJ, 660, L35

—. 2012, ApJ, 758, 106

Kaufman, M. J., Wolfire, M. G., & Hollenbach, D. J. 2006, ApJ, 644, 283

Kaufman, M. J., Wolfire, M. G., Hollenbach, D. J., & Luhman, M. L. 1999, ApJ, 527, 795

Kelvin, L. S., Driver, S. P., Robotham, A. S. G., et al. 2012, MNRAS, 421, 1007

Kennicutt, Robert C., J. 1998a, ApJ, 498, 541

Kennicutt, Robert C., J., Armus, L., Bendo, G., et al. 2003, PASP, 115, 928

Kennicutt, Robert C., J., Calzetti, D., Walter, F., et al. 2007, ApJ, 671, 333

Kennicutt, R. C., Calzetti, D., Aniano, G., et al. 2011, PASP, 123, 1347

Kennicutt, Jr., R. C. 1998b, ARA&A, 36, 189

Kereš, D., Katz, N., Weinberg, D. H., & Davé, R. 2005, MNRAS, 363, 2

Kewley, L. J., Maier, C., Yabe, K., et al. 2013, ApJ, 774, L10

Khostovan, A. A., Sobral, D., Mobasher, B., et al. 2015, MNRAS, 452, 3948

Koekemoer, A. M., Faber, S. M., Ferguson, H. C., et al. 2011, ApJS, 197, 36

Koo, D. C., Guzman, R., Faber, S. M., et al. 1995, ApJ, 440, L49

Kormendy, J., & Kennicutt, Robert C., J. 2004, ARA&A, 42, 603

Krajnović, D., Cappellari, M., de Zeeuw, P. T., & Copin, Y. 2006, MNRAS, 366, 787

Krajnović, D., Emsellem, E., Cappellari, M., et al. 2011, MNRAS, 414, 2923

Kramer, C., Abreu-Vicente, J., García-Burillo, S., et al. 2013, A&A, 553, A114

Kronberger, T., Kapferer, W., Schindler, S., & Ziegler, B. L. 2007, A&A, 473, 761

Krumholz, M. R., & Burkhart, B. 2016, MNRAS, 458, 1671

Krumholz, M. R., Dekel, A., & McKee, C. F. 2012, ApJ, 745, 69

Krumholz, M. R., & McKee, C. F. 2005, ApJ, 630, 250

Krumholz, M. R., & Tan, J. C. 2007, ApJ, 654, 304

Laag, E., Croft, S., Canalizo, G., & Lacy, M. 2010, AJ, 140, 2052

Lacey, C., & Cole, S. 1993, MNRAS, 262, 627

Lang, P., Wuyts, S., Somerville, R. S., et al. 2014, ApJ, 788, 11

Lang, P., Förster Schreiber, N. M., Genzel, R., et al. 2017, ApJ, 840, 92

Lara-López, M. A., Cepa, J., Bongiovanni, A., et al. 2010, A&A, 521, L53

Lara-López, M. A., Hopkins, A. M., López-Sánchez, A. R., et al. 2013, MNRAS, 434, 451

Larson, K. L., Sanders, D. B., Barnes, J. E., et al. 2016, ApJ, 825, 128

Larson, R. B. 1981, MNRAS, 194, 809

Law, D. R., Steidel, C. C., Erb, D. K., et al. 2007, ApJ, 669, 929

—. 2009, ApJ, 697, 2057

Law, D. R., Steidel, C. C., Shapley, A. E., et al. 2012, ApJ, 745, 85

Lehnert, M. D., Nesvadba, N. P. H., Le Tiran, L., et al. 2009, ApJ, 699, 1660

Lequeux, J. 1979, A&A, 80, 35

Leroy, A. K., Walter, F., Brinks, E., et al. 2008, AJ, 136, 2782

Leroy, A. K., Walter, F., Bigiel, F., et al. 2009, AJ, 137, 4670

Leroy, A. K., Walter, F., Sandstrom, K., et al. 2013, AJ, 146, 19

Leung, G. Y. C., Leaman, R., van de Ven, G., et al. 2018, MNRAS, 477, 254

Levy, R. C., Bolatto, A. D., Teuben, P., et al. 2018, ApJ, 860, 92

Lilly, S. J., Le Fevre, O., Crampton, D., Hammer, F., & Tresse, L. 1995, ApJ, 455, 50

Lin, C. C., & Shu, F. H. 1964, ApJ, 140, 646

—. 1966, Proceedings of the National Academy of Science, 55, 229

Lin, L., Patton, D. R., Koo, D. C., et al. 2008, ApJ, 681, 232

Lindblad, B. 1959, Handbuch der Physik, 53, 21

Liske, J., Baldry, I. K., Driver, S. P., et al. 2015, MNRAS, 452, 2087

Lotz, J. M., Primack, J., & Madau, P. 2004, AJ, 128, 163

Lotz, J. M., Davis, M., Faber, S. M., et al. 2008, ApJ, 672, 177

Lovell, M. R., Pillepich, A., Genel, S., et al. 2018, MNRAS, 481, 1950

Lowe, S. A., Roberts, W. W., Yang, J., Bertin, G., & Lin, C. C. 1994, ApJ, 427, 184

Madau, P., & Dickinson, M. 2014, ARA&A, 52, 415

Madau, P., Ferguson, H. C., Dickinson, M. E., et al. 1996, MNRAS, 283, 1388

Madden, S. C., Geis, N., Genzel, R., et al. 1993, ApJ, 407, 579

Malhotra, S., Helou, G., Stacey, G., et al. 1997, ApJ, 491, L27

Malhotra, S., Kaufman, M. J., Hollenbach, D., et al. 2001, ApJ, 561, 766

Mannucci, F., Cresci, G., Maiolino, R., Marconi, A., & Gnerucci, A. 2010, MNRAS, 408, 2115

Markwardt, C. B. 2009, in Astronomical Society of the Pacific Conference Series, Vol. 411, Astronomical Data Analysis Software and Systems XVIII, ed. D. A. Bohlender, D. Durand, & P. Dowler, 251

Martig, M., Bournaud, F., Teyssier, R., & Dekel, A. 2009, ApJ, 707, 250

Max, C., McGrath, E., Gavel, D., et al. 2008, in Society of Photo-Optical Instrumentation Engineers (SPIE) Conference Series, Vol. 7015, Proc. SPIE, 701507

Mayall, N. U., & Aller, L. H. 1942, ApJ, 95, 5

McCarthy, I. G., Font, A. S., Crain, R. A., et al. 2012, MNRAS, 420, 2245

McGaugh, S. S. 2012, AJ, 143, 40

McGaugh, S. S., & de Blok, W. J. G. 1998, ApJ, 499, 41

Miller, S. H., Bundy, K., Sullivan, M., Ellis, R. S., & Treu, T. 2011, ApJ, 741, 115

Miller, S. H., Ellis, R. S., Sullivan, M., et al. 2012, ApJ, 753, 74

Mogotsi, K. M., de Blok, W. J. G., Caldú-Primo, A., et al. 2016, AJ, 151, 15

Molina, J., Ibar, E., Smail, I., et al. 2019a, MNRAS, 487, 4856

Molina, J., Ibar, E., Swinbank, A. M., et al. 2017, MNRAS, 466, 892

Molina, J., Ibar, E., Villanueva, V., et al. 2019b, MNRAS, 482, 1499

Mosenkov, A. V., Sotnikova, N. Y., Reshetnikov, V. P., Bizyaev, D. V., & Kautsch, S. J. 2015, MNRAS, 451, 2376

Motta, V., Ibar, E., Verdugo, T., et al. 2018, ApJ, 863, L16

Narayanan, D., Krumholz, M. R., Ostriker, E. C., & Hernquist, L. 2012, MNRAS, 421, 3127

Neugebauer, G., Habing, H. J., van Duinen, R., et al. 1984, ApJ, 278, L1

Newman, S. F., Genzel, R., Förster Schreiber, N. M., et al. 2013, ApJ, 767, 104

Noeske, K. G., Weiner, B. J., Faber, S. M., et al. 2007, ApJ, 660, L43

Nozawa, T., & Kozasa, T. 2013, ApJ, 776, 24

Oberst, T. E., Parshley, S. C., Stacey, G. J., et al. 2006, ApJ, 652, L125

Obreschkow, D., Croton, D., De Lucia, G., Khochfar, S., & Rawlings, S. 2009, ApJ, 698, 1467

Osterbrock, D. E. 1989, Astrophysics of gaseous nebulae and active galactic nuclei

Pannella, M., Carilli, C. L., Daddi, E., et al. 2009, ApJL, 698, L116

Papadopoulos, P. P., & Seaquist, E. R. 1999, ApJ, 516, 114

Papadopoulos, P. P., van der Werf, P., Xilouris, E., Isaak, K. G., & Gao, Y. 2012, ApJ, 751, 10

Pasetto, S., Grebel, E. K., Zwitter, T., et al. 2012, A&A, 547, A70

Patrício, V., Richard, J., Carton, D., et al. 2018, MNRAS, 477, 18

Pease, F. G. 1916, Proceedings of the National Academy of Science, 2, 517

Peng, C. Y., Ho, L. C., Impey, C. D., & Rix, H.-W. 2010, AJ, 139, 2097

Pérez, E., Cid Fernandes, R., González Delgado, R. M., et al. 2013, ApJ, 764, L1

Peterson, C. J., Rubin, V. C., Ford, W. K., J., & Thonnard, N. 1978, ApJ, 219, 31

Pettini, M., & Pagel, B. E. J. 2004, MNRAS, 348, L59

Pilbratt, G. L., Riedinger, J. R., Passvogel, T., et al. 2010, A&A, 518, L1

Pineda, J. L., Langer, W. D., & Goldsmith, P. F. 2014, A&A, 570, A121

Pineda, J. L., Langer, W. D., Velusamy, T., & Goldsmith, P. F. 2013, A&A, 554, A103

Piqueras López, J., Colina, L., Arribas, S., Alonso-Herrero, A., & Bedregal, A. G. 2012, A&A, 546, A64

Pizagno, J., Prada, F., Weinberg, D. H., et al. 2005, ApJ, 633, 844

Poglitsch, A., Waelkens, C., Geis, N., et al. 2010, A&A, 518, L2

Price, S. H., Kriek, M., Barro, G., et al. 2019, arXiv e-prints, arXiv:1902.09554

Queyrel, J., Contini, T., Kissler-Patig, M., et al. 2012, A&A, 539, A93

Rafikov, R. R. 2001, MNRAS, 323, 445

Rahman, N., Bolatto, A. D., Wong, T., et al. 2011, ApJ, 730, 72

Rahman, N., Bolatto, A. D., Xue, R., et al. 2012, ApJ, 745, 183

Reddy, N. A., Steidel, C. C., Pettini, M., et al. 2008, ApJS, 175, 48

Regan, M. W., Thornley, M. D., Helfer, T. T., et al. 2001, ApJ, 561, 218

Rengarajan, T. N., & Verma, R. P. 1986, A&A, 165, 300

Rickard, L. J., Palmer, P., Morris, M., Zuckerman, B., & Turner, B. E. 1975, ApJ, 199, L75

Roberts, M. S., & Rots, A. H. 1973, A&A, 26, 483

Rodighiero, G., Daddi, E., Baronchelli, I., et al. 2011, ApJL, 739, L40

Rodríguez del Pino, B., Arribas, S., Piqueras López, J., Villar-Martín, M., & Colina, L. 2019, MNRAS, 486, 344

Röllig, M., Abel, N. P., Bell, T., et al. 2007, A&A, 467, 187

Romeo, A. B. 1992, MNRAS, 256, 307

Romeo, A. B., Burkert, A., & Agertz, O. 2010, MNRAS, 407, 1223

Romeo, A. B., & Falstad, N. 2013, MNRAS, 433, 1389

Romeo, A. B., & Wiegert, J. 2011, MNRAS, 416, 1191

Rots, A. H. 1975, A&A, 45, 43

Rubin, V. C., Ford, W. K., J., & Thonnard, N. 1978, ApJ, 225, L107

Rubin, V. C., & Ford, W. Kent, J. 1970, ApJ, 159, 379

Saintonge, A., Kauffmann, G., Wang, J., et al. 2011, MNRAS, 415, 61

Saintonge, A., Tacconi, L. J., Fabello, S., et al. 2012, ApJ, 758, 73

Saintonge, A., Lutz, D., Genzel, R., et al. 2013, ApJ, 778, 2

Sakamoto, S., Hasegawa, T., Handa, T., Hayashi, M., & Oka, T. 1997, ApJ, 486, 276

Sánchez, S. F., Kennicutt, R. C., Gil de Paz, A., et al. 2012, A&A, 538, A8

Sánchez, S. F., Rosales-Ortega, F. F., Iglesias-Páramo, J., et al. 2014, A&A, 563, A49

Sandstrom, K. M., Leroy, A. K., Walter, F., et al. 2013, ApJ, 777, 5

Sargent, M. T., Béthermin, M., Daddi, E., & Elbaz, D. 2012, ApJL, 747, L31

Schaye, J., Crain, R. A., Bower, R. G., et al. 2015, MNRAS, 446, 521

Schmidt, M. 1959, ApJ, 129, 243

Schreiber, C., Elbaz, D., Pannella, M., et al. 2016, A&A, 589, A35

Scoville, N. Z., & Solomon, P. M. 1975, ApJ, 199, L105

Sérsic, J. L. 1963, Boletin de la Asociacion Argentina de Astronomia La Plata Argentina, 6, 41

Shapiro, K. L., Genzel, R., Förster Schreiber, N. M., et al. 2008, ApJ, 682, 231

Shapley, A. E. 2011, ARA&A, 49, 525

Sheth, K., Vogel, S. N., Regan, M. W., Thornley, M. D., & Teuben, P. J. 2005, ApJ, 632, 217

Shetty, R., Glover, S. C., Dullemond, C. P., et al. 2011, MNRAS, 415, 3253

Shields, G. A. 1990, ARA&A, 28, 525

Silk, J. 1997, ApJ, 481, 703

Simard, L., & Pritchet, C. J. 1998, ApJ, 505, 96

Simons, R. C., Kassin, S. A., Weiner, B. J., et al. 2017, ApJ, 843, 46

Simpson, J. M., Smail, I., Swinbank, A. M., et al. 2015, ApJ, 799, 81

Slipher, V. M. 1914, Popular Astronomy, 22, 19

Smith, J. D. T., Croxall, K., Draine, B., et al. 2017, ApJ, 834, 5

Sobral, D., Best, P. N., Geach, J. E., et al. 2010, MNRAS, 404, 1551

Sobral, D., Best, P. N., Matsuda, Y., et al. 2012, MNRAS, 420, 1926

Sobral, D., Best, P. N., Smail, I., et al. 2011, MNRAS, 411, 675

—. 2014, MNRAS, 437, 3516

Sobral, D., Kohn, S. A., Best, P. N., et al. 2016, MNRAS, 457, 1739

Sobral, D., Smail, I., Best, P. N., et al. 2013a, MNRAS, 428, 1128

Sobral, D., Best, P. N., Geach, J. E., et al. 2009, MNRAS, 398, 75

Sobral, D., Swinbank, A. M., Stott, J. P., et al. 2013b, ApJ, 779, 139

Sobral, D., Matthee, J., Best, P. N., et al. 2015, MNRAS, 451, 2303

Solomon, P. M., Downes, D., Radford, S. J. E., & Barrett, J. W. 1997, ApJ, 478, 144

Solomon, P. M., Rivolo, A. R., Barrett, J., & Yahil, A. 1987, ApJ, 319, 730

Solomon, P. M., Scoville, N. Z., Penzias, A. A., Wilson, R. W., & Jefferts, K. B. 1972, ApJ, 178, 125

Solomon, P. M., & Vanden Bout, P. A. 2005, Annual Review of Astronomy and Astrophysics, 43, 677

Sorba, R., & Sawicki, M. 2018, MNRAS, 476, 1532

Spergel, D. N., Bean, R., Doré, O., et al. 2007, ApJS, 170, 377

Springel, V., & Hernquist, L. 2003, MNRAS, 339, 289

Springel, V., White, S. D. M., Jenkins, A., et al. 2005, Nature, 435, 629

Stacey, G. J., Geis, N., Genzel, R., et al. 1991, ApJ, 373, 423

Stacey, G. J., Hailey-Dunsheath, S., Ferkinhoff, C., et al. 2010, ApJ, 724, 957

Stark, D. P., Swinbank, A. M., Ellis, R. S., et al. 2008, Nature, 455, 775

Stecker, F. W., Solomon, P. M., Scoville, N. Z., & Ryter, C. E. 1975, ApJ, 201, 90

Stott, J. P., Sobral, D., Smail, I., et al. 2013a, MNRAS, 430, 1158

Stott, J. P., Sobral, D., Bower, R., et al. 2013b, MNRAS, 436, 1130

Stott, J. P., Sobral, D., Swinbank, A. M., et al. 2014, MNRAS, 443, 2695

Stott, J. P., Swinbank, A. M., Johnson, H. L., et al. 2016, MNRAS, 457, 1888

Strateva, I., Ivezić, Ž., Knapp, G. R., et al. 2001, AJ, 122, 1861

Swinbank, A. M., Bower, R. G., Smith, G. P., et al. 2006, MNRAS, 368, 1631

Swinbank, A. M., Smail, I., Sobral, D., et al. 2012a, ApJ, 760, 130

Swinbank, A. M., Sobral, D., Smail, I., et al. 2012b, MNRAS, 426, 935

Swinbank, A. M., Papadopoulos, P. P., Cox, P., et al. 2011, ApJ, 742, 11

Swinbank, A. M., Dye, S., Nightingale, J. W., et al. 2015, ApJL, 806, L17

Swinbank, A. M., Harrison, C. M., Trayford, J., et al. 2017, MNRAS, 467, 3140

Tacconi, L. J., & Young, J. S. 1987, ApJ, 322, 681

Tacconi, L. J., Genzel, R., Smail, I., et al. 2008, ApJ, 680, 246

Tacconi, L. J., Genzel, R., Neri, R., et al. 2010, Nature, 463, 781

Tacconi, L. J., Neri, R., Genzel, R., et al. 2013, ApJ, 768, 74

Tacconi, L. J., Genzel, R., Saintonge, A., et al. 2018, ApJ, 853, 179

Teklu, A. F., Remus, R.-S., Dolag, K., et al. 2018, ApJ, 854, L28

Tescari, E., Cortese, L., Power, C., et al. 2018, MNRAS, 473, 380

Thomson, A. P., Simpson, J. M., Smail, I., et al. 2017, ApJ, 838, 119

Tielens, A. G. G. M., & Hollenbach, D. 1985, ApJ, 291, 722

Tiley, A. L., Bureau, M., Saintonge, A., et al. 2016a, MNRAS, 461, 3494

Tiley, A. L., Stott, J. P., Swinbank, A. M., et al. 2016b, MNRAS, 460, 103

Tiley, A. L., Swinbank, A. M., Harrison, C. M., et al. 2019, MNRAS, 485, 934

Tissera, P. B., Pedrosa, S. E., Sillero, E., & Vilchez, J. M. 2016, MNRAS, 456, 2982

Toomre, A. 1964, ApJ, 139, 1217

Topal, S., Bureau, M., Tiley, A. L., Davis, T. A., & Torii, K. 2018, MNRAS, 479, 3319

Tully, R. B., & Fisher, J. R. 1977, A&A, 500, 105

Turner, O. J., Cirasuolo, M., Harrison, C. M., et al. 2017, MNRAS, 471, 1280

Tyson, J. A. 2002, in Society of Photo-Optical Instrumentation Engineers (SPIE) Conference Series, Vol. 4836, Proc. SPIE, ed. J. A. Tyson & S. Wolff, 10–20

Übler, H., Genzel, R., Tacconi, L. J., et al. 2018, ApJ, 854, L24

Utreras, J., Becerra, F., & Escala, A. 2016, ApJ, 833, 13

Valiante, E., Smith, M. W. L., Eales, S., et al. 2016, MNRAS, 462, 3146

van de Hulst, H. C., Raimond, E., & van Woerden, H. 1957, Bulletin of the Astronomical Institutes of the Netherlands, 14, 1

van de Sande, J., Bland-Hawthorn, J., Fogarty, L. M. R., et al. 2017, ApJ, 835, 104

van der Kruit, P. C., & Allen, R. J. 1978, ARA&A, 16, 103

van der Kruit, P. C., & Freeman, K. C. 2011, ARA&A, 49, 301

van Dokkum, P. G., Franx, M., Kriek, M., et al. 2008, ApJL, 677, L5

Vergani, D., Epinat, B., Contini, T., et al. 2012, A&A, 546, A118

Verheijen, M. A. W. 2001, ApJ, 563, 694

Villanueva, V., Ibar, E., Hughes, T. M., et al. 2017, MNRAS, 470, 3775

Vincenzo, F., Belfiore, F., Maiolino, R., Matteucci, F., & Ventura, P. 2016, MNRAS, 458, 3466

Vogelsberger, M., Genel, S., Springel, V., et al. 2014, MNRAS, 444, 1518

Vogt, N. P., Forbes, D. A., Phillips, A. C., et al. 1996, ApJ, 465, L15

Walcher, C. J., Wisotzki, L., Bekeraité, S., et al. 2014, A&A, 569, A1

Walter, F., Brinks, E., de Blok, W. J. G., et al. 2008, AJ, 136, 2563

Walter, F., Cannon, J. M., Roussel, H., et al. 2007, ApJ, 661, 102

Warner, P. J., Wright, M. C. H., & Baldwin, J. E. 1973, MNRAS, 163, 163

Weiner, B. J., Willmer, C. N. A., Faber, S. M., et al. 2006, ApJ, 653, 1027

Welch, W. J., Thornton, D. D., Plambeck, R. L., et al. 1996, PASP, 108, 93

Westmoquette, M. S., Smith, L. J., & Gallagher, J. S. 2008, MNRAS, 383, 864

Whitaker, K. E., van Dokkum, P. G., Brammer, G., & Franx, M. 2012, ApJ, 754, L29

Whitaker, K. E., Franx, M., Leja, J., et al. 2014, ApJ, 795, 104

White, H. A., Fisher, D. B., Murray, N., et al. 2017, ApJ, 846, 35

Wiersma, R. P. C., Schaye, J., Theuns, T., Dalla Vecchia, C., & Tornatore, L. 2009, MNRAS, 399, 574

Wilkinson, D. M., Maraston, C., Thomas, D., et al. 2015, MNRAS, 449, 328

Wilson, R. W., Jefferts, K. B., & Penzias, A. A. 1970, ApJ, 161, L43

Wisnioski, E., Glazebrook, K., Blake, C., et al. 2012, MNRAS, 422, 3339

—. 2011, MNRAS, 417, 2601

Wisnioski, E., Förster Schreiber, N. M., Wuyts, S., et al. 2015, ApJ, 799, 209

Wong, T., & Blitz, L. 2002, ApJ, 569, 157

Wright, E. L., Eisenhardt, P. R. M., Mainzer, A. K., et al. 2010, AJ, 140, 1868

Wuyts, E., Wisnioski, E., Fossati, M., et al. 2016, ApJ, 827, 74

Wuyts, S., Förster Schreiber, N. M., van der Wel, A., et al. 2011, ApJ, 742, 96

Xu, C. K., Zhao, Y., Scoville, N., et al. 2012, ApJ, 747, 85

Xue, R., Fu, H., Isbell, J., et al. 2018, ApJ, 864, L11

Yoachim, P., & Dalcanton, J. J. 2008, ApJ, 682, 1004

Young, J. S., & Scoville, N. Z. 1991, ARA&A, 29, 581

Young, J. S., Xie, S., Tacconi, L., et al. 1995, ApJS, 98, 219

Zhang, K., Yan, R., Bundy, K., et al. 2017, MNRAS, 466, 3217

Zhou, L., Federrath, C., Yuan, T., et al. 2017, MNRAS, 470, 4573

Zolotov, A., Dekel, A., Mandelker, N., et al. 2015, MNRAS, 450, 2327